Technische Universität München
Physik Department E21 (Lehrstuhl für Experimentalphysik III)

Vortex Lattices in Superconducting Niobium and Skyrmion Lattices in Chiral MnSi: An Investigation by Neutron Scattering

Dipl.-Phys. Univ. Sebastian C. Mühlbauer

Vollständiger Abdruck der von der Fakultät für Physik der Technischen Universität München zur Erlangung des akademischen Grades eines

Doktors der Naturwissenschaften (Dr. rer. nat.)

genehmigten Dissertation.

Vorsitzender:	Univ.-Prof. (Komm. L.) Dr. Markus Garst
Prüfer der Dissertation:	1. Univ.-Prof. Dr. Peter Böni
	2. Univ.-Prof. Dr. Winfried Petry

Die Dissertation wurde am 04.11.2009 an der Technischen Universität München eingereicht und durch die Fakultät für Physik am 10.12.2009 angenommen.

0.1 Abstract

In our work we use small angle neutron scattering (SANS) as a versatile tool for the investigation of two different kinds of complex magnetic order: We examine the static and dynamic properties of the vortex lattice (VL) of the conventional superconductor niobium and we prove that a skyrmion lattice exists in the A-phase of the weak itinerant heli-magnet MnSi. Both the VL in superconductors and the skyrmion lattice in MnSi can be regarded as a macroscopic lattice, formed by topological entities with particle-like properties, emerging from continuous fields.

The structure and elasticity of condensed matter is determined by the particular interactions between their building blocks, the atoms. Similar to *crystal* lattices, the structural and dynamic properties of *superconducting* VLs reveal a deep insight into the characteristic vortex-vortex interactions. Especially deviations from the ideal six-fold VL symmetry sensitively reflect both the symmetry and nature of the superconducting order parameter, the morphology of the underlying Fermi surface as well as individual sample properties and purity [1]. The elastic matrix $\Phi_{\alpha,\beta}$ of a VL describes the energy, associated with a distortion of the VL due to thermal fluctuations, gradients of magnetic field or temperature, pinning and transport currents. Similar to the symmetry of VLs, the elastic constants c_{11} for compression, c_{44} for tilt and c_{66} for shear sensitively reflect the microscopic nature of the superconductivity [2, 3, 4, 5]. In addition, $\Phi_{\alpha,\beta}$ strongly influences the pinning/depinning properties of vortices and determines the thermal stability and the state of aggregation of vortex matter. This leads to a particular relevance for technical applications of superconductors.

However, the unambiguous mapping of different sources of anisotropy is intricate [1] for both the symmetry and the elastic matrix of VLs. The variety of different influences thus raises the question how to generalize the behaviour of VLs and vortex matter:

With its low Ginzburg-Landau parameter $\kappa = \lambda/\xi$, situated at the border of type-I and type-II superconductivity and the corresponding flat free energy landscape, niobium (Nb) is ideally suited as model system for systematic studies of vortex matter. Nb is characterized by isotropic single gap s-wave superconductivity [6, 7], avoiding the complexities of multi-gap systems and unconventional order parameters [1]. The low κ causes a high value of the lower critical field H_{c1}. For samples with a finite demagnetizing factor, this leads to an extended intermediate mixed state (IMS). The IMS is characterized by the macroscopic coexistence of Meissner phase and VL in Shubnikov-islands, reminiscent of the intermediate state of type-I superconductors. The emergence of the IMS reflects the underlying crossover from attractive to repulsive vortex interaction as function of temperature and magnetic field. The superconductivity in Nb thus allows to precisely tune the vortex-vortex interaction.

In this thesis, we present a comprehensive small angle neutron scattering study of the VL in an ultra-pure Nb single crystal sample, characterized by a residual resistivity ratio of $\sim 10^4$. We systematically investigate the morphology of vortex structures with the magnetic field applied along a four-fold $\langle 100 \rangle$ axis. Caused by the interplay of the four-fold crystal and the six-fold VL symmetry, a cornucopia of four different VL

phases emerges, comprising symmetry breaking structures combined with various lock-in transitions [8, 9, 10]. We succeed to deconvolute the general morphology of the VL and its orientation to three dominant mechanisms: First, non-local contributions, second, the transition between open and closed Fermi surface sheets and, third, the IMS between the Meissner and the Shubnikov phase [10]. Our study paves the way for systematic studies of superconducting VLs exhibiting a complex symmetry of the order parameter.

Until now, the microscopic access to the elastic matrix of VLs was only possible by means of surface sensitive techniques, however, strongly hampered by surface induced pinning effects. In this thesis, we present first time microscopic measurements of the intrinsic bulk VL tilt modulus c_{44} by means of time resolved stroboscopic small angle neutron scattering [11] in combination with a tailored magnetic field setup. In our study we find that the VL in Nb responds to an external force — in the form of a changed magnetic field — with an exponential relaxation, described qualitatively in good agreement with a damped diffusion model proposed by Brandt [12] and Kes [13].

As expected, the relaxation process shows increasing VL stiffness with increasing magnetic field and reduced damping with increasing temperature. Besides this general trend, we observe a dramatic changeover of the relaxation process associated with the non-trivial VL morphology in the IMS and the crossover from attractive to repulsive vortex-vortex interaction. This changeover is attributed to the decomposition of the VL into Shubnikov domains including a Landau-branching of the Shubnikov domains at the surface of the sample. Our study represents a show-case how to access directly VL melting, the formation of vortex-glass states and vortex pinning in unconventional superconductors, notably the cuprates, heavy-fermion, boro-carbide or ironarsenide systems.

It was discussed recently whether vortex-like structures and forms of order comprised of topological entities also occur in magnetism [14, 15, 16, 17, 18]. Similar to VLs in superconductors which are stabilized by the negative energy associated with a normal/superconducting interface, the stabilization of vortices by Bloch domain walls was proposed in ferromagnets [19, 20, 21, 22]. Especially systems exhibiting a helical magnetic order seem to be promising candidates for such structures, as they naturally favour a rotation of magnetic moments similar to Bloch domain walls. For ferro- or antiferromagnetic systems, crystallizing in structures lacking inversion symmetry, the Dyzhaloshinskii-Moriya (DM) interaction [23, 24] emerges which favours a perpendicular alignment of neighbouring spins. Together with ferromagnetic exchange on a stronger energy scale, this can lead to the formation of a helical arrangement of magnetic moments with a long pitch on an atomic scale. Furthermore, the long pitch leads to an efficient decoupling of the magnetic structure and the crystal lattice.

The archetypal helical magnet MnSi crystallizes in the cubic B20 structure, lacking inversion symmetry. MnSi exhibits itinerant helical ferromagnetism below a transition temperature $T_c = 29.5\,\mathrm{K}$, explained quantitatively by a Stoner model, including corrections arising from enhanced fluctuations [25] in combination with the DM interaction. The magnetic phase diagram of MnSi is characterized by four distinct phases: Below the critical field H_{c1}, the helices are pinned by weak crystal field anisotropy to the crystalline $\langle 111 \rangle$ directions. Above H_{c1}, the helices realign into the magnetic field direction until at

H_{c2} a field polarized state is reached. In vicinity of T_c at approximately $1/2H_{c2}$, a small phase pocket, called A-phase, separated by weak first order phase transitions [26] was found where neutron scattering studies established a perpendicular alignment of helices and magnetic field [27, 28, 29].

In our work, we use small angle neutron scattering to establish the existence of a skyrmion lattice in the A-phase of MnSi [30]. Due to a parallel alignment of the magnetic field with respect to the neutron beam, we are able to resolve the complete magnetic structure of the A-phase: The structure in the A-phase, reminiscent of a vortex lattice, consists of topological knots of the magnetization with particle-like properties, arranged in a regular six-fold lattice. The orientation of this lattice is strictly driven by the orientation of the applied magnetic field, regardless of the underlying crystal symmetry. The periodicity of the observed structure is much larger, compared to the atomic spacing of MnSi.

A Ginzburg-Landau ansatz analog to [31] shows that in the presence of a uniform magnetization $\mathbf{M}_f$, the quartic $\mathbf{M}^4$-term is effectively cubic in the modulated moment amplitudes, giving rise to a triple-$\mathbf{q}$ structure: A mean field model yields that a spin crystal, composed by the superposition of three single-$\mathbf{k}$ helices perpendicular to the magnetic field inclined at an angle of 120° with respect to each other represents a meta-stable state. Including Gaussian fluctuations reduces the energy of the spin crystal which then assumes a stable ground state. The spin crystal was identified as skyrmion lattice: The integration of the winding density yields a topological charge $C_{top} = -1$ per unit cell of the skyrmion lattice, proving the existence of stable topological solitons of the magnetization.

Zusammenfassung

In dieser Dissertation wird Neutronen Kleinwinkelstreuung als vielseitige Messmethode benutzt, um zwei verschiedene Formen von komplexer magnetischer Ordnung zu untersuchen: Es werden sowohl die statischen als auch die dynamischen Eigenschaften des Flussgitters des konventionellen Supraleiters Niob untersucht. Weitere durchgeführte Messungen weisen die Existenz eines Skyrmion-Gitters in der A-Phase des schwachen itineranten helikalen Magneten MnSi nach. Sowohl Flussgitter in Supraleitern als auch das Skyrmion-Gitter in MnSi können als makroskopisches Gitter, bestehend aus topologischen Objekten mit teilchenartigen Eigenschaften beschrieben werden.

Die strukturellen und dynamischen Eigenschaften kondensierter Materie werden durch die zugrundeliegenden Wechselwirkungen zwischen ihren Bausteinen, den Atomen, bestimmt. Ebenso wie bei *Kristallgittern* erlauben die strukturellen und dynamischen Eigenschaften supraleitender *Flussgitter* einen tiefen Einblick in die Wechselwirkung der einzelnen Flussfäden. Insbesondere Abweichungen von der idealen hexagonalen Symmetrie des Flussgitters spiegeln dabei sowohl die Symmetrie des supraleitenden Ordnungsparameters, die Morphologie der Fermifläche des supraleitenden Materials als auch individuelle Eigenschaften der Proben wie ihre Reinheit wieder [1]. Die Elastizitätsmatrix $\Phi_{\alpha,\beta}$ eines Flussgitters beschreibt die elastische Energie, welche durch eine Verzerrung des Flussgitters durch thermische Fluktuationen, Gradienten des Magnetfeldes oder der Temperatur, durch Pinning oder in der Gegenwart von Transportströmen verursacht wird. Ähnlich wie die Symmetrie des Flussgitters spiegeln auch die elastischen Moduli c_{11} für Kompression, c_{44} für Verkippung und c_{66} für Scherung die mikroskopischen Eigenschaften der Supraleitung wieder [2, 3, 4, 5]. Darüber hinaus beeinflusst $\Phi_{\alpha,\beta}$ sowohl die thermische Stabilität und den Aggregatszustand der Flussgittermaterie als auch die Pinning/Depinning Vorgänge der Flussfäden. Dies führt zu einer großen Relevanz für den technologischen Einsatz von Supraleitern.

Die eindeutige Zuordnung verschiedener Ursachen für anisotropes Verhalten des Flussgitters ist jedoch schwierig, sowohl für die Symmetrie als auch die Elastizitätsmatrix [1]. Die Vielzahl unterschiedlicher Einflüsse wirft die Frage auf, wie die Eigenschaften von Flussgittern und Flussgittermaterie verallgemeinert werden können:

Der klassische Typ-II Supraleiter Niob ist ideal als Modellsystem zur Untersuchung von Flussgittermaterie geeignet. Niob zeigt eine isotrope single-gap s-Welle Supraleitung [6, 7] und ist durch einen kleinen Wert des Ginzburg-Landau Parameters $\kappa = \lambda/\xi \sim 1/\sqrt{2}$ nahe am Typ-I Verhalten ausgezeichnet. Mögliche Beiträge einer unkonventionellen Symmetrie des supraleitenden Ordnungsparameters werden also vermieden [1]. Der niedrige Wert von κ führt zu einem hohen Wert für das untere kritische Feld H_{c1}. Darüber hinaus führt der niedrige Wert von κ bei Proben mit endlichen Demagnetisierungsfaktor zu der Ausbildung des gemischten Zwischenzustandes (IMS), analog dem Zwischenzustand bei Typ-I Supraleitern. Der IMS ist durch die makroskopische Koexistenz von Meissner Domänen und Shubnikov Domänen, die ein Flussgitter tragen, gekennzeichnet. Das Auftreten des IMS wird durch eine in diesem Temperatur- und Magnetfeldbereich anziehende Wechselwirkung zwischen den einzelnen Flussfäden getrieben. Die Supraleitung in Niob erlaubt

es daher, die Wechselwirkung zwischen den Flussfäden gezielt zu beeinflussen.

In dieser Arbeit werden mit Hilfe von Neutronen Kleinwinkelstreuung die Eigenschaften des Flussgitters in einem höchst reinen Niob Einkristall systematisch untersucht. Die verwendete Niob Probe ist durch ein außergewöhnlich hohes Restwiderstandsverhältnis von $\sim 10^4$ ausgezeichnet. Es wird dabei im Speziellen die Morphologie der Flussgitterstrukturen für eine Orientierung des Magnetfeldes parallel zur vierzähligen $\langle 100 \rangle$ Kristallrichtung untersucht. Durch das Zusammenspiel der hexagonalen Symmetrie des Flussgitters und der vierzähligen Symmtrie des Kristalles ergibt sich ein reiches Phasendiagramm, das vier verschiedene Flussgitterphasen beinhaltet. Die einzelnen Phasen des Flussgitters brechen dabei spontan die Kristallsymmetrie [8, 9, 10]. Mit Hilfe von Messungen der Flussgittersymmetrie als Funktion des Winkels zwischen Magnetfeldrichtung und der $\langle 100 \rangle$ Kristallrichtung gelingt es, die verschiedenen Ursachen für die spezielle Morphologie des Flussgitters zu separieren und drei dominanten Mechanismen zuzuordnen: Erstens nicht-lokalen Korrekturtermen, zweitens dem Übergang von offenen zu geschlossenen Elektronenbahnen auf der Fermifläche und drittens dem IMS zwischen Meissner und Shubnikov Phase [10]. Unsere Arbeit liefert die Basis für nachfolgende systematische Untersuchungen des Flussgitters von Supraleitern mit komplexer Symmetrie des supraleitenden Ordnungsparameters.

Messungen der Elastizität von Flussgittern auf mikroskopischer Skala sind nur mit Hilfe von oberflächensensitiven Messmethoden möglich. Diese werden jedoch stark durch parasitäre Einflüsse, insbesondere durch Oberflächenpinning beeinträchtigt. In dieser Arbeit wird erstmals zeitaufgelöste stroboskopische Neutronen Kleinwinkelstreuung in Kombination mit einem speziellen Magnetfeldaufbau benutzt, um das intrinsische Kippmodul c_{44} des Flussgitters im Inneren der Probe direkt zu messen. Die Reaktion des Flussgitters in Niob auf eine Änderung des Magnetfeldes lässt sich dabei durch eine exponentielle Relaxation mit einem Diffusionsmodell nach Brandt [12] und Kes [13] beschreiben.

Die Relaxation des Flussgitters zeigt dabei, wie theoretisch erwartet, eine mit dem Magnetfeld wachsende Steifigkeit und eine abnehmende Dämpfung der Relaxation mit steigender Temperatur. Neben diesem generellen Trend zeigen die Messungen qualitativ eine scharfe Änderung des Relaxationsprozesses, der durch die nicht-triviale Morphologie des Flussgitters im IMS und dem Übergang von anziehender zu abstoßender Wechselwirkung der Flussfäden verursacht wird. Die Änderung des Relaxationsvorganges wird dem Zerfallen des Flussgitters in die einzelnen Shubnikov-Domänen und der Aufzweigung dieser Domänen an der Oberfäche der Probe (Landau-branching) zugeschrieben. Die entwickelte Messtechnik ermöglicht darüber hinaus die direkte Messung von Flussgitterschmelzen, die Bildung von Flussgittergläsern und die Bestimmung des Pinningverhaltens, insbesondere in unkonventionellen Supraleitern in der Gegenwart von Transportströmen.

Die Existenz von Wirbeln und ähnlichen topologisch stabilen Strukturen in magnetisch geordneten Systemen wird aktuell diskutiert [14, 15, 16, 17, 18]. Analog zu supraleitenden Flussfäden, die thermodynamisch durch die negative Grenzflächenenergie zwischen normal- und supraleitendem Bereich stabilisiert werden, wurde die Stabilisierung von magnetischen Wirbeln in ferromagnetischen Materialien durch Bloch Domänenwände vorgeschlagen [19, 20, 21, 22]. Insbesondere Systeme, die eine helikale magnetische Ord-

nung zeigen, scheinen vielverspechende Kandidaten für solche Strukturen zu sein, da sie eine Rotation der magnetischen Momente, wie sie in Bloch Domänenwänden beobachtet wird, inhärent unterstützen. In ferro- oder antiferromagnetischen Systemen, die in Kristallstrukturen ohne Inversionssymmetrie kristallisieren, erlaubt die fehlende Inversionsymmetrie die sogenannte Dyzhaloshinskii-Moriya (DM) Wechselwirkung [23, 24], welche eine senkrechte Ausrichtung benachbarter magnetischer Momente bevorzugt. Zusammen mit einer ferromagnetischen Austauschwechselwirkung auf einer größeren Energieskala führt dies zur Ausbildung einer helikalen magnetischen Ordnung, die durch eine lange Wellenlänge auf atomarer Skala gekennzeichnet ist. Die lange Wellenlänge der helikalen magnetischen Struktur führt darüber hinaus zu einer effizienten Entkopplung von magnetischer und kristalliner Ordnung.

Die intermetallische Verbindung MnSi kristallisiert in der kubischen B20 Struktur, die keine Inversionssymmetrie aufweist. Unterhalb einer kritischen Temperatur $T_c = 29.5\,\mathrm{K}$ zeigt MnSi schwache itinerante helikale magnetische Ordnung, die durch ein erweitertes Stoner Modell, das erhöhte Fluktuationen berücksichtigt, in Kombination mit der DM Wechselwirkung beschrieben werden kann. Das magnetische Phasendiagramm von MnSi ist durch vier verschiedene Phasen gekennzeichnet: Unterhalb des kritischen Feldes H_{c1} sind die Helices durch die schwache Kristallfeldanisotropie an die kristallinen $\langle 111 \rangle$ Richtungen gepinnt. Oberhalb von H_{c1} reorientieren sich die Helices in die Richtung des Magnetfeldes und bilden die konische Phase, bis am oberen kritischen Feld H_{c2} ein feldpolarisierter ferromagnetischer Zustand erreicht ist. Knapp unterhalb von T_c bei etwa $1/2H_{c2}$ wird in einem kleinen Temperatur- und Magnetfeldbereich die sogenannte A-Phase beobachtet, die durch Phasenübergänge schwacher erster Ordnung von der konischen Phase getrennt ist [26]. Messungen mit Hilfe von Neutronenstreuung zeigten dabei eine senkrechte Anordnung des Propagationsvektors der Helices und des Magnetfeldes in der A-Phase [27, 28, 29].

In dieser Arbeit wird mit Hilfe von Neutronen Kleinwinkelstreuung die Existenz eines Skyrmion Gitters in der A-Phase von MnSi gezeigt [30]. Durch eine parallele Anordnung von Magnetfeld und Neutronenstrahl kann die vollständige magnetische Struktur der A-Phase beobachtet werden: Die A-Phase besteht aus topologischen Knoten der Magnetisierung mit teilchenartigen Eigenschaften, die sich — ähnlich wie bei einem supraleitenden Flussgitter — in einem hexagonalen Gitter anordnen. Die Orientierung dieses Gitters ist dabei, unabhängig von der Kristallrichtung, ausschließlich durch die Richtung des Magnetfeldes gegeben. Die Periodizität des beobachteten Gitters ist viel größer als der atomare Gitterabstand von MnSi und entspricht der Wellenlänge der helikalen Ordnung.

Mit Hilfe eines Ginzburg-Landau Ansatzes nach [31] wird gezeigt, dass der quartische Term $\mathbf{M}^4$ in Gegenwart einer uniformen Magnetisierung $\mathbf{M}_f$ effektiv kubisch in den modulierten Momenten ist. Dies führt zu einer 3-$\mathbf{q}$ Struktur: Ein Mean-Field Modell zeigt, dass ein magnetischer Spinkristall, der aus der Superposition von drei Helices, die untereinander einen Winkel von 120° einschließen, und jeweils senkrecht zum Magnetfeld orientiert sind, ein metastabiler Zustand ist. Werden Gauss'sche Fluktuationen einbezogen, so wird die freie Energie des Spinkristalls im Vergleich zur konischen Phase reduziert und dieser stellt einen stabilen Grundzustand dar. Durch die Integration der Windungsdichte

über eine Einheitszelle des Spinkristalles wurde dieser als Skyrmion Gitter identifiziert: Die Integration ergibt eine topologische Ladung von $C_{top} = -1$ pro Einheitszelle und beweist die Existenz stabiler topologischer Solitonen der Magnetisierung.

Contents

Chapter 1

Vortices in Superconductors and Ferromagnets

1.1 Introduction

Vortices — originating from latin *vertere*, to turn — are a widely spread phenomenon in physics and nature. Vortex structures can be found over many orders of magnitude in size. Our galaxy — the milky way — owns a spiral shape with a diameter of $\sim 10^{21}$ m. Vortices are present everywhere in our daily life: The rotating water in the sink of a bath tub, whirl winds of several kinds reaching from harmless small dust devils to enormous hurricanes in the atmosphere of the earth. But vortices can also be found on a sub-μm scale, e.g., in superconductors [32] and ultra-cold Bose-Einstein condensates of ^{4}He or trapped atoms [33]. Some selected examples of vortices of different dimensions are shown in Fig. 1.1.

In the focus of this thesis are studies of the properties of vortices and vortex lattices in superconductors and similar vortex structures in ferromagnets. Following this introduction and historical overview, a brief mathematical description of vortices is given in section (1.2). We then introduce in detail the properties of vortex lattices in superconductors and vortices in magnetically ordered systems in sections (1.3) and (1.4), respectively, where we also motivate our research. This chapter is closed with a short outline on the structure of this thesis (section (1.5)).

The history of vortices is actually quite old. An overview has been given by Brandt *et al.* [34, 35]: Already in 1644 René Descartes [36] proposed in his book *Principia Philosophiæ* a model of the universe, based on a mechanism of weighty fluid celestial matter, moving as vortices: Due to the dense filling of space with celestial matter, the rectilinear motion of matter will be deflected into a rotation. Descartes compared this mechanism with some light pieces of wood swimming in a basin filled with water. If the water is put into rotation, the pieces of wood will gather in the centre of the rotation. With this model of celestial vortices (cf. Fig. 1.2), gravitation and the rotation of planetary objects were explained.

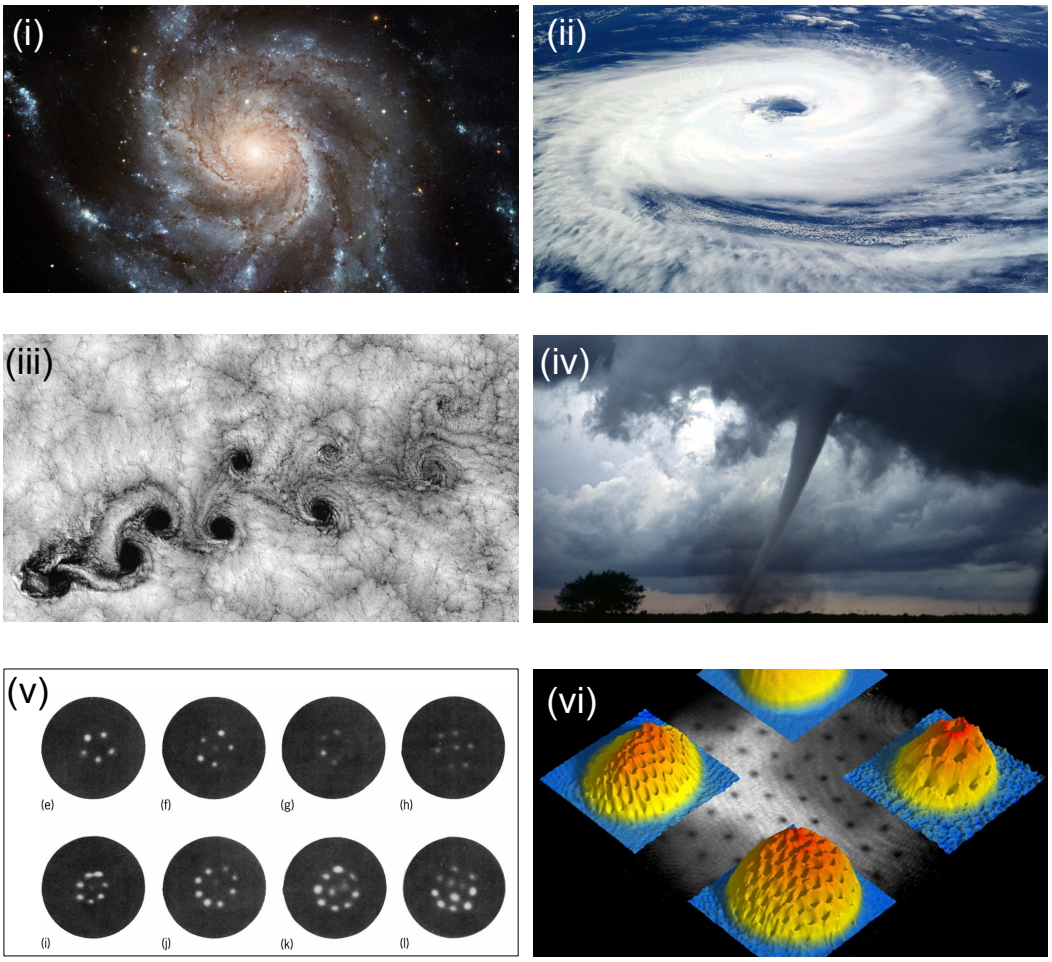

Figure 1.1: Vortices of different magnitudes. The spiral shape of the galaxy M101 is shown in panel (i). The diameter of galaxies is typically $\sim 10^{21}$ m. Panel (ii) shows an image of a hurricane taken from the ISS on March 26th 2005 [37] on the southern Brazilian state of Santa Catarina. Note the clockwise circulation of southern Hemisphere cyclones. The Kármán vortex street, a series of vortices with alternating rotation is shown in panel (iii), observed off the Chilean coast near the Juan Fernandez Islands [38]. A picture of a tornado is shown in panel (iv) [39]. Different configurations of vortices, emerging in a Bose-Einstein-condensate of superfluid ^{4}He (typical size $\sim 100\,\mu$m) [40] and of trapped, ultra-cold sodium atoms (typical size $\sim 50\,\mu$m) observed after ballistic expansion [41] are shown in panels (v) and (vi), respectively.

In the 1800s, the stability of vortex loops in fluids has been examined by Lord Kelvin [42] and J. J. Thomson [43], who solved the case for two up to seven vortices, whereby instability was predicted for seven vortices. Kelvin and Thomson initially suggested a model of the atoms, based on a knotted structure in an ideal fluid, where the manifold of knot types represents the different elements [44]. In 1911, the picture of the *vortex street* was introduced by Theodore von Kármán, a fluid dynamist, writing in his autobiography later on: *Vortices were observed and recorded many years before I came on scene. In a museum in Bologna, Italy, I remember seeing a painting of the great Christoph (Saint Christopher) wading through water with the child Jesus on his shoulder. Behind his heels was a series of alternating vortices* [45]. The so-called Kármán vortex street is of great

importance for the aerodynamically stable design of bridges and buildings amongst other applications. A depiction can be found in Fig. 1.1.

The concept of superfluid quantum vortices was introduced by Onsager in 1949 [46], the description was later generalized by Feynman in 1955 [47] and Abrikosov. In 1957, Abrikosov predicted the existence of vortices in type-II superconductors by a solution of the Ginzburg-Landau equations with spatially varying order parameter [32]. Besides type-II superconductors, vortex structures have been identified in a variety of strongly correlated condensed matter systems, amongst others in superfluid ^{4}Helium (cf. Fig. 1.1) [48] and superfluid ^{3}Helium. Ketterle *et al.* received the Nobel prize 2001 for the discovery of vortices in a Bose-Einstein condensate of *bosonic* sodium atoms [33]. The first atomic *fermionic* condensate has been achieved by Greiner *et al.* [49] (2003).

In the following paragraphs, we briefly introduce the topological properties of vortices and their description as solitons [51]: In a nonlinear and dispersive medium, a self-reinforcing solitary wave is called *soliton*. Solitons emerge due to the cancellation of nonlinear and dispersive effects. Solitons are characterized by three typical properties: Their form is permanent, they are localized within a region and they can interact with other solitons. Vortices as topological objects are a matter of studies since the 1960s and 1970s, where a novel approach to quantum field theory was introduced: The classical field equations were studied in detail, including their fully non-linear form and excitations: A characteristic feature of the newly obtained solutions was their topology: In contrast to excitations from the vacuum, associated with the quantization of smooth wave-like deformations of a field, the new *particle-like solitons* own their stability from a different *topology*.

The different topology arises mostly due to particular boundary conditions of the underlying set of differential equations. We assume that the boundary has a non-trivial homo-

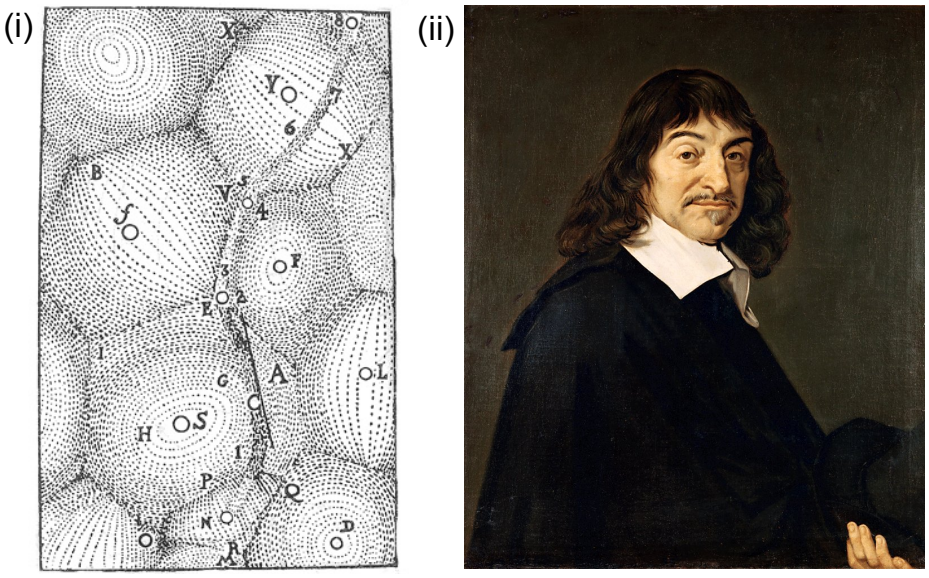

Figure 1.2: Panel (i): Descartes' celestial vortices from *Principia Philosophiæ*, 1644 [36]. Panel (ii): Portrait of René Descartes by Frans Hals, 1649 [50].

topy group, which will be preserved by the differential equations. The solutions of the differential equation may then be classified into homotopy classes as well. Since there is no continuous transformation that will map a solution in one homotopy class to another, the solutions are truly distinct, and maintain their integrity even in the presence of powerful forces [52]. The topology of such a solution may be described by a single integer C_{top}, which is called generalized winding number or topological charge [14, 53]. A field configuration with $C_{top} = 1$ is a classical stable solution, which is called *topological soliton.*

Historically, the first successful example of a topological soliton was the skyrmion, named after Tony Skyrme. Skyrme firstly managed to show that particle-like excitations of continuous fields emerge in the presence of non-linear excitations. In Skyrme's pioneering work, the constituents of the nucleus, protons and neutrons emerge naturally as the soliton states of the pion medium, consisting of spinless (π^+, π^-, π^0) [54]. *Skyrmionic* states have also been observed in numerous different condensed matter systems:

The vortices in superconductors arrange themselves into a macroscopic lattice — analog to the crystallization of atoms into a crystal lattice — they also own particle-like properties. They further are characterized by a non trivial topology: Due to continuity conditions for the superconducting phase on a closed loop around the vortex, the magnetic flux of a vortex is quantized. A vortex in a superconductor thus can be solely nucleated at the surface of the sample or as closed vortex loop inside the superconductor. Vortices observed in superconductors (or superfluid condensates) may therefore be described as *topological solitons of the superconducting order parameter* [51].

Besides superconductivity and superfluidity, forms of order composed by topological entities have been identified in numerous systems, e.g., Turing patterns in classical liquids [55], which are stationary and periodic in space. They result from the interplay between diffusion and non-linear reaction kinetics, firstly observed in chemical reaction-diffusion systems. A depiction of a typical Turing pattern is given in Fig. 1.3, panel (i). A further example are the so-called *blue phases* in liquid crystals [56], which have been firstly observed in the melting behaviour of cholesteryl benzoate, which briefly turned blue upon changing from clear to cloudy during cooling. This is attributed to the existence of a twisted structure of chiral nematic liquid crystals: A large structure, composed of twisted cylinders, as schematically given in Fig. 1.3, panel (ii) is observed. Yet at the contact points of the cylinders, as marked in Fig. 1.3, panel (iii), defects naturally occur which are then arranged in a cubic lattice akin to a crystal lattice. As the characteristic size of such a crystal of topological defects is of the same order of magnitude compared to the wavelength of light, a blue colour arises due to Bragg reflections. Skyrmion states have also been found in the spin textures in quantum Hall magnets [57], stabilized by charge as additional freedom, where the two-dimensional electron gas was studied in a high magnetic field for a filling factor $v = 1$. A depiction is given in Fig. 1.3, panel (iv).

However, these given examples of skyrmionic states are either limited to non-equilibrium states or stabilized by external fields or topological defects. Recently, forms of order composed of topological entities have also been discovered in so-called topological insulators at *zero* field, where a robust quantum hall state is found on the boundaries of two-dimensional band insulators with large spin-orbit effects. This *quantum spin Hall effect*

leads to topological non-trivial states of quasi non-interacting gapped fermions [58, 59].

It was discussed whether such vortex-like topological forms of order also occur in the field of magnetism: On the one hand, smectic, nematic and hexatic forms of order, akin to liquid crystals as well as multi-**q** structures have been proposed for spin-liquids or spin-glasses. Such states can be found for systems, which are characterized by frustration as e.g. Kagomé lattices or 3D Pyrochlore antiferromagnets [60, 61]. On the other hand, Bogdanov, Jablonskii and Hubert *et al.* [19, 20, 21, 22] propose the stabilization of vortices in ferromagnets by Bloch domain walls, similar to vortex lattices in superconductors which are stabilized by the negative energy associated with a normal to superconducting interface.

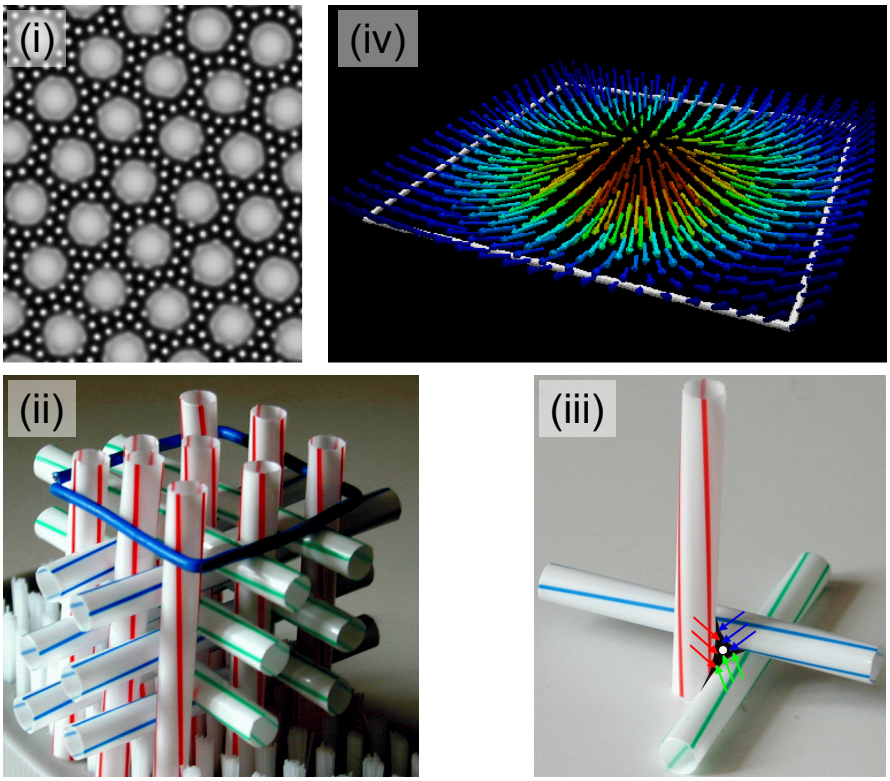

Figure 1.3: Panel (i) depicts a so-called Turing pattern arising from spatial resonances and superposition patterns in a reaction-diffusion model with interacting Turing mode, adopted from [62]. Panel (ii) and panel (iii) schematically depict the structure of twisted cylinders – where straws represent the twisted cholesterol cylinders – as observed in the so-called blue phase of liquid crystals, adopted from [63]. Panel (iv) presents the skyrmionic state, observed in the two-dimensional electron gas of quantum hall systems in the presence of strong magnetic fields, taken from [64].

We have shown in the previous paragraphs, that the universal concept of vortices and vortex lattices, where topological entities with particle-like properties emerge from continuous fields is applied in numerous systems. The properties of the vortices thereby not only sensitively reflect the underlying physics, but also are of general importance for fundamental questions in quantum physics.

1.2 Mathematical Description of Vortices

In this paragraph, we briefly present the fundamental mathematical properties of vortices. We thereby follow the work by Brandt [34]. In classical fluid dynamics, two general types of vortices have to be distinguished: The forced or *rotational* vortex and the free or *irrotational* vortex. The first type is best described by a rotating pool of water, where a parabolic shape of the surface is observed; the forced vortex is only possible in media with *finite* viscosity. Vortices in superconductors are characterized by the *irrotational* vortex type, reminiscent of water being drawn down a plug hole, which has the mathematical form of a potential field, i.e., owns no vorticity if one neglects the vortex core.

At sufficiently large distance from the vortex core, which is situated at $(x, y) = (0, 0)$, such a vortex is characterized by a vector field $\mathbf{v}(\mathbf{r})$ with $\mathbf{r} = (x, y, z)$

$$\mathbf{v}(\mathbf{r}) = \frac{\kappa_v}{2\pi r_\perp}\mathbf{e}_\phi \tag{1.1}$$

with the distance to the vortex center $r_\perp = (x^2 + y^2)^{1/2}$, the unit vector in azimuthal direction $\mathbf{e}_\phi$ and the circulation of the vortex $\kappa_v = \oint \mathbf{v} \cdot \mathrm{d}\mathbf{l}$. The flow of the fluid is rotational free for a irrotational or free vortex field in a superconducting medium

$$\nabla \times \mathbf{v}(\mathbf{r}) = 0 \ . \tag{1.2}$$

For arbitrarily curved vortices where the position of the vortex core is described by the function $C_s : \mathbf{r}_v(s) = [x_v(s), y_v(s), z_v(s)]$ with the line element $\mathrm{d}\mathbf{r}_v(s) = [x'_v(s), y'_v(s), z'_v(s)]$ and the line parameter s, the rotation reads in three dimensions

$$\nabla \times \mathbf{v}(\mathbf{r}) = \kappa_v \int_{C_s} \mathrm{d}\mathbf{r}_v \delta_3(\mathbf{r} - \mathbf{r}_v) \ . \tag{1.3}$$

The ideal vortex core is thereby described by the delta function $\delta_3 = \delta(x)\delta(y)\delta(z)$. In real systems, the core size of the vortex is either finite, i.e. the delta function is replaced by a Gaussian or a Heavyside function (for a rigidly rotating cylinder) or the core is sharply defined by a delta function and thus the velocity field follows $v \propto 1/r_\perp$. In this case, the density of the fluid n_s has to vanish close to the core at least as $n_s \propto r_\perp^2$, reminiscent of the water in the bath tub, rotating around an empty funnel. For superconducting vortices, the density of superconducting electrons vanishes with $n_s = |\psi|^2 \propto r_\perp^2$.

In contrast to vortices of water in the sink of a bath tub, *quantum vortices* as observed in superconductors own a second characteristic feature: Superconductors exhibit the property of having a phase $\phi(\mathbf{r})$. Due to the continuity conditions for the superconducting order parameter, a closed loop at a sufficiently large distance around a vortex center requires for the phase $\oint \nabla\phi \cdot \mathrm{d}\mathbf{l} = 2\pi n$ with an integer $n = 0, \pm 1, \pm 2$, etc. This yields for the magnetic flux ϕ_{mag} of a superconducting vortex (due to the coupling to the vector potential $\mathbf{A}$)

$$\phi_{mag} = \oint \mathbf{A} \cdot \mathrm{d}\mathbf{l} = \frac{\hbar}{2e} \oint \nabla\phi \cdot \mathrm{d}\mathbf{l} = n\frac{h}{2e} = n\phi_0 \tag{1.4}$$

with the flux quantum ϕ_0.

Generalizing the description given above, two different types of quantum vortices are distinguished [51]: We already have introduced, that the phase of $\mathbf{v}(\mathbf{r})$ has to increase by a factor of $2\pi n$ with an integer n upon a closed loop around the vortex. (i) The so-called *global* vortex is simply defined by the basic scalar field $\mathbf{v}(\mathbf{r})$. (ii) For a *gauged* vortex, e.g., in superconductors, the scalar field $\mathbf{v}(\mathbf{r})$ is electromagnetically coupled with a gauge group U(1). We now have to deal with two fields, namely $\mathbf{v}(\mathbf{r})$ and the gauge field $a_\mu(\mathbf{r})$. The consequence is, that the fixed phase relation leads to a quantized magnetic flux, which is not the case for a global vortex.

1.3 Vortex Lattices in Superconductors

1.3.1 Introduction

Although superconductivity was firstly observed almost a century ago by Kammerlingh Onnes (1911) in mercury, it is still one of the most fascinating and important fields of interest in modern physics. The superconducting state is characterized both by the vanishing electrical resistivity as well as the complete expulsion of magnetic fields, regardless whether the magnetic field was applied below or above the superconducting transition temperature T_c. The expulsion of external magnetic fields, which is denoted Meissner-Ochsenfeld effect (1933) [65] established superconductivity as own thermodynamic phase. A first phenomenological description of superconductivity was given by London [66] based on the Maxwell equations.

The superconducting state was then described by the phenomenological Ginzburg-Landau theory (1950) [67] by introducing a superconducting wavefunction ψ with finite stiffness ξ_{GL}. The superconducting groundstate was derived by an expansion of the free energy F in terms of $|\psi|^2$ for temperatures close to the transition temperature T_c, where $|\psi|^2$ is still small. The Ginzburg-Landau framework introduces and explains the different behaviour of type-I and type-II superconductors in a magnetic field by means of the energy, associated with a normal- to superconducting interface, characterized by the parameter κ. The Ginzburg-Landau theory further yields the correct values for the critical fields of various superconductors.

The Ginzburg-Landau theory was extended by Abrikosov [32] to type-II superconductors with negative interface energy by introducing a periodic solution of the phenomenological Ginzburg-Landau equations, where the magnetic field can penetrate bulk type-II superconductors in form of vortices, each carrying one flux quantum $\phi_0 = h/2e$. This is referred to as Shubnikov phase. The vortices arrange themselves in a so-called superconducting vortex lattice with Bravais properties, reflecting the minimal free energy landscape, where a regular hexagonal symmetry was obtained for isotropic superconductors. However, the difference of energy between a six-fold symmetry and a four-fold symmetry is only a few percent. The experimental evidence of vortex lattices in superconductors was given by Cribier *et al.* in 1964 [68] by Bragg diffraction of cold neutrons from the vortex lattice.

A first microscopic explanation of superconductivity was given independently by Bardeen,

Cooper and Schrieffer (BCS) [69] and Bogoliubov [70]. By means of a *retarded* phonon mediated interaction between two conduction electrons close to the Fermi surface with opposite wavevector and spin (a schematic depiction is given in Fig 1.4), a net attractive potential leads to the formation of a bound state called Cooper-pair. The total spin of both electrons in a Cooper-pair adds up to zero. This leads to a macroscopically occupied new groundstate, a condensate of Cooper-pairs, separated by the energy gap Δ and characterized by a single, macroscopically coherent phase $\phi(\mathbf{r})$ of the superconducting wavefunction ψ.

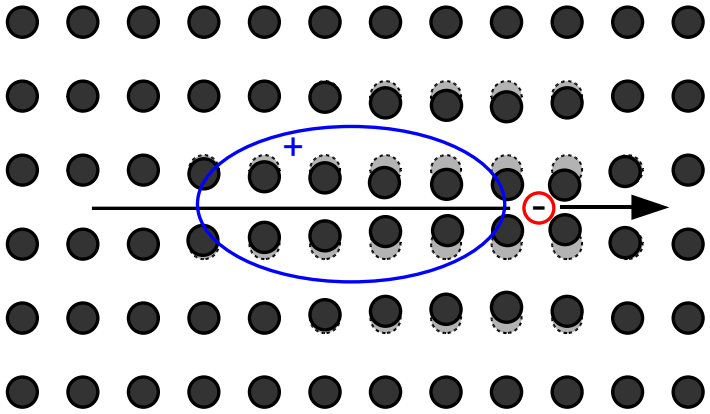

Figure 1.4: Schematic depiction of an electron moving through a crystal lattice. The electron causes a *dynamic* polarisation of the crystal lattice. By means of a retarded electron-phonon interaction, overscreening can lead to a net attractive potential (marked with the blue ellipsoid) for a second electron.

While prior to the 1970s, all superconducting materials could be identified as phonon-mediated condensate of Cooper-pairs, this dogma fell after the discovery of superfluidity in ^{3}He [71], providing an example of non-phonon induced coupling. The observation of high temperature superconductivity in cuprate and ruthenate systems in the 1980s, initially by Bednorz and Müller [72] has led to a burst of new superconducting materials. The discovery of superconductivity in heavy fermion systems which are characterized by a renormalized electron mass by a factor of up to three orders of magnitude — firstly observed in the compound $CeCu_2Si_2$ by Steglich *et al.* [73] — has been a prime example for non-electron-phonon superconductivity with possible complicated order parameters. A depiction of two different symmetries of the superconducting order parameter is given in Fig 1.5.

Today, a cornucopia of superconducting materials is known, leading from phonon-mediated coupling in niobium below a T_c of 9.2 K over superconductivity in $Bi_2Sr_2Ca_2Cu_3O_{10+\delta}$ (BSSCO) with a T_c of 120 K, to pressure induced superconductivity in Hg-compounds with a T_c of 164 K [74, 75]. Recently, high temperature superconductivity was observed in oxypnictide materials as, e.g., FeAs [76]. In addition, superconductivity is also observed in organic materials, e.g., $(TMTSF)_2PF_6$, in the alcalic-metal-fullerene K_3C_{60} and at the quasi two-dimensional interface of the insulating oxides $LaAlO_3$ and $SrTiO_3$ [77]. On the other hand, a close interplay of magnetism and superconductivity is observed in

particular in the heavy fermion compounds. Besides electron-phonon mediated superconductivity, spin fluctuations at the border of instabilities and competing or coexisting forms of electronic order (mostly antiferromagnetism) are recently discussed [78] as alternative coupling mechanisms.

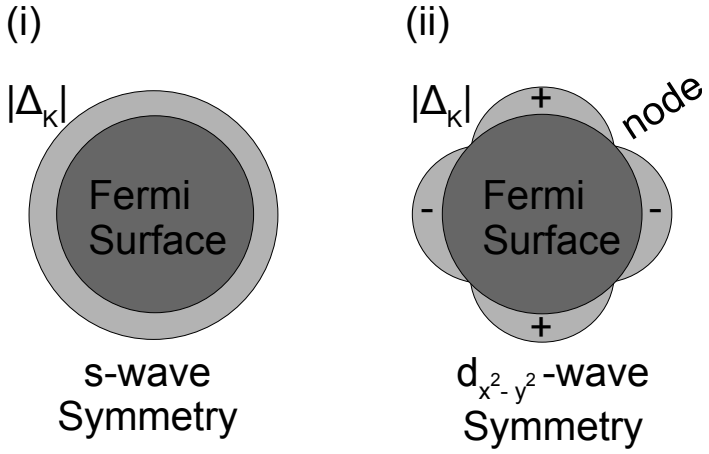

Figure 1.5: Panel (i) schematically depicts the superconducting gap for an isotropic s-wave order parameter in **k**-space. Panel (ii) shows the symmetry of the superconducting gap for $d_{x^2-y^2}$-wave symmetry of the order parameter, where nodes of the superconducting gap occur for certain directions in **k**-space.

1.3.2 Properties of Superconducting Vortex Lattices

Similar to crystals lattices, composed of atoms, the defining properties of superconducting vortex lattices and vortex matter are their symmetry and structure as well as their elastic matrix. Anisotropy and deviations from the ideal six-fold vortex lattice symmetry reflect sensitively the fundamental electronic properties of the superconducting material as well as the number and symmetry of the superconducting gaps due to non local corrections and individual sample properties as, e.g., pinning or mean free electron path. However, the unambiguous mapping of different sources of anisotropy is intricate [1].

The symmetry and structure of superconducting vortex lattices is mostly determined by means of small angle neutron scattering measurements, exploiting the weak interaction of the charge-neutral neutron with the magnetic field distribution of the superconducting vortex lattice on the one hand and the Bravais properties of the vortex lattices on the other hand.

A reentrant square to hexagonal to square vortex lattice transition in the compound $LuNiB_2C$ [79], inferred from small angle neutron scattering measurements, was attributed to the interplay of superconducting gap symmetry and Fermi symmetry [80]. If the magnetic field is applied along a four fold $\langle 100 \rangle$ axis in the isotropic s-wave superconductor niobium, four different vortex lattice phases emerge, comprising symmetry breaking vortex structures combined with various lock-in transitions [8, 9] caused by the interplay of the

four-fold crystal symmetry and the six-fold vortex lattice symmetry. However, the origin of the symmetry breaking and tilting was not completely understood for both $LuNiB_2C$ and niobium. For materials exhibiting strong anisotropy or possible unconventional order parameter symmetries, the situation is even more complicated:

The pronounced anisotropy of the layered cuprate compounds can yield significant distortions of the vortex lattice. Such as for the high-T_c compound YBCO, where a distortion of the vortex lattice symmetry to an ellipsoidal shape was found by Keimer *et al.* [81] by means of neutron scattering, which was explained by the four-fold symmetry of the order parameter near the vortex core. In contrast, the field and temperature dependence of vortex lattice distortions in the heavy fermion compound $PrOs_4Sb_{12}$ by Huxley *et al.* [82] was attributed to the presence of gap nodes in the superconducting state on at least some Fermi surface sheets. In $CeCoIn_5$, the increase of the form factor of the vortex lattice with increasing field was attributed to a Fulde-Ferrell-Larkin-Ovchinnikov FFLO state [83]. Small angle neutron scattering measurements on the complicated vortex lattice phase diagram of the heavy fermion compound UPt_3, where three different vortex phases are distinguished, lead to an unconventional two-component picture [84].

The elastic matrix $\Phi_{\alpha,\beta}$ of a vortex lattice describes the energy associated with a distortion of the vortex lattice due to thermal fluctuations, gradients of magnetic field or temperature, pinning and transport currents. $\Phi_{\alpha,\beta}$ also determines the dynamic properties of superconducting vortex matter in non-equilibrium states. Similar to the symmetry of vortex lattices, the elastic constants of the vortex lattice c_{11} for compression, c_{44} for tilt and c_{66} for shear sensitively reflect the microscopic nature of the superconductivity [2, 3, 4, 5]. In addition, the elastic matrix of the superconducting vortex lattice is closely related to the pinning and depinning properties of vortices, leading to a particular relevance for technical applications of superconductors.

In analogy to properties of ordinary matter, the thermal stability and the state of aggregation of vortex matter is determined by $\Phi_{\alpha\beta}$. A variety of different vortex matter has been identified, comprising, e.g., vortex lattice melting transitions as observed by means of small angle neutron scattering in the high-T_c material BSCCO [85] and other high-T_c compounds [86]. Vortex lattice Bragg glasses, liquids and ices have been identified by transport and magnetization measurements, e.g., in $NbSe_2$ and MgB_2 [87],[88],[89].

In contrast to the symmetry of vortex lattices, which can be directly measured by means of small angle neutron scattering, neutron scattering measurements only give limited access to the dynamic properties of superconducting vortex matter [90]. Microscopic measurements of the intrinsic elastic constants of vortex lattices are typically performed by means of surface sensitive techniques, however, strongly hampered by surface induced pinning effects and geometrical constrains in the commonly used thin film samples [2]. In contrast, bulk techniques as measurements of teh transport properties and the magnetization can give no micropcopic information.

1.3.3 Motivation

The broad variety of different influences on the properties of superconducting vortex lattices raises the question how to generalize the behaviour of superconducting vortex matter and makes studies of conventional superconductors of general interest. In this thesis, we particular focus on the symmetry and structure on the one hand and on the elasticity of superconducting vortex lattices on the other hand:

The superconductivity in niobium is ideally suited to provide such general information of the vortex lattice [8, 9, 10], avoiding the complexities of multi-gap systems and complex order parameter symmetries [91, 82, 92]. The low value of the Ginzburg-Landau parameter, $\kappa \approx 0.8$, places niobium at the immediate border between type-I and type-II superconductivity. This makes the underlying change from attractive to repulsive vortex interactions experimentally accessible [93]. Moreover, the large coherence length of niobium implies that the Fermi surface topology and thus non-local effects are important.

We have already mentioned, that the structure and symmetry of the superconducting vortex lattice of niobium — for the magnetic field applied along a four-fold $\langle 100 \rangle$ crystalline direction — comprises gradual variations with various lock-in transitions and symmetry breaking rotations [8, 9] caused by the interplay of the four-fold crystal symmetry and the six-fold vortex lattice symmetry. However, in these studies the precise evolution of the vortex lattice morphology as a function of the direction of the magnetic field, necessary to identify the origin of the morphology and tilting, remained open. This originated in incomplete data sets and, more importantly, in the purity of the samples studied so far, which still displayed distinct pinning effects.

In our work, we use small-angle neutron scattering to systematically study the vortex lattice in an ultra-pure single crystal of niobium as a function of the orientation of the applied magnetic field. With our study, we succeed to deconvolute the general morphology of the vortex lattice and its orientation to three dominant mechanisms. First, non-local contributions to the free energy due to the general four-fold Fermi symmetry, second, the transition between open and closed Fermi surface sheets and, third, the intermediate mixed state between the Meissner and the Shubnikov phase [10]. On the one hand, our study paves the way to systematic examinations of samples with reduced purity and reduced mean free electron path to quantify to influence of non-local corrections. On the other hand, our study provides an ansatz how to deconvolute the symmetry and structure of the superconducting vortex lattice in systems exhibiting an unconventional symmetry of the superconducting order parameter.

We have introduced, that microscopic measurements of the vortex lattice elasticity are strongly hampered by surface induced pinning effects. In our work, we exploit a novel time-resolved neutron scattering technique in combination with a tailored magnetic field setup for first-time direct microscopic measurements of the superconducting vortex lattice tilt modulus c_{44} in ultra-pure niobium. This technique allows to measure the intrinsic tilt modulus c_{44} for bulk samples on a microscopic scale. With the used setup, we can overcome the limitations due to surface pinning effects in the commonly used thin film samples:

In our study we find, that the vortex lattice in niobium responds to an external force — in the form of a changed magnetic field — with an exponential relaxation, described qualitatively in good agreement with a damped diffusion model proposed by Brandt [12] and Kes [13]. As expected, the relaxation process shows increasing vortex lattice stiffness with increasing magnetic field and reduced damping with increasing temperature. Besides this general trend, we observe a dramatic changeover of the relaxation process associated with the non-trivial vortex lattice morphology in the intermediate mixed state and the crossover from attractive vortex-vortex interaction to repulsive vortex interaction in the Shubnikov phase. Whereas the relaxation exhibits a single exponential shape in the Shubnikov phase, an additional second process on a very fast time scale is observed in the intermediate mixed state. This changeover is attributed to a Landau-branching of the Shubnikov domains at the surface of the sample. This study represents a show-case how to access directly vortex lattice melting and the formation of vortex glass states in unconventional superconductors, notably the cuprates, heavy-fermion systems, borocarbide or ironarsenide systems.

1.4 Vortices in Magnetically Ordered Systems

1.4.1 Properties of Vortices in Magnetically Ordered Systems

We have already introduced that similar to vortex lattices in superconductors, which are stabilized by the surface energy associated with a superconducting to normal conducting interface, Bogdanov, Jablonskii and Hubert *et al.* [19, 20, 21, 22] propose the stabilization of vortices in ferromagnets by Bloch domain walls. As they naturally favour a rotation of magnetic moments similar to Bloch domain walls, ferromagnetic systems exhibiting helical order are promising candidates for the formation of magnetic vortex lattices with topological properties:

Helical instabilities of ferromagnetic order are mostly provided by the Dzyaloshinskii-Moriya interaction: For systems crystallizing in a structure lacking inversion symmetry, the competition between the Dzyaloshinskii-Moriya interaction [23, 24], which favours a perpendicular alignment of neighbouring spins, and ferromagnetic coupling, which favours a parallel alignment, leads to the formation of an incommensurable spiral order with long periodicity. The periodicity is thereby given by the ratio of both competing energy scales. A depiction of a typical helical and conical arrangement of magnetic moments is given in Fig. 1.6, panel (i).

In contrast to magnetic vortices and multi-$\mathbf{q}$ structures, which are caused by geometrical frustration of the magnetic exchange interaction with respect to the crystalline structure [61], the long pitch observed in helical magnets leads to an efficient decoupling of the magnetic order from the underlying crystal lattice on the one hand. On the other hand, the Dzyaloshinskii-Moriya interaction naturally provides the non-linear coupling terms in the field theory, necessary for the formation of skyrmionic topological order as pointed out by Bogdanov and coworkers [21, 20]. Finally, the spatial size of the magnetic vortices

is determined by the pitch of the helical order, leading to large structures on an atomic scale. However, clear experimental evidence for the existence of stable vortices in ferro- or antiferro magnetic systems was missing. A schematic depiction of the proposed magnetic vortices and the corresponding magnetic vortex lattice is given in panels (ii) and (iii) of Fig. 1.6.

Recently, the ideas of Bogdanov and coworkers have been revitalized by a number of experimental findings in the archetypal helical magnet MnSi, which crystallizes in the cubic B20 structure, lacking inversion symmetry. MnSi exhibits weak itinerant ferromagnetism below a transition temperature $T_c = 29.5\,\mathrm{K}$, explained quantitatively by a Stoner model, including corrections arising from enhanced fluctuations [25]. The magnetic phase diagram of MnSi is characterized by four distinct phases, a depiction is given in Fig. 1.7. Below the critical field H_{c1}, the helices are pinned by weak crystal field anisotropy to the crystalline $\langle 111 \rangle$ directions. Above H_{c1}, the helices realign into the magnetic field direction until at H_{c2} a field polarized state is reached. In vicinity of T_c at approximately $1/2H_{c2}$, a small phase pocket, called A-phase, separated by a weak first order phase transition was found. Neutron scattering studies established a perpendicular alignment of helices and magnetic field [27, 28] in the A-phase.

The possible existence of an intermediate phase in MnSi [95, 96] in the vicinity of T_c at ambient field and pressure was interpreted theoretically in terms of a spontaneous skyrmion ground state [18], stabilized by a phenomenological parameter. However, the authors of this study point out, that the conical phase always has lower energy compared to the skyrmionic state in a mean field calculation for cubic systems [18]. Furthermore, a partial order with unusual scattering pattern was observed above a critical pressure p_c in an extended non-Fermi-liquid regime in MnSi by Pfleiderer *et al.* [97]. The partial order thereby survives far into the non-Fermi-liquid phase. It supports the existence of novel phases with partial ordering of the conduction electrons similar to liquid crystals.

Calculations by Binz *et al.* and Fischer by means of Landau theory [15, 14, 16] compare favourably with existing data on the high pressure behaviour: Binz *et al.* construct a

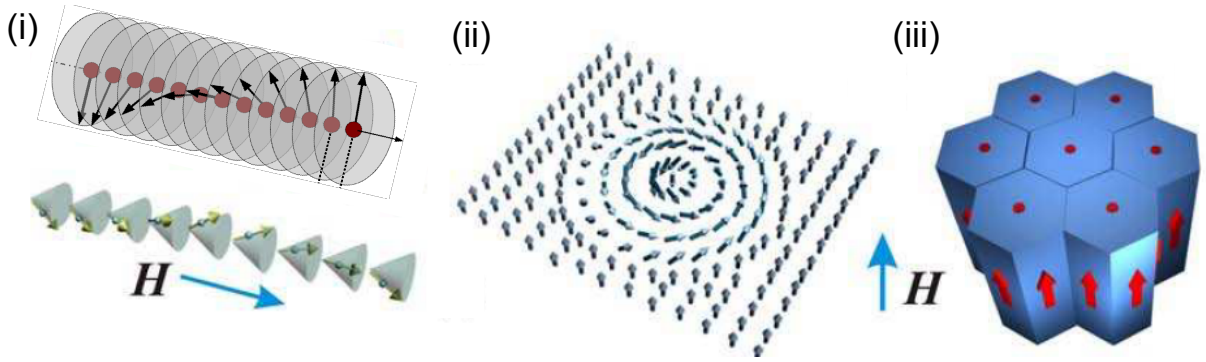

Figure 1.6: Panel (i) shows a schematical drawing of a helical order (upper illustration) and a conically distorted helical order in the presence of a magnetic field (lower illustration), as observed e.g. in MnSi. Panel (ii) represents a single magnetic vortex, panel(iii) depicts a hexagonal arrangement of vortices to a skyrmion lattice. Panels (i) to (iii) adopted from [94].

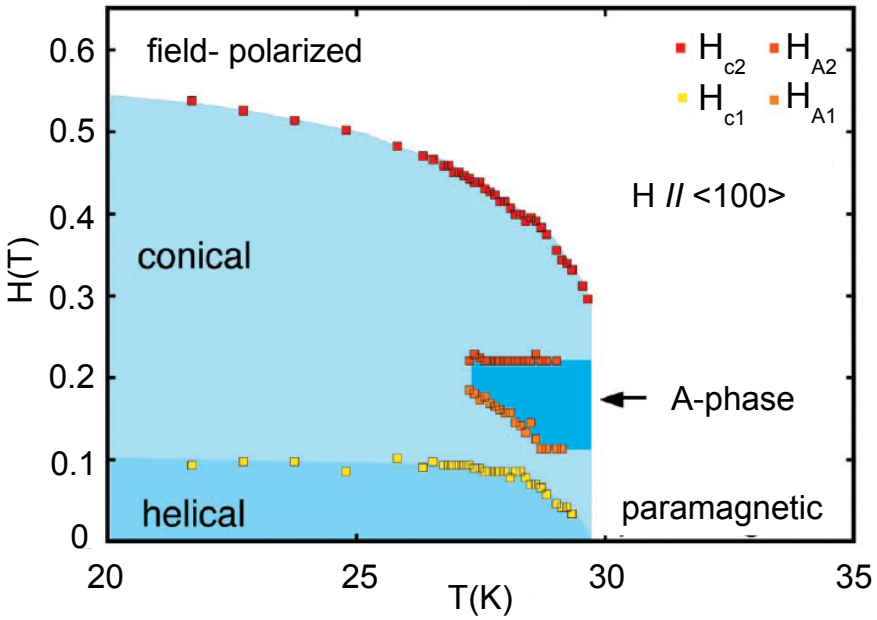

Figure 1.7: The magnetic phase diagram of MnSi is shown at ambient pressure as function of temperature T and applied magnetic field H. Plot adopted from [30].

magnetic spin crystal by a linear superposition of helices and calculate its stability by means of Landau theory, where they find, that the *bcc* spin crystal is favoured. Tewari *et al.* [17] evoke close analogies to the blue phases in cholesteric liquid crystals and propose that similar condensation transition involving a chiral order parameter can occur in itinerant helimagnets. Recent calculations by Butenko *et al.* [94] show that skyrmion textures are stabilized by uniaxial distortions in noncentrosymmetric cubic heli-magnets.

1.4.2 Motivation

In this thesis, we use small angle neutron scattering to revisit the magnetic phase diagram of the archetypal helical magnet MnSi in detail. In contrast to previous studies [27, 28], we choose both a parallel alignment of the magnetic field with respect to the incoming neutron beam as well as a perpendicular alignment. In particular, the parallel alignment of the magnetic field with respect to the incident neutron beam allows to resolve the complete magnetic structure of the A-phase, which is characterized by a perpendicular alignment of the propagation vector $\mathbf{k}$ of the helical order and the magnetic field.

With our experiments, we establish the existence of a skyrmion lattice in the A-phase of MnSi [30]: The observed scattering pattern in the A-phase exhibits a regular, hexagonal symmetry reminiscent of a vortex lattice. The orientation of this lattice is strictly driven by the orientation of the applied magnetic field, regardless of the underlying crystal symmetry, whereas the periodicity of the observed structure is identical to the pitch of the helical magnetic spiral, observed in MnSi under zero field.

We interpret our experimental findings as lattice of topological knots of the magnetization

with particle-like properties, arranged in a regular six-fold manner. A Ginzburg-Landau ansatz following earlier work by Bak and Jensen [31] shows, that in the presence of a uniform magnetization $\mathbf{M}_f$, the quartic $\mathbf{M}^4$-term, which describes the mode-mode interactions is effectively cubic in the modulated moment amplitudes. This naturally gives rise to a triple-$\mathbf{Q}$ structure: An expansion of the free energy including numerical calculations of Gaussian fluctuations confirms, that a spin crystal, composed by the superposition of three helices with $\mathbf{Q} = \mathbf{k}$, inclined at an angle of 120° with respect to each other and perpendicular to the magnetic field represents a stable groundstate. The integration of the winding density yields a topological charge $C_{top} = -1$ per unit cell, proving the existence of a stable magnetic topology and identifies the spin-crystal as skyrmion lattice.

1.5 Outline

In the following paragraph we give a brief overview of the structure of this thesis:

Both, vortex lattices in superconductors and heli-magnets exhibit large scale magnetic structures with respect to atomic scales. The charge-neutral neutron deeply penetrates condensed matter samples but nevertheless weakly interacts with magnetic moments due to its spin. The wavelength of a cold neutron beam typically meets several atomic lattice constants, thus avoiding contributions from nuclear scattering. Using a cold neutron beam, neutron scattering thus is ideally suited to measure the structure and symmetry of superconducting vortex lattices and complex forms of long range magnetic order. In the following chapter (2), we briefly introduce the technique of neutron scattering on superconducting vortex lattices and helical magnets.

The main part of this thesis work splits into two parts. For a better readability, both parts are self-contained.

In the first part, we focus on the studies performed on the properties of the superconducting vortex lattice of the model system niobium (chapter (3)). We therefore introduce in detail the symmetry and structure as well as the dynamic properties of vortex lattices, using a Ginzburg-Landau ansatz. We then focus on the special properties of low-κ superconductors before presenting the details of our measurements on the morphology and elasticity of the vortex lattice in the model system niobium.

In the second part, we briefly review the properties of weak helical ferromagnets and introduce the Dzyaloshinkii-Moriya interaction and the Bak-Jensen model for helical magnets. We then introduce the properties of the weak itinerant heli-magnet MnSi, before we present our small angle neutron scattering measurements of the magnetic phase diagram of MnSi (chapter (4)).

We finally close with a brief summary on recent studies on the evolution of the skyrmion lattice under presence of doping and disorder in the isostructural siblings of MnSi, $Fe_{1-x}Co_xSi$, $Mn_{1-x}Co_xSi$ and $Mn_{1-x}Fe_xSi$ and give an outlook on future studies.

Chapter 2

Neutron Scattering

2.1 Introduction

We have introduced the properties of vortex lattices in superconductors and vortex structures in helical ferromagnets in chapter (1). Both superconducting vortex lattices and akin structures in helical ferromagnets exhibit complex magnetic superstructures with long periodicity on atomic scales. Neutron scattering is a powerful and versatile tool for the examination of the static and dynamic properties of such structures. This is due to the unique interaction of the charge-neutral neutron with condensed matter. In the following, we give a brief introduction into the fundamental principles of neutron scattering from nonmagnetic and magnetic samples using unpolarised neutrons in sections (2.2) and (2.3). We then derive the elastic neutron scattering cross-section of vortex lattices in superconductors and of the helical order in the weak ferromagnet MnSi in sections (2.4) and (2.5), respectively. Finally, the typical small angle neutron scattering setup as used for our studies is introduced.

Salient features of the interaction of neutrons with condensed matter are:

- The de-Broglie wavelength of thermal neutrons is of the same order of magnitude compared to the atomic distance of solid or liquid condensed matter (typically a few Å). If neutrons are scattered from such a sample, interference effects occur which yield valuable information on the structure and dynamics of the scattering system. The energy of a thermal neutron beam ($E_n = 81.81/\lambda^2$ [meV] with λ in Å) and its momentum are of the same order of magnitude as elementary excitations in condensed matter systems. Inelastic neutron scattering thus gives easy access to phonon or magnon excitations throughout the complete Brillioun-zone. However, the use of a cold neutron beam, where the wavelength typically meets several atomic lattice constants allows to suppress nuclear Bragg reflections.

- The interaction of the charge-neutral neutron with matter is determined by the nuclear force. Due to its short range, the interaction may be treated as point-like, leading to a high, $\mathbf{q}$ independent form factor for nuclear Bragg reflections. In

contrast to X-ray scattering, the nuclear interaction is no monotonic function of the atomic number. In contrast, it varies strongly for neighbouring elements and even for different isotopes of the same element. This allows to tailor scattering contrasts, which can be favourable especially for light or strongly absorbing elements. The absence of charge and hence missing Coulomb interaction permits neutrons to deeply penetrate into matter, allowing to study the bulk properties of samples.

- Due to their spin, neutrons weakly interact with the magnetic fields present in the sample with a dipolar interaction. Neutron scattering thus also yields valuable insight into the magnetic properties of condensed matter systems.

The de-Broglie relation for the wavelength of a free neutron reads

$$\lambda = \frac{h}{p} \tag{2.1}$$

with the momentum of the neutron

$$\mathbf{p} = \hbar\mathbf{k} \tag{2.2}$$

and its energy

$$E = \frac{1}{2}mv^2. \tag{2.3}$$

In a typical neutron scattering experiment, neutrons with wavelength λ_i and wavevector $\mathbf{k_i}$ and associated energy E_i are impinged on the sample to be investigated. Due to the scattering process at the sample, the momentum and energy of the neutrons change from the initial states $\mathbf{k_i}$ and E_i into the final states $\mathbf{k_f}$ and E_f, respectively. The conservation of momentum and energy for the scattering process yields

$$\begin{aligned} \mathbf{q} &= \mathbf{k}_i - \mathbf{k}_f \\ \hbar\omega &= E_i - E_f = \frac{\hbar^2}{2m_n}(|\boldsymbol{k}_i|^2 - |\boldsymbol{k}_f|^2) \end{aligned} \tag{2.4}$$

with the momentum transfer $\mathbf{q}$ and the energy transfer $\hbar\omega$.

The probability of neutrons being scattered in a particular direction $\mathbf{k}_f$ with the energy transfer $\hbar\omega$ is described by the scattering function $S(\mathbf{q},\omega)$, which yields the Fourier transform of the scattering potential in real space and time. The cross-section σ is defined by the ratio of scattered neutrons per second per incident neutron flux Φ. The double differential cross-section then reads

$$\frac{\mathrm{d}^2\sigma}{\mathrm{d}\Omega_f \mathrm{d}E_f} = \frac{\text{Neutrons, scattered into the solid angle } \mathrm{d}\Omega_f \text{ and the energy interval } \mathrm{d}E_f}{\text{Incident flux of neutrons } \Phi \mathrm{d}\Omega_f \mathrm{d}E_f}\,. \tag{2.5}$$

A schematic depiction of the double differential cross-section is given in Fig. 2.1.

It is convenient, to express the double differential cross-section as sum over coherent and incoherent scattering, where the coherent part contains information on collective effects amongst the scattering entities such as Bragg scattering, magnons or phonons. In contrast, the incoherent part yields information on the individual particle motion due

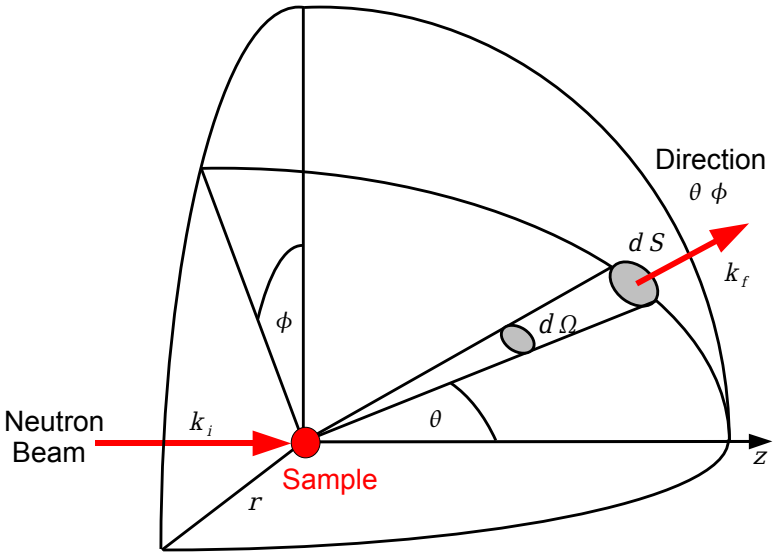

Figure 2.1: Depiction of the scattering process: Neutrons with initial wavevector $\mathbf{k}_i$ are scattered into the solid angle $\mathrm{d}\Omega_f$ with the final energy E_f.

to fluctuations, diffusion or isotope variations. In contrast to coherent scattering, the incoherent scattering cross-section is isotropic in $\mathbf{q}$.

$$\frac{\mathrm{d}^2\sigma}{\mathrm{d}\Omega_f \mathrm{d}E_f} = \frac{\mathrm{d}^2\sigma}{\mathrm{d}\Omega_f \mathrm{d}E_f}\bigg|_{coh} + \frac{\mathrm{d}^2\sigma}{\mathrm{d}\Omega_f \mathrm{d}E_f}\bigg|_{inc} \tag{2.6}$$

For a detailed review on neutron scattering, we refer to the books by Bacon [98], Lovesey [99] and Squires [100]. In the following, we derive the basic scattering formulæ for elastic nuclear and magnetic scattering with unpolarized neutrons following the description given by Shirane, Shapiro and Tranquada [101].

2.2 Nuclear Neutron Scattering

A neutron beam with wavevector $\mathbf{k}_i$ impinging on a sample can be treated as weak perturbation of the sample. A scattering neutron yet can cause a transition from one quantum state of the sample to another, but the quantum states themselves remain conserved. The scattering cross-section can therefore be derived using Fermi's Golden Rule. The interaction operator is represented by V, the initial and final states are labeled with the quantum numbers λ_i and λ_f. The double differential cross-section then reads

$$\frac{d^2\sigma}{d\Omega_f dE_f}\bigg|_{\lambda_i \Rightarrow \lambda_f} = \frac{k_f}{k_i}\left(\frac{m_n}{2\pi\hbar^2}\right)^2 |\langle \mathbf{k}_f\lambda_f|V|\mathbf{k}_i\lambda_i\rangle|^2 \delta(\hbar\omega + E_i - E_f)\ . \tag{2.7}$$

As the effective interaction is weak and its range is small compared to the neutron wavelength λ, the scattering process can be treated in Born approximation, describing both

incoming and outgoing neutrons with plane waves. This yields for the interaction matrix element

$$\langle \mathbf{k}_f \lambda_f | V | \mathbf{k}_i \lambda_i \rangle = V(\mathbf{q}) \langle \lambda_f | \sum_j e^{i\mathbf{q}\cdot\mathbf{r}_j} | \lambda_i \rangle \ , \tag{2.8}$$

with $\mathbf{r}_j$ representing the position of the scattering centres, which are assumed to be identical, and the nuclear pseudopotential

$$V(\mathbf{q}) = \int d\mathbf{r} V(\mathbf{r}) e^{i\mathbf{q}\cdot\mathbf{r}} \ . \tag{2.9}$$

Due to the short range of the interaction, the nuclear pseudopotential is represented by a delta function in $\mathbf{r}$

$$V(\mathbf{r}) = \frac{2\pi\hbar^2}{m_n} \sum_j b_j \delta(\mathbf{r} - \mathbf{R}_j) \ . \tag{2.10}$$

This yields

$$V_j(\mathbf{q}) = \frac{2\pi\hbar^2}{m_n} b_j \tag{2.11}$$

with the nuclear scattering length b_j of the j'th atom.

For coherent elastic scattering on a sample, whose nuclear scattering centres are arranged on a Bravais lattice, the double differential cross-section then simplifies to [101]

$$\left.\frac{d\sigma}{d\Omega}\right|_{el} = N_n \frac{(2\pi)^3}{v_0} \sum_G \delta(\mathbf{q} - \mathbf{G}) |F_n(\mathbf{G})|^2, \tag{2.12}$$

with the static nuclear structure factor F_n containing the scattering length $\overline{b_j}$ and the position $\mathbf{d}_j$ of the j'th atom within the unit cell

$$F_n(G) = \overline{b}_j e^{iG\cdot d_j} e^{-W_j} \ . \tag{2.13}$$

v_0 identifies the volume of the unit cell whereas the vectors $\mathbf{G}$ represent the unit vectors of the associated reciprocal lattice. This means, that scattered intensity is observed solely, when the momentum transfer $\mathbf{q}$ coincides with a reciprocal lattice vector $\mathbf{G}$, referred to as Bragg peak. The Debye-Waller factor W_j is a measure of the fluctuations of the atoms around their equilibrium position. The Debye-Waller effect reduces the intensity of the Bragg peaks leading to an incoherent background.

2.3 Magnetic Neutron Scattering

As neutrons own a magnetic dipole moment, every *ordered* magnetic structure of the sample likewise contributes to coherent scattering. The magnetic moment of a neutron reads

$$\boldsymbol{m}_n = -\gamma \mu_n \boldsymbol{\sigma} \tag{2.14}$$

with the gyromagnetic ratio γ, the nuclear magneton μ_n and the spin operator $\boldsymbol{\sigma}$. The potential energy of a neutron in a magnetic field $\mathbf{B}$ then yields

$$E = -\gamma\mu_n \boldsymbol{\sigma} \cdot \mathbf{B} \ . \tag{2.15}$$

In an unpolarized neutron beam, all polarization directions are equally distributed, the probability for spin up and spin down is equal. The scattering length then consists of two components: The nuclear and the magnetic contribution.

Magnetic moments in condensed matter can be generated by the spin of the nuclei and the spin or angular momentum of the electron shell. As the nuclear and the magnetic scattering centres often share the same position in the unit cell but their scattering lengths can be of opposite sign, interference effects do occur. In analogy to nuclear scattering, the magnetic form factor $f(\mathbf{q})$ is the Fourier transform of the normalized unpaired spin density $\varrho_m(\mathbf{r})$ of an atom. As the magnetic moment of the neutrons as well as the magnetic moments of the systems examined are vectorial quantities, the magnetic cross-section depends on their relative orientation. The magnetic form factor reads

$$f(\mathbf{q}) = \int \varrho_m(\mathbf{r}) e^{i\mathbf{q}\cdot\mathbf{r}} d\mathbf{r} \tag{2.16}$$

with $f(0) \equiv 1$.

Neglecting the contribution of the angular momentum of the electrons at first, the cross-section for magnetic scattering was derived by Halpern and Johnson (1939) [102]. The cross-section depends not only on the initial and final wavevector of the scattered neutron but also on the corresponding neutron spin states $\mathbf{s}_i$ and $\mathbf{s}_f$ with $\mathbf{s} = \boldsymbol{\sigma}/2$. Generalizing equation (2.7) then yields for the double differential cross-section, summing over all possible initial states λ_i and final states λ_f

$$\left.\frac{d^2\sigma}{d\Omega_f dE_f}\right|_{s_i \to s_f} = \frac{k_f}{k_i} \sum P(\lambda_i) \left| \langle \lambda_f \left| \sum_l e^{i\mathbf{q}\cdot\mathbf{r}l} U_l^{s_i s_f} \right| \lambda_i \rangle \right|^2 \delta(\hbar\omega + E_i - E_f) \ . \tag{2.17}$$

The atomic scattering amplitude $U_l^{s_i s_f}$, associated with a transition from the spin state $\mathbf{s}_i$ to $\mathbf{s}_f$ of the neutron being scattered at the atomic site l reads

$$U_l^{s_i s_f} = \langle s_f | b_j - p_l \mathbf{S}_{\perp l} \boldsymbol{\sigma} + B_l \mathbf{I}_l \boldsymbol{\sigma} | s_i \rangle \tag{2.18}$$

with the coherent nuclear scattering length b_j. B_l represents the spin-dependent nuclear amplitude with the nuclear spin operator $\mathbf{I}$. $\mathbf{S}_\perp$ denotes the magnetic interaction vector, firstly introduced by de Gennes (1963)[103] and later adopted by Moon, Riste and Koehler (1969) [104]

$$\mathbf{S}_\perp = \mathbf{q}_e \times (\mathbf{S} \times \mathbf{q}_e) \ , \tag{2.19}$$

with the unit vector $\mathbf{q}_e$ in direction of $\mathbf{q}$. Thus, only the components of $\mathbf{S}$, which are oriented perpendicular to $\mathbf{q}$, contribute to magnetic scattering. This effect is also denoted *magnetic selection rule*.

Considering only moments attributed to spin yields

$$\mathbf{M}(\mathbf{q})/\mu_b = g\mathbf{S}f(\mathbf{q}) \tag{2.20}$$

with $g = 2$. We now relax this restriction and include the magnetic moment, associated with the angular momentum of the electron shell. With the radial wavefunction $\Phi(r)$ corresponding to the unpaired spin, this yields for the magnetic form factor in the dipole approximation

$$f(\mathbf{q}) = \int_0^\infty r^2 j_o(Qr)|\Phi(r)|^2 dr = \langle j_0 \rangle \tag{2.21}$$

where j_n is a spherical Bessel function of the order n, ignoring aspherical contributions.

In analogy to the nuclear cross-section, the coherent elastic cross-section for magnetic scattering of unpolarized neutrons can be simplified, if the magnetic moments of the scattering sample are arranged on a Bravais lattice. The cross-section then reads

$$\left.\frac{d\sigma}{d\Omega}\right|_{el} = N_m \frac{(2\pi)^3}{v_m} \sum_{G_m} \delta(\mathbf{q} - \mathbf{G}_m)|\mathbf{F}_m(\mathbf{G}_m)|^2 \tag{2.22}$$

with the static magnetic structure factor $\mathbf{F}_m$

$$\mathbf{F}_m(\mathbf{G}_m) = \sum_j p_j \mathbf{S}_{\perp j} e^{i\mathbf{G}_m \cdot \mathbf{d}_j} e^{W_j}. \tag{2.23}$$

where the index m identifies the volume v_m of the magnetic unit cell and the number of magnetic unit cells N_m in the sample. The sum in equation (2.23) is over sites within the magnetic unit cell.

2.4 Neutron Scattering from Superconducting Vortex Lattices

We have already introduced, that superconducting vortex lattices are magnetic Bravais lattices with a lattice constant that is large compared to the underlying crystal lattice. The magnetic structure of a vortex is *not* carried by localized magnetic moments, associated with magnetic ions: The spatial magnetic field distribution of the vortex lattice is determined by the direction and modulus of the applied magnetic field, the vortex lattice symmetry and structure and the London penetration depth λ, which characterizes the magnetic field profile of a single vortex.

In a neutron scattering experiment, the *magnetic* contribution to the scattering cross-section is solely caused by the superconducting vortex lattice. Due to the long periodicity of the vortex lattice the use of a long wavelength cold neutron beam is necessary. The wavelength of a cold neutron beam typically meets several atomic lattice constants. The Bragg condition for nuclear diffraction can therefore not be satisfied. Thus, also no scattering can arise from the interference between nuclear and magnetic scattering.

The superconducting vortex lattice owns the symmetry of a two-dimensional Bravais line lattice, whereby the vortices are oriented strictly parallel to the applied magnetic field. The reciprocal lattice of the vortex lattice can then be easily obtained by a rotation around the magnetic field axis by 90° and vice versa. Accordingly, the reciprocal lattice vectors $\mathbf{G}_{VL}$ of the superconducting vortex lattice are oriented strictly perpendicular to the magnetization direction. However, the demagnetizing factor N of the sample and the refraction of the magnetic field at the surface of the sample cause a bending of the vortex lattice, which is neglected for this description.

The lattice constant a_i of a superconducting vortex lattice is defined solely by its symmetry and the equilibrium induction B. This yields the useful equation

$$|\mathbf{a}_i| = \left(\frac{2\phi_0}{\sqrt{B}}\right)^{1/2} = \frac{2\pi}{|\mathbf{G}_{VL}|} \tag{2.24}$$

for a regular six-fold symmetry. For instance, an equilibrium induction of B =150 mT then leads to a lattice spacing of ∼1260 Å.

The scattering geometry used for our examinations of superconducting vortex lattices is sketched in Fig. 2.2, panels (i) to (iii): The incoming neutron beam is oriented almost parallel to the applied magnetic field, hence perpendicular to $\mathbf{G}_{VL}$. As the wave vector $\mathbf{k}_i$ of a cold neutron beam is typically much larger compared to the reciprocal lattice vector $\mathbf{G}_{VL}$ of the vortex lattice, the Bragg angles of vortex lattices are of the order of a few tenths of a degree. This means, that the reciprocal lattice of the superconducting vortex lattice has to be rocked by a small angle ϕ to satisfy the Bragg condition (cf. panel (ii)).

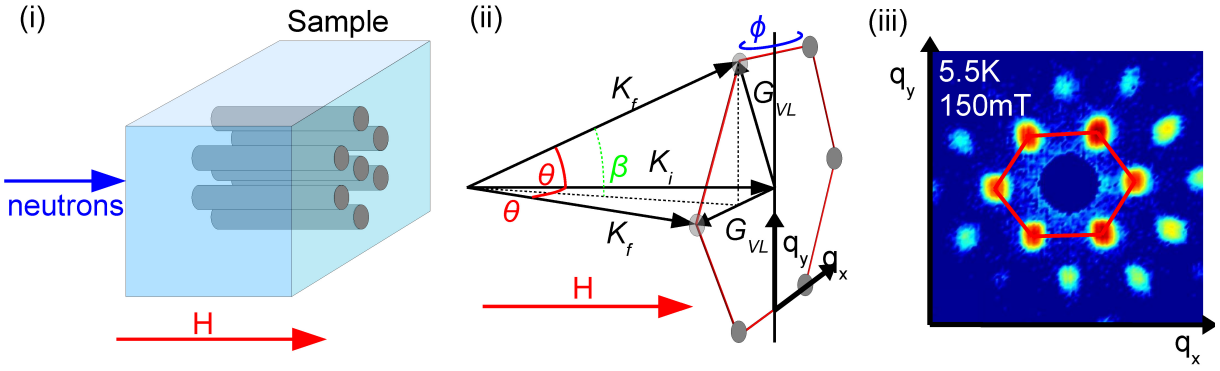

Figure 2.2: Panel (i) schematically depicts the sample with the superconducting vortex lattice in real space. The resulting scattering geometry (in reciprocal space) for small angle neutron scattering on a vortex lattice is given in panel (ii). Panel (iii) shows typical small angle neutron scattering data of a vortex lattice of superconducting niobium at $T = 5.5\,\mathrm{K}$ and $\mu_0 H = 150\,\mathrm{mT}$, obtained by a summation over a rocking scan.

By rocking the magnetic field and the sample together with respect to a vertical axis perpendicular to the neutron beam by the angle ϕ, the reciprocal lattice of the vortex lattice is rotated through the Ewald sphere. In this manner, all Bragg peaks of the superconducting vortex lattice not lying on the axis of rotation can be observed. Typical data is shown in

Fig. 2.2, panel (iii). Due to the small scattering angles, neutron diffraction experiments on superconducting vortex lattices are usually performed on so-called small angle neutron scattering instruments. The setup of a typical small angle neutron scattering instrument, as it was used for our studies, is described in section (2.6).

Integrated Intensity of a Vortex Lattice Bragg Reflection

For the derivation of the integrated intensity of a vortex lattice Bragg peak, we follow the description given by Huxley, Brandt and Eskildsen [1, 105, 106]. The magnetic scattering length of a regular vortex lattice is defined by

$$b_{VL} = \frac{\gamma\mu_N}{\pi\hbar^2/2m_n}\boldsymbol{\sigma}\int d\mathbf{r}\mathbf{B}(\mathbf{r})e^{i\mathbf{qr}} \tag{2.25}$$

with the neutron gyromagnetic ratio γ and the neutron spin $(1/2)\boldsymbol{\sigma}$.

Exploiting the periodicity of the vortex lattice, it is possible to express its field distribution by a two-dimensional Fourier series

$$\mathbf{B}(\mathbf{r}) = \sum_{\mathbf{q}} \mathbf{h}(\mathbf{q})e^{i\mathbf{qr}} \ . \tag{2.26}$$

With

$$\mathbf{B}(\mathbf{q}) = A_0 t\mathbf{h}(\mathbf{q}) \tag{2.27}$$

and the unit cell area of the vortex lattice $A_0 = \phi_0/B$, the sample thickness t and the nuclear magneton $\mu_n/(4\pi\hbar^2/2m_n)$, one finds for the scattering length

$$b_{VL} = \frac{\gamma}{4\phi_0}A_0 t\boldsymbol{\sigma}\mathbf{h}(\mathbf{q}) \tag{2.28}$$

and the elastic differential scattering cross-section

$$\left.\frac{d\sigma}{d\Omega}\right|_{el} = (2\pi)^3\left(\frac{\gamma}{4\pi_0}\right)^2 A_{sample}t\sum_{\mathbf{q}}\delta(\mathbf{q}-\mathbf{G}_{VL})|\mathbf{h}(\mathbf{q})|^2 \tag{2.29}$$

with the vortex lattice form factor $|\mathbf{h}(\mathbf{q})|$.

To compute the form factor of a vortex lattice, the detailed knowledge of the spatial distribution of the magnetic field $\mathbf{B}(\mathbf{r})$ and the order parameter $|\Psi(\mathbf{r})|^2$ is necessary. As will be derived in section (3.2.3), this leads to the following limitations: For low inductions, a linear superposition of the vortex fields yields a valid description. In contrast, the Ginzburg-Landau formalism describes the vortex lattice in the limit $T \to T_c$ and $B \to B_c$ with strongly overlapping vortex cores. Nevertheless, neutron scattering experiments on vortex lattices are often performed in the intermediate field range to assure either a sufficient separation of scattered neutrons and direct beam and a reasonable signal to noise ratio.

The form factor of vortex lattices has been calculated within various approximations. Mostly used for superconductors with high κ is a modified London model, where the effects of the vortex cores are included by multiplying the London equations with a cut-off function. The form factor is approximately given by

$$\mathbf{h}(\mathbf{q}) = \frac{\phi_0}{(2\pi\lambda)^2} e^{-2\pi^2 B\xi^2/\phi_0} \tag{2.30}$$

with a Gaussian cut-off. For the integrated reflectivity of a vortex lattice Bragg peak, obtained by a rocking scan of ϕ then follows

$$R = \frac{N}{I_0 A_{sample}} = \frac{2\pi\gamma^2\lambda_n^2 t}{16\phi_0^2|\mathbf{q}|\cos(\beta_Q)}|\mathbf{h}(\mathbf{q})|^2 \tag{2.31}$$

with the total number of scattered neutrons $N = I_0 \int d\Omega \int dt \frac{d\sigma}{d\Omega}$, the incident neutron flux I_0, the vortex lattice form factor $|\mathbf{h}(\mathbf{q})|^2$ and the Lorentz factor $\cos(\beta_Q)$.

Measurements of the form factor of vortices can yield valuable information on the penetration depth λ and the Ginzburg-Landau coherence length ξ. However, the pronounced dependence of $\mathbf{h}(\mathbf{q})$ on the penetration depth λ leads to significant loss of scattering intensity for strong type-II superconductors. Measurements of the penetration depth yield $\lambda(T \to 0)$=470±50 Å for pure niobium [107]. In contrast, the heavy fermion compound $CePt_3Si$ exhibits $\lambda(T \to 0) \sim 11000$ Å [108]. This leads to a reduction of the integrated reflectivity by a factor $3.3{\cdot}10^{-6}$. For a detailed description, we refer to Brandt [105], Pesch and Kramer [109] and Clem [110].

2.5 Neutron scattering from Helical Magnets

In the following section we derive the elastic magnetic cross-section of the incommensurate helical order observed in the weak itinerant magnet MnSi. We follow the work by Izyumov *et al.* [111] and Janoschek [96].

MnSi exhibits helical magnetic order below a transition temperature $T_c = 29.5$ K. The magnetic moments are arranged in spirals with a pitch of 180 Å. The propagation vector of the helical order $\mathbf{k}$ is aligned perpendicular to the magnetic moments. A sketch of the helical order is given in Fig. 2.3, panel (i). Using the description by Bak and Jensen [31] the incommensurate helical order in MnSi can be written in terms of

$$\mathbf{S}(\mathbf{r}) = \alpha_k \cos(\mathbf{kr}) - \beta_k \sin(\mathbf{kr}) \tag{2.32}$$

with its propagation vector $\mathbf{k}$. Similar to the description of the scattering length of a superconducting vortex lattice, we also perform an expansion in Fourier modes. Then follows for the total spin (or angular momentum) with the magnetic ion on site d in the

unit cell l

$$\begin{aligned}\langle \mathbf{S}_{ld} \rangle &= \mathbf{R}_d^{\mathbf{k}} \cos\left(\mathbf{k}\cdot\mathbf{l}+\phi_d\right) + \mathbf{I}_d^{\mathbf{k}} \sin\left(\mathbf{k}\cdot\mathbf{l}+\phi_d\right) \\ &= \frac{\mathbf{R}_d^{\mathbf{k}}}{2}\left(e^{i(\mathbf{k}\cdot\mathbf{l}+\phi_d)} + e^{-i(\mathbf{k}\cdot\mathbf{l}+\phi_d)}\right) + \frac{\mathbf{I}_d^{\mathbf{k}}}{2i}\left(e^{i(\mathbf{k}\cdot\mathbf{l}+\phi_d)} - e^{-i(\mathbf{k}\cdot\mathbf{l}+\phi_d)}\right) \\ &= \underbrace{\frac{\mathbf{R}_d^{\mathbf{k}} - i\mathbf{I}_d^{\mathbf{k}}}{2} e^{i\phi_d} e^{i\mathbf{k}\cdot\mathbf{l}}}_{\equiv \mathbf{S}_d^{\mathbf{k}}} + \underbrace{\frac{\mathbf{R}_d^{\mathbf{k}} + i\mathbf{I}_d^{\mathbf{k}}}{2} e^{-i\phi_d} e^{-i\mathbf{k}\cdot\mathbf{l}}}_{\equiv \mathbf{S}_d^{-\mathbf{k}}}\end{aligned} \tag{2.33}$$

where $\mathbf{R}_d^{\mathbf{k}}$ and $\mathbf{I}_d^{\mathbf{k}}$ represent the real and imaginary part of the magnetic Fourier mode $\mathbf{S}_d^{\mathbf{k}}$ with the propagation vector $\mathbf{k}$, respectively. ϕ_d defines the phase with respect to the origin. Different magnetic structures with different periodicities can be modeled upon varying $\mathbf{S}_d^{\mathbf{k}}$ and $\mathbf{k}$. Avoiding some lengthy maths, it follows for the cross-section of both terms $\mathbf{k}$ and $-\mathbf{k}$, taking all prefactors and the magnetic form factors into account [111]

$$\left.\frac{\mathrm{d}\sigma}{\mathrm{d}\Omega}\right|_{mag,el} = N(\gamma r_0)^2 \frac{(2\pi)^3}{v_0} \sum_{\mathbf{G}} \sum_{\mathbf{k}} \sum_{\alpha,\beta} (\delta_{\alpha\beta} - \hat{q_\alpha}\hat{q_\beta} F_M^{\mathbf{k}\alpha\dagger} F_M^{\mathbf{k}\beta} \delta(\mathbf{q}-\mathbf{k}-\mathbf{G}), \tag{2.34}$$

with the magnetic structure factor

$$\mathbf{M}_M^{\mathbf{k}} = \sum_d g_d F_d(\mathbf{q}) e^{-W_d(\mathbf{q})} e^{i\mathbf{q}\cdot\mathbf{d}} \mathbf{S}_d^{\mathbf{k}} \ . \tag{2.35}$$

The summation is taken over both positive and negative propagation vectors $\pm\mathbf{k}$. It is immediately clear from eq. (2.34), that if neutrons are scattered at an incommensurate *magnetic* structure, intensity appears at satellite positions $\mathbf{q} = \mathbf{G} \pm \mathbf{k}$ around *nuclear* Bragg peaks situated at $\mathbf{G}$. Note, that the magnetic moments are associated with the crystalline lattice positions for the incommensurate helical magnetic structure in MnSi.

The helical order in MnSi is characteristic of a sinusoidal modulation of magnetic moments (cf. eq. (4.8)), yielding only a single Fourier component $\mathbf{k}$. Thus no higher order reflections can be detected in a neutron diffraction experiment. In contrast, in the presence of an external magnetic field, anharmonic components arise due to the distortion of the helical order, as either the sinusoidal modulation of spins distorts from its ideal helical form or the length of the magnetic moments varies. Similar effects have been observed by Lebech *et al.* [29] and Grigoriev *et al.* [112, 27, 113].

In MnSi, four degenerate domains of the helical order are observed for the four $\langle 111 \rangle$ directions, each giving rise to scattering intensity for $\pm\mathbf{k}$, respectively. A schematic depiction of the reciprocal lattice of MnSi, where therefore eight satellite peaks appear in the $\langle 111 \rangle$ directions around a nuclear Bragg peak is given in Fig. 2.3, panel (ii). A sketch of the scattering geometry is given in Fig. 2.3, panel (iii). By rocking the sample akin to an experiment on vortex lattices, all Bragg spots of the helical order not lying on the axis of rotation can be rotated through the Ewald sphere formed by $\mathbf{k}_i$ and $\mathbf{k}_f$. Similar to superconducting vortex lattices, the long pitch of the helical order in MnSi leads to small Bragg angles, e.g., $\sim 1.7°$ for a neutron wavelength of $\sim 10\,\text{Å}$.

A small angle neutron scattering instrument is thus used for our studies, as introduced in section (2.6). In a typical small angle setup, the satellite peaks of the helical order are investigated around the (000) nuclear Bragg reflection, which is identical to the direct beam. Due to the finite divergence of the neutron beam and the large intrinsic mosaicity of the helical order — which is typically of the same order of magnitude or even larger compared to the scattering angle for cold neutrons — both domains of the helical order can be observed simultaneously. Typical small angle scattering data of the helical order in MnSi is given in panel (iv), where two pairs of diffraction spots correspond to $\pm\mathbf{k}$ for two $\langle 111 \rangle$ directions.

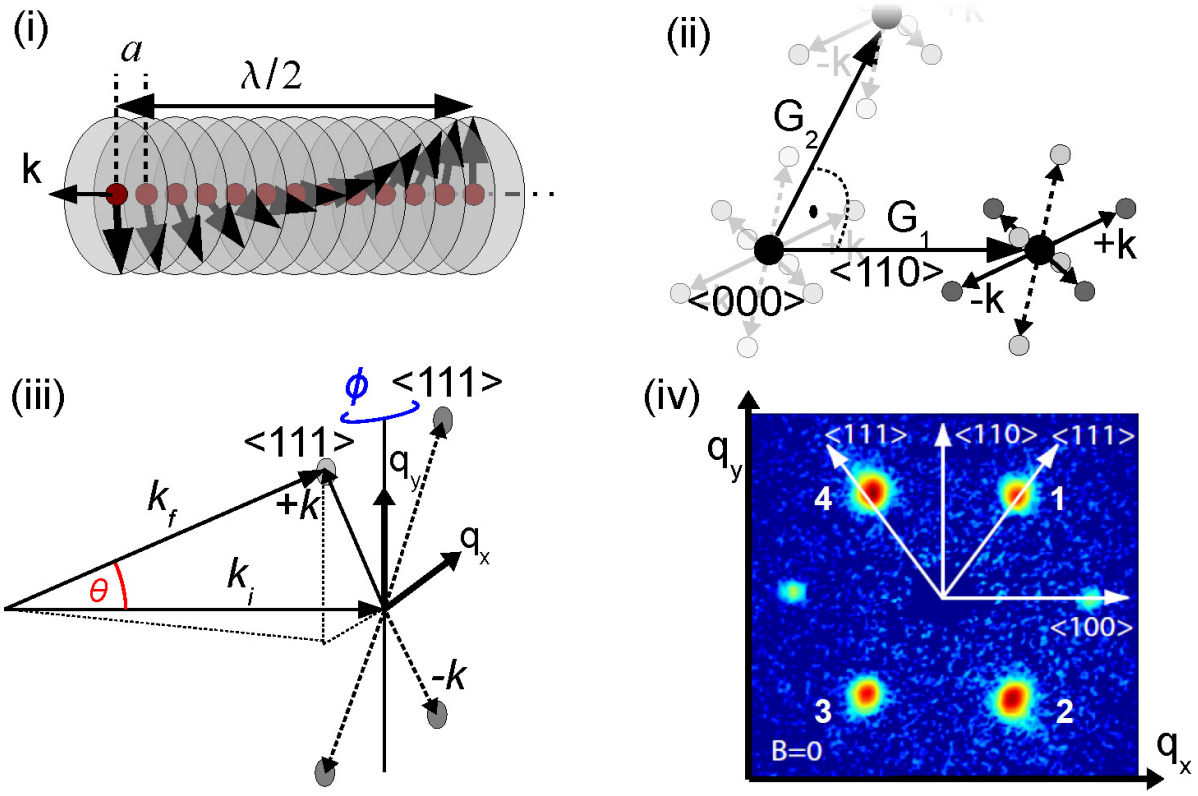

Figure 2.3: Panel (i) schematically depicts the helical order in MnSi, characterized by the propagation vector $\mathbf{k}$. Panel (ii): Depiction of the relative orientation (in reciprocal space) of the satellite peaks associated with the propagation vectors $\mathbf{k}$ of the helical order in MnSi with respect to the nuclear reciprocal lattice vectors $\mathbf{G}_1$ and $\mathbf{G}_2$. For a typical triple axis experiment, the satellite peaks are measured around a nuclear $\langle 110 \rangle$, $\langle 111 \rangle$ or $\langle 222 \rangle$ reflection due to the magnetic structure factor and an insufficient energy transfer at the $\langle 000 \rangle$ reflection. In contrast, in a small angle neutron experiment, the satellite peaks are measured around the direct beam, corresponding to the nuclear (000) reflection. (iii) Schematic depiction of the scattering geometry, as used for our work. Panel (iv) depicts typical data, obtained for the helical phase of MnSi at a temperature of 27 K and zero applied magnetic field, obtained by the summation over a rocking scan.

2.6 Experimental Setup

In this paragraph, we present the typical setup of a small angle neutron scattering instrument, as it is used for the measurements on superconducting vortex lattices in niobium and the helical magnetic order in MnSi throughout this thesis. A small angle neutron scattering instrument is optimized for small scattering angles: A schematic setup is shown in Fig. 2.4: In a small angle neutron scattering instrument, the neutron beam is collimated over a large distance L_1 (typical 10-20 m) by a slit system upstream of the sample position. The scattered neutrons are detected by a two-dimensional position sensitive detector at the distance L_2 to the sample. To prevent scattering by air, the collimation system and the detector flight tube are evacuated.

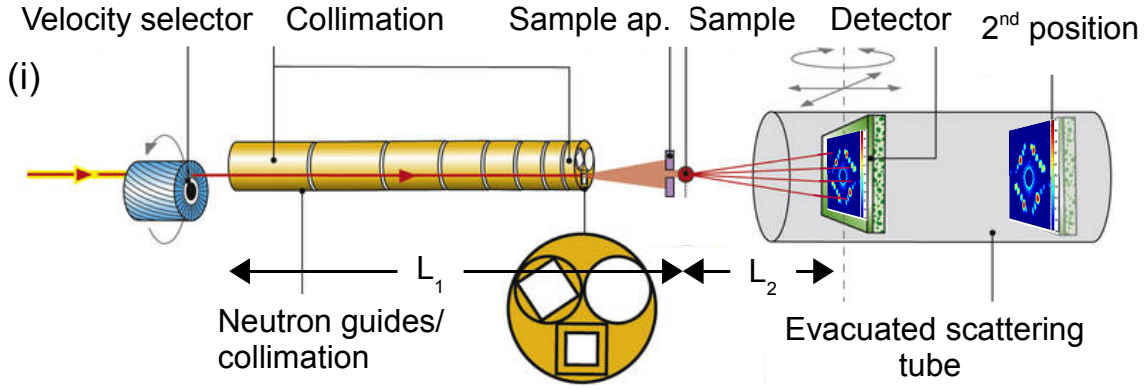

Figure 2.4: Typical setup of a small angle neutron scattering instrument. For details, see text.

The measurements of the static and dynamic properties of superconducting vortex lattices in niobium covered in this thesis have been performed at the small angle neutron scattering instrument V4 at BENSC [114]: The experimental settings for these measurements will be introduced in-depth in sections (3.6.2) and (3.7.2), respectively.

The measurements of the magnetic structure of MnSi have been performed on the cold diffractometer MIRA at FRM II [115], where MIRA was used like a small angle scattering instrument. The specific experimental settings will be introduced in-depth in section (4.4.2). The instrumental resolution of the different setups, arising from the finite collimation of the neutron beam, the wavelength spread and the detector resolution will be derived in section (A.1).

Chapter 3

Static and Dynamic properties of Superconducting Vortex Lattices

3.1 Introduction

We have introduced in section (1) that both the static and dynamic properties of superconducting vortex lattices and vortex matter, namely their symmetry and structure as well as their elastic matrix $\Phi_{\alpha\beta}$ sensitively reflect the microscopic nature of the superconductivity as well as individual sample properties. In addition, the elastic matrix of vortex lattices defines the state of aggregation and the pinning/depinning properties of vortex matter, leading to a strong relevance for technical applications of superconductors. However, the unambiguous mapping of different sources of anisotropy is intricate [1] for both the symmetry and the elastic matrix of superconducting vortex lattices. We have further illustrated that the manifold of different influences on the properties of vortex matter raises the question how to generalize the behaviour of vortex matter and makes studies of conventional superconductors of general interest.

The conventional, isotropic single gap superconductor niobium [6, 7] is ideally suited to provide such general information [8, 9, 10]. As we have already introduced and motivated in section (1.3), small angle neutron scattering measurements of the static and dynamic properties of the superconducting vortex lattice in the model system niobium represent a major focus of this thesis. In particular, we study the multitude of vortex lattice structures, emerging due to frustration between the six-fold vortex lattice symmetry and the four-fold crystal symmetry for the magnetic field applied parallel and in vicinity of a four-fold $\langle 100 \rangle$ axis. We further present direct microscopic measurements of the intrinsic vortex lattice tilt modulus c_{44} of bulk samples by a novel time resolved small angle neutron scattering technique.

In the following section (3.2), we therefore briefly review the framework of the Ginzburg-Landau theory which we use to derive the symmetry of an ideal superconducting vortex lattice in the region close to the superconducting transition temperature T_c. We then abandon the limit close to T_c and use the BCS theory to derive the symmetry of vortex

lattices for the complete superconducting phase region. In our description, we particular focus on different origins of anisotropy on the vortex lattice symmetry.

In section (3.3), the elastic energy and the elastic matrix of a distorted vortex lattice for an ideal bulk, pinning-free superconductor is derived by means of a Ginzburg-Landau approach. In particular, we focus on the elastic constants for uniform distortions and briefly introduce the thermal stability and melting of vortex lattices. In section (3.4) we summarize the topology of the vortex lattice for a low-κ superconductor like niobium with non-zero demagnetizing factor. In particular, we concentrate on the morphology of the intermediate-mixed state and its intimate analogy to the intermediate state in type-I superconductors. The properties of the ultra-pure niobium sample, used for our studies, are presented in depth in section (3.5).

In section (3.6) we finally present the small angle neutron scattering study on the vortex lattice structure and symmetry in niobium where the phase diagram is examined close to a $\langle 100 \rangle$ axis. In section (3.7) we explain microscopic measurements of the vortex lattice tilt modulus c_{44} by means of time resolved stroboscopic small angle neutron scattering.

3.2 Vortex Lattice Symmetry from Ginzburg-Landau and BCS Theory

In the following section, we first derive the different magnetic field behaviour of type-I and type-II superconductors before we briefly review the different sources of anisotropy influencing the symmetry and structure of superconducting vortex lattices within the Ginzburg-Landau and BCS theory.

3.2.1 Ginzburg-Landau Theory

The unique property of the superconducting state is the existence of a macroscopic, coherent wavefunction $\psi(\mathbf{r}) = \sqrt{(n_s/2)}e^{i\phi}$ with the condensate density of superconducting electrons n_s and a phase $\phi(\mathbf{r})$. The Ginzburg-Landau theory introduces a spatially varying n_s, allowing a non-linear coupling between magnetic fields and $|\psi|^2$. The Ginzburg-Landau theory is based on an expansion of the free energy F in terms of $|\psi|^2$ in the limit close to T_c, where $|\psi|^2$ is a small quantity,

$$F = F_{n0} + \alpha|\psi|^2 + \frac{\beta}{2}|\psi|^4 + \frac{1}{2m^*}\left|\left(\frac{\hbar}{i}\nabla - \frac{e^*}{c}\mathbf{A}\right)\psi\right|^2 + \frac{h^2}{8\pi} \tag{3.1}$$

where F_{n0} describes the free energy of the normal conducting state and α and β are the expansion coefficients. m^* and e^* denote the mass and the charge of the Cooper-pairs. The so-called Ginzburg-Landau equations are derived from equation (3.1) by variation with respect to ψ and the vector potential $\mathbf{A}$. They read

$$\alpha\psi + \beta|\psi|^2\psi + \frac{1}{2m^*}\left(\frac{\hbar}{i}\nabla - \frac{e^*}{c}\mathbf{A}\right)^2\psi = 0 \tag{3.2}$$

and

$$\mathbf{J} = \frac{c}{4\pi} \times \mathbf{H} = \frac{e^*\hbar}{2m^*i}(\psi^*\nabla\psi - \psi\nabla\psi^*) - \frac{e^{*2}}{m^*c}\psi\psi^*\mathbf{A}\,. \tag{3.3}$$

with the density of the superconducting screening currents $\mathbf{J}$.

Two characteristic length scales can be deduced from the Ginzburg-Landau equations (cf. Fig. 3.1, panels (i) and (ii)): The first is denoted London penetration depth λ

$$\lambda^2(T) = \frac{m^*c^2}{4\pi n_s e^{*2}}\ . \tag{3.4}$$

λ describes the characteristic penetration of an external magnetic field into the bulk superconductor. The temperature dependence of $|\psi|^2$ yields $\lambda^2(T) \propto (1 - \frac{T}{T_c})^{-1}$. The second length scale is the Ginzburg-Landau coherence length

$$\xi^2(T) = \frac{\hbar^2}{2m^*|\alpha(T)|} \propto \frac{1}{1 - \frac{T}{T_c}} \tag{3.5}$$

describing the characteristic stiffness of the superconducting wavefunction ψ. The Ginzburg-Landau parameter $\kappa = \lambda/\xi$ is then a direct measure for the energy, associated with a normal- to superconducting interface (cf. Fig. 3.1): A long London penetration depth leads to a gain of energy, as the magnetic field has not to be expelled. Due to the superconducting condensation energy a short coherence length leads to a gain of energy as well. κ is independent of T within the valid range of the Ginzburg-Landau theory for temperatures close to T_c.

For superconducting materials with $\kappa < 1/\sqrt{2}$, the surface energy is positive, thus the magnetic flux of an external field is totally expelled out of the superconductor except a surface layer with thickness λ. For such materials, the magnetic field is expelled for increasing magnitude until the superconductivity breaks down at the thermodynamical critical field B_c. B_c reads

$$B_c = \frac{\phi_0}{\sqrt{8}\pi\xi\lambda}\ . \tag{3.6}$$

This behaviour is called type-I superconductivity. The magnetic phase diagram of a type-I superconductor is sketched in Fig. 3.1, panel (iii).

For so-called type-II superconductors with $\kappa > 1/\sqrt{2}$, the formation of interfaces between normal and superconducting regions leads to a gain of energy. The solution for this problem was obtained by Abrikosov [32] by extending the Ginzburg-Landau equations to the parameter regime of type-II superconductors: Abrikosov introduced a solution of the phenomenological Ginzburg-Landau theory where the superconducting order parameter exhibits periodic nodes. The magnetic field can penetrate bulk type-II superconductors in form of vortices, situated at the nodes, each carrying one flux quantum $\phi_0 = h/2e$. As introduced in section (1.2), the magnetic flux is quantized due to the continuity conditions for the superconducting phase on a closed loop around a vortex and the electromagnetic coupling to the gauge field $\mathbf{A}$. The magnetic field behaviour of ideal type-II superconductors is characterized by two distinct phases (cf. Fig. 3.1, panel (iv)): For

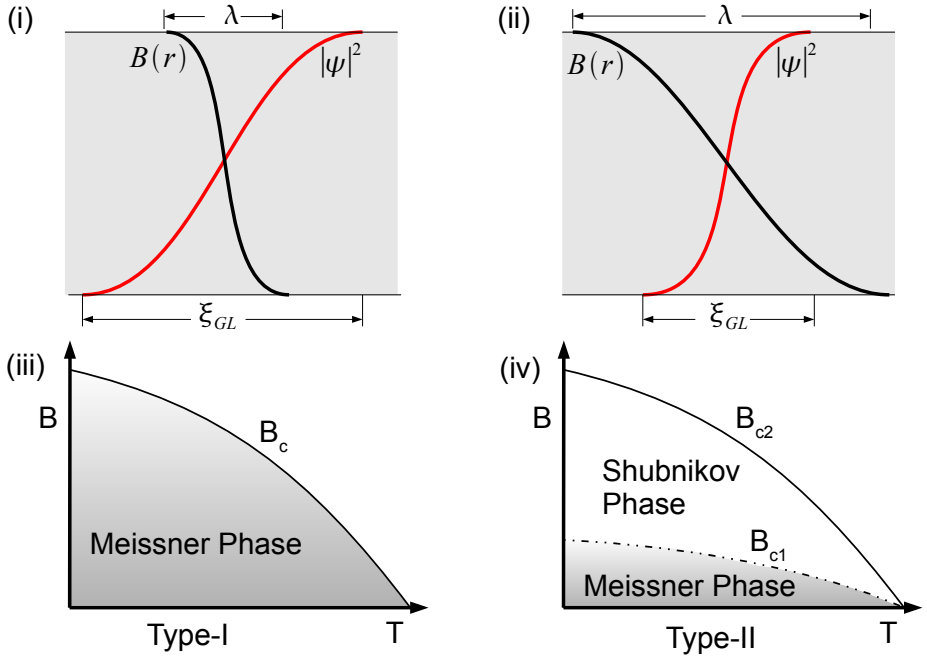

Figure 3.1: Schematic profiles of the order parameter $\psi(x, y)$ and the magnetic field $B(r)$ along a normal- to superconducting interface for type-I (panel (i)) and type-II superconductors (panel(ii)). A sketch of the magnetic phase diagram for a type-I and type-II superconductor is given in panels (iii) and (iv).

$B < B_{c1}(T) \leq B_c(T)$ the material is in the Meissner phase, the magnetic field is expelled. The lower critical field B_{c1} reads

$$B_{c1} \sim \frac{\phi_0}{4\pi\lambda^2}(\ln\kappa + 0.5) \ . \tag{3.7}$$

In the field range $B_{c1}(T) \leq B \leq B_{c2}(T)$ the so-called Shubnikov phase is formed where the vortices penetrate the sample and form a vortex lattice. For increasing field the vortex density increases until the upper critical field B_{c2} is reached, where the cores of the vortices, given by the coherence length ξ, completely overlap and the superconductivity vanishes. B_{c2} reads

$$B_{c2} = \frac{\phi_0}{2\pi\xi^2} = \sqrt{2}\kappa B_c \ . \tag{3.8}$$

The order parameter $|\psi(\mathbf{r})|^2$ and the magnetic field of an *isolated* flux line are given approximately by Clem *et al.* [116] and Hao *et al.* [110]

$$|\psi(\mathbf{r})|^2 \sim 1/(1 + 2\xi^2/\mathbf{r}^2) \tag{3.9}$$

and

$$B(\mathbf{r}) \sim \frac{\phi_0}{2\pi\lambda^2} K_0[(\mathbf{r}^2 + 2\xi^2)^{1/2}/\lambda] \tag{3.10}$$

with $\mathbf{r} = (x^2 + y^2)^{1/2}$, $B \parallel z$ and the modified Bessel function $K_0(x)$.

Similar to the energy, associated with a normal- to superconducting interface, the interaction of vortices may naively be separated into the electromagnetic interaction due to the London penetration depth λ and the interaction due to the condensation energy with the characteristic length scale ξ: The free energy of straight parallel vortices was instructively expressed by Brandt [117] by

$$F(\mathbf{r}_i) = \frac{\phi_0^2}{2\pi\lambda^2\mu_0} \sum_i \sum_{i>j} \left[K_0 \left(\frac{|\mathbf{r}_i - \mathbf{r}_j|}{\lambda'} \right) - K_0 \left(\frac{|\mathbf{r}_i - \mathbf{r}_j|}{\xi'} \right) \right] \tag{3.11}$$

$$\begin{aligned} \lambda' &= \lambda / \langle |\psi|^2 \rangle^{1/2} \sim \lambda/(1-b)^{1/2} \\ \xi' &= \xi/[2(1-b)]^{1/2} \\ b &= B/B_{c2} \end{aligned} \tag{3.12}$$

where the first term after the summation in eq. (3.11) represents the *repulsive* electromagnetic vortex-vortex interaction with an effective London penetration depth λ'. The second term represents the *attractive* interaction with an effective coherence length ξ' for reduced fields $b = B/B_{c2}$.

One easily realizes that the energy landscape is flattening for superconductors with κ close to $1/\sqrt{2}$. For $\kappa = 1/\sqrt{2}$, all vortex lattice arrangements have the same energy. This establishes superconductors with low κ as sensitive tools, analyzing different influences on vortex lattice symmetries and properties. Moreover, a crossover from attractive to repulsive vortex-vortex interaction is observed for low-κ superconductors at low inductions (cf. section (3.4).

3.2.2 Ideal Vortex Lattice Symmetry

The ideal spatial arrangement of vortices is determined by the minimum of the free energy. For low inductions $B < 0.2\, B_{c2}$, the profile of the superconducting order parameter is given by a product of terms of the form eq. (3.9) whereby the field distribution can be obtained by a linear superposition of terms as given in eq. (3.10), often referred to as London approximation. This approximation holds for arbitrary arrangements of non-overlapping vortices at distances greater than $\sim 5\,\xi$. The free energy is given by the simple expression

$$F = \frac{\phi_0}{8\pi} \sum_{i,j} h_j(\boldsymbol{r}_j) \tag{3.13}$$

with the magnetic field of a vortex h_j. Due to the large vortex spacing, only nearest neighbour interactions have to be considered. A repulsive vortex-vortex interaction then leads to a six-fold symmetry of the vortex lattice where the inter-vortex distance is maximized.

In contrast, at high inductions $B > 0.5\, B_{c2}$, the Ginzburg-Landau theory for a periodic vortex lattice yields for the magnetic field distribution and the order parameter [117]:

$$|\psi(\mathbf{r})|^2 = \frac{1 - B/B_{c2}}{[1 - 1/(2\kappa^2)]\beta_A} \sum_{\mathbf{K}} a_{\mathbf{K}} \cos \mathbf{K}\mathbf{r} \tag{3.14}$$

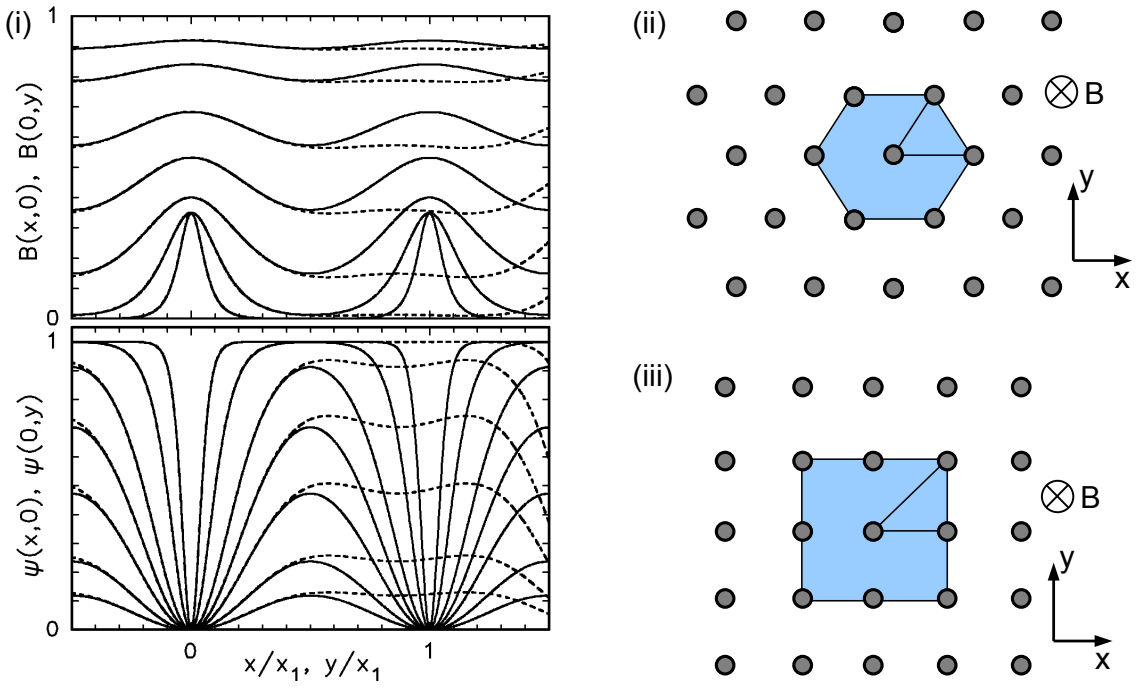

Figure 3.2: Panel (i): Profiles of order parameter $\psi(x,y)$ and magnetic field $B(x,y)/B_{c2}$ for a triangular vortex lattice at reduced inductions $b = B/B_{c2} = 0.9,\ 0.8,\ 0.6,\ 0.4,\ 0.2,\ 0.05,\ 0.01$ for κ= 1.5. Plot taken from Brandt [118]. Panel (ii) and (iii) depict the typical hexagonal and quadratic symmetry of vortex lattices.

$$B(\mathbf{r}) = B - (\phi_0/4\pi\lambda^2)|\psi(\mathbf{r})|^2 \tag{3.15}$$

The summation is carried out over all reciprocal vortex lattice vectors $\mathbf{K}_{mn} = (2\pi/x_1y_2)$ $(my_2; -mx_2 + nx_1)$ at the positions $\mathbf{R}_{nm} = (my_2; -mx_2 + nx_1)$. Schematic profiles for the order parameter and the magnetic field are given in Fig. 3.2, panel (i).

The Fourier coefficients a_K and the Abrikosov parameter β_A yield for general vortex lattice symmetries [119]

$$a_K = (-1)^{m+mn+n} e^{-K_{mn}^2 x_1 y_2/8\pi} \qquad \beta_A = \sum_K a_K^2 \,. \tag{3.16}$$

This yields (still for $B > 0.5\,B_{c2}$) for the free energy and the negative magnetization $-M = \mu_0 H - B \geq 0$ of an arbitrary vortex arrangement

$$F(B) = \frac{B^2}{2\mu_0} - \frac{(B_{c2} - B)^2}{2\mu_0(2\kappa^2 - 1)\beta_A} \tag{3.17}$$

$$M(B) = \frac{B_{c2} - B}{(2\kappa^2 - 1)\beta_A} = \frac{\phi_0}{4\pi\lambda^2}\langle|\psi|^2\rangle \tag{3.18}$$

with the applied magnetic field $\mu_0 H = \mu_0 \partial F/\partial B$, which is in local equilibrium with the vortices at the induction B and the magnetization $-M$, averaging over several unit cells of the vortex lattice.

The Abrikosov parameter obtained for the ideal hexagonal symmetry reads $\beta_A = 1.16$, whereas $\beta_A = 1.18$ for a square vortex lattice symmetry. A depiction of the square and hexagonal vortex lattice symmetry is given in Fig. 3.2, panels (ii) and (iii). This demonstrates that the energy landscape is rather flat, leading to strong deviations from the ideal hexagonal symmetry, e.g. for an anisotropic Fermi mass or velocity. As we have pointed out in the previous section, this is of particular importance for superconductors characterized by a Ginzburg-Landau parameter close to $1/\sqrt{2}$ as, e.g., niobium.

3.2.3 Vortex Lattice Symmetries from Microscopic Theory

We have presented the Ginzburg-Landau model and the London model which yield a good qualitative description of vortex lattices symmetries for both low and high inductions. However, for intermediate inductions $0.2\,B_{c2} < B < 0.5\,B_{c2}$ both models fail to explain the magnetic field distribution and the vortex lattice symmetry due to an invalid parameter regime. Nevertheless, small angle neutron scattering measurements on superconducting vortex lattices — including the measurements performed for this thesis — are mostly performed in the intermediate field region: For low inductions, the lattice spacing of the vortex lattice is large, leading to very small Bragg angles. In contrast for high inductions, the form factor of the vortex lattice decreases as given by eq. (2.30).

According to Brandt [117], a valid description of the vortex lattice symmetry over the complete superconducting phase region can be achieved by a Ritz variational method using Fourier series as trial functions for $|\psi(\mathbf{r})|^2$ and $B(\mathbf{r})$ [120] extending the early analytical solutions by Kleiner *et al.* [121] and Eilenberger [122]. A similar variational method was employed to derive the ideal symmetry of vortex lattices for the complete superconducting phase diagram for superconductors with arbitrary purity from microscopic BCS theory, as firstly done by Eilenberger [123]. Eilenberger expresses the free energy in terms of energy integrated Greens functions. Numerical calculations which use the circular cell method, have been performed by various groups for many different applications: They comprise various accounts allowing for different mean free electron paths and purity, for multi-gap systems with non-conventional order parameters, anisotropies of the superconducting gap and non-local corrections due to Fermi anisotropies.

However, the determination between different sources of deviations from the ideal six-fold symmetry is intricate: Allowing for anisotropies of the Fermi mass leads to a distortion of the vortex lattice, that can be described by an anisotropic mass tensor $m_{ij} = \langle \Delta^2 v_{fi} v_{fj} \rangle / \det(m)$. This model is widely used for the layered cuprate and ruthenate compounds as a first approximation [124]. The resulting anisotropy of the vortex lattice shows almost no temperature and magnetic field dependence.

In contrast, anisotropy introduced by non-local corrections to the Ginzburg-Landau or Eilenberger theory show a pronounced magnetic field dependence as they are corrections to the free energy. The non-locality arises due to the stiffness of the superconducting wavefunction: The current at a certain point is then given by the vector potential in the region with an extent given by ξ. In addition, such corrections depend on the magnitude of the coherence length ξ and, in particular, on the ratio of the mean free electron path

with respect to ξ, showing an increasing influence with increasing purity of the sample. For instance, the weak four-fold anisotropy of the critical fields and the superconducting gap for *bcc* niobium is explained by non-local corrections due to the four-fold crystal lattice symmetry [125, 126].

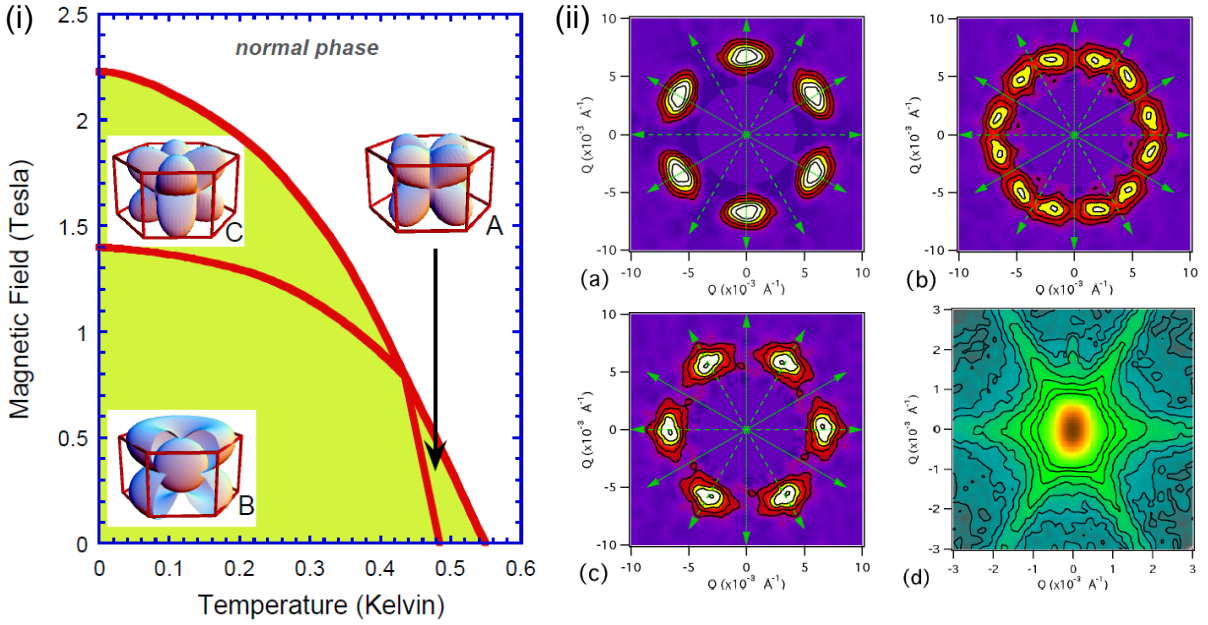

Figure 3.3: Panel (i) shows the low temperature phase diagram of UPt_3 for the magnetic field applied along the hexagonal crystalline c direction. Three different superconducting phases, denoted A, B and C are separated by second order phase transitions. The gap symmetries for A, B and C, are schematically depicted for the E_{2u} model [127]. Panel (ii) shows the vortex lattice structures, obtained by small angle neutron scattering on UPt_3 [1]. The magnetic field of 0.19 T is aligned parallel to the hexagonal c direction. (a) corresponds to the vortex lattice formed at low temperature in the B-phase after zero field cooling. (b) depicts the frozen vortex lattice of the A-phase during a field cooling procedure starting from 475 mK. (c) depicts the vortex lattice resulting from field cooling above $T_c \sim 520$ mK where the vortex lattice is aligned with extended metallurgical defects. These metallurgical defects are present in the star-like shaped background (d).

Recently Nakai *et al.* [80] have calculated the symmetry of vortex lattices using the microscopic Eilenberger formalism comprising a weak four-fold symmetry of the Fermi velocity $v_F(\theta) = v_F(\pi/8)(1+\beta\cos 4\theta)$ and a weak four-fold symmetry of the superconducting gap $|\Delta(\mathbf{r},\theta)|^2 = |\Delta(\mathbf{r},\pi/8)|^2(1-\alpha\cos 4\theta)$ with the polar angle θ, finding a reentrant vortex lattice transition from rhombic to square back to rhombic symmetry as function of applied magnetic field and temperature, explaining the reentrant square to hexagonal to square vortex lattice transition identified in the compound $LuNiB_2C$ [79].

The interplay of gap and Fermi surface anisotropy can therefore yield various vortex lattice symmetry changes and lock-in transitions. We have already pointed out that such effects have also been observed in the isotropic s-wave superconductor niobium [8, 9, 10] caused by the interplay of the four-fold crystal and the six-fold vortex lattice symmetry. The

deconvolution of the different sources of anisotropy to the vortex lattice in niobium is a central point of this thesis.

The intrinsic symmetry of the order parameter is a further source of anisotropic behaviour, as e.g. for the heavy fermion compound $PrOs_4Sb_{12}$ [82] where the presence of nodes of the superconducting gap on at least some Fermi surface sheets is assumed. Small angle neutron scattering measurements on the complicated vortex lattice phase diagram of the heavy fermion compound UPt_3, where three different vortex phases are distinguished, lead to an unconventional two-component picture. The phase diagram of UPt_3 is given in Fig. 3.3. A review of the physics of UPt_3 can be found in the book by Mineev and Samokhin [84].

Summarizing, both for the case of conventional and unconventional superconductivity the superconducting gap can be anisotropic. Yet for conventional systems, the anisotropy rarely exceeds 10%, whereas for unconventional order parameter symmetry nodes are expected to occur. For a summary on vortex lattice symmetries we refer to the work by Brandt [117], Goll [128] and Huxley [1] and the references therein.

3.3 Vortex Lattice Elasticity

In this section, we introduce the dynamic behaviour of vortex lattices. We first concentrate on the derivation of the free energy of an arbitrarily curved vortex lattice using a Ginzburg-Landau ansatz. We then derive the elastic matrix $\Phi_{\alpha\beta}$ and deduce the eigenfrequencies, characteristic timescales and the moduli for compression, tilt and shear of superconducting vortex lattices. In particular, we discuss the elastic moduli for uniform tilt which are relevant for the interpretation of our measurements of the vortex lattice elasticity in superconducting niobium. Finally, we briefly discuss the criterions for vortex lattice melting transitions. For a detailed theoretical description on vortex lattice elasticity, we refer to [12, 117, 129, 13].

3.3.1 Elastic Energy of Vortex Lattices

Similar to the elasticity of crystal lattices, which is determined by electrostatic or covalent forces, the elasticity of superconducting vortex lattices is determined by the vortex-vortex interactions. The free energy F of an arrangement of arbitrarily curved vortices in the Ginzburg-Landau regime close to T_c may be approximated according to Brandt [117] by the following expression: In analogy to eq. (3.11) for the interaction for *parallel* vortices, the free energy for *curved* vortices can be written in terms of three components

$$F(r_i\{z\}) = \frac{\phi_0^2}{8\pi\lambda^2\mu_0}\sum_i\sum_j\left(\int d\mathbf{r}_i\int d\mathbf{r}_j\frac{e^{-r_{ij}/\lambda'}}{r_{ij}} - \int|d\mathbf{r}_i|\int|d\mathbf{r}_j|\,\frac{e^{-r_{ij}/\xi'}}{r_{ij}}\right) . \tag{3.19}$$

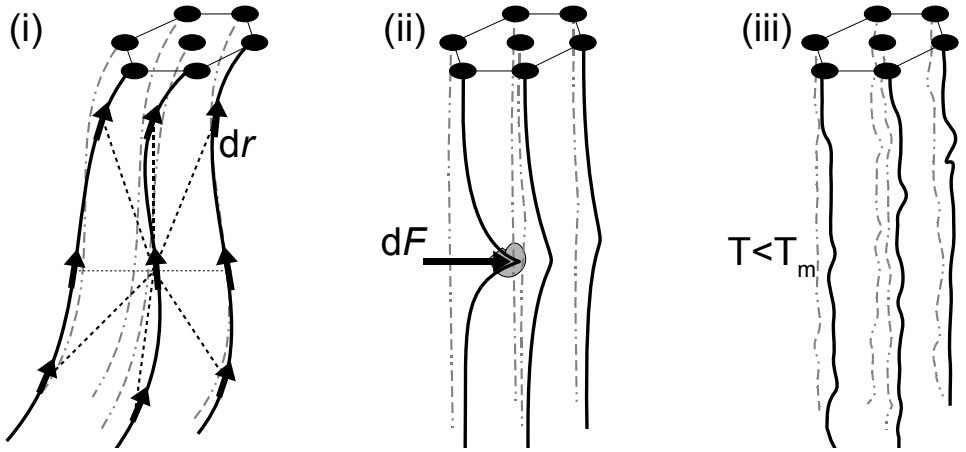

Figure 3.4: Panel (i) schematically depicts the vortex-vortex (electromagnetic interaction and condensation energy) and intra-vortex interactions (self energy or string tension) determining a particular symmetry, structure and elasticity of a superconducting vortex lattice. Panel (ii) depicts the cusp-like reaction of a superconducting vortex lattice to a pinning force dF. Panel (iii) schematically depicts a thermally fluctuating superconducting vortex lattice for a temperature $T \leq T_m$ compared to the melting temperature T_m.

with

$$\begin{aligned} r_{ij} &= |\mathbf{r}_i - \mathbf{r}_j|, \\ \lambda' &= \lambda/\langle|\psi|^2\rangle^{1/2} \sim \lambda/(1-b)^{1/2}, \\ \xi' &= \xi/[2(1-b)]^{1/2}. \end{aligned} \tag{3.20}$$

Again, the first term of the sum in eq. (3.19) represents the repulsive electromagnetic vortex-vortex interaction with an effective London penetration depth λ'. The second term represents the attractive interaction of vortex lines due to the superconducting condensation energy of overlapping vortices with an effective coherence length ξ'. The vortex self energy or line tension is included in the diagonal terms $i = j$. A schematic sketch is given in Fig. 3.4, panel (i).

The elastic energy of a distorted vortex lattice, caused by pinning, structural defects, field gradients or transport currents, temperature gradients or thermal fluctuations, however, is small for most cases. Therefore, it can be calculated by linear elastic theory, most conveniently expressed in k-space. The displacements of a vortex line $\mathbf{u}_i(z) = \mathbf{r}_i(z) - \mathbf{R}_i(z) = (u_{i,x}; u_{i,y}; 0)$ from its ideal position $\mathbf{R}_i = (X_i; Y_i; z)$ is expressed by its Fourier components

$$\mathbf{u}_i(z) = \int_{BZ} \frac{d^3k}{8\pi^3} \mathbf{u}(\mathbf{k}) e^{i\mathbf{k}\mathbf{R}_i} \tag{3.21}$$

and

$$\mathbf{u}(k) = \frac{\phi_0}{B} \sum_i \int dz \ \mathbf{u}_i(z) e^{-i\mathbf{k}\mathbf{R}_i}. \tag{3.22}$$

With $u(\mathbf{k}) = (u_x; u_y; 0)$ the elastic energy reads

$$F_{\text{elast}} = \frac{1}{2} \int_{BZ} \frac{d^3k}{8\pi^3} u_\alpha(k) \Phi_{\alpha\beta}(k) u^\star_\beta(k) \tag{3.23}$$

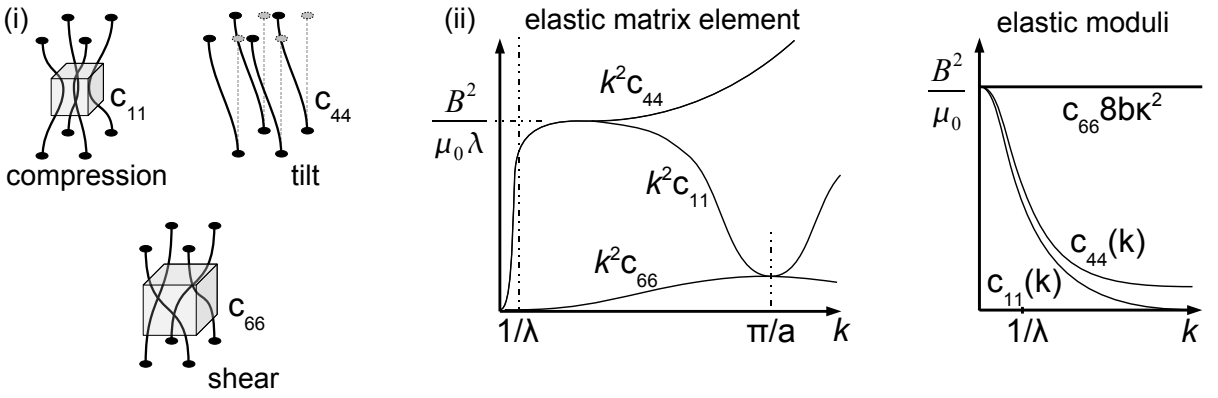

Figure 3.5: A schematic depiction of the elastic constants of a superconducting vortex lattice is given on the left-hand side. The right-hand side depicts the **k** dependence of the elastic matrix $\Phi_{\alpha,\beta}$ and of the elastic constants c_{11}, c_{44} and c_{66} of the vortex lattice. Note the different scaling for c_{66}.

where $(\alpha, \beta) = (x, y)$. The integrals in eq. (3.21) and eq. (3.22) cover the first Brillouin zone of the vortex lattice in k-space and $-\xi^{-1} \leq k_z \leq \xi^{-1}$, respectively. $\Phi_{\alpha\beta}(\mathbf{k})$ is called the elastic matrix of the vortex lattice.

$\Phi_{\alpha\beta}(\mathbf{k})$ is real, symmetric and periodic in k-space and is related to the elastic moduli c_{11} for compression, c_{44} for tilt and c_{66} for shear within continuum theory by

$$\begin{aligned} \Phi_{\alpha\beta}(\ bfk) &= (c_{11} - c_{66})k_\alpha k_\beta + \\ &\delta_{\alpha\beta}[k_\perp c_{66} + k_z^2 c_{44} + \alpha_L(k)] \end{aligned} \tag{3.24}$$

with $k_\perp = (k_x^2 + k_y^2)$. The k-dependence of the elastic matrix is plotted in Fig. 3.5, panel (ii). The Labusch parameter α_L describes the elastic interaction of the vortex lattice with pinning potentials caused by material inhomogeneities. For individual pinning, α_L is k-independent [130], for weak collective pinning [131], $\alpha_L(\mathbf{k})$ decreases when $k_\perp > R_c^{-1}$ or $k_z > L_c^{-1}$ where R_c and $L_c = (c_{44}/c_{66})^{1/2} R_c$ are the radius and length of the coherent short range ordered regions of the pinned vortex lattice.

3.3.2 Uniform Distortions

For uniform distortions, the elastic moduli of the vortex lattice can be written as [117]

$$\begin{aligned} c_{11} - c_{66} &= \frac{B^2 \partial^2 F}{\partial B^2} = \frac{B^2 \partial \mu_0 H}{\mu_0 \partial B} \\ c_{44} &= \frac{B \partial F}{\partial B} = \frac{B \mu_0 H}{\mu_0} = BH \\ c_{66} &\approx \left(\frac{B \phi_o}{16 \pi \lambda^2 \mu_0} \right) \left(1 - \frac{1}{2\kappa^2} \right) (1 - b)^2 \end{aligned} \tag{3.25}$$

with the reduced field $b = B/B_{c2}$ and the Ginzburg-Landau parameter κ. $c_{11} - c_{66}$ is the modulus for isotropic compression. H is the applied field, which is in equilibrium with the

vortex lattice at the equilibrium induction B, given by the magnetization $M = \mu_0 H - B \leq 0$. The magnetic field and temperature dependence of the equilibrium induction B will be derived in depth in section (3.4). The response of a vortex lattice to a change of the magnetic field direction is characterized by the tilt modulus c_{44} of the vortex lattice. Note that c_{66} vanishes either for $B \to B_{c2}$, which corresponds to strongly overlapping vortex cores, for $\lambda \to \infty$, corresponding to strongly overlapping vortex fields, or for $\kappa = 1/\sqrt{2}$. As we already have pointed out, in the special case $\kappa = 1/\sqrt{2}$, all vortex lattice arrangements have the same free energy.

3.3.3 Non-local Elasticity

Due to the long effective interaction lengths λ' and ξ', c_{11} and c_{44} strongly depend on the k-vector of the disturbance which is referred to as non-locality of the vortex lattice. This leads to a strong softening of the vortex lattice for short range distortions. This non-locality is giving rise to large distortions, caused by pinning, disorder or thermal fluctuations, whereby the vortex lattice reacts to external forces in the form of a sharp cusp and not like pulling a string (cf. Fig. 3.4). The lattice softening is caused mainly by the dispersion of c_{44}, whereas the dispersion and reduction of c_{11} is not crucial. c_{66} is typically much smaller compared to c_{11} (cf. Fig 3.5, panel (ii)). Thus, the shear modes of the vortex lattice deformations dominate the modes for compression [117]. Summarizing, this means that the vortex lattice is softer for short wavelength tilt or compression than it is for long wavelengths.

3.3.4 Characteristic Timescales

Until now, we have derived the elastic matrix of superconducting vortex lattices which determines the restoring force of **k**-dependent distortions. However, the eigenfrequencies of vortex lattice fluctuations are determined by the restoring force as well as the viscous damping of the vortex lattice motion. The movement of the vortices with the velocity v is damped by the viscosity

$$\eta = \frac{B^2}{\varrho_{FF}} \approx \frac{B B_{c2}}{\varrho_n} \tag{3.26}$$

creating a drag force $v\eta$ per unit volume, where ϱ_{FF} represents the flux-flow and ϱ_n the normal conducting resistivity. The elastic eigenmodes of the vortex lattice are given by a diagonalization of the elastic matrix $\phi_{\alpha\beta}$. The result is a compressional and a shear eigenmode, relaxing with exponential time dependencies [117]. In continuum approximation, this yields:

$$\begin{aligned} \Gamma_1(\mathbf{k}) &= (c_{11}(\mathbf{k})k_\perp^2 + c_{44}(\mathbf{k})k_z^2)/\eta \approx \Gamma_1 \\ \Gamma_2(\mathbf{k}) &= (c_{66}k_\perp^2 + c_{44}(\mathbf{k})k_z^2)/\eta \approx \Gamma_1 k_z^2/k^2 \end{aligned} \tag{3.27}$$

For the vortex lattice in a typical clean low κ superconductor as e.g. niobium, the eigenfrequencies Γ_1 and Γ_2 of the vortex lattice are in the range of 10^{-9} s^{-1}.

3.3.5 Vortex Lattice Melting and Transport Properties

The magnitude of thermal fluctuations of superconducting vortex lattices are mostly determined by the vortex lattice shear modulus c_{66}. Strong thermal fluctuations of the vortices can lead to vortex lattice melting transitions at the melting temperature T_m, akin to the melting of ordinary crystals. A typical phase diagram is given in Fig. 3.6, panel (i): A vortex disordered state, a lattice Bragg glass and vortex lattice liquid are distinguished. A simple melting criterion for vortex lattices can be estimated from the Lindemann criterion for thermal fluctuations of vortex lattices [117]: At the melting temperature T_m, thermal fluctuations $\langle u^2 \rangle$ yield $\langle u^2 \rangle = c_L^2 a^2$ with the Lindemann parameter $c_L \approx 0.1 \ldots - 0.2$ and the vortex lattice spacing a.

Melting transitions of vortex lattices show up as characteristic dips of the differential resistivity. Melting of vortex lattices can also lead to tiny jumps of the local magnetization of the order of few tenths of a Gauss, detectable with sensitive Hall probes [132]. The temperature and magnetic field dependence of the elastic constants of vortex lattices and their melting can also be determined by vibrating reed measurements. However, measurements to detect vortex lattice melting transitions are intricate, as effects induced by pinning can yield similar results. In particular, the presence of pinning is required in general, as a perfect, pinning free vortex lattice shows no signature in the resistivity or local magnetization at the melting transition [117]. In contrast to the discussed bulk measurement techniques, small angle neutron scattering gives a clear indication of melting transitions: The sharply defined Bragg-reflections of the superconducting vortex lattice smear out to an isotropic ring [85] as the long range order of the vortex lattice vanishes at the melting transition.

Vortex lattice melting was observed for various superconducting systems, mostly for high-T_c compounds due to their high transition temperature [85, 86], but also in $NbSe_2$ and MgB_2 [87],[88],[89] which are characterized by disorder. Surprisingly, a vortex lattice melting transition was recently reported also for the heavy fermion compound URu_2Si_2

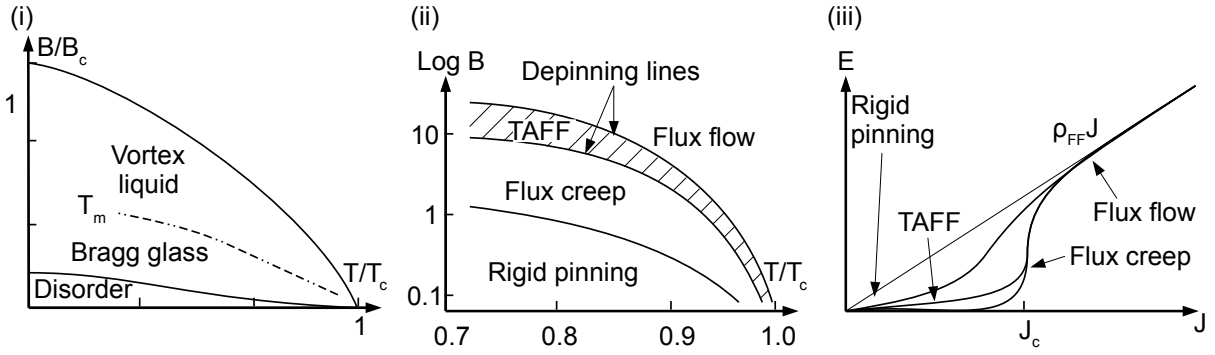

Figure 3.6: Panel (i) shows a typical phase diagram of a high T_c-superconductor. Above the melting line at T_m, a vortex liquid is found. Panel (ii) depicts the phase diagram for superconducting vortex lattices under transport current, where rigid pinning, flux creep, thermally assisted flux flow (TAFF) and flux flow are distinguished. Panel (iii) depicts the corresponding IV-characteristic.

[133]. For clean niobium, the melting temperature was estimated using the Lindemann criterion to be $\sim 10\,\mathrm{mK}$ below T_c. However, measurements by Ling *et al.* [134] using small angle neutron scattering on niobium report a melting transition and strongly hysteretic behaviour of the vortex lattice. This order to disorder transition was attributed to a lack of sample quality by Forgan *et al.* [135] in later studies.

Furthermore, the magnitude of thermal fluctuations and the elastic matrix of vortex lattices also strongly influence the pinning/depinning properties, in particular in the presence of a transport current where the Lorentz force additionally acts on the vortices. As moving vortices lead to the dissipation of energy, the pinning properties are of particular importance for applications of superconductors. Four different regions are distinguished: For small current densities $\boldsymbol{J}$, the vortex lattice is rigidly pinned. Increasing the current density first leads to flux creep [136], thermally assisted flux flow (TAFF) [13] and finally flux flow [137]. Both the I-V characteristic and the phase diagram for increasing transport current J are given in Fig. 3.6, panels (ii) and (iii).

3.4 Vortex Lattices of low κ Superconductors

The morphology and the topological properties of superconducting vortex lattice phases sensitively depend on the Ginzburg-Landau parameter κ and on demagnetizing effects. In the following, we qualitatively derive the phase diagram and the equilibrium magnetization B for a low-κ type-II superconductor like niobium where the crossover from attractive to repulsive vortex-vortex interaction has proven a drastic influence on the properties of the vortex lattice: It leads to an extended intermediate mixed state. We particularly concentrate on the morphology of the intermediate mixed state and its analogon, the intermediate state in type-I superconductors.

3.4.1 Phase Diagram and Critical Fields for low κ Superconductors with Non-Zero Demagnetizing Factor

We have already introduced that the Ginzburg-Landau parameter κ describes the surface energy associated with a superconducting/normal conducting interface. For type-II superconductors with $\kappa > \frac{1}{\sqrt{2}}$, this leads to the nucleation of vortices, each carrying one flux quantum $\phi_0 = h/2e$. Neglecting demagnetizing and pinning effects, the first fluxoid enters the bulk superconductor at the lower critical field $B_{c1} = \mu_0 H_{c1}$. In the Shubnikov phase between $B_{c1} = \mu_0 H_{c1}$ and $B_{c2} = \mu_0 H_{c2}$, the sample fills with vortex lattice according to eq. (2.24) until the vortex cores completely overlap at the upper critical field $B_{c2} = \mu_0 H_{c2}$. For superconductors with large $\kappa \gg 1$, thus $H_{c1} \ll H_{c2}$, a homogeneous distribution of vortex lattice throughout the Shubnikov phase can be assumed [138] due to the repulsive vortex-vortex interaction throughout the superconducting phase diagram.

For superconductors with κ close to type-I behaviour as niobium and non-zero demagnetizing factor, the situation is more complicated [139, 93, 140]. In the following, we

again denote with H the values for the applied magnetic field, whereas B stands for the equilibrium induction with the magnetization $M = \mu_0 H - B \leq 0$. Please note, that the equilibrium induction was defined being in a local equilibrium with the vortex lattice, assuming a spatial average over several vortices. Due to an inhomogeneous filling of the sample with vortices, the induction obtained by integration over the complete sample varies.

We have introduced that for low κ superconductors, a crossover from long-range attractive to repulsive vortex-vortex interaction can occur as function of magnetic field and temperature. Solely for superconducting specimens with non-zero demagnetizing factor N, this leads — in analogy to type-I superconductors — to the formation of an intermediate state of macroscopic coexisting domains, where normal conducting regions in the intermediate state of type-I superconductors correspond to the Shubnikov phase in the intermediate *mixed* state of low κ type-II superconductors. Due to the long-range attractive vortex interaction, the lattice spacing in the intermediate mixed state is constant. In contrast to conventional type-II superconductors, exhibiting a second order phase transition at the lower critical field H_{c1}, the transition at H_{c1} is of first order for type-II superconductors with low κ [125].

Fig. 3.7 panel (i) shows a typical phase diagram, obtained for a low κ type-II superconductor with non-zero demagnetizing factor N. No vortex lattice is observed in the Meissner phase for $H < H_1 = (1-N)H_{c1}$ where $B_{c1} = \mu_0 H_{c1}$ defines the lower critical field. For $H_1 < H < H_2$, with $H_2 = (1-N)H_{c1} + NB_0/\mu_0)$, the sample is in the so-called intermediate mixed state. The constant vortex lattice spacing in the intermediate mixed state is thereby described by the equilibrium induction B_0. For further increasing the magnetic field $(1-N)H_{c1} + NB_0/\mu_0 < H < H_{c2}$ with $B_{c2} = \mu_0 H_{c2}$ the sample is completely filled with vortex lattice in the Shubnikov phase [1]. Panel (ii) shows the corresponding magnetization curve obtained at the temperature T_A. In the Meissner phase, the sample exhibits ideal diamagnetism, in the intermediate mixed state and the Shubnikov phase, vortices fill the sample and reduce the diamagnetism.

The vortex lattice spacing is shown in panel (iii) where the reciprocal lattice vector $|\mathbf{G}_{VL}|$ of the vortex lattice at the temperature T_A is depicted as function of H: The value of $|\mathbf{G}_{VL}|$ reversibly assumes a constant value between H_1 and H_2, identifying this regime as the intermediate mixed state, whereas in the Shubnikov phase, $|\mathbf{G}_{VL}| \propto H^{1/2}$. Panel (iv) shows the integrated scattering intensity of a vortex lattice Bragg peak obtained by means of neutron scattering at the temperature T_A, indicating a linear dependence of the filling factor V of the sample with vortex lattice with respect to increasing applied magnetic field in the intermediate mixed state, as is also indicated by the magnetization curve [125]. Hysteretic effects are observed due to the first order phase transition at H_{c1} for superconductors with a low κ type-II behaviour. At H_2, the Shubnikov phase completely fills the sample.

Panel (v) depicts the magnetic field dependence of the vortex lattice equilibrium induction B which is obtained by averaging over a few vortex lattice unit cells. In the Meissner

[1] Note, that demagnetizing effects disappear at the upper critical field H_{c2} due to the vanishing magnetization M for conventional type-II superconductors

phase, one has $B = 0$ due to the perfect diamagnetism of the sample. Between H_1 and H_2, B jumps to B_0, associated with the constant vortex lattice spacing in the intermediate mixed state, while the macroscopic magnetization of the sample rises due to the intrusion of flux as indicated by the broken line. For further increasing magnetic field in the Shubnikov phase, the vortex lattice spacing shrinks $|a| \propto H^{-1/2}$ and B increases, until the magnetization is zero for the breakdown of superconductivity at $H = H_{c2}$.

The temperature dependence of the equilibrium induction B is given in panel (vi) for two different values of a constant applied magnetic field H, yielding a constant value above $H_{c2}(T)$, neglecting possible weak dia- or paramagnetism of the superconducting material. Due to the negative $\mathrm{d}H_{c1}/\mathrm{d}T$, $\mathrm{d}H_{c2}/\mathrm{d}T$ and $\mathrm{d}B_0/\mathrm{d}T$, the vortex lattice spacing grows for decreasing T during the Shubnikov phase due to the rising diamagnetism of the superconductor. In the Shubnikov phase, the vortex lattice is homogeneously distributed over the sample. Thus also the equilibrium induction B decreases for decreasing T, until $B_0(T)$ is reached and the sample enters the intermediate mixed state. For further decreasing T, the equilibrium induction B follows $B_0(T)$. This corresponds to the intermediate mixed state where islands of vortex lattice with constant spacing coexist with Meissner phase. Following the $B_0(T)$ line, the filling factor V shrinks until the vortex lattice is completely expelled out of the sample at $(1 - N)H_{c1}(T)$. For detailed studies on magnetization and small angle neutron scattering measurements on the intermediate mixed state of niobium, we refer to the studies by Christen and Kerchner [141, 125, 142].

3.4.2 Morphology of the Intermediate Mixed State

The morphology of the intermediate state of type-I superconductors and the intermediate mixed state of type-II superconductors is determined by the surface energy, associated with interfaces between the different phases. Note, that a vortex lattice region inside a Meissner domain exhibits a surface tension, due to the different vortex lattice coordination number for vortices at the surface of the Shubnikov region. A theoretical description has been given by Landau [143, 144], minimizing the free energy of simply connected normal conducting laminae including a branching of the normal conducting laminae at the sample surface. Numerous experiments on the topology of the intermediate state of type-I superconductors show a variety of different patterns including striped, dendritic and bubble phases [145, 146, 147, 148, 149], as shown in Fig. 3.8, panels (i) and (ii).

In particular, the morphology of the intermediate state is strongly depending on the path in the $B(H) - T$ phase diagram. Three different paths are generally distinguished [150]: Increasing the field after having performed a zero field cooling to the desired temperature (ZFC), decreasing the field from $H > H_c$ for the desired temperature (HFC) and finally cooling the sample in field (FC). It has been found experimentally for type-I superconductors, that the ZFC transition produces magnetic flux structures with closed morphology where normal conducting material is surrounded with superconducting laminae. In contrast, the HFC transition leads to an open morphology with normal domains which are open and connected to the sample edges [150]. Further decoration experiments on the type-II superconductor niobium show both Shubnikov islands in a multiply connected

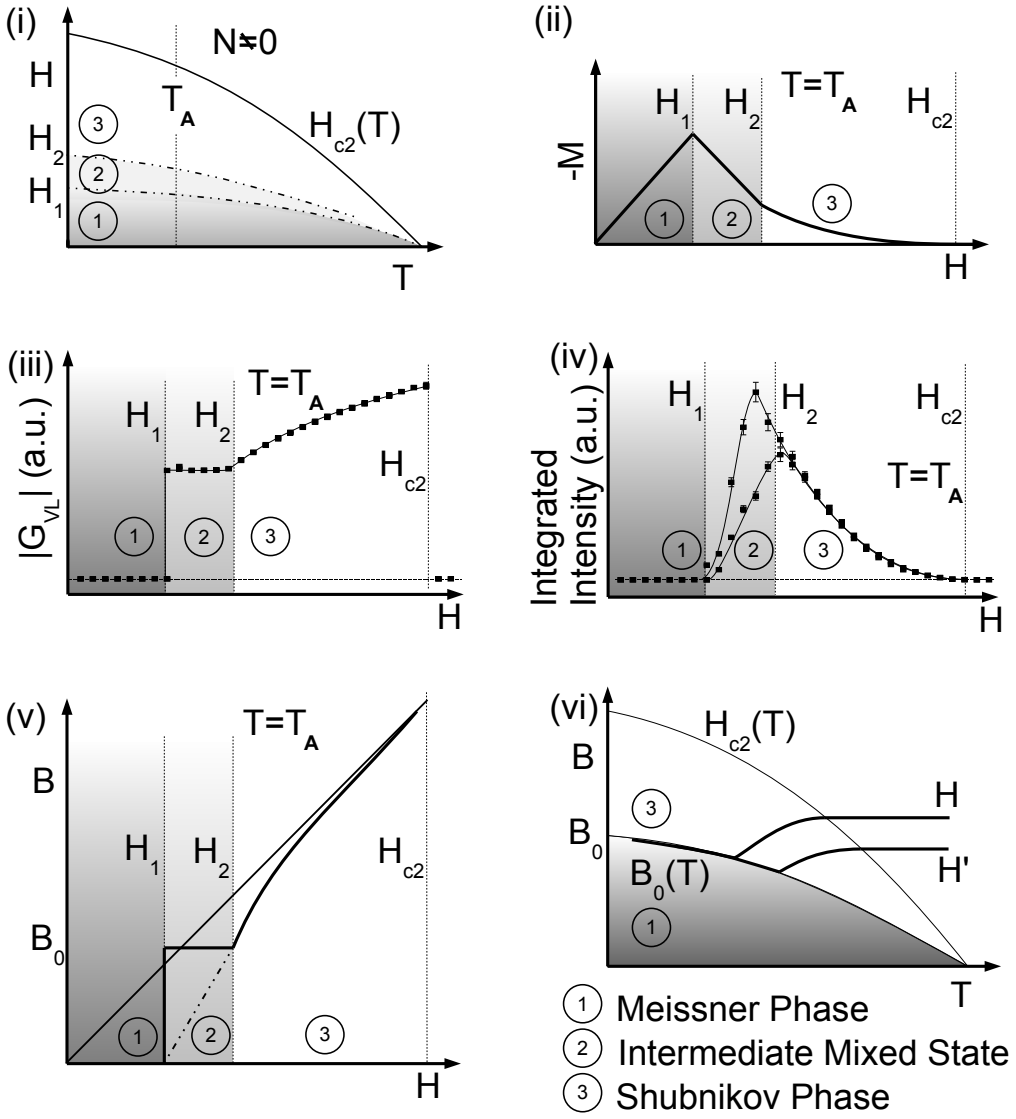

Figure 3.7: Panel (i) shows the phase diagram of a type-II superconductor with non-zero demagnetizing factor N and low κ as measured with small angle neutron scattering. No vortex lattice is observed in the Meissner phase below H_1. For $H_1 < H < H_2$, the sample is in the so-called intermediate mixed state, characterized by the coexistence of macroscopic domains of Meissner and Shubnikov phase with constant vortex lattice spacing. For the Shubnikov phase $H_2 < H < H_{c2}$, the sample is completely filled with vortex lattice. Panel (ii) shows the corresponding magnetization curve and panel (iii) depicts the dependence of the reciprocal lattice vector $|\mathbf{G}_{VL}|$ of the vortex lattice with respect to the applied magnetic field H for the temperature T_A. The intermediate mixed state is characterized by a constant vortex lattice spacing. Panel (iv) shows the integrated scattered intensity of a vortex lattice obtained with neutron scattering for the temperature T_A. The increasing filling factor V of the sample is proportional to H in the intermediate mixed state. Panel (v) shows the typical dependence of the equilibrium induction B on the applied magnetic field H for a temperature T_A, whereas the broken line depicts $\mathbf{M}$. Panel (vi) gives the temperature dependence of B. For details see text.

Meissner state and vice versa [151].

In the Shubnikov phase for a type-II superconductor, a homogeneous distribution of vortex lattice in the sample is assumed. In the intermediate mixed state, the sample is characterized by coexisting domains of Shubnikov and Meissner phase. The equilibrium induction follows the $B_0(T)$ line for decreasing temperature in the intermediate mixed state, thus the spacing of the vortex lattice remains almost constant while the filling factor decreases (cf. Fig. 3.7). Thus, the vortex lattice is expelled out of the sample for a FC path. In analogy to a HFC process in type-I superconductors, where the flux is also expelled for decreasing field, a similar morphology is expected for the intermediate mixed state in type-II superconductors on field cooling, namely an open, multiply connected structure of Shubnikov phase (Fig. 3.8, panel (ii)). In addition, the morphology is characterized by Landau branching at the surface of the sample.

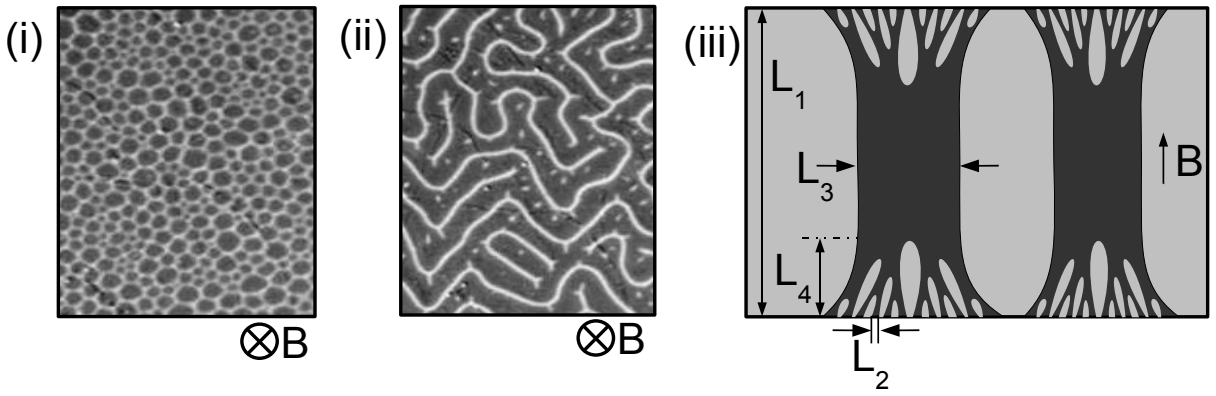

Figure 3.8: Panel (i) and Panel (i) (taken from [146]) show different structures of the intermediate state in type-I superconductors, obtained by magneto-optical experiments on Pb single crystal discs. Bright region correspond to superconducting material, dark regions to normal conducting material. Panel (iii) schematically shows the branched morphology on the intermediate mixed state in a low κ superconductor with non-zero demagnetizing factor. The dark shaded regime corresponds to Shubnikov phase, the light shaded area corresponds to Meissner phase.

Branching is supposed to occur only in rather thick samples. A sketch is given in Fig. 3.8, panel (iii). Note that in type-II superconductors, branching is more pronounced due to the lower energy density at the boundary between Meissner and Shubnikov phase. For niobium at low inductions, branching of Shubnikov domains in the intermediate mixed state was indeed observed at the surface of bulk samples of 0.1 mm and 6 mm thickness by means of a high resolution decoration technique [152, 151]. The characteristic length scale of the intermediate mixed state, observed at the surface of the sample was 10μm for the sample of $100\,\mu$m thickness. In contrast, the sample with 6 mm thickness showed a characteristic length scale of $1\,\mu$m. According to Landau, for the length scale of the unbranched intermediate mixed state in the bulk sample follows $\sim 250\,\mu$m [152].

3.5 Superconducting Model System Niobium

The following section splits into two parts: In the first part, we introduce the bulk properties of the low-κ superconducting model system niobium. In the second part, we present detailed information on the ultra-pure niobium sample *Nb 1* which was used for our studies.

3.5.1 Properties of Superconducting Niobium

Niobium crystallizes in the cubic *bcc* structure with a lattice constant of a_{Nb} =3.3 Å. The properties of the strong coupling type-II superconductor niobium are characteristic of an isotropic single gap [6, 7] that opens below the superconducting transition temperature T_c =9.2 K. The complexities, arising from multi-gap systems or multi-component order parameters, are thus avoided [91, 82, 92].

We have introduced in section (3.3), that for exactly $\kappa = 1/\sqrt{2}$, all vortex lattice arrangements are degenerate. The Ginzburg-Landau parameter of niobium is close to $1/\sqrt{2}$ and decreases with increasing purity. There have been speculations that niobium even displays type-I superconducting behaviour in the pure limit [126] close to T_c. This places high purity niobium at the immediate border between type-I and type-II superconductivity. As introduced in section (3.4), this leads to the formation of an extended intermediate mixed state for samples with non-zero demagnetizing factor [93]. The low κ further leads to a remarkable high value of the lower critical field $\mu_0 H_{c1}(T \to 0) = 120\,\mathrm{mT}$.

The low κ of niobium therefore allows to tune the vortex-vortex interactions from attractive to repulsive as function of temperature and applied magnetic field. This establishes niobium as model system for sensitive examinations of vortex-vortex interactions and vortex matter. The low Ginzburg-Landau parameter κ further implies that the coherence length $\xi(T \to 0) = 660\,\text{Å}$ in pure niobium is large. As introduced in section (3.2.3), the superconductivity in niobium is therefore strongly dependent on the Fermi surface topology and thus on non-local effects: For the upper critical field $\mu_0 H_{c2}(T \to 0)$ ∼380 mT, the lower critical field $\mu_0 H_{c1}(T \to 0)$ ∼120 mT as well as for the equilibrium induction B_0 in the intermediate mixed state of pure niobium single crystals, a weak four-fold anisotropy of a few percent [125, 142] is observed which is attributed to general four-fold non-local corrections due to the four-fold Fermi topology.

Niobium is characterized by a complicated Fermi topology which has been calculated by Mattheiss by means of the augmented-plane-wave method [153]. The reduced Brillouin zone schemes of the second and third zone are depicted in Fig. 3.9, panels (i) and (ii). The third zone contains closed hole pockets centered at the symmetry points Γ and N of the *bcc* Brillouin zone plus a multiply connected open sheet which extends from Γ to H along $\langle 100 \rangle$ directions, often referred to as "jungle gym" geometry. Panel (iii) shows a stereographic projection of the Fermi topology of niobium with open orbits around the $\langle 100 \rangle$ directions.

The reflectivity of a vortex lattice Bragg reflection is given by eqs. (2.30) and (2.31) and

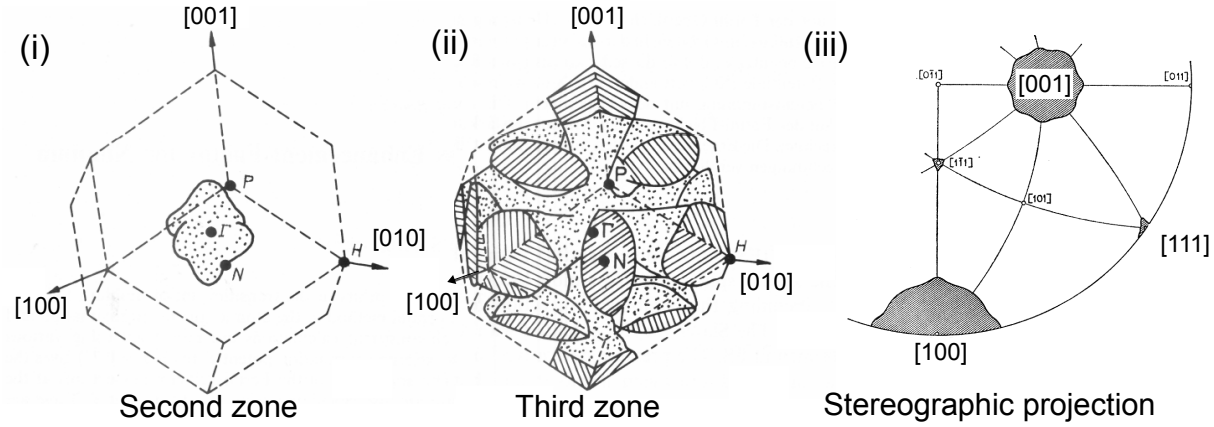

Figure 3.9: Fermi surface of niobium, calculated by Mattheiss [153] by means of the augmented-plane-wave method. Panel (i) and panel (ii) show the second and third Brillouin zone. Panel (iii) shows a stereographic projection of the Fermi topology of niobium.

exhibits a strong dependence on the London penetration depth λ. Niobium is characterized by a small value of $\lambda \sim 470 \pm 50$ Å, which leads to a large form factor. The resulting high reflectivity of the vortex lattice Bragg reflections allows to use a high resolution small angle neutron scattering setup with reasonable counting times.

3.5.2 Sample Used for Investigation

For our studies, a cylindrical niobium single crystal *Nb 1* with a length of 20 mm and a diameter of 4.5 mm was cut by spark erosion from a rod that had been produced at the ZFW Dresden [154] more than 30 years ago (cf. Fig. 3.10). A crystallographic $\langle 110 \rangle$ axis is oriented parallel to the cylinder axis of the sample. The preparation process consisted of purification by liquid-liquid extraction combined with chlorination and thermal decomposition of $NbCl_5$ followed by electron beam floating zone melting, decarburization in oxygen atmosphere and annealing in UHV [126, 155]. The impurity content was estimated to be less than 1 ppm for interstitial and better than 2 ppm for substitutional impurities.

To remove the surface layer, the sample was etched with a mixture of HF and HNO_3 for several minutes. Thereafter, the sample was again RF-annealed in UHV above 2000° at the University of Birmingham for one week to remove interstitials followed by surface oxygenation to reduce the Bean-Livingston barrier for surface pinning [8]. The residual resistivity ratio was measured with an eddy current decay method at the University of Birmingham. The residual resistivity ratio was extrapolated to $T \to 0$ at $B = 0$ for 14.5 K - 9.3 K using $\varrho_{phonon} \propto T^3$ as well as extrapolated to $B = 0$ from $B_{c2}(4.2\,\mathrm{K})$ using $\varrho_B \propto B$, yielding values from 8000 to 16000, respectively. However, the first extrapolation is more realistic, leading to a residual resistivity ratio $\sim 10^4$. According to [126], this leads to a Ginzburg-Landau coefficient $\kappa \sim 0.74$ at $0.9T/T_c$. The AC susceptibility and the magnetization, measured at the Technische Universität München were consistent with the

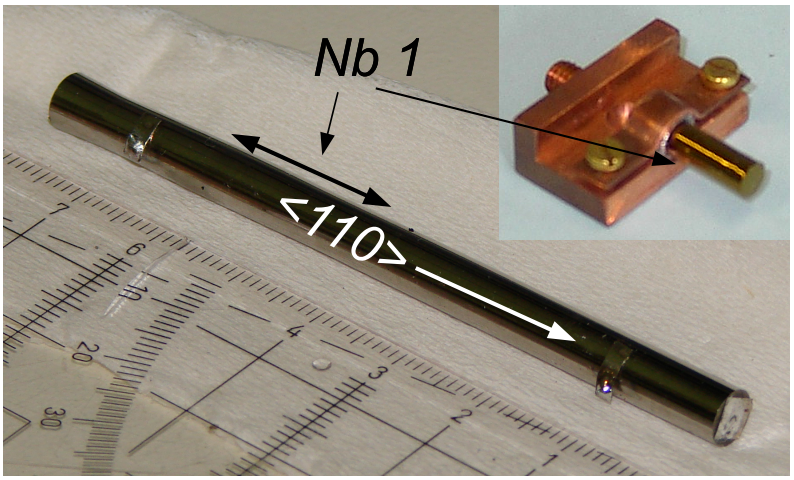

Figure 3.10: The picture shows the niobium rod which was produced at the ZFW Dresden [154]. The position where the sample *Nb 1* was cut is marked. The inset shows *Nb 1* in a copper sample holder as used for the neutron scattering experiments. The crystallographic ⟨110⟩ axis is oriented parallel to the cylinder axis of the sample. Note the golden colour of *Nb 1* due to the surface oxygenation.

literature.

The flux-flow resistivity ϱ_{FF} determines the damping of vortex motion in superconductors. ϱ_{FF} is closely related with the normal conducting resistivity by eq. (3.26). For high purity niobium, the normal conducting resistivity was determined by Berthel [126] in the clean limit and numerically approximated by

$$\begin{aligned}\varrho_n(T) =& \varrho_0 + c_n \left(bT^2 + \frac{cT^3}{7.212} \int_{\Theta_{min}/T}^{\Theta_D/T} \frac{x^3}{(e^x-1)(1-e^x)} dx + \right. \\ &\left. + \frac{dT^5}{124.4} \int_{\Theta_{min}/T}^{\Theta_D/T} \frac{x^5}{(e^x-1)(1-e^x)} dx \right),\end{aligned} \tag{3.28}$$

where

$$\begin{aligned} c_n &= 1.8 \cdot 10^{-7} \\ b &= 1.63 \cdot 10^{-6} \frac{1}{\mathrm{K}^2} \\ c &= (2.864 \pm 0.003) \cdot 10^{-7} \frac{1}{\mathrm{K}^3} \\ d &= (1.81 \pm 0.004) \cdot 10^{-10} \frac{1}{\mathrm{K}^5} \end{aligned} \tag{3.29}$$

with $\Theta_D = 270\,\mathrm{K}$, $\Theta_{min} = 35\,\mathrm{K}$ and the normalization constant c_n. The measured residual resistivity ratio of *Nb 1* of $\sim 10^4$ and the literature value for $\varrho_n(300\,\mathrm{K}) \sim 1.3 \cdot 10^{-7}\,\Omega\mathrm{m}$ [156] lead to $\varrho_0 \sim 1.3 \cdot 10^{-11}\,\Omega\mathrm{m}$. This yields an increase of the normal conduction resistivity ϱ_n in the relevant temperature range from 4 K to 8 K by a factor of about 2 from 1.8 nΩcm to 3.2 nΩcm.

In small angle neutron scattering measurements on the superconducting vortex lattice in *Nb 1* as described in section (3.6), the systematic behaviour of the vortex lattice, namely intensity, reciprocal lattice vector and mosaicity was investigated as function of magnetic field and temperature. Typical data is given in Fig. 3.11 for $T = 3.6\,\mathrm{K}$, where the field dependence of the integrated scattering intensity of a vortex lattice Bragg spot and its reciprocal lattice spacing $|\mathbf{G}_{VL}|$ are shown. The magnetic field behaviour of low-κ superconductors has been introduced in section (3.4) where we denote the constant flux density due to the attractive flux line interactions in the intermediate mixed state with B_0. As expected for our cylindrical sample with demagnetization factor of $\frac{1}{2}$, no intensity is observed for both increasing and decreasing magnetic field up to $\mu_0 H_1 = \frac{1}{2}\mu_0 H_{c1} = 70\,\mathrm{mT}$, followed by a gradual increase up to $\mu_0 H_2 = \frac{1}{2}B_0 + \frac{1}{2}\mu_0 H_{c1} \approx 115\,\mathrm{mT}$ [141].

Above $\mu_0 H_2 = \frac{1}{2}B_0 + \frac{1}{2}\mu_0 H_{c1}$ the intensity decreases characteristic of a conventional Shubnikov phase. The value of $\mathbf{G}_{VL}$ reversibly assumes a constant value $G_{VL} \approx 0.004\,\mathrm{\AA}^{-1}$ between $\mu_0 H_1 = \frac{1}{2}\mu_0 H_{c1}$ and $\mu_0 H_2 = \frac{1}{2}B_0 + \frac{1}{2}\mu_0 H_{c1}$, identifying this regime as the intermediate mixed state, approximately in agreement with $B_0 \sim 90\,\mathrm{mT}$. In contrast the integrated intensity displays hysteretic behaviour between 110 mT and 125 mT. Moreover, also the rocking width of the vortex lattice is increased for decreasing field. The same behaviour in sign and magnitude has been observed in the intermediate mixed state in low quality niobium [142]. The data in our high quality sample hence reflect an intrinsic property, most likely due to dendritic flux intrusion for increasing fields in contrast to vortex lattice islands for decreasing fields [151].

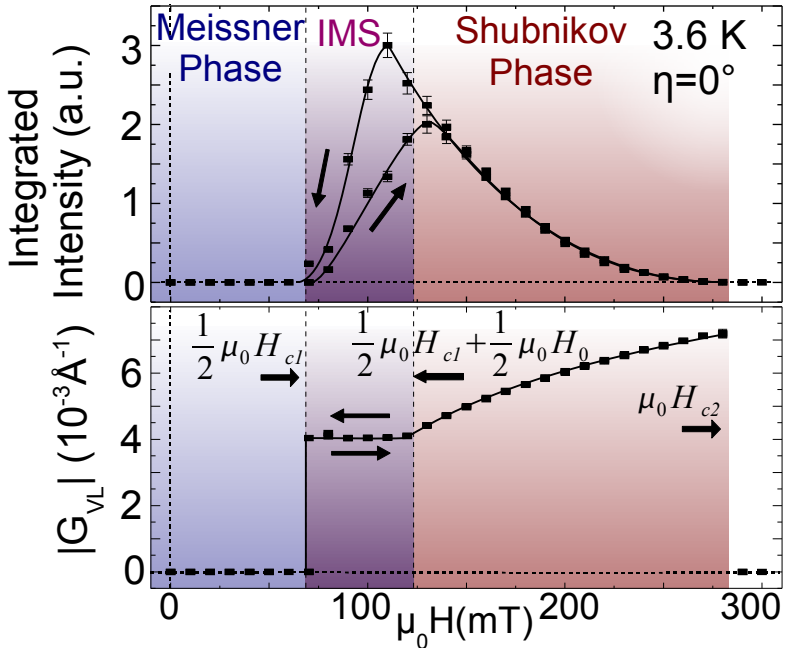

Figure 3.11: Integrated scattering intensity over a rocking curve and reciprocal lattice vector of the SANS diffraction pattern as a function of increasing and decreasing applied magnetic field. The characteristic values of $|\mathbf{G}_{VL}|$ are shown. Note the complete Meissner flux expulsion for both increasing and decreasing field.

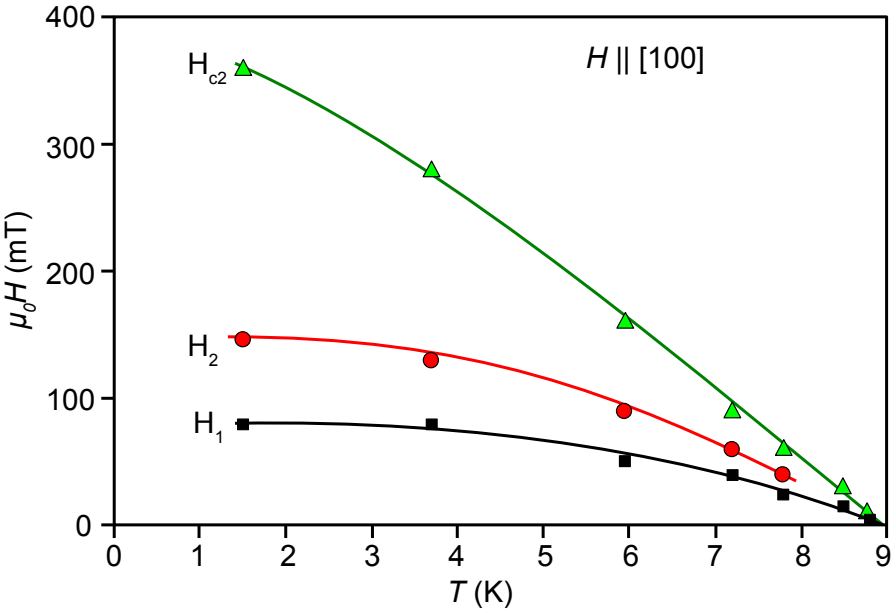

Figure 3.12: Superconducting phase diagram of the ultra pure niobium sample *Nb 1*, obtained by small angle neutron scattering measurements for $H \parallel [100]$.

The superconducting phase diagram of *Nb 1* as inferred from the small angle neutron scattering measurements is given in Fi. 3.12 for the magnetic field applied along a [100] crystalline direction. The data points have been obtained by both field ramps at constant temperature as well as temperature ramps at constant field. Due to the small values of $H_2(T)$ for temperatures close to the superconducting transition temperature T_c and due to the finite **q** resolution, the $H_2(T)$ line cannot be followed above 8 K. Note, that below H_1, a complete Meissner flux expulsion is observed for all temperatures throughout the superconducting temperature regime [10] for both HFC and ZFC paths. To the best of our knowledge such a complete Meissner flux expulsion, even for decreasing fields, has never been seen before in small angle neutron scattering, underscoring the outstanding purity and perfection of our sample.

3.6 Morphology of the Vortex Lattice in Ultra-Pure Niobium for Magnetic Fields along a [100] Axis.

In the following section, we present our small angle neutron scattering measurements on the vortex structures and symmetries in the superconducting model system ultra pure niobium, which unfold for the magnetic field applied along a four-fold $\langle 100 \rangle$ crystalline symmetry direction. We systematically map out the vortex structure as function of the direction of the magnetic field with respect to the $\langle 100 \rangle$ high symmetry direction, where we identify the systematic trends and succeed to deconvolute the different origins of the observed symmetry breaking and tilting transitions. This work has been published in [10] as well.

A theoretical overview of the different sources of anisotropy, which influence the symmetry of superconducting vortex lattices has been given in section (3.2) within the Ginzburg-Landau and BCS theory. The bulk properties of the ultra pure niobium sample, used for our studies have been introduced in section (3.5). The magnetic cross-section of superconducting vortex lattices for small angle neutron scattering experiments and the schematic scattering geometry have been introduced in sections (2.4) and (2.6), respectively.

In the following paragraph, we first give an overview of the existing studies of vortex lattice structures in niobium by Schelten [157], Fischer *et al.* [158], Christen *et al.* [141, 142], Laver *et al.* [8, 9], which have been performed prior to our work. We particularly focus either on the symmetry breaking vortex structures emerging for the magnetic field $H \parallel \langle 100 \rangle$ as well as on the vortex lattice domain structure and degeneracy. We then present the experimental setup, which was used for our studies before we continue with the presentation of the experimental data and their interpretation.

3.6.1 Vortex Structures in Niobium for Magnetic Fields along a [100] Axis.

Vortex Lattice Symmetry in Niobium

We have already introduced, that the existence of superconducting vortex lattices was proven by Cribier [68] in 1964 in a superconducting niobium sample by means of neutron diffraction. Since then, the vortex lattice symmetry and structure of superconducting niobium has been systematically investigated by various groups as function of sample purity and crystalline direction:

For a magnetic field H applied along a three-fold $\langle 111 \rangle$ crystalline direction, an ideal hexagonal vortex lattice symmetry with nearest neighbour direction in a $\langle 110 \rangle$ crystalline direction was reported by various groups [125, 158, 157] for the complete superconducting phase region. In contrast, for H parallel $\langle 110 \rangle$, the underlying two-fold crystalline symmetry leads to a distortion of the regular hexagonal vortex lattice symmetry on an ellipsoidal shape. An isosceles half unit cell was observed where the opening angle varies

from $\sim 65°$ [158] to 61.5° [157]. The nearest neighbour direction of the vortex lattice coincides with a $\langle 100 \rangle$ crystalline direction. The distortion of the vortex lattice symmetry was attributed to an anisotropic Fermi mass.

In contrast, for the magnetic field H aligned along a four-fold $\langle 100 \rangle$ crystalline direction[2], a rich manifold of vortex lattice structures unfolds: For low fields and temperatures, both Fischer *et al.* [158] as well as Schelten and Christen *et al.* [157, 142] report a square vortex lattice unit cell, however, the precise orientation of the nearest neighbour direction of the vortex lattice was inconclusive, which was attributed to varying sample purity. For intermediate fields at temperatures above $T = 2\,\mathrm{K}$ an isosceles vortex lattice structure with an opening angle of 63.4° was reported [142]. The nearest neighbour direction was found to be a $\langle 100 \rangle$ crystalline direction. In conclusion, due to the varying sample purity no coherent picture of the superconducting phase diagram of the vortex lattice symmetry for the magnetic field H aligned along $\langle 100 \rangle$ could be obtained.

The complete phase diagram of the vortex lattice in superconducting niobium with magnetic field H applied along a [100] direction was unraveled by Laver *et al.* [8] by means of small angle neutron scattering measurements. A high purity single crystal niobium sphere, characterized by a residual resistivity ratio RRR $\sim$ 1000 was used. Fig. 3.13, panel (i) schematically depicts the phase diagram as reported by Laver: A two-fold isosceles phase and three distinct vortex lattice phases are observed in the vicinity of T_c and at low temperatures, respectively. For increasing magnetic field H at low temperature these are at first a square phase (low-field-square), a scalene phase at intermediate fields and a square phase near H_{c2} (high-field-square).

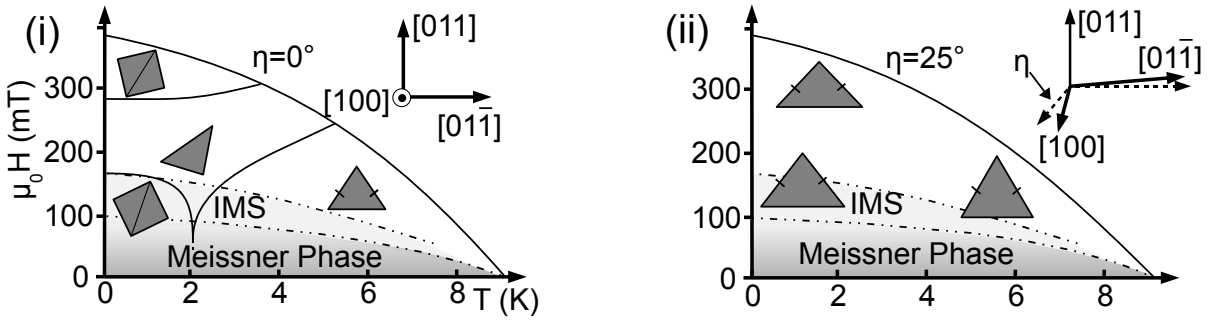

Figure 3.13: Panel (i): Schematic vortex lattice phase diagram (in reciprocal space) for a niobium sample with a finite demagnetizing factor with the magnetic field applied along a four-fold $\langle 100 \rangle$ axis, where $\eta = 0°$ denotes the angle between the applied magnetic field and the $\langle 100 \rangle$ axis in a (011) plane. Panel (ii): Phase diagram for $\eta = 25°$. See text for further details.

It had been further established [8] that the three low-T phases are tilted with respect to the four-fold symmetry of the underlying crystal structure into a low symmetry direction, thus additionally breaking the crystal mirror symmetry. For instance, the nearest neighbour direction of the low-field-square phase is tilted by 15° with respect to the crystalline [01$\bar{1}$] direction. For increasing field, the symmetry and the orientation of the vortex lattice

[2]In our work, we use (...) to denote crystal lattice planes, $\langle ... \rangle$ for a set of symmetry equivalent lattice directions and [...] for particular crystalline directions.

changes at a first order transition to a scalene vortex lattice symmetry, characterized by the lowest possible Bravais symmetry. Based on the magnetic field and temperature dependence of the low-field-square phase for H parallel $\langle 100 \rangle$ and the first order transition, separating the low-field-square and the scalene phase, it had been speculated that the low-field-square may be related to the intermediate mixed state [8].

Upon further increasing field, the scalene vortex lattice phase smoothly distorts to the high-field square phase which is tilted by 11° with respect to the crystalline $[01\bar{1}]$ direction. In contrast, the two-fold isosceles phase observed at high temperatures breaks crystal rotational symmetry but still obeys mirror symmetry.

Vortex Lattice Domain Structures and Degeneracy

We have introduced in the previous section, that for magnetic field applied along a four-fold crystal symmetry direction, frustration between the six-fold vortex lattice symmetry and the underlying crystal symmetry leads to the observation of vortex structures, which either do not share the crystal symmetry or are furthermore tilted with respect to the crystal symmetry directions. This allows the existence of several degenerate vortex lattice domains, as described by Laver *et al.* [8, 9]. The vortex lattice domain structure thus sensitively reflects the degeneracy of the vortex lattice symmetry with respect to the magnetic field direction and crystal direction.

In the scalene phase, the vortex lattice nearest neighbour direction is aligned in a low symmetry direction with respect to the underlying crystal lattice. This structure therefore leads to the existence of four degenerate vortex lattice domains, which may be constructed using the crystalline symmetry directions as mirror planes. The construction of the different vortex lattice domains is schematically depicted in Fig. 3.14, panel (i), where the half unit cell of each domain is shaded, respectively.

The domain population sensitively changes, if the direction of the magnetic field is rotated away from a high symmetry direction, here [100]. Typical data for the domain population of the scalene phase, taken from Laver *et al.* [9], is shown in Fig. 3.14, panel (ii), where the domains are colour-coded as introduced in panel (i). For this plot, the direction of the magnetic field was rotated close to (011) plane around the [100] axis at the magnetic field $\mu_0 H = 200\,\mathrm{mT}$ and a temperature of $T = 2\,\mathrm{K}$. A polar schematic of the domain population close to the [100] axis is given in Fig. 3.14 panel (iii), where the radial coordinate illustrates the domain strength. The domain population is well fitted by the function with the required periodicity $A_0 + \sum_{n=1}^{3}(A_n \cos 2n\tau + B_n \sin 2n\tau)$ with $\tau = \pm\eta, -\pi/2 \pm \eta$ for the four scalene domains, respectively. Strong changes of the domain population within rotation angles below 1° are observed. The population and degeneracy of vortex lattice domains thus may be used for a precise alignment of the sample with respect to the magnetic field direction.

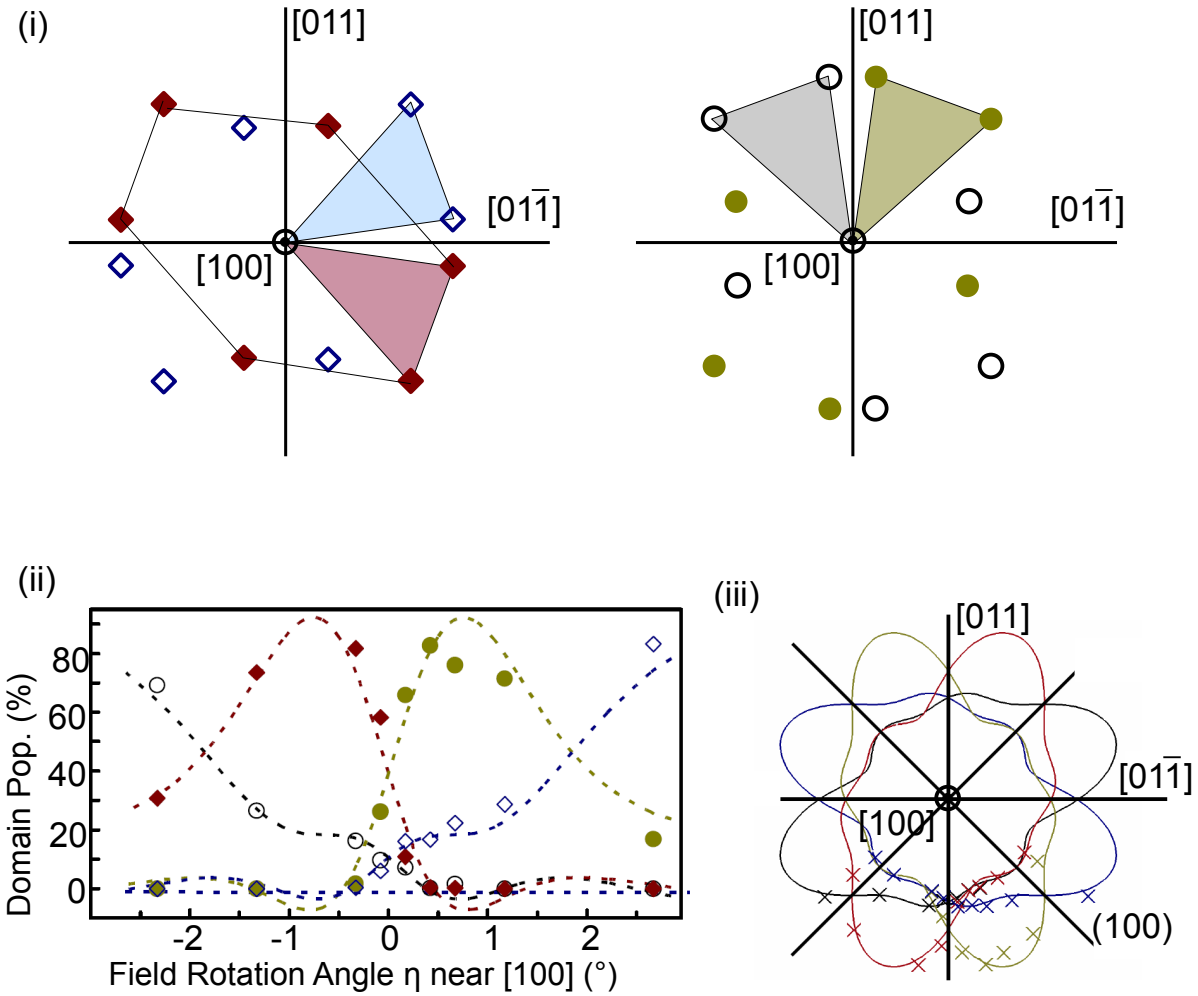

Figure 3.14: Panel (i): For a scalene vortex lattice with lowest possible Bravais symmetry, where the nearest neighbour direction is not aligned in a high symmetry direction, four degenerate vortex lattice domains are observed. The domains are constructed, using the crystal symmetry directions, namely the (011) plane and (01$\bar{1}$) plane as mirror planes. The half unit cell is shaded, respectively. The population of four degenerate scalene vortex lattice domains for a magnetic field $\mu_0 H = 200\,\mathrm{mT}$ and temperature $T = 2\,\mathrm{K}$ as function of the magnetic field direction with respect to the [100] axis is shown in panel (ii), taken from Laver *et al.* [9]. The four domains are colour-coded as introduced in panel (i). The magnetic field is applied close to the (110) plane and rotated by the angle η with respect to a [100] axis. Panel (iii) shows a polar schematic of the domain population where the radial distance represents the domain population. The solid lines are fits as described in the text.

Vortex Lattice Evolution close to $\langle 100 \rangle$

It had finally been established in further neutron scattering studies [9] that the vortex lattice symmetry and tilt/orientation is very sensitive to the direction of the magnetic field H with respect to the crystalline $\langle 100 \rangle$ direction: Rotating the magnetic field H away from the high symmetry direction $\langle 100 \rangle$, both the symmetry breaking tilt of the vortex lattice as well as the symmetry of the vortex lattice unit cell gradually evolve until the equilateral vortex lattice symmetry is recovered for $\langle 111 \rangle$. In these studies, the magnetic field was rotated away from the direction [100] both in a (110) as well as in a (100) plane. A qualitative phase diagram of the vortex lattice, where $\eta = 25^\circ$ denotes the angle between the applied magnetic field and the [100] axis in a (011) plane is given in Fig. 3.13, panel (ii): For $\eta = 25^\circ$, a gradual evolution from equilateral to square vortex lattice symmetry is observed, however, the nearest neighbour direction of the vortex lattice is aligned in a crystalline [011] direction throughout the superconducting phase regime.

The evolution of the vortex lattice symmetry and tilt/orientation as function of the magnetic field direction close to a (110) plane is is given in Fig. 3.15 [9]. Panel (i) introduces the nomenclature to describe the internal angles and the tilt/orientation of half unit cell of the vortex lattice with respect to the crystal lattice: α, β and γ denote the internal angles of the vortex lattice half unit cell. The orientation of the vortex lattice unit cell with respect to the crystalline (110) plane is denoted by μ: Shown in panel (ii) is the behaviour for the high field square phase: In the high-field-square phase for $\mu_0 H$=350 mT and T=2 K, the symmetry of the vortex lattice half unit cell smoothly distorts until a equilateral shape is observed for H parallel $[\bar{1}11]$. Shown in the inset of panel (ii) is the tilt/orientation of the nearest neighbour direction of the vortex lattice with respect to the crystal axis, which already disappears in a pronounced transition between 12° and 15° rotation of the magnetic field with respect to the [001] direction.

As shown in panel (iii), a gradual distortion of the vortex lattice symmetry — similar to the high-field-square phase — is also observed for $\mu_0 H$=200 mT and T=2 K (red symbols), $\mu_0 H$=200 mT and T=4.5 K (black symbols) and for T=2 K in the intermediate mixed state (IMS) in blue: For the magnetic field along $[\bar{1}11]$, a equilateral vortex lattice is again observed. Panel (iv) shows the evolution of the vortex lattice tilt/orientation for $\mu_0 H$ =200 mT and T =2 K (red symbols), $\mu_0 H$ =200 mT and T =4.5 K (black symbols) and for T =2 K in the intermediate mixed state (IMS) (blue symbols) as function of the rotation angle of the magnetic field. For the data obtained in the intermediate mixed state at T =4.3 K the tilting with respect to the crystalline direction vanishes with a sharp transition at a rotation angle $\sim 20^\circ$ similar to the high-field-square phase.

For the magnetic field direction applied in a (100) plane, similar phenomena have been reported [9]. However, in the presented studies the precise evolution of the vortex lattice morphology as a function of field orientation, necessary to identify the nature of the morphology and tilt/orientation, remained open. This originated in incomplete data sets and, more importantly, in the purity of the samples studied so far, which still displayed distinct pinning effects despite their residual resistivity ratios RRR $\approx$ 1000. In particular, no angle resolved systematic study of the reorientation transition with respect to the crys-

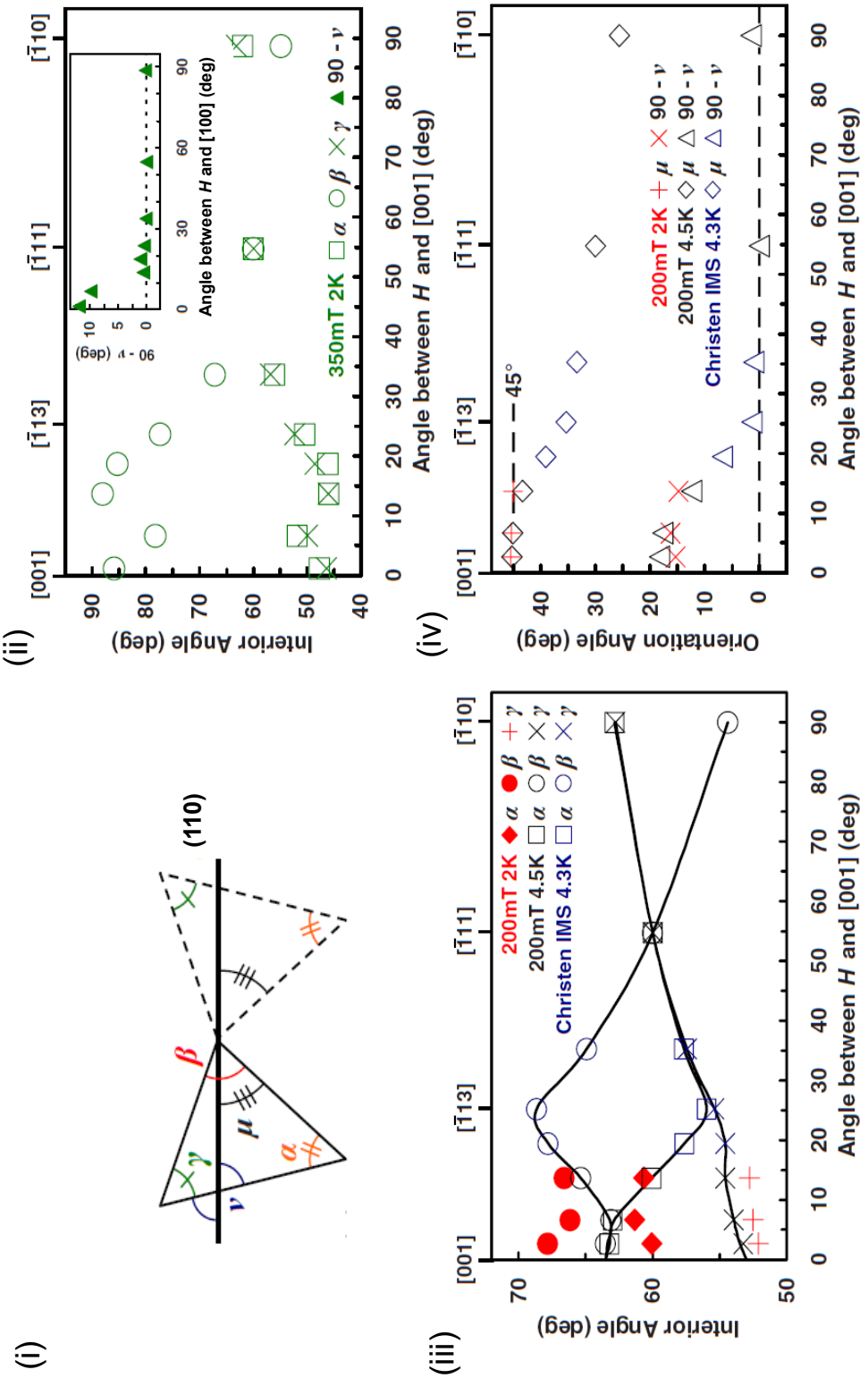

Figure 3.15: Vortex lattice internal angles and orientation for magnetic fields close to a (110) plane, adopted from Laver [9]: Panel (i) depicts the nomenclature for describing the vortex lattice symmetry and orientation with respect to the crystalline directions. Panel (ii) shows the evolution of the internal angles of the vortex lattice as function on the direction of the magnetic field with respect to the [001] direction close to a (110) plane for $\mu_0 H$ =350 mT, T =2 K in green symbols, where the inset of panel (ii) depicts the tilt/orientation of the vortex lattice with respect to the crystalline direction. Panel (iii) shows the evolution of the internal angles of the vortex lattice for $\mu_0 H$ =200 mT and T =2 K in red symbols, $\mu_0 H$ =200 mT and T =4.5 K in black symbols and for T =2 K in the intermediate mixed state (IMS) with blue symbols. Panel (iv) shows the evolution of the vortex lattice tilt/orientation for $\mu_0 H$ =200 mT and T =2 K in red symbols, $\mu_0 H$ =200 mT and T =4.5 K in black symbols and for T =2 K in the intermediate mixed state (IMS) with blue symbols.

talline direction of the four vortex lattice phases was available. Moreover, the evolution of the vortex lattice symmetry in the intermediate mixed state remained unclear as well.

Motivation

To resolve the open issues we have studied the ultra-pure single crystal sample *Nb 1* by means of small angle neutron scattering. *Nb 1* is of unprecedented purity, characterized by a residual resistivity ratio $\sim 10^4$. Previous small angle neutron scattering studies of *Nb 1* have proven excellent sample quality and vanishing pinning effects. Due to the high purity, non-local corrections due to gap or Fermi anisotropy are suspected to strongly influence the symmetry of the vortex lattice, vanishing pinning effects allow the observation of the intrinsic vortex lattice properties of the model system niobium. A brief description of the bulk properties of *Nb 1* can be found in section (3.5). In our study, we systematically map the evolution of the vortex lattice symmetry for magnetic fields around the [100] crystalline direction close to an (011) plane for the complete superconducting phase. In particular, we either focus on the evolution of the low-field-square phase and the assumed connection to the intermediate mixed state as well as on the field and temperature dependence of the tilt/reorientation transition of the different vortex lattice phases.

3.6.2 Experimental Setup

The small angle scattering measurements were carried out at the small angle neutron scattering diffractometer V4 at BENSC [114]. The typical setup of a small angle neutron scattering instrument has been introduced in section (2.6), a detailed description of neutron scattering experiments on vortex lattices is given in section (2.4).

For our experiment, neutrons with a wavelength $\lambda = 12\,\text{Å} \pm 5.5\%$ were collimated over a distance of L_1=12 m before reaching the sample, with a multidetector at a distance of L_2=12 m from the sample. An 'orange' cryomagnet was used for measurements down to 1.5 K and a horizontal magnet for fields up to 500 mT. The sample was mounted on a motorized sample stick that could be rotated about the vertical axis with an accuracy of $\pm 0.05°$. A sketch of the scattering geometry is given in Fig. 3.16 (i). The cylinder axis of the sample *Nb 1* coincided with the rotation axis and corresponded to a crystalline [011] direction. Magnetic fields were applied in the (011) plane, perpendicular to the cylinder axis so that demagnetizing effects ($N = 1/2$) did not change during our measurements. Thus the direction of H could be rotated away from the [100] axis towards a $[1\bar{1}1]$ axis in the (011) plane [3]. In the following we denote with ϕ the rocking-angle between the incoming neutron beam and H, while η denotes the angle between H and the $\langle 100 \rangle$ direction. For the precise sample alignment within $\pm 0.2°$ we exploited the degeneracy of the superconducting domains for field parallel $\langle 100 \rangle$ as described above (cf. ref. [9]).

[3] Due to a small sample misalignment of $\approx 1°$ around the beam axis, the rotation plane is not exactly a (011) plane.

Rocking scans of ϕ were performed for each measurement point. To avoid any hysteretic effects, each data point was taken after field cooling the sample [4].

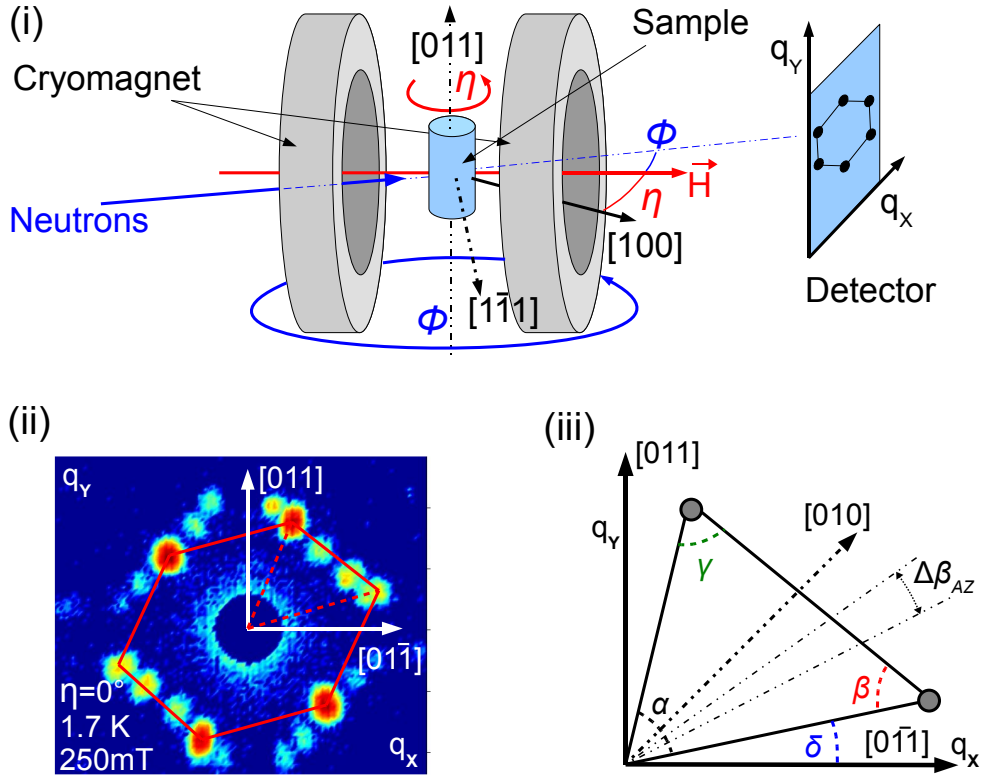

Figure 3.16: Panel (i): Small angle neutron scattering set-up. ϕ denotes the angle between the incoming neutron beam and the magnetic field, while η denotes the angle between magnetic field and the crystallographic [100] direction. Panel (ii): Typical detector image in the scalene vortex lattice phase. For clarity just one domain is marked in red. Panel (iii): The nomenclature for describing the vortex lattice: α, β and γ represent the internal angles of the half vortex lattice unit cell, δ represents the tilting angle of the vortex lattice with respect to the horizontal $[01\bar{1}]$ axis. The azimuthal instrumental resolution is denoted $\Delta\beta_{AZ}$.

Typical data is shown in Fig. 3.16 panel (ii) for a rotation angle $\eta = 0$ at the magnetic field $\mu_0 H = 250\,\mathrm{mT}$ and a temperature of $T = 1.7\,\mathrm{K}$. As expected, several domain populations may be seen due to the degeneracy of the vortex lattice domains with respect to the four-fold symmetry of the crystal lattice. For clarity only one of these domains has been marked with red lines. Due to a slight misalignment of a few tenths of a degree, one domain is favoured. To extract the symmetry and orientation of the vortex lattice the scattered intensities were fitted by 2D-Gaussians. The azimuthal instrumental resolution $\Delta\beta_{az}$ depends on the magnitude of the reciprocal lattice vector of the vortex lattice, which in turn is determined by the applied magnetic field. The azimuthal resolution as derived in section (A.1) yields $\Delta\beta_{az} = 15°$ for 100 mT, $\Delta\beta_{az} = 10°$ for 200 mT and $\Delta\beta_{az} = 8°$ for a field of 300 mT. However, due to the high count rate, the quality of the 2-D-Gaussian fit allows a precise determination of the position of the vortex lattice Bragg spots which

[4]However, the results for a zero field path with following field ramp showed identical results.

is significantly better compared to the instrumental resolution.

As shown in Fig. 3.16 panels (ii) and (iii) α, β and γ describe the internal angles of the scattering pattern, defining the structure of the primitive half unit cell, while δ describes the orientation of the vortex lattice with respect to the horizontal $[01\bar{1}]$ axis. As given in Fig. 3.14, measurements have shown that changes of domain population of the vortex lattice already occur within small changes of η, while the shape and orientation of the unit cell are conserved [9]. We thus focus on the morphology of the vortex lattice.

3.6.3 Experimental Results

We have studied the evolution of the vortex lattice morphology in detail for temperatures $1.5\,\mathrm{K} < T < 5.5\,\mathrm{K}$, magnetic fields $110\,\mathrm{mT} < \mu_0 H < 330\,\mathrm{mT}$, and $\eta \leq |\pm 25°|$. This covered the parameter range necessary to determine the vortex lattice phase diagram with special regard on the vortex lattice tilt/reorientation and lock-in transitions. In the following paragraphs, the precise evolution of the vortex lattice morphology will be presented for the four characteristic vortex lattice phases.

High-Field-Square Vortex Lattice Phase

Shown in Fig. 3.17 are typical scattering patterns of the vortex lattice in the high-field-square phase obtained at $\mu_0 H = 330\,\mathrm{mT}$ and T =1.5 K as function of the rotation angle η: For $\eta = 0°$, one of two degenerate square vortex lattice domains is visible, which is tilted with respect to the crystalline $[01\bar{1}]$ direction by the angle δ [5]. The square unit cell is marked with red lines, the half unit cell of the vortex lattice is indicated with broken red lines. For increasing rotation angle η, the domain population changes between $\eta = 0°$ and $\eta = 5°$. The change of domain population is attributed to a a slight misalignment of $\approx 1°$ around the beam axis, leading to a rotation of the magnetic field *close* to the (011) plane. For further increasing rotation angle η, the tilting angle δ decreases until the vortex lattice realigns with the crystal lattice at $\eta_c \approx 15°$, lifting the degeneracy of both vortex lattice domains.

The precise evolution of the internal angles and the orientation of the vortex lattice as obtained by the 2-D Gaussian fits for the high-field-square phase at $\mu_0 H = 330\,\mathrm{mT}$ and T =1.5 K is shown in depth in Fig. 3.21, panel (i): For $\eta = 0°$, $\alpha = \beta \approx 45°$, $\gamma \approx 90°$ and a tilting angle $\delta \approx 11°$ is observed. As a function of increasing rotation angle η the symmetry breaking tilt vanishes gradually until for $\eta_c \approx 15°$ the nearest neighbour direction coincides with a crystalline $[01\bar{1}]$ direction. Above η_c the internal angles $\alpha = \beta$ increase and γ decreases characteristic of an isosceles lattice that transforms into the hexagonal lattice with $\alpha = \beta = \gamma = 60°$ for H $\parallel \langle 111 \rangle$.

[5] Again, due to a slight misalignment of a few tenths of a degree, one domain is favoured.

Scalene Vortex Lattice Phase

Fig. 3.18 shows typical scattering patterns of the vortex lattice in the scalene phase at $\mu_0 H = 250\,\mathrm{mT}$ and $T = 1.7\,\mathrm{K}$ as function of the rotation angle η: The scalene phase is characterized by lowest Bravais symmetry with its nearest neighbour direction aligned in a low symmetry direction. For $\eta = 0°$, four degenerate vortex lattice domains are thus observed. For increasing rotation angle η, the scalene vortex lattice symmetry smoothly distorts to an isosceles symmetry and the symmetry breaking transition vanishes above $\eta_c \approx 15°$. Similar to the vortex lattice in the high-field-square phase, a change of domain population is observed for small rotation angles η between $0° \leq \eta \leq 4°$.

Fig. 3.21 panel (ii) shows the detailed evolution of the internal angles and orientation of the scalene phase, as obtained by the 2-D Gaussian fits. For $\eta = 0°$, the scalene phase is characterized by $\alpha \approx 50°$, $\beta \approx 60°$ and $\gamma \approx 70°$. Like the high-field-square the scalene phase is tilted, where $\delta \approx 14°$. The tilting vanishes at $\eta_c \approx 15°$, where the scalene structure turns isosceles, i.e., $\alpha = \beta \approx 50°$ and $\gamma \approx 80°$. Approaching the $\langle 111 \rangle$ direction the vortex lattice finally turns hexagonal.

Low-Field-Square Vortex Lattice Phase

We now address the evolution of the low-field-square phase as function of the rotation angle η for temperature $T = 1.5\,\mathrm{K}$ and magnetic field $\mu_0 H = 100\,\mathrm{mT}$, as given in Fig. 3.19 [6]. For $\eta = 0°$, the square unit cell of the vortex lattice is marked in red lines. Due to the tilted alignment of the *square* vortex lattice with respect to the *square* crystal lattice, two degenerate vortex domains are visible. For rotation angles $5° \leq \eta \leq 7.5°$, the vortex lattice symmetry abruptly turns into a scalene symmetry, while the tilting of the vortex lattice with respect to the crystal axis remains constant. For increasing rotation angle η the tilted scalene vortex lattice symmetry then gradually evolves to a isosceles symmetry as well as the symmetry breaking tilting simultaneously vanishes for $\eta \geq 20°$.

The precise evolution of the internal angles and orientation for the low-field-square phase as obtained by the 2-D Gaussian fits is again shown in Fig. 3.21 panel (iii): For $\eta \leq 5°$ $\alpha = \beta = 45°$ and $\gamma = 90°$, which abruptly turns scalene lattice already for an angle $\eta_1 \approx 5°$, while the tilting of the flux lattice exists up to $\eta_c \approx 20°$, i.e., in contrast to all other phases the fundamental symmetry and the tilting exhibit distinctly different critical angles.

Isosceles Vortex Lattice Phase

We finally address the isosceles vortex lattice phase for high temperatures, given in Fig. 3.20 for the temperature $T = 5.5\,\mathrm{K}$ and the magnetic field $H = 150\,\mathrm{mT}$. The evolution of the internal angles and orientation as obtained by the 2-D Gaussian fits is given

[6] Note the large intensity of the diffraction spots of the vortex lattice for low magnetic field and temperature, which result from the magnetic field and temperature dependence of the form factor.

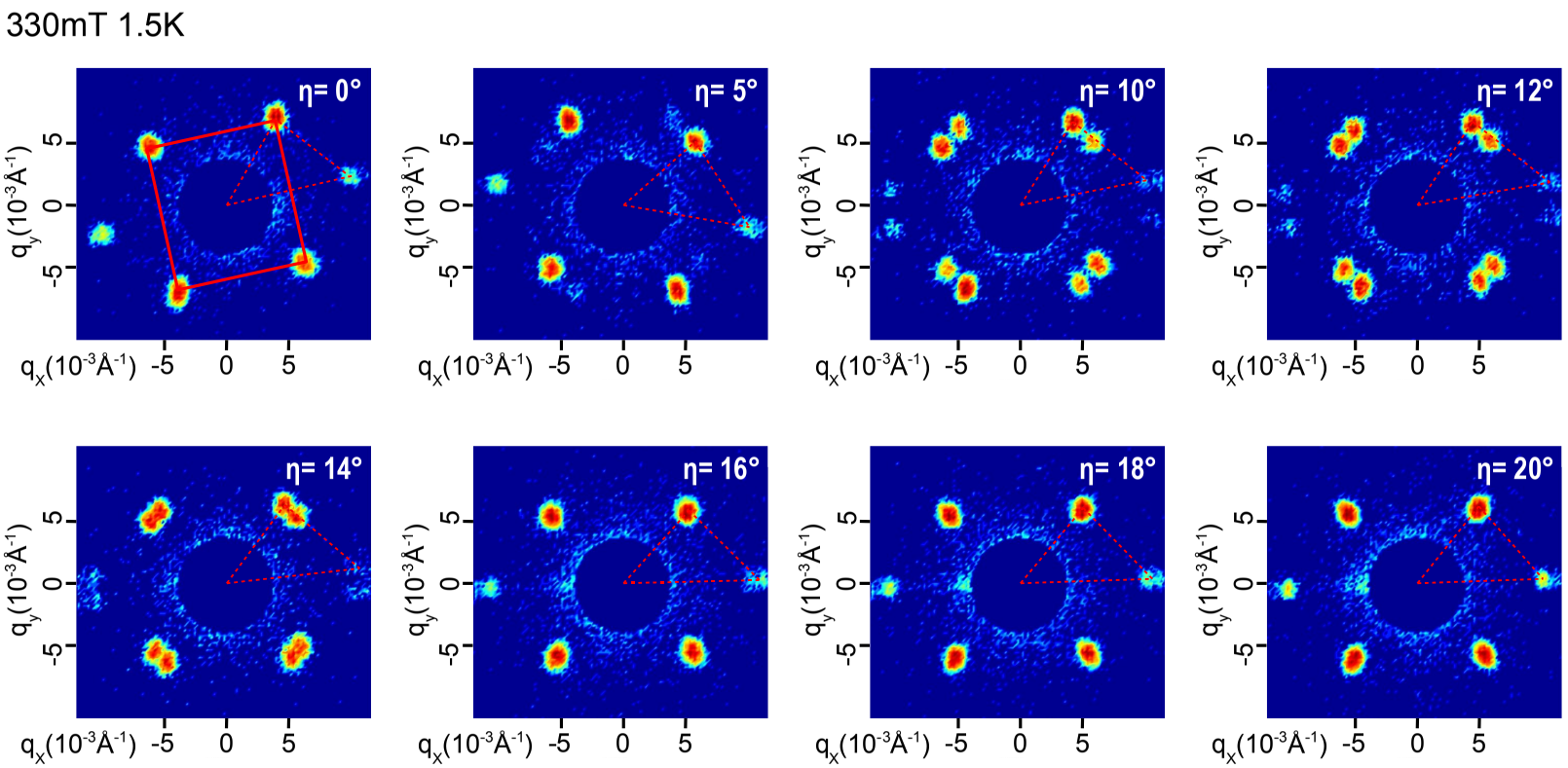

Figure 3.17: Evolution of the vortex lattice in the high-field-square vortex lattice phase as a function of the rotation angle η with respect to a [100] axis for temperature $T = 1.5\,\mathrm{K}$ and magnetic field $\mu_0 H$ =330 mT, where typical sums over rocking scans are shown. The half unit cell of the vortex lattice is marked in broken red lines. For details see text.

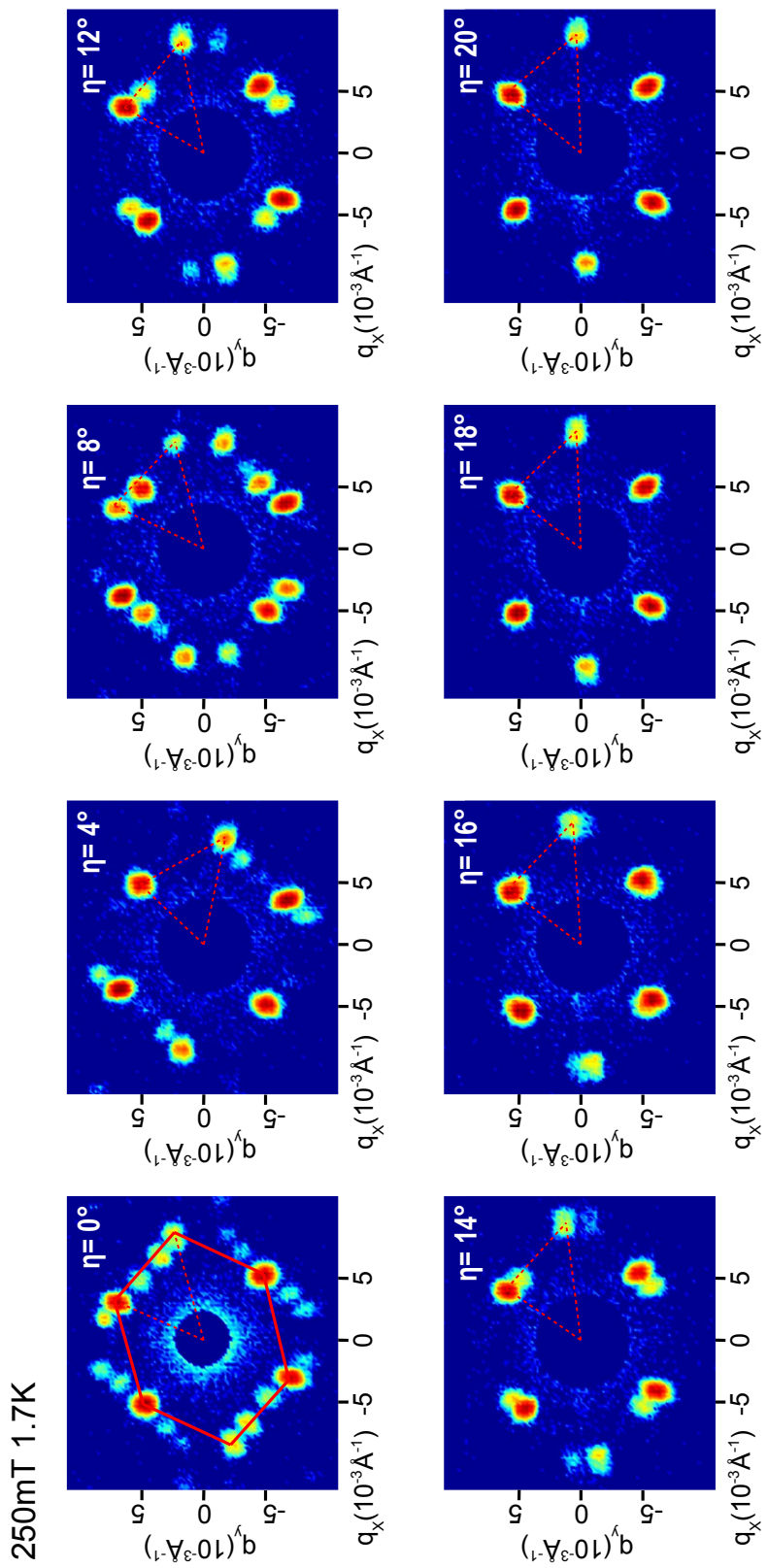

Figure 3.18: Evolution of the vortex lattice in the scalene vortex lattice phase as a function of the rotation angle η with respect to a [100] axis for temperature $T = 1.7\,\mathrm{K}$ and magnetic field $\mu_0 H = 250\,\mathrm{mT}$, where typical sums over rocking scans are shown. The half unit cell of the vortex lattice is marked in broken red lines. For details see text.

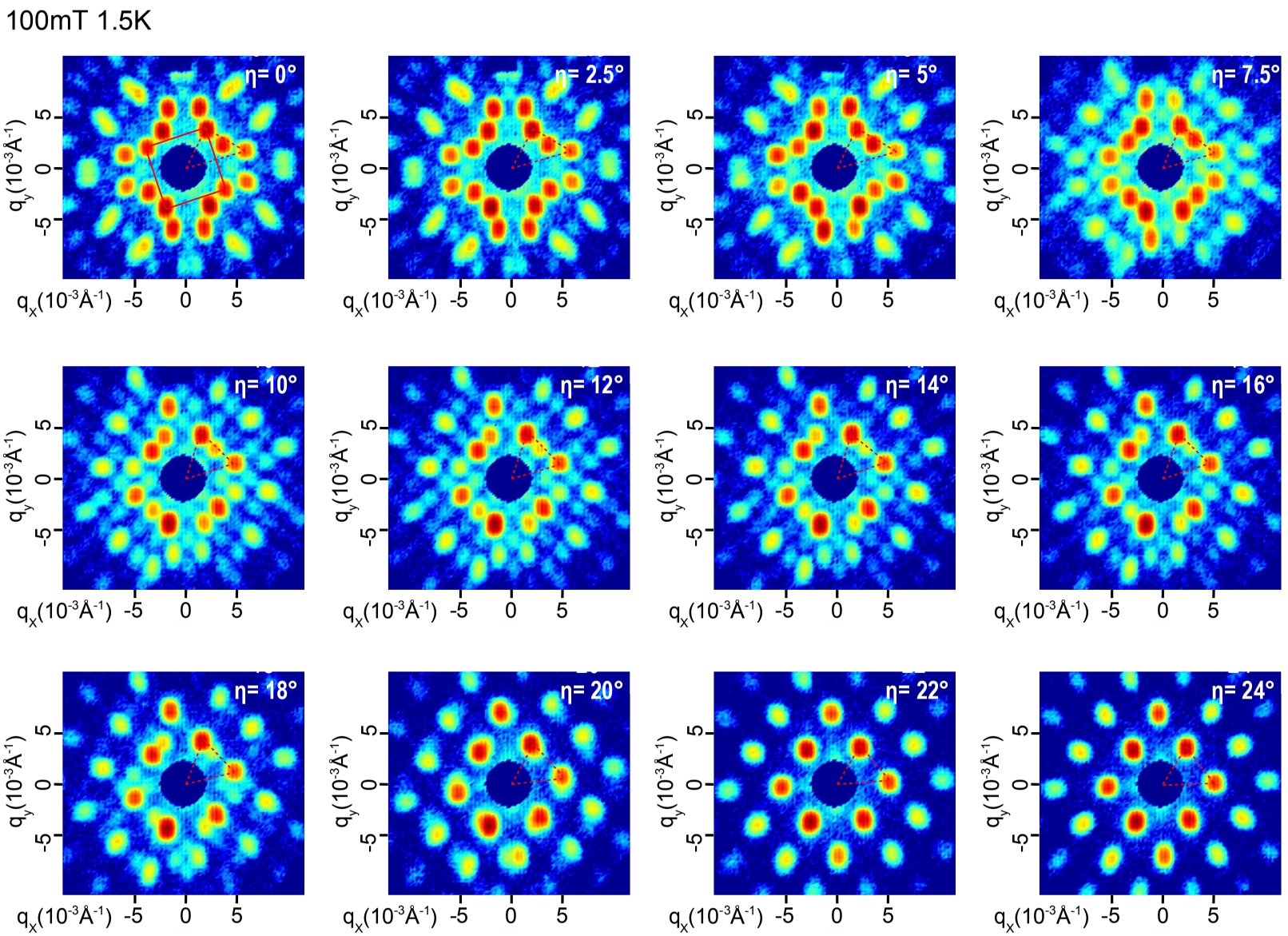

Figure 3.19: Evolution of the vortex lattice in the low-field-square vortex lattice phase as a function of the rotation angle η with respect to a [100] axis for temperature $T = 1.5\,\mathrm{K}$ and magnetic field $\mu_0 H$ =100 mT, where typical sums over rocking scans are shown. The half unit cell of the vortex lattice is marked in broken red lines. For details see text.

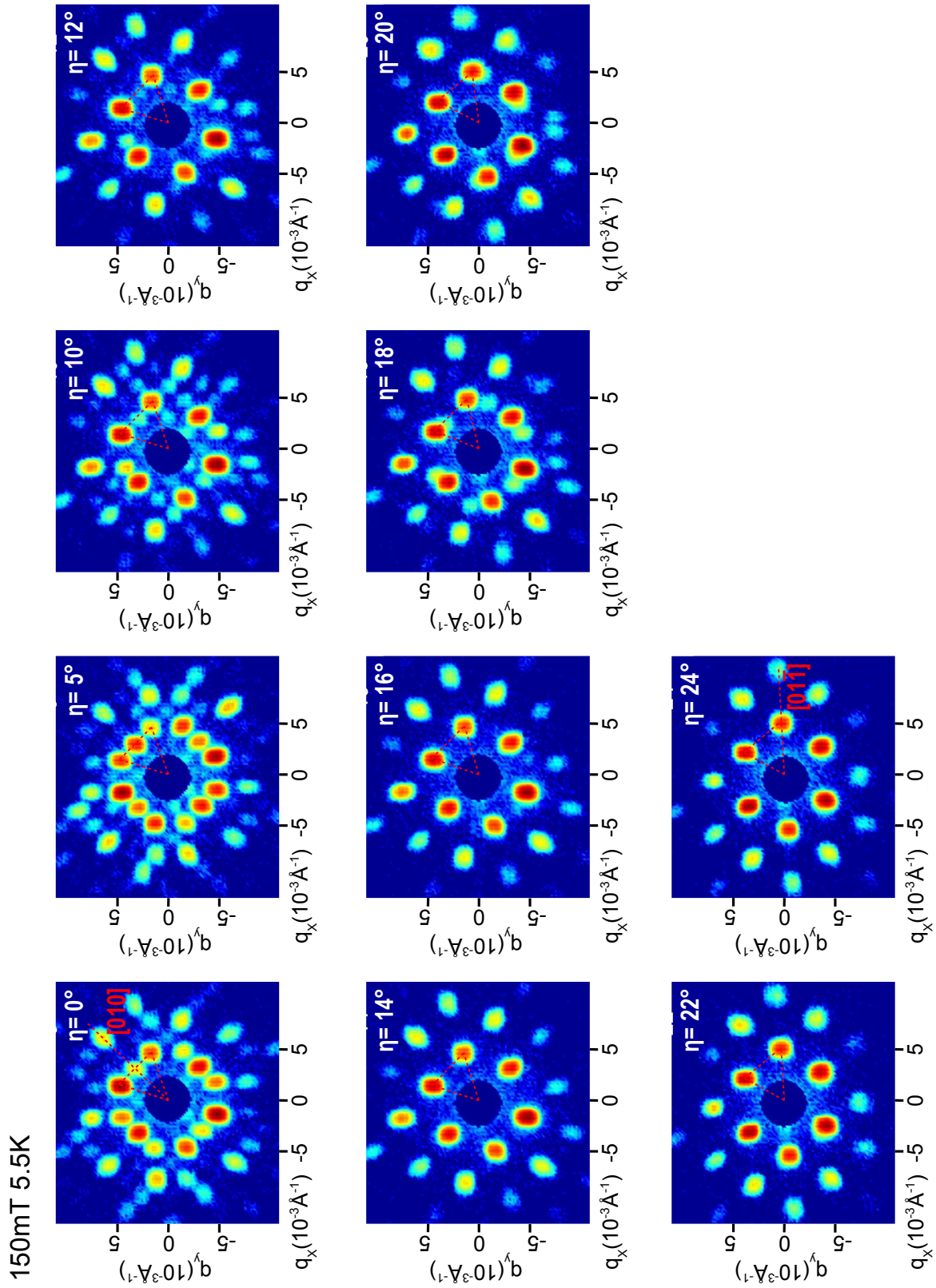

Figure 3.20: Evolution of the vortex lattice in the isosceles vortex lattice phase as a function of the rotation angle η with respect to a [100] axis for temperature $T = 5.5\,\mathrm{K}$ and magnetic field $\mu_0 H = 150\,\mathrm{mT}$, where typical sums over rocking scans are shown. The half unit cell of the vortex lattice is marked in broken red lines. For details see text.

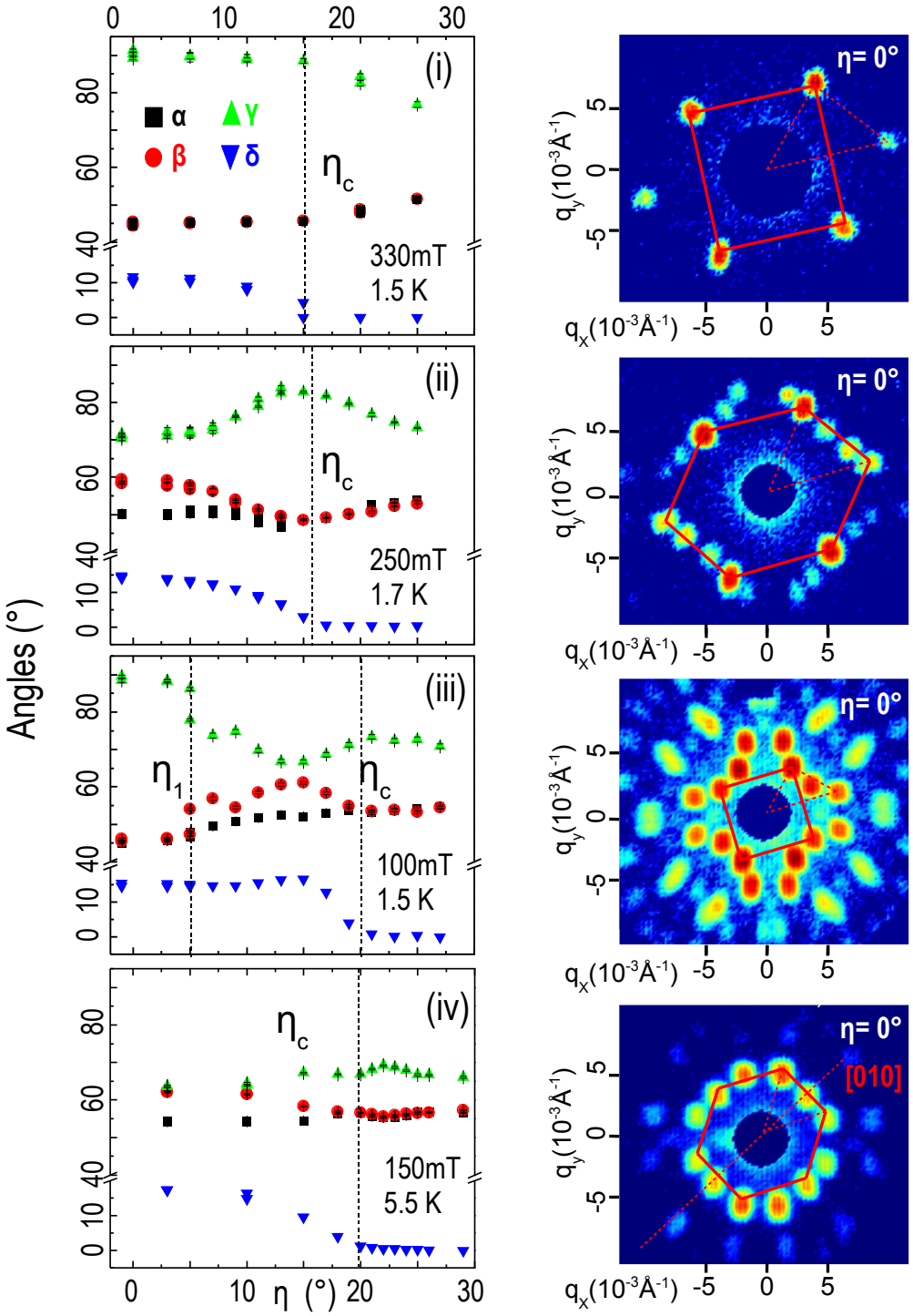

Figure 3.21: Evolution of the vortex lattice as a function of η for various temperatures and magnetic fields, where typical sums over rocking scans are shown for the high-field-square (i), scalene (ii), low field square (iii) and isosceles (iv) structures. All vortex lattice structures are given in reciprocal space, with the angles plotted in the left hand side panels. The nomenclature was defined in Fig.3.16. The scattered intensity is plotted on a logarithmic scale. Due to a slight misalignment of the sample, the scattering patterns are rotated by $\approx 1°$ around the beam axis. Note, that due to a small sample misalignment of $\approx 1°$ around the beam axis, the rotation plane is not exactly a (011) plane.

in Fig. 3.21, panel (iv), where $\beta = \gamma \approx 62°$ [141]. The reorientation angle $\eta_c \approx 20°$ is also important in the isosceles phase: For $\eta = 0°$ the unit cell is orientated such that a [010] axis acts as mirror plane, yielding $\frac{\alpha}{2} + \delta = 45°$, i.e., $\delta \approx 16°$. The *two-fold* isosceles phase hence *does* break the underlying *four-fold* rotational symmetry of the lattice at $\eta = 0°$ but still obeys mirror symmetry. With increasing η this orientation changes between $\eta \approx 10°$ and η_c such that $[01\bar{1}]$ becomes a mirror plane of the isosceles unit cell (δ=0). During reorientation, the unit cell is scalene. This may be compared with the low-field-square shown in Fig. 3.21 panel (iii), which becomes scalene already at $\eta_1 \approx 5°$ as discussed above. At $\eta_c \approx 20°$ both the tilting vanishes and the lattice returns to the isosceles structure.

3.6.4 Interpretation

In the following section we make use of our systematic measurements of the vortex lattice structure and orientation to identify the systematic trends and explain the different sources of anisotropy, responsible for the vortex lattice symmetry and the lock-in angles of the tilting transition.

Magic Angle η_c

For the magnetic field H aligned parallel to [100] ($\eta = 0°$), the vortex lattice orientation is tilted with respect to the underlying crystalline directions for all four vortex lattice phases by the angle denoted δ_c. If the direction of the magnetic field is rotated away from the [100] direction, the vortex lattice tilting vanishes at the rotation angle η_c, whereas the symmetry of the vortex lattice unit cell shows a smooth crossover at η_c. The magnetic field and temperature dependence of the angle η_c is shown in Fig. 3.22 panels (i) and (ii) where the error bars indicate the width of the transition. The show that η_c represents a magic angle $\eta_c \approx 17°$ that is essentially the same for all vortex lattice phases. The physical origin of the specific tilting angle δ and the magic angle η_c and will be discussed in the next paragraphs.

Low-Field-Square Vortex Lattice Phase

The constant value $\eta_c = 17°$ is strongly contrasted by $\eta_1 = 5°$ of the low-field-square phase, where the square symmetry abruptly changes to a scalene symmetry of the half unit cell, whereas the tilt/orientation δ remains constant at η_1. Moreover, the reversible transition fields of the low-field-square phase and the phase boundaries of the intermediate mixed state (the superconducting phase diagram inferred from previous small angle scattering measurements is depicted in Fig. 3.11) places the low-field-square vortex lattice phase right in the intermediate mixed state.

We have introduced the properties of superconducting niobium, which is characterized by a low value of κ in section (3.4). Due to the large ξ_{GL} as compared to the spacing of the

flux lines, the interaction between vortices includes contributions from an overlap of the vortices for low inductions. For samples with a non-zero demagnetizing factor this leads to a long-range attractive vortex-vortex interaction, responsible for the emergence of an intermediate mixed state. For low-κ superconductors, a square vortex lattice is expected closely above the lower critical field H_{c1} in a theoretical analysis, ignoring any symmetries imposed by the crystal lattice [159], consistent with our experiment. Taken together this identifies the low-field-square phase as a property of the intermediate mixed state.

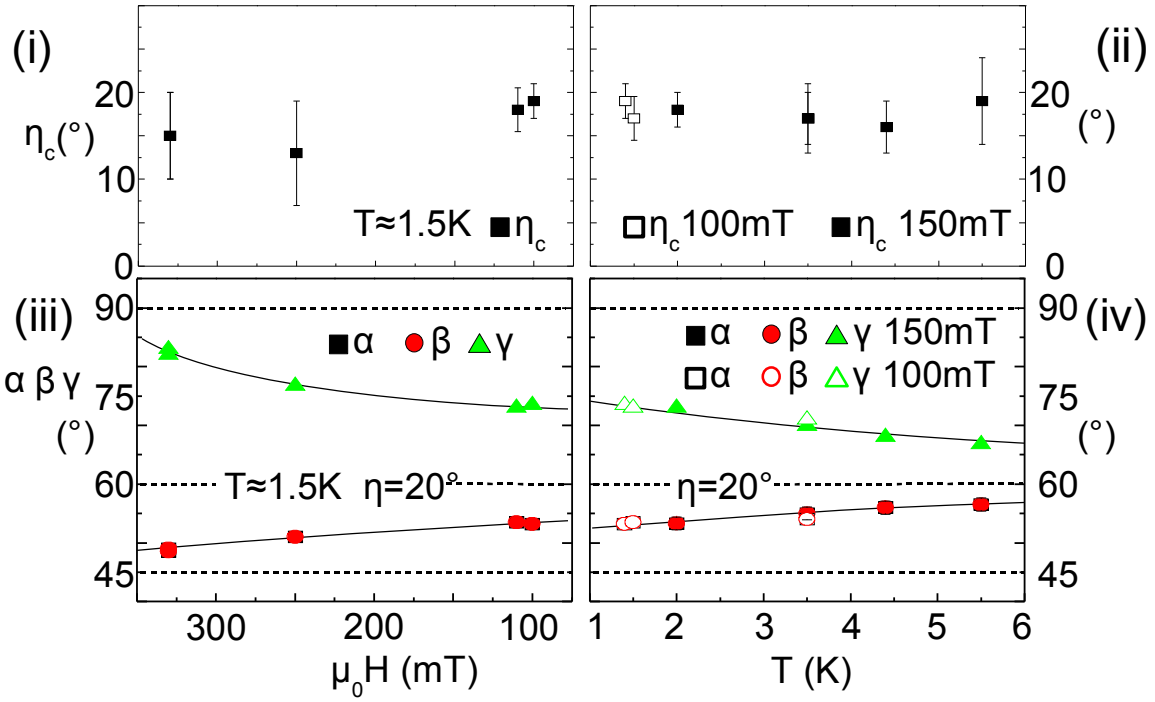

Figure 3.22: Panels (i) and (ii) show the temperature and field dependence of η_c, which is essentially unchanged, where the error bars indicate the range of the transition. The evolution of the internal angles α,β and γ for $\eta = 20°$ is depicted as a function of magnetic field for low temperatures (panel (i)) and as a function of temperature for 100 mT and 150 mT (panel (ii)). Note the trend towards a square lattice for low T and high H. The lines serve as guide to the eye.

Isosceles to Square Trend

With the low-field-square vortex lattice phase being a property of the intermediate mixed state we may now address the remaining phase diagram. We first consider gradual variations of the vortex lattice morphologies, where it is instructive to begin with the isosceles phase for $\eta > \eta_c$ (cf Fig. 3.13 panel (ii)). As shown in Fig. 3.22 panels (iii) and (iv) for $\eta \approx 20°$ we find that $\alpha = \beta \to 45°$ and $\gamma \to 90°$ for decreasing temperature and increasing magnetic field. In other words the lower the temperature and the higher the magnetic field the stronger the trend to form a square lattice. This is underscored by the weak four-fold anisotropy of B_0,H_{c1} and H_{c2} [125, 142]. The same trend to form a square lattice is also

present for $\eta < \eta_c$, where the vortex lattice morphology locks into distinct vortex lattice phases.

In a pioneering study Nakai *et al.* [80] have shown for high-κ superconductors, that the trend observed here is expected for a four-fold Fermi surface symmetry and related four-fold gap anisotropy: A reentrant vortex lattice transition from rhombic to square back to rhombic symmetry as function of applied magnetic field and temperature was found, explaining the reentrant square to hexagonal to square vortex lattice transitions identified in the compound $LuNiB_2C$ [79]. Here, the low field symmetry is driven by the anisotropy induced by the Fermi surface and the high field symmetry driven by non-local corrections due to the four-fold gap anisotropy.

We have pointed out in section (3.2.3), that the influence of non-local corrections is expected to increase for increasing purity. We have also introduced, that the influence of non-local correction increases for increasing magnetic field. Ultra pure niobium is characterized by a low Ginzburg-Landau parameter $\kappa \leq 1/\sqrt{2}$, close to type-I behaviour and a long coherence length $\xi \sim 660\,\text{Å}$. This leads to a low energy difference of different vortex lattice symmetries. We therefore conclude, that the isoscleses to square trend for increasing magnetic field and decreasing temperature for $H \parallel \langle 100 \rangle$ is driven by four-fold non-local corrections due to the general four-fold Fermi symmetry, where a decreasing amount of this trend may be expected to survive when the direction of the magnetic field is turned towards the $\langle 111 \rangle$ crystalline direction.

Scalene Vortex Lattice Symmetry

Our data further show, that the scalene vortex lattice symmetry and phase thereby always emerges in the transition regime between structures and vortex lattice phases with higher symmetry (isosceles or square), i.e., under conditions of maximum frustration. This may be readily seen in Fig. 3.21 panels (ii), (iii) and (iv), where we find that α and β differ for $\eta < \eta_c$, while $\alpha = \beta$ for $\eta > \eta_c$. Likewise, a scalene vortex lattice due to frustration is also seen during the rotation between the two isosceles phases in Fig. 3.21 panel (iv) with $[01\bar{1}]$ and [010] acting as mirror planes, respectively. Hence the same systematic trend is observed for all reorientation transitions shown in Fig. 3.21 panels (ii), (iii) and (iv), but the width of the transition differs.

Vortex Lattice Lock-In Transitions

We finally note, that roughly the same value of η_c and the size of the tilting, δ_c, are observed across the entire phase diagram. These values are remarkably close to the angle separating open and closed Fermi surface sheets inferred from the magnetoresistance and Fermi surface calculations: The reduced zone scheme of the Fermi surface in niobium as calculated by Mattheiss [153] was depicted in Fig. 3.9 panels (i) and (ii). The Fermi surface of niobium is characterized by closed hole pockets centered at the symmetry points Γ and N of the *bcc* Brillouin zone plus a multiply connected open sheet which extends from Γ to H along $\langle 100 \rangle$ directions, often referred to as "jungle gym" geometry. A schematic

depiction of the "jungle gym" sheet is given in Fig 3.24, panel (i). The rod-like rungs of the "jungle gym" are aligned along $\langle 100 \rangle$ crystalline directions.

In Fig. 3.23, panel (i), magnetoresistance data of niobium is shown as function of the rotation angle with respect to the [100] axis [160]. Pronounced maxima are observed roughly at $\eta_c \sim 15°$ reflecting the crossover from open to closed orbits in the "jungle gym" Fermi surface, empirically suspected to be important for the superconductivity [126]. Fig 3.24 panel (i) and panel (ii) schematically depict the associated open and closed orbits as function of the angle η. Moreover, the tilting angle δ_c compares very well with the size of certain necks in the "jungle gym" Fermi surface (cf. Fig. 3.23, panel (ii)) [161]. Thus the trend of the vortex lattice morphology to lock into stable phases wins at the expense of the symmetry breaking rotations as driven by the Fermi surface topology.

3.6.5 Conclusion and Outlook

In conclusion, we attribute the general morphology of the vortex lattice in niobium for magnetic field parallel to $\langle 100 \rangle$ and its orientation to three dominant mechanisms:

- First, non-local contributions as described by Nakai in an Eilenberger [123] treatment of a Fermi surface with four-fold symmetry [80] for high-κ superconductors, leading to a gradual evolution from an equilateral vortex lattice at high temperature and low field to a square vortex lattice at low temperature and high field.

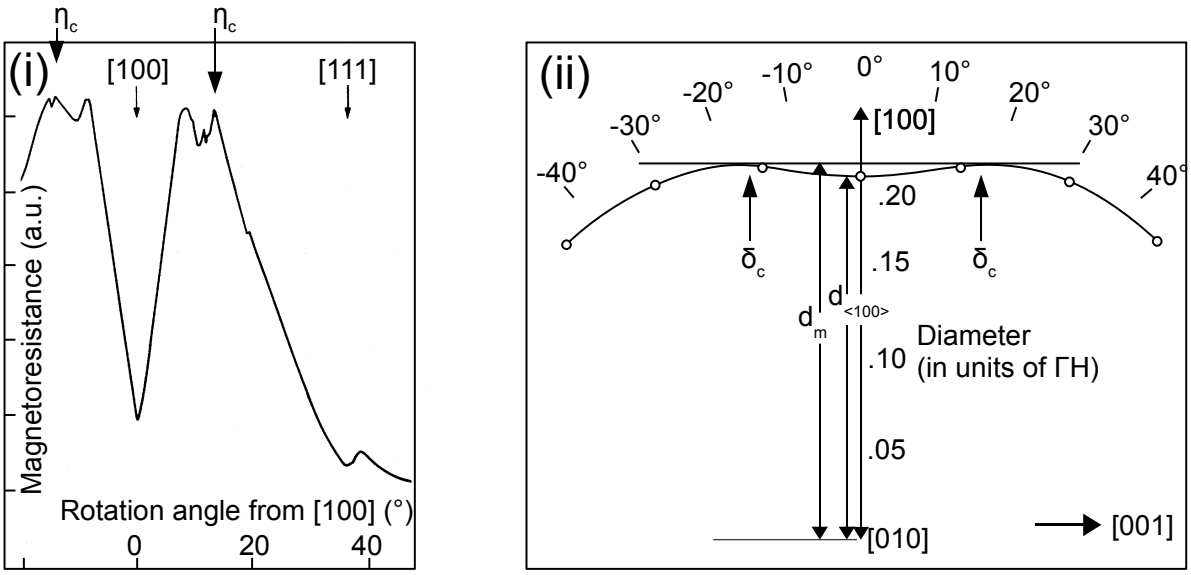

Figure 3.23: Panel (i) shows magnetoresistance data of a niobium single crystal sample, measured by Fawcett [160] as function of the orientation of the magnetic field H with respect to a crystalline $\langle 100 \rangle$ direction, where the magnetic field was applied in a $\langle 110 \rangle$ plane. Pronounced maxima at rotation angles $\eta \sim |15°|$ indicate the crossover from open to closed orbits. Panel (ii) shows the minimal crossection through the Fermi surface necks of the open "jungle gym" surface. The plot is adopted from Reed [161].

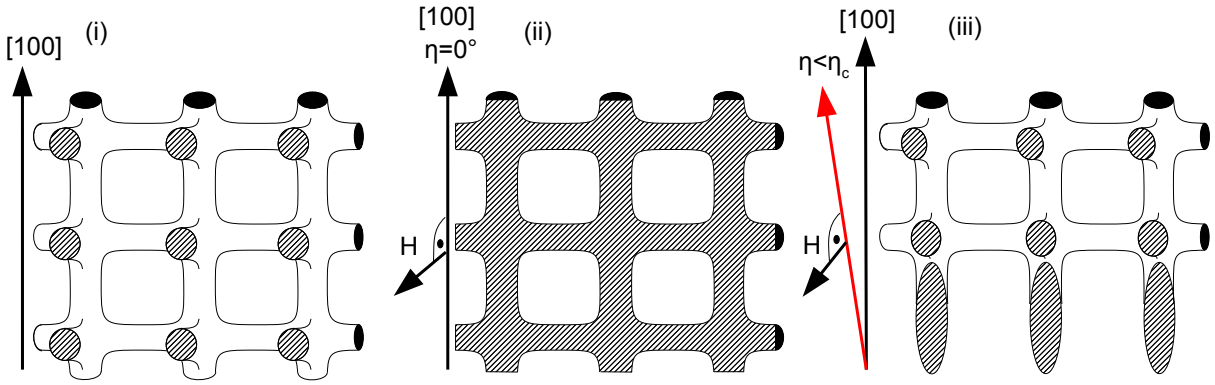

Figure 3.24: Panel (i) schematically depicts the multiply connected, open "jungle gym" Fermi surface of niobium, where the rod-like rungs are oriented along the crystalline ⟨100⟩ directions. Panel (ii) shows the multiply connected *open* Fermi surface sheet for the magnetic H field applied parallel to a crystalline ⟨100⟩ direction. Panel (iii) schematically depicts the *closed* Fermi surface sheets for the magnetic field tilted by an angle $\eta \leq \eta_c$ with respect to a crystalline ⟨100⟩ direction.

- Second, the transition between open and closed Fermi surface sheets, leading to lock-in transitions of the vortex lattice below a magic angle near ⟨100⟩, where the locked phases are also tilted: The magic angle of the transition to tilting corresponds remarkably well to a change between open and closed Fermi surface sheets, empirically suspected to affect the superconductivity [126]. The scalene vortex lattice thereby appears in transitional regions of high frustration.
- Finally, our study identifies the low-field-square as a property of the intermediate mixed state at the border between the Meissner and the Shubnikov phase.

In our study we show, that ultra pure niobium is an appropriate model system for the examination of the morphology of vortex lattices in superconductors: On the one hand, our work paves the way to further systematic analysis of the superconducting vortex lattice symmetry and structure in niobium samples with reduced purity and reduced mean free electron path to quantify to influence of the non-local corrections and the Fermi topology in a controlled way. On the other hand, our study provides an ansatz how to deconvolute and structure of the superconducting vortex lattice in systems exhibiting both an unconventional symmetry of the superconducting order parameter as well as a complicated Fermi topology.

3.7 Dynamic Properties of Vortex Lattices in Superconducting Niobium

We have deconvoluted the different sources of anisotropy influencing the symmetry of the superconducting vortex lattice in niobium in the previous section of chapter (3). In the following section, we present first time direct microscopic measurements of the intrinsic vortex lattice elasticity: For our measurements we use a novel time resolved neutron scattering technique where we measure the magnetic field and temperature dependence of the vortex lattice tilt modulus c_{44}. Our study of the vortex lattice elasticity was performed on the superconducting model system niobium as well.

The elastic matrix $\Phi_{\alpha\beta}$ of superconducting vortex lattices and their dynamic properties have already been derived in section (3.3). The properties of the ultra pure niobium single crystal sample used for our investigations and the typical small angle neutron scattering setup for experiments on vortex lattices have been given in sections (3.5) and (2).

We give a short outline: In the following section (3.7.1), we briefly revisit the salient features of the elasticity of superconducting vortex lattices and review different experimental techniques for their measurement. The experimental setup which was developed for our measurements is discussed in depth in section (3.7.2). We present the results obtained for the tilt modulus c_{44} in section (3.7.3): The response of the vortex lattice to a changed magnetic field environment is discussed in the $k = 0$ limit with a diffusion ansatz [12, 117, 129, 13] (section (3.7.4)). Finally, the relevance of our experimental setup for the investigation of different magnetic systems showing complex forms of long range order is discussed in section (3.7.5).

3.7.1 Vortex Lattice Elasticity

Vortex Lattice Elasticity

Salient features of the elasticity of vortex lattices are: (i) Three different vortex-vortex interactions have to be considered. The electromagnetic vortex-vortex interaction, characterized by the effective London penetration depth λ', the interaction due to the superconducting condensation energy characterized by the effective coherence length ξ' and finally the self energy or line tension [117]. (ii) For small dislocations of the vortices associated either with pinning forces, magnetic field gradients, temperature gradients or driving currents, the elastic matrix $\Phi_{\alpha\beta}$ of the distorted vortex lattice can be derived within linear elasticity theory. The elastic constants of the vortex lattice c_{11} for compression, c_{44} for tilt and c_{66} for shear hence depend on the microscopic nature of the superconductivity as well as impurity or surface properties of the superconducting sample due to pinning [2, 3, 4, 5].

Due to the long range effective interaction between vortices — either by the electromagnetic force or due to the superconducting condensation energy — the elasticity of

superconducting vortex lattices is strongly dispersive, which is denoted as *non-local* elasticity [117]. The non-locality gives rise to a pronounced softening of the vortex lattice with increasing k of the vortex lattice perturbation, leading to large vortex dislocations induced by thermal fluctuations and pinning. The vortex lattice thereby responds to external forces in the form of a sharp cusp, not like pulling a string. In contrast, the vortex lattice elasticity for uniform distortions $k = 0$ can be described as damped diffusion process [13, 12].

We have already introduced in sections (3.1) and (3.3) that in analogy to condensed matter composed of atoms, a large variety of different superconducting vortex matter has been observed in numerous superconducting systems, e.g., molten vortex lattices, vortex lattice Bragg glasses and liquid phases. The elastic matrix $\phi_{\alpha\beta}$ of a vortex lattice, especially the shear modulus c_{66} thereby determines the thermal stability and the state of aggregation of superconducting vortex matter. In particular, the shear modulus assumes $c_{66} = 0$ at vortex lattice melting transitions, where the long range order vanishes. Moreover, we have also introduced that the elastic matrix of vortex lattices is intimately related to the pinning and depinning properties of superconductors, leading to a particular relevance for technical applications: If transport currents are applied to superconducting materials, the Lorentz force acting on the vortices leads — with increasing current — to dissipative processes as vortex creep [136], thermally assisted flux-flow (TAFF) [13] and flux-flow (FF) [137]. Therefore, the ability of superconducting materials to carry large transport currents for technical applications is intimately related to the pinning properties of superconductors and the elasticity of the vortex lattice.

The experimental access to the dynamic properties of vortex lattices and their elastic matrix — in particular for non-equilibrium states — is, on the one hand, possible by macroscopic bulk techniques as, e.g., measurements of the transport properties [2], measurements of the magnetization [132] or measurements using vibrating reeds [162]. However, as we have introduced in section (3.3), parasitic effects induced by volume and surface pinning as well as geometrical effects significantly hamper the unambiguous determination of the intrinsic elastic constants of vortex lattices. Moreover, the mapping of the k-dependence of the elasticity of vortex lattices cannot be performed by macroscopic measurements. Microscopic surface sensitive measurement techniques, e.g., decoration or magneto-optical methods suffer from similar or even stronger pinning and geometry induced effects: This is due to the commonly used thin film samples. On the other hand, local probes as muon spin relaxation μSR and scattering techniques as neutron scattering can yield microscopic information on bulk vortex lattices. However, as the accessible timescale of inelastic neutron scattering techniques is still to short for vortex lattice dynamical properties, neutron scattering was up to now limited to characterize the static properties of vortex lattices with only a few exceptions [90, 163].

Motivation

To overcome the limitations induced by pinning, hindering microscopic measurements of the intrinsic elastic constants of superconducting vortex lattices, we exploit a new

time resolved stroboscopic small angle neutron scattering technique [11] combined with a tailored magnetic field setup consisting of two orthogonal magnetic fields — one of them time-dependent— for the microscopic measurements of the intrinsic bulk vortex lattice tilt modulus c_{44}. On the one hand, stroboscopic small angle scattering allows the access to long time-scales inaccessible with inelastic neutron scattering methods. On the other hand, neutron scattering allows direct microscopic measurements of the properties of bulk vortex lattices, with less or even without surface induced pinning effects.

Our niobium sample is of unprecedented purity, characterized by a residual resistivity ratio $\sim 10^4$ and has proven to exhibit vanishing volume and surface pinning in previous studies [10]. Moreover due to the low κ, the model system niobium is ideally suited to provide general information on the vortex lattice elasticity: Niobium is situated directly at the border between type-I and type-II superconductivity, thus making the underlying change from attractive to repulsive vortex interactions experimentally accessible [93, 140]: The vortex-vortex interaction in pure niobium can be tuned as a function of temperature and magnetic field in a controlled way.

3.7.2 Experimental Setup

To measure the vortex lattice tilt modulus c_{44} by means of time resolved small angle neutron scattering, a *time varying magnetic field setup*, consisting of two orthogonal pairs of Helmholtz-coils has been designed. The vortex lattice thereby follows the magnetic field direction, the time dependent relaxation is measured by means of stroboscopic neutron scattering. The time resolved stroboscopic small angle neutron scattering measurements have been performed on the small angle diffractometer V4 at BENSC [114, 11]. In the following paragraphs, we introduce the details of the experimental setup, used for time resolved study.

Stroboscopic Small Angle Neutron Scattering

In contrast to inelastic neutron scattering, where the change of energy $\hbar\omega$ of the scattered neutrons is analyzed by means of a Bragg reflection at the monochromator and at the analyzer, by time-of-flight (TOF), or by neutron resonance spin echo (NRSE) methods, the fundamental principle of stroboscopic neutron scattering is the excitation of the sample by an external control parameter followed by a measurement of the time dependent dynamic response and relaxation of the system [7]. To increase time resolution and signal statistics, these measurements are performed in a *stroboscopic* manner, i.e. the measurement is repeated many times where the data obtained for the individual cycles is summed coherently [11]. The stroboscopic small angle neutron scattering technique is realized, using a standard small angle neutron scattering setup (cf. section (2.4)), extended by a *time resolved* position sensitive detector. Both repetition cycles of the time resolved detector and the control parameter have to be phase locked.

[7] Note, that only elastic scattering is considered for the stroboscopic small angle neutron scattering technique used for our experiment.

The time resolution of the setup is merely determined by a time-smearing of the single frames, caused by the wavelength spread $\Delta\lambda/\lambda$ of the neutron beam. The different velocities of the neutrons lead to a variation of their time of flight from the sample to the detector. The time of flight of the neutrons is given by the equation [11]

$$t_{TOF}[\mathrm{ms}] = \lambda[\mathrm{\AA}] \cdot L_2[\mathrm{m}] \cdot 0.253 \tag{3.30}$$

with the wavelength of the neutron beam λ and the sample-detector distance L_2, respectively. For small angle neutron scattering measurements, L_2 and λ determine the accessible q-range. A large sample-detector distance L_2 and large wavelength λ have to be chosen in order to resolve large real space structures associated with small q-vectors. This leads to a significant loss in time resolution. For our time resolved measurements on the vortex lattice in niobium, presented in this manuscript, a wavelength λ =8Å with a wavelength spread $\Delta\lambda/\lambda = 0.1$ and a detector distance L_2=8 m was chosen, leading to a time resolution of 5 ms.

Time Varying Magnetic Field Setup

A schematic drawing of the magnetic field setup is given in Fig. 3.25. The static main field $\mathbf{H}_{\mathrm{stat}} \leq 150\,\mathrm{mT}$, applied along the Y-axis is generated by bespoke water cooled copper coils [164]. The time varying field $\mathbf{H}_{\mathrm{osc}} \leq 5\,\mathrm{mT}$ is generated by a small air-cooled set of Helmholtz-coils inside the main coil, driven with an arbitrary waveform generator and an amplifier. $\mathbf{H}_{\mathrm{osc}}$ is oriented along the X-axis perpendicular to $\mathbf{H}_{\mathrm{stat}}$. The resulting field $\mathbf{H}_{\mathrm{total}}$ is rotated with respect to $\mathbf{H}_{\mathrm{stat}}$ by the angle $\epsilon = \arctan\frac{|\mathbf{H}_{\mathrm{osc}}|}{|\mathbf{H}_{\mathrm{stat}}|}$ in the XY plane. $\mathbf{H}_{\mathrm{stat}} \gg \mathbf{H}_{\mathrm{osc}}$, yields that $|\mathbf{H}_{\mathrm{total}}| \approx |\mathbf{H}_{\mathrm{stat}}| = |\mathbf{H}|$ [8]. H is oriented approximately parallel to the incoming neutron beam. The rise and fall time of the amplifier used for H_{osc} causes a smearing of the applied pulses. They have been determined with a Hall-probe at the sample position and found to be in the range of $\sim 5\,\mathrm{ms}$.

Experimental Setup

The sample is located in the center of both Helmholtz-coils, cooled with a closed-cycle cryostat to a minimum temperature of 4 K. Both magnetic fields and the sample can be rocked together with respect to the vertical Z-axis. The angle enclosed between H_{stat} and the incoming neutron beam, which is also applied in the XY plane, is denoted rocking angle ϕ. The sample *Nb1* (cf. section 3.5) is of cylindric shape with its symmetry axis aligned parallel to the Z-axis, i.e. a constant demagnetizing factor $N = 1/2$ applies for all angles ϵ. The vertical symmetry axis of the sample coincides with a crystallographic $\langle 110\rangle$ axis. A further $\langle 110\rangle$ axis is oriented parallel to the incident neutron beam.

The oscillating magnetic field H_{osc} was driven with a rectangular pulse shape with an amplitude of H_{osc} =0 mT$\leftrightarrow$5 mT and a repetition cycle of 0.2 Hz. A magnetic field 75 mT$\leq H_{stat} \leq$135 mT was applied. Two equilibrium positions for the magnetic field

[8] Due to the perpendicular alignment we omit the vectorial notation of $\mathbf{H}_{\mathrm{stat}}$ and $\mathbf{H}_{\mathrm{osc}}$.

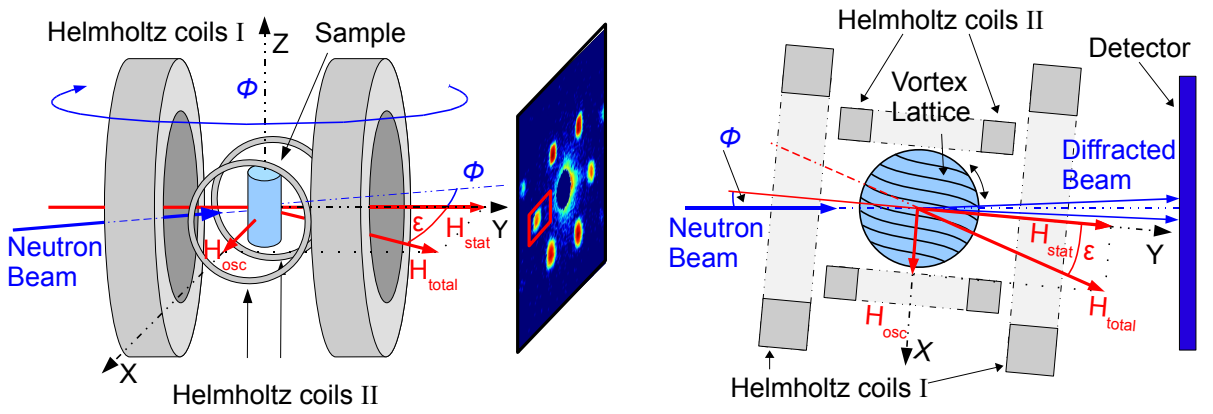

Figure 3.25: Schematic depiction of the experimental setup, used for time resolved small angle neutron scattering measurements of the vortex lattice tilt modulus c_{44}. The sample is located in the centre of two orthogonal magnetic fields, generated by Helmholtz coils. With a combination of a static magnetic field $H_{stat} \parallel Y$ and a time-varying magnetic field $H_{osc} \parallel X$ with $H_{osc} \ll H_{stat}$, the resulting magnetic field can be rotated with respect to the sample in the XY plane. Both magnetic fields and the sample can be rocked around the vertical Z-axis with respect to the incoming neutron beam by the angle ϕ, whereas the resulting magnetic field H_{total} is roughly parallel to the incoming neutron beam. The scattered intensity is recorded on a two-dimensional detector.

and the vortex lattice emerge, which are separated by $\epsilon \approx 2°$ if H_{osc} is alternated between H_{osc} =0 mT and H_{osc} =5 mT (cf. Fig. 3.25). For a typical field $\mu_0 H$ =100 mT, the vortex lattice assumes a six-fold scattering pattern with a Bragg angle of $\approx 0.17°$. The instrumental resolution for the width of a rocking scan $\Delta\beta_{\mathbf{kf}}$ yields a value of 0.2° for $L_1 = 8$ m, $L_2 = 8$ m, $R_1 = 10$ mm and $R_2 = 2$ mm (cf. section (A.1)).

Measurements of the tilt modulus c_{44} of the vortex lattice have been performed for an applied magnetic field $\mu_0 H$ =75 mT, 100 mT and 135 mT, each for sample temperatures between 4 K and T_c. A schematic sketch of the measurement range with respect to the phase diagram, obtained in previous small angle neutron scattering on *Nb 1* [10] is given in Fig. 3.26, panel (i): Both, the intermediate mixed state and the crossover to the Shubnikov phase are covered, where the vortex-vortex interaction changes from attractive to repulsive. The intrinsic mosaicity of the vortex lattice as inferred from static rocking scans is given in panel (ii): For the highest temperatures the mosaicity of the vortex lattice is limited by the instrumental resolution. For decreasing temperatures $T \leq$6 K for $\mu_0 H$ =75 mT and $T \leq$5 K for $\mu_0 H$ =100 mT the mosaic spread shows a pronounced increase. However, in the Shubnikov phase for $\mu_0 H$ =135 mT only a weak increase of the mosaic spread is observed for decreasing temperatures. This increase of mosaicity is attributed to the crossover to the intermediate mixed state where an additional bending of vortices is caused by the complicated vortex lattice domain structure in combination with increasing demagnetizing effects with increasing Meissner effect for decreasing temperature. The transition from the Shubnikov phase to the intermediate mixed state is furthermore characterized by hysteretic behaviour of the integrated intensity (cf. Fig 3.11, panel (i)) and mosaicity.

To avoid hysteretic effects, all measurements have been taken after cooling in a field to the desired temperature (FC). Furthermore, the direction of the magnetic field is oscillated continuously due to H_{osc}. This leads to an effective depinning of the vortex lattice. Summarizing, an equilibrium state can be assumed. In analogy to HFC paths in the B-T phase diagram of type-I superconductors in the intermediate state, where the magnetic flux is expelled for decreasing field, a similar behaviour and morphology is expected in the intermediate mixed state for type-II superconductors upon FC. The result is supposed to be an open, multiply connected topology of Shubnikov domains enclosing regions of Meissner phase. In addition, the intermediate mixed state is characterized by Landau branching at the surface of the sample. The detailed topology of the intermediate mixed state has been reviewed in section (3.4).

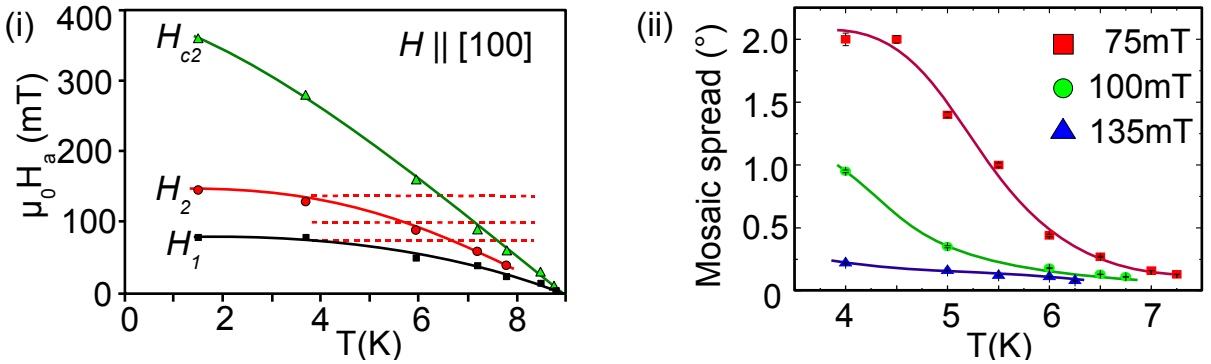

Figure 3.26: Panel (i) depicts the phase diagram for *Nb 1*, obtained by previous small angle neutron scattering measurements [10]. Note that a demagnetizing factor $N = 1/2$ applies. The dashed red lines locate scans, performed for our measurements of c_{44}, in the phase diagram. Panel (ii) depicts the intrinsic mosaicity of the vortex lattice as measured with small angle neutron scattering as function of temperature for magnetic fields $\mu_0 H = 75\,\mathrm{mT}$, $100\,\mathrm{mT}$ and $135\,\mathrm{mT}$. The lines serve as guide to the eye.

Measuring Principle

The vortex lattice motion and relaxation, driven by the changed magnetic field direction was measured in two different ways:

- The rocking angle ϕ is precisely adjusted to satisfy the Bragg condition for a reciprocal lattice vector of the vortex lattice $\mathbf{q} = \mathbf{G_{VL}} = \mathbf{k}_i - \mathbf{k}_f$ (lying in the XY plane) exactly for $H_{osc} = 0$, i.e. $\epsilon = 0°$. The observed scattering intensity at the 2D detector at $\mathbf{G_{VL}}$ thus is a measure for the quantity of vortex lattice which points into this direction. H_{osc} is oscillated between $\mu_0 H_{osc} = 0\,\mathrm{mT}$ and $\mu_0 H_{osc} = 5\,\mathrm{mT}$. Thus, the relaxation process between these two equilibrium positions can be followed by measuring the integrated intensity at the Bragg reflection at $\mathbf{G_{VL}}$ as function of time. We emphasize that two different time-dependent processes have to be considered: The characteristic time-scale observed for $\mu_0 H_{osc}$ decreasing from $5\,\mathrm{mT}$ to $0\,\mathrm{mT}$ corresponds to a different physical relaxation process, compared to $\mu_0 H_{osc}$ increasing from $0\,\mathrm{mT}$ to $5\,\mathrm{mT}$:

(i) The first process ($\mu_0 H_{osc}$ decreases from 5 mT to 0 mT) is attributed to the vortex lattice relaxing *into* the Bragg condition which yields a macroscopic displacement of the vortices. The instrumental resolution $\Delta\beta_{\mathbf{kf}} = 0.2°$ is significantly smaller compared to the angular separation of both vortex lattice equilibrium positions $\epsilon \approx 2°$. The corresponding time-scale is denoted τ_1.

(ii) The latter process ($\mu_0 H_{osc}$ increases from 0 mT to 5 mT) describes a time-scale, necessary to pull the vortex lattice out of the Bragg condition denoted as τ_3.

In the following, this method is denoted *fixed angle scan*. An exemplary *fixed angle scan* for a temperature of $T = 4$ K and a magnetic field of $\mu_0 H$ =100 mT is shown in Fig. 3.27, panel (i), where the red line indicates the modulus of H_{osc}

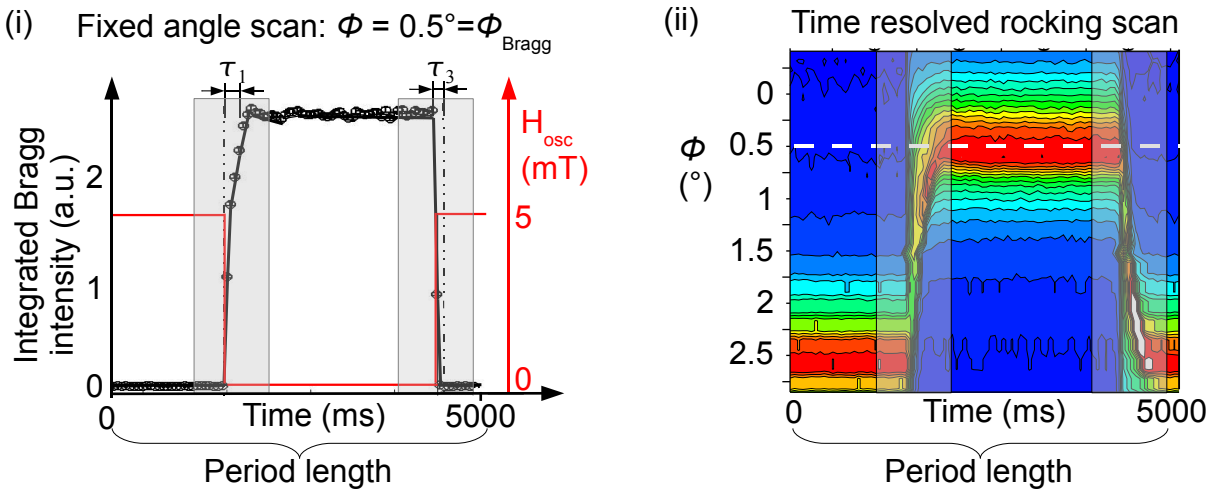

Figure 3.27: Panel (i) shows a typical time resolved measurement for a rectangular pulse shape of H_{osc} for a fixed rocking angle ϕ denoted as *fixed angle scan*. The red line indicates the modulus of H_{osc}. The change in magnetic field direction yields a changed direction of the vortex lattice in the sample, thus leading to a different scattering intensity. Panel (ii) shows a typical time resolved scan for varying rocking angles ϕ denoted *time resolved rocking scan*, again for rectangular pulses of H_{osc}. Two equilibrium positions for the vortex lattice, as induced by the change of H_{osc}, are visible for $\phi = 0.5°$ and $\phi = 2.75°$. The switching process between these equilibrium positions can be monitored as a function of time. The horizontal broken white line in panel (ii) represents the *fixed angle scan* given in panel (i). Both, scans (i) and (ii) have been performed at $T = 4$ K and $\mu_0 H$ =100 mT. For details see text.

- The whole relaxation process of the vortex lattice can be traced angle and time resolved, when *fixed angle scans* are performed for each rocking angle ϕ. The latter method is denoted *time resolved rocking scan*. A typical representative scan is given in Fig. 3.27, panel (ii) for $T = 4$ K and $\mu_0 H$ =100mT.

It is important to note that the angular distribution of the vortex lattice is always integrated over the complete sample and thus is additionally convoluted with the intrinsic vortex lattice mosaicity and the angular resolution of the small angle scattering instrument. Further note that *fixed angle scans* are represented by cuts at a fixed rocking angle ϕ in the *time resolved rocking scans*.

3.7.3 Experimental Results

Time Resolved Rocking Scans

In the following paragraphs we present our data obtained for the vortex lattice relaxation and diffusion. First, we focus on the *time resolved rocking scans*. Fig. 3.28 depicts the relaxation of the vortex lattice at a magnetic field $\mu_0 H$=100 mT for a temperature of T =6.5 K (panels (i) and (ii)) and $T = 4$ K (panels (iii) and (iv)). The relaxation of the vortex lattice is plotted as function of time and rocking angle ϕ. The integrated intensity is plotted on a linear scale. The horizontal broken white lines marked with the black arrows indicate the time when the magnetic field direction is switched between the two equilibrium positions. Note, that the time-range displayed corresponds to the gray shading in Fig. 3.27, panel (ii), however, the axes have been rotated for better visibility. Both equilibrium positions, at $\phi = 0.5°$ and $\phi = 2.75°$ are clearly visible for the data obtained at $T = 4$ K (indicated with vertical broken white lines), whereas the measurements range was reduced for $T = 6.5$ K due to the limited beamtime. Salient features of the vortex lattice relaxation are:

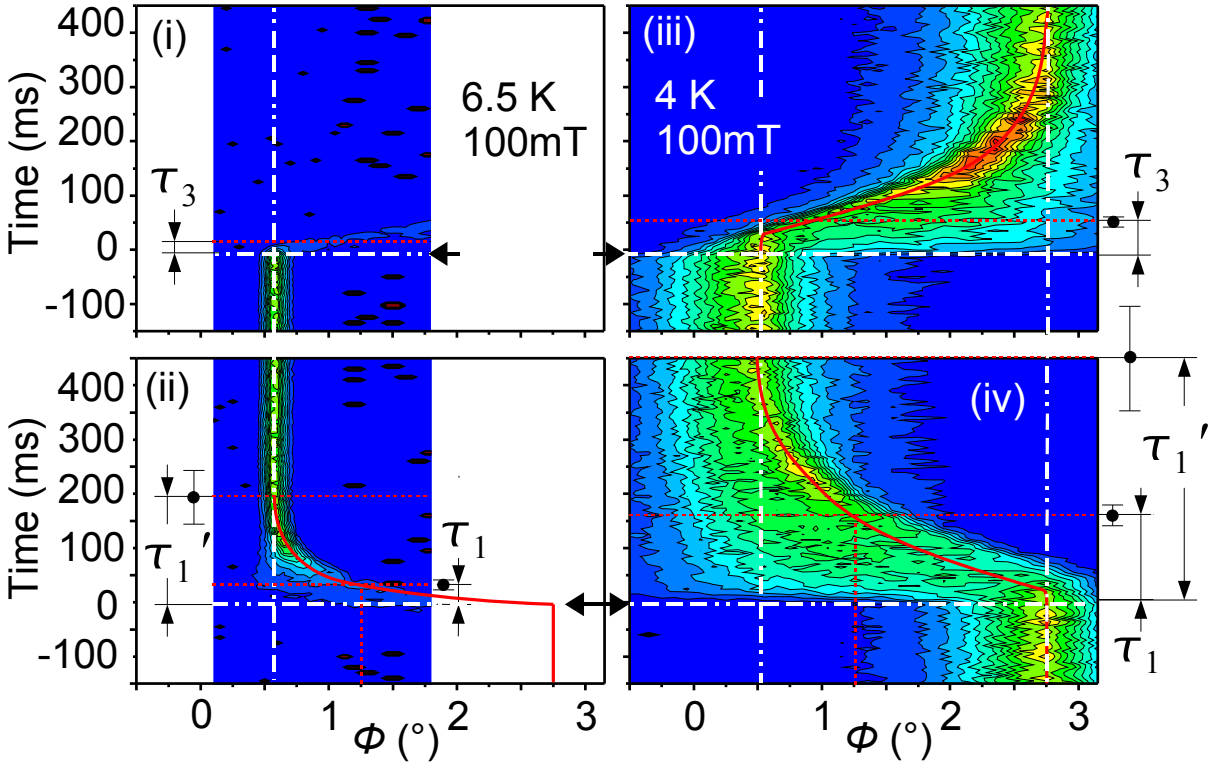

Figure 3.28: Panels (i) and (ii) depict *time resolved rocking scans* for an applied magnetic field $\mu_0 H$=100 mT and a temperature of 6.5 K, whereas panels (iii) and (iv) depict similar scans for $\mu_0 H$=100 mT and 4 K. Note the reduced measurement range for $T = 6.5$ K. The contours are plotted on a linear scale. The change of magnetic field direction is indicated by horizontal broken white lines marked with black arrows, whereas the equilibrium positions of the vortex lattice are marked with vertical broken white lines. The continuous red lines indicate the relaxation process of the vortex lattice. The red lines serve as guide to the eye.

(i) A larger intrinsic mosaicity of the vortex lattice is observed for $T = 4\,\mathrm{K}$ in comparison to $T = 6.5\,\mathrm{K}$. The additional mosaic spread, caused by a possible bending of the vortices due to the domain structure of the intermediate mixed state in combination with demagnetizing effects is in agreement with static data as displayed in panel (ii) of Fig. 3.26.

(ii) As expected, the general trend is a relaxation characteristic of an exponential decay $\propto e^{-t/\tau_1}$ for both $T = 4\,\mathrm{K}$ and $T = 6.5\,\mathrm{K}$, as indicated by the continuous red lines. The corresponding time constant τ_1, obtained for $T = 6.5\,\mathrm{K}$ yields $0.04\pm0.008\,\mathrm{s}$, whereas τ_1 yields $0.16\pm0.02\,\mathrm{s}$ for $T = 4\,\mathrm{K}$. In addition, we further define τ_1' as the characteristic time-scale, when the vortex lattice has reached its new equilibrium position. τ_1', obtained for $T = 6.5\,\mathrm{K}$ yields $0.2\pm0.05\,\mathrm{s}$, whereas τ_1' yields $0.45\pm0.1\,\mathrm{s}$ for $T = 4\,\mathrm{K}$.

(iii) τ_3 indicates the time, where the intensity at the Bragg spot $\mathbf{G}_{VL}$ has decreased to $1/e$ of its initial value. The values obtained for τ_3 yield $0.06\pm0.008\,\mathrm{s}$ for $T = 4\,\mathrm{K}$ and $0.025\pm0.005\,\mathrm{s}$ for $T = 6.5\,\mathrm{K}$, respectively.

(iv) The intensity map, obtained for $T = 4\,\mathrm{K}$ is characterized by a drastic increase of mosaic spread immediately after the magnetic field direction is changed. The time-scale observed for this drastic increase of mosaicity is faster, i.e. below τ_3. In contrast, only a moderate increase of mosaic spread is observed for $T = 6.5\,\mathrm{K}$. In particular, no edge-like step is observed for very short timescales after the magnetic field direction is changed, i.e. the vortex lattice changes its direction coherently.

Fixed Angle Scans

New light is shed on the details of the vortex lattice relaxation process, focusing on the *fixed angle scans* as function of applied magnetic field H and temperature T, as given in Fig. 3.29, panels (i) and (ii) for a magnetic field of $\mu_0 H = 75\,\mathrm{mT}$, Fig. 3.30, panels (i) and (ii) for $\mu_0 H = 100\,\mathrm{mT}$ and Fig. 3.31, panels (i) and (ii) for $\mu_0 H = 135\,\mathrm{mT}$. The time-range displayed for the three figures also corresponds to the gray shadings in Fig. 3.27, panel (i).

- We first focus on panels (i) of Figs. 3.29, 3.30 and 3.31 which show *fixed angle scans* for $\mu_0 H$ =75 mT, 100 mT and 135 mT, respectively, each for increasing sample temperature from $T = 4\,\mathrm{K}$ to T_c (as labeled in panels (ii)). The increase of scattering intensity after the vertical line, labeled with *trigger* is attributed to the relaxation of the vortex lattice *into* the Bragg condition $\mathbf{q} = \mathbf{G_{VL}} = \mathbf{k}_i - \mathbf{k}_f$ as function of time for $\mu_0 H_{osc}$ decreasing from 5 mT to 0 mT. The characteristic relaxation time for this process was denoted τ_1. However, it turns out that the qualitative shape of the relaxation process changes as function of temperature. It is therefore not possible to determine the characteristic times-scale τ_1, in a way similar to the *time resolved rocking scans* [9]. However, to cover the systematic trends, the magnetic field and temperature dependence of τ_1' was analyzed. Salient features are:

[9] Due to the limited beamtime, the systematic temperature and magnetic field dependence of the vortex lattice relaxation was measured only for the *fixed angle scans*.

(i) The same general trend as observed for the *time resolved rocking scans* can also be identified here: Increasing temperature and increasing applied magnetic field lead to a significantly faster relaxation. The relaxation time τ_1' is indicated with a black marker in each *fixed angle scan*. The resulting magnetic field and temperature dependence of τ_1' is shown in Fig. 3.32, panel (i): For low temperatures $T \approx 4\,\mathrm{K}$ and magnetic fields of $\mu_0 H = 75\,\mathrm{mT}$ and $100\,\mathrm{mT}$, $\tau_1' = 0.5 \pm 0.1\,\mathrm{s}$. For increasing temperatures, τ_1' decreases characteristic of a smooth crossover to values of $\tau_1' = 0.2 \pm 0.05\,\mathrm{s}$. The crossover temperature thereby decreases with increasing field from $T = 6.5\,\mathrm{K}$ at $\mu_0 H = 75\,\mathrm{mT}$ to $T = 5.5\,\mathrm{K}$ at $\mu_0 H = 100\,\mathrm{mT}$. In contrast, for a magnetic field of $\mu_0 H = 135\,\mathrm{mT}$, τ_1' assumes a constant value of $\tau_1 = 0.2 \pm 0.05\,\mathrm{s}$ except at the lowest temperature where a slight shift to $\tau_1' = 0.25\,\mathrm{s} \pm 0.05\,\mathrm{s}$ is observed. The crossover temperature for $\mu_0 H = 135\,\mathrm{mT}$ is expected to be at $\approx 3.5\,\mathrm{K}$, i.e. slightly below the accessible temperature regime. The magnetic field dependence of the crossover temperature of τ_1' corresponds to the crossover from the intermediate mixed state to the Shubnikov phase.

The data points obtained for τ_1 from the *time resolved rocking scans* are given in Fig. 3.32, panel (i) as well.

(ii) The characteristic shape of the relaxation changes as function of temperature and magnetic field: For the low temperature data points at each magnetic field, namely for $T = 4\,\mathrm{K}$ to $T = 6\,\mathrm{K}$ at $\mu_0 H = 75\,\mathrm{mT}$, for $T = 4\,\mathrm{K}$ to $T = 5\,\mathrm{K}$ at $\mu_0 H = 100\,\mathrm{mT}$ and for $T = 4\,\mathrm{K}$ at $\mu_0 H = 135\,\mathrm{mT}$, the relaxation is characterized by a sharp kink, associated with a distinct increase of intensity immediately after the magnetic field is changed. This sharp increase is more pronounced for the lowest temperatures. It is associated with the step-like broadening of the vortex lattice mosaic, as observed in the *time resolved rocking scans*, e.g., for $T = 4\,\mathrm{K}$ and $\mu_0 H = 100\,\mathrm{mT}$ (Fig. 3.28, panels (iii) and (iv)). This step-like increase is followed by a slow relaxation characteristic of the time-scale τ_1'. Note, that the data points at low temperatures and low fields, where the additional sharp increase is observed, are situated in the intermediate mixed state.

(iii) In contrast, the characteristic shape of the relaxation process exhibits a smooth increase with exponential shape for high temperatures, namely for $T = 6.5\,\mathrm{K}$ to $T = 7.25\,\mathrm{K}$ at a magnetic field of $\mu_0 H = 75\,\mathrm{mT}$, for $T = 6\,\mathrm{K}$ to $T = 6.75\,\mathrm{K}$ at $\mu_0 H = 100\,\mathrm{mT}$ and for $T = 5\,\mathrm{K}$ to $T = 6.25\,\mathrm{K}$ at $\mu_0 H = 135\,\mathrm{mT}$. This is attributed to the lack of the above-mentioned sharp increase of intensity directly after the magnetic field is changed.

- We now concentrate on Figs. 3.29, 3.30 and 3.31, panels (ii), showing so-called *fixed angle scans* for a magnetic field of $\mu_0 H = 75\,\mathrm{mT}$, $100\,\mathrm{mT}$ and $135\,\mathrm{mT}$, each for increasing temperature. The decrease of intensity after the vertical line, labeled with *trigger*, is attributed to the vortex lattice being pulled *out* of the Bragg condition for $\mu_0 H_{osc}$ increasing from $0\,\mathrm{mT}$ to $5\,\mathrm{mT}$. The decreasing intensity is characterized by two different time-scales: τ_3 characterizes the overall time after the change of magnetic field direction when the scattering intensity has decreased to $1/e$ of its initial value. τ_3 is indicated with a blue marker in each scan. In contrast, τ_2, indicated

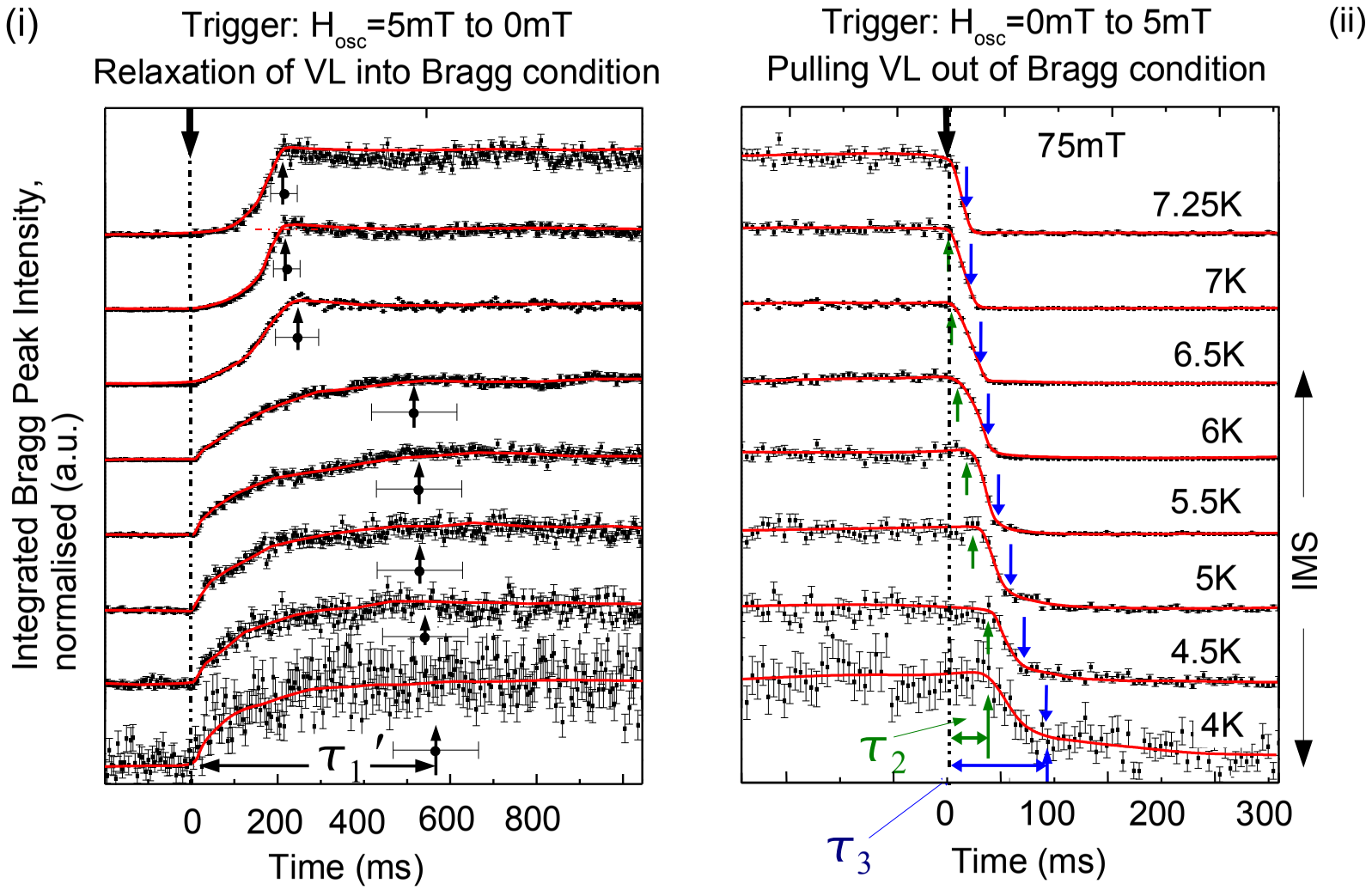

Figure 3.29: Panel (i) shows *fixed angle scans* for $\mu_0 H$ =75 mT for increasing temperature as labeled in panel (ii). The increase of scattering intensity after the trigger is attributed to the relaxation of the vortex lattice *into* the Bragg condition as function of time for $\mu_0 H_{osc}$ decreasing from 5 mT to 0 mT. The characteristic relaxation time is denoted τ_1', indicated with black markers. Panel (ii) shows *fixed angle scans* for $\mu_0 H$ =75 mT for increasing temperature. The decrease of intensity after the trigger is attributed to the vortex lattice being pulled *out* of the Bragg condition for $\mu_0 H_{osc}$ increasing from 0 mT to 5 mT. The characteristic relaxation times are denoted τ_2 and τ_3, indicated with green and blue markers, respectively. Note the different timescale for panel (i) compared to panel (ii). The different plots have been shifted vertically for clarity reasons, the lines serve as guide to the eye.

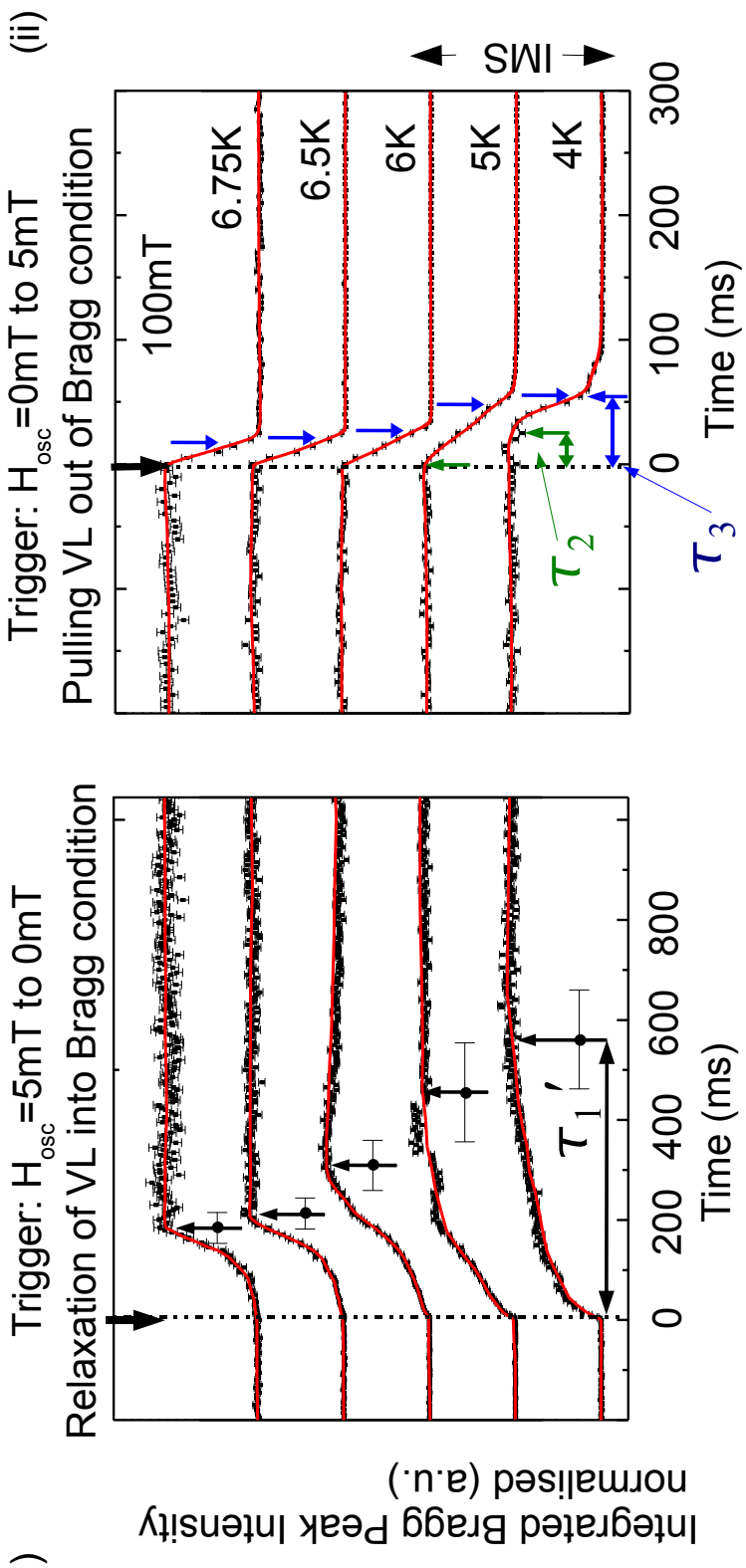

Figure 3.30: Panel (i) shows *fixed angle scans* for $\mu_0 H$ =100 mT for increasing temperature as labeled in panel (ii). The increase of scattering intensity after the trigger is attributed to the relaxation of the vortex lattice *into* the Bragg condition as function of time for $\mu_0 H_{osc}$ decreasing from 5 mT to 0 mT. The characteristic relaxation time is denoted τ_1', indicated with black markers. Panel (ii) shows *fixed angle scans* for $\mu_0 H$ =100 mT for increasing temperature. The decrease of intensity after the trigger is attributed to the vortex lattice being pulled *out* of the Bragg condition for $\mu_0 H_{osc}$ increasing from 0 mT to 5 mT. The characteristic relaxation times are denoted τ_2 and τ_3, indicated with green and blue markers, respectively. Note the different timescale for panel (i) compared to panel (ii). The different plots have been shifted vertically for clarity reasons, the lines serve as guide to the eye.

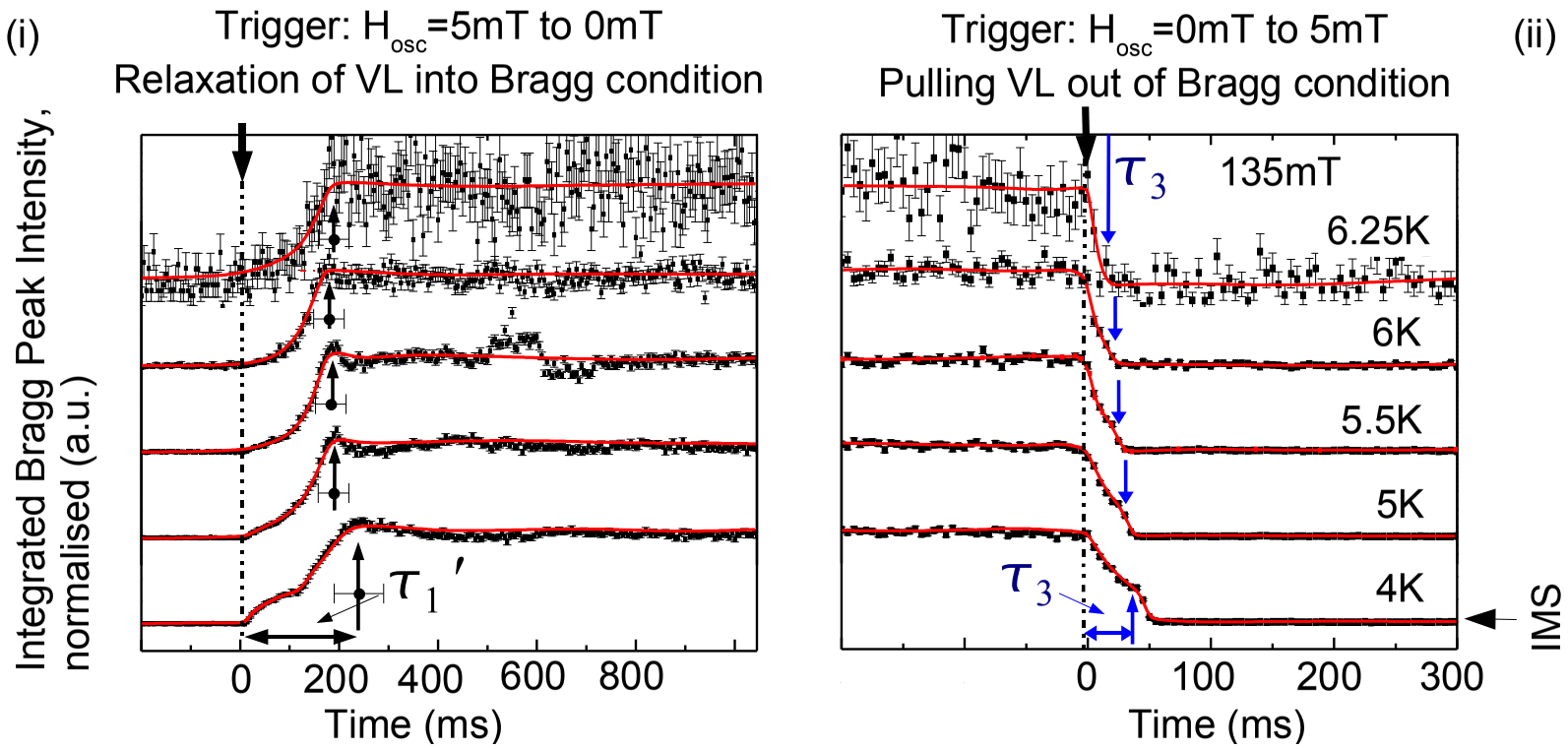

Figure 3.31: Panel (i) shows *fixed angle scans* for $\mu_0 H$ =135 mT for increasing temperature as labeled in panel (ii). The increase of scattering intensity after the trigger is attributed to the relaxation of the vortex lattice *into* the Bragg condition as function of time for $\mu_0 H_{osc}$ decreasing from 5 mT to 0 mT. The characteristic relaxation time is denoted τ_1', indicated with black markers. Panel (ii) shows *fixed angle scans* for $\mu_0 H$ =135 mT for increasing temperature. The decrease of intensity after the trigger is attributed to the vortex lattice being pulled *out* of the Bragg condition for $\mu_0 H_{osc}$ increasing from 0 mT to 5 mT. The characteristic relaxation times are denoted τ_2 and τ_3, indicated with green and blue markers, respectively. Note the different timescale for panel (i) compared to panel (ii). The different plots have been shifted vertically for clarity reasons, the lines serve as guide to the eye.

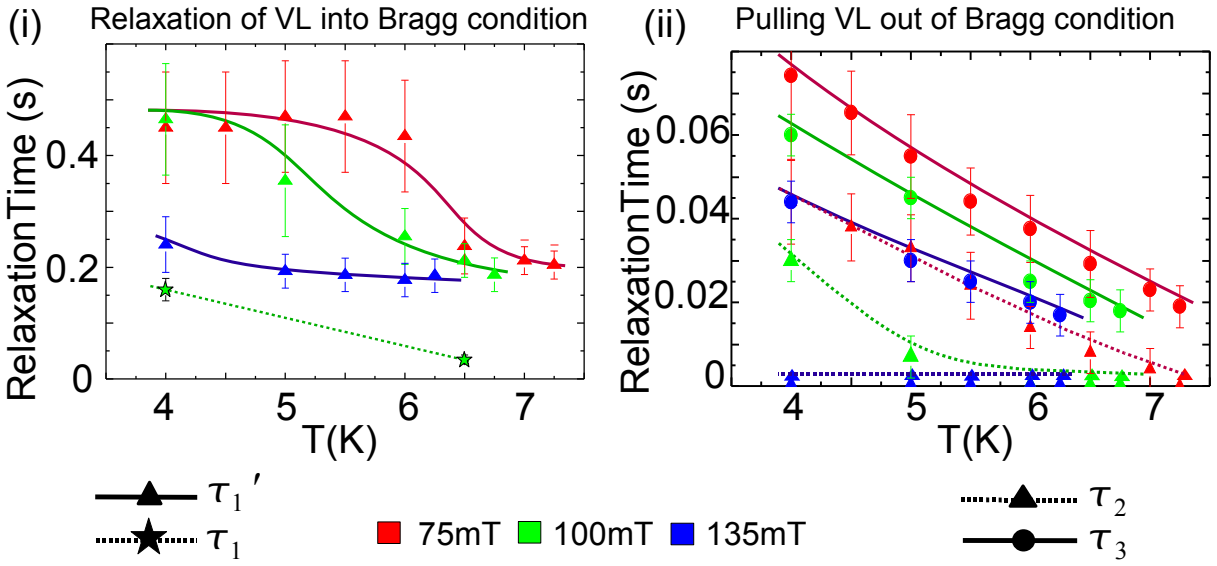

Figure 3.32: Panels (i) and (ii) show the values measured for time constants τ_1, τ_1', τ_2 and τ_3 as function of temperature T and magnetic field $\mu_0 H$. Note the different scaling for panel (i) and panel (ii). The lines serve as guide to the eye.

with a green marker, describes the characteristic delay-time between the change of magnetic field direction and the response of the vortex lattice. The temperature and magnetic field dependence of τ_2 and τ_3 is shown in Fig. 3.32, panel (ii):

(i) τ_3 exhibits a linear decrease as a function of increasing temperature for all magnetic fields measured: For $\mu_0 H$ =75 mT, τ_3 decreases from 0.08±0.01 s at T = 4 K to 0.02±0.005 s at T = 7.25 K. For $\mu_0 H$ =100 mT, τ_3 decreases from 0.06±0.01 s at T = 4 K to 0.02±0.005 s at T = 6.75 K and for $\mu_0 H$ =135 mT, τ_3 decreases from 0.045±0.01 s at T = 4 K to 0.02±0.005 s at T = 6.25 K. No signature of a crossover from the intermediate mixed state to the Shubnikov phase is observed in the temperature and magnetic field dependence of τ_3.

(ii) The temperature dependence of τ_2 is characterized by a linear decrease from τ_2 =0.047±0.01 s at T = 4 K to τ_2 = 0 at T = 7.25 K for a magnetic field of $\mu_0 H$ =75 mT. For a magnetic field of $\mu_0 H$ =100 mT, τ_2 decreases from τ_2 =0.03±0.005 s at T = 4 K to τ_2 = 0 for temperatures above T = 6 K. In contrast, for $\mu_0 H$=135 mT, τ_2 = 0 for all temperatures. Note, that the observation of $\tau_2 \neq 0$ seems to be associated with the phase region of the intermediate mixed state as well.

3.7.4 Interpretation

For an interpretation of our data, we first review the vortex lattice diffusion for uniform tilt before we start with a qualitative description of the vortex lattice relaxation for a displacement of the magnetic field direction. Adjacent, we calculate the temperature and magnetic field dependence of the vortex lattice tilt modulus c_{44}, using the vortex lattice

diffusion model for uniform distortions.

Vortex Lattice Elasticity and Diffusion for Uniform Distortions

We have derived the eigenfrequencies of vortex lattices in section (3.3). For the vortex lattice in a typical clean low κ superconductor such as niobium, the eigenfrequencies Γ_1 and Γ_2 of the vortex lattice are in the range of 10^{-9} s^{-1}. In our experimental setup, the magnetic field direction was oscillated with a repetition frequency of 0.2 Hz. Therefore, the associated relaxation process of the superconducting vortex lattice can be calculated in the $\mathbf{k} = 0$ limit. For a change of the magnetic field direction, as used in our experimental setup, the relaxation process is essentially given by the vortex lattice tilt modulus $c_{44}(\mathbf{k} = 0)$.

For uniform distortions, the vortex lattice tilt modulus $c_{44} = BH$ depends only on the applied magnetic field H which is in local equilibrium with the equilibrium induction B resulting in a magnetization $M = \mu_0 H - B \leq 0$ [117]. For the case that the spatially varying part of B is smaller than the average value of B, the highly nonlinear equations of motion may be linearized. The response of the vortex lattice in a bulk sample (sample diameter $r >> \lambda'$) to a changed magnetic direction field may then be written as damped diffusion process [12], using the diffusion equation derived by Kes [13].

It is important to note that the vortex lattice initially responds to a change of applied magnetic field H solely at the surface of the superconductor, as the magnetic field is screened by supercurrents from the bulk of the specimen (in particular by the Meissner domains in the intermediate mixed state). Note that due to continuity conditions, the slope of the vortex lattice is slightly refracted at the surface of the sample. However, for the following description, the refraction of the magnetic field is neglected.

According to the diffusion model, the distortion of the vortex lattice propagates from the surface of the sample into the bulk due to the finite elastic constants of the vortex lattice. The resulting diffusion equation of the tilt distortion $u(x,t)$ of the vortex lattice is given by

$$\frac{\mathrm{d}u}{\mathrm{d}t} = D \cdot u'' \tag{3.31}$$

with the diffusion constant D given by the ratio of the tilt modulus c_{44} and the viscosity η [165]:

$$D = \frac{c_{44}}{\eta}. \tag{3.32}$$

η describes the viscous damping of the vortex motion by flux flow resistivity, assuming either vanishing pinning effects or an efficient depinning due to thermally assisted flux flow effects (cf. section (3.3), eq. (3.26)):

$$\eta = \frac{B^2}{\varrho_{FF}} \approx \frac{BB_{c2}}{\varrho_n} \tag{3.33}$$

η depends on the upper critical magnetic field B_{c2}, the equilibrium induction B and the

resistivity ϱ_n in the normal conducting state. This yields for the diffusion constant D:

$$D(T) = \frac{H\varrho_n(T)}{B_{c2}(T)} \tag{3.34}$$

The diffusion equation can be solved easily, if the sample is approximated by a flat plate with thickness $2r$, ignoring the pre-existing field H_{stat}: We consider a conducting plate to which the transverse field H_{osc} is applied at $t = 0$. The distribution of the field across the plate is then described through a square wave. As time progresses, the edges and then the middle of the sample relax to the outside applied field. This corresponds to the so-called Dirichlet condition of the diffusion equation which is generally solved by a sum of cosine waves with a half period of $2r$:

$$u(x,t) = \sum_{n=1}^{\infty} D_n(\cos\frac{n\pi x}{2r})e^{\frac{-n^2\pi^2 Dt}{4r^2}} \tag{3.35}$$

where $n = 1, 3, 5...$ and

$$D_n = \frac{2}{2r}\int_0^{2r} f(x)\cos\frac{n\pi x}{2r}\mathrm{d}x \tag{3.36}$$

with the initial condition $f(x, t = 0)$.

The Fourier components thereby decay *independently* with a characteristic time $\propto 1/n^2$, so that after a short time, only the fundamental remains. This yields for the relaxation time for the mode with $n = 1$

$$\tau = -\frac{4r^2}{D\pi^2}\,. \tag{3.37}$$

For a sample of cylindrical shape and radius r with the magnetic field applied perpendicular to the cylinder axis, the resulting diffusion constant for a *rotation* of the magnetic field with respect to the cylinder axis was calculated by Brandt [12]. The resulting relaxation time is

$$\tau_r \approx \frac{r^2}{(2.405)^2 D} \tag{3.38}$$

where $x_0 = 2.405$ is the first node in the Bessel function $J_0(x)$.

Vortex Lattice Relaxation Process

We start with a qualitative description of the diffusion process of the vortex lattice. As the repetition cycle of $H_{osc} = 0.2\,\mathrm{Hz}$ is slow compared to the involved relaxation processes τ_1, τ_1', τ_2 and τ_3 of the vortex lattice, a complete relaxation can be presumed for each measurement cycle of the stroboscopic measurement, i.e. the vortex lattice is in an equilibrium state before each change of magnetic field direction.

We assume that the vortex lattice has relaxed for $\mu_0 H_{osc} = 5\,\mathrm{mT}$. The vortex lattice thus does not satisfy the Bragg condition. No scattering intensity is observed at detector for $\mathbf{G_{VL}}$. We then consider the next cycle of the stroboscopic measurement where $\mu_0 H_{osc} =$

5 mT is decreased to $\mu_0 H_{osc} = 0$ mT: The vortex lattice firstly interacts with the changed magnetic field direction at the surface of the sample. The perturbance then diffuses into the sample. The vortex lattice relaxates *into* the Bragg condition, the scattering intensity at the detector thus increases. The relaxation of the vortex lattice from the equilibrium position for $\mu_0 H_{osc} = 5$ mT (and thus $\epsilon = 2°$) to $\mu_0 H_{osc} = 0$ mT (and thus $\epsilon = 0°$) yields a large displacement $u \gg \lambda'$ of the vortices. This relaxation process is characteristic of a slow exponential relaxation with the timescales τ_1 and τ_1' as defined in the previous section. The temperature and magnetic field dependence of τ_1 and τ_1' was given in Fig 3.32, panel (i).

We now assume that the vortex lattice has relaxed for $\mu_0 H_{osc} = 0$ mT, giving rise to maximum scattering intensity. If the direction of the magnetic field is shifted as H_{osc} is increased from $\mu_0 H_{osc}$ =0 mT to 5 mT, the vortex lattice again interacts with the changed magnetic field direction at the surface of the sample. The perturbance diffuses into the sample, the vortex lattice is pulled out of the Bragg condition, the scattering intensity at the detector decreases. After τ_3, the intensity has decreased to $1/e$ of its initial value. τ_3 is thus a measure for the time-scale when the perturbance of the vortex lattice propagates across the complete sample [10].

Vortex Lattice Tilt Modulus c_{44}

According to the diffusion model introduced by Kes [13] and Brandt [117, 12] for uniform distortions, the vortex lattice tilt modulus c_{44} can be derived from τ_1 and τ_3 using the eqs. (3.32), (3.33), (3.34) and (3.38). The temperature dependence of $\varrho_n(T)$ thereby is given by eq. (3.28) as introduced in section (3.5). It is depicted in Fig. 3.33, panel (i). The characteristic properties of the equilibrium induction B were derived in section (3.4). B is inferred from the modulus of the reciprocal lattice vector $|\mathbf{G}_{VL}|$ of the vortex lattice according to eq. (2.24). Its temperature and magnetic field dependence is given in Fig. 3.33, panel (ii).

The temperature and field dependence of $c_{44}^{\tau_1}(T, H)$, calculated from the measured values of τ_1, $c_{44}^{\tau_1'}(T, H)$ calculated from the measured values of τ_1' and $c_{44}^{\tau_3}(T, H)$, calculated from the measured values of τ_3 is given in Fig. 3.34, panel (i) and panel (ii), respectively.

Only two data points could be obtained for $c_{44}^{\tau_1}(T, H)$ at $\mu_0 H = 100$ mT for $T = 4$ K and $T = 6.5$ K from the *time resolved rocking scans*. $c_{44}^{\tau_1}$ shows increasing vortex stiffness with increasing temperature, increasing from $c_{44}^{\tau_1} \approx 1 \cdot 10^4$ TAm^{-1} for $T = 4$ K to $c_{44}^{\tau_1} \approx 1.4 \cdot 10^4$ TAm^{-1} for $T = 6.5$ K.

The vortex lattice tilt modulus $c_{44}^{\tau_1'}(T, H)$ shows increasing vortex lattice stiffness with increasing magnetic field. For a temperature of $T = 4$ K and a magnetic field of $\mu_0 H$ =135 mT $c_{44}^{\tau_1'}$ yields $c_{44}^{\tau_1'} \approx 1 \cdot 10^4$ TAm^{-1}. For a temperature of $T = 4$ K and magnetic fields of $\mu_0 H$ =75 mT and $\mu_0 H$ =100 mT the vortex lattice tilt modulus $c_{44}^{\tau_1'} \approx 0.3 \cdot 10^4$ TAm^{-1}.

[10] Strictly speaking, the perturbance propagates through the sample from both sides as the geometry is symmetric.

Moreover, for magnetic fields $\mu_0 H$ =75 mT and $\mu_0 H$ =135 mT, $c_{44}^{\tau_1'}$ exhibits a weak decrease by a factor of two for increasing temperature from $T = 4$ K to T_c. In contrast, for $\mu_0 H$ =100 mT $c_{44}^{\tau_1'} = 0.3 \cdot 10^4$ TAm^{-1} shows no temperature dependence.

$c_{44}^{\tau_3}(T, H)$ also shows increasing vortex lattice stiffness with increasing magnetic field. However, no significant temperature dependence is observed. Due to $\tau_1' \gg \tau_3$, $c_{44}^{\tau_3}$ yields $c_{44}^{\tau_3} \approx 5.5 \cdot 10^4$ TAm^{-1} for $\mu_0 H$ =135 mT, $c_{44}^{\tau_3} \approx 2.5 \cdot 10^4$ TAm^{-1} for $\mu_0 H$ =100 mT, and $c_{44}^{\tau_3} \approx 2 \cdot 10^4$ TAm^{-1} for $\mu_0 H$ =75 mT.

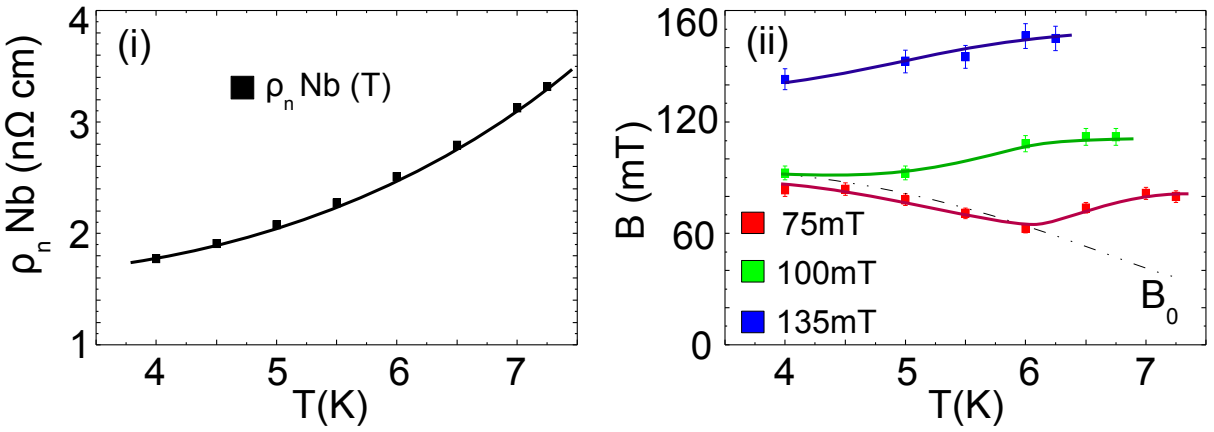

Figure 3.33: Panel (i) depicts the resistivity of niobium in the non-superconducting state in the pure limit for a residual resistivity ratio of $\sim 10^4$ according to Berthel [126]. The temperature dependence of the equilibrium magnetization B is given in panel (ii) for $\mu_0 H = 75$ mT, 100 mT and 135 mT. The lines serve as guide to the eye.

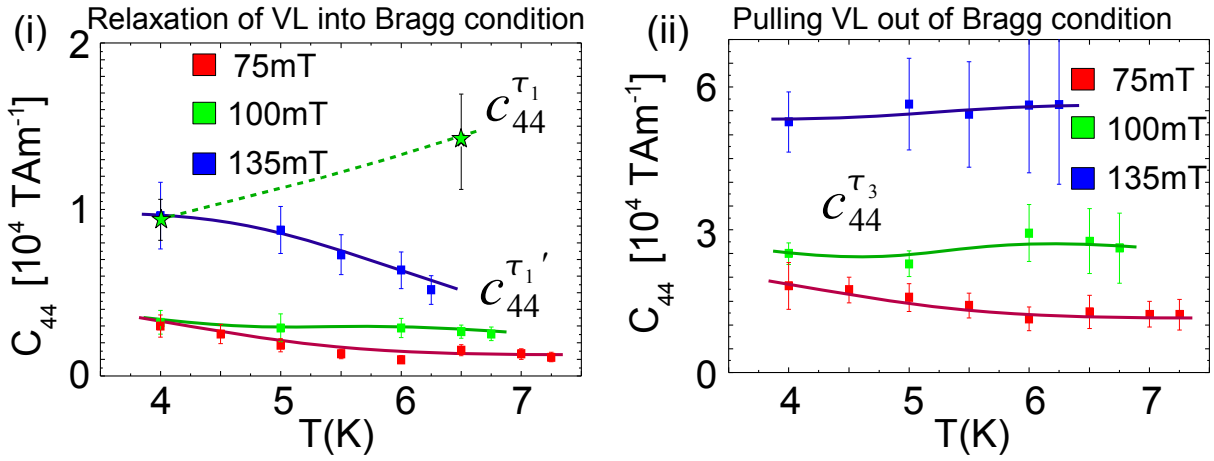

Figure 3.34: Panels (i) and (ii) show the calculated temperature and magnetic field dependence of the vortex lattice tilt modulus $c_{44}^{\tau_1}(T, H)$, $c_{44}^{\tau_1'}(T, H)$ and $c_{44}^{\tau_3}(T, H)$, according to the model of Brandt [12]. The lines serve as guide to the eye.

The expected temperature and magnetic field dependence of c_{44}, calculated from literature values of niobium is given in Fig. 3.35, panel (i). The calculated diffusion time τ_D is

given in panel (ii). Again, the temperature and magnetic field dependence of the equilibrium induction B as given in Fig. 3.33, panel (ii), and the normal conducting resistivity ϱ_n (panel (i)) are used. The effects of thermal depinning have been neglected. For a magnetic field of $\mu_0 H$ =135 mT c_{44} assumes a value of $1.7{\cdot}10^4\,\mathrm{TAm}^{-1}$, for $\mu_0 H$ =100 mT c_{44} =$0.8{\cdot}10^4\,\mathrm{TAm}^{-1}$ and finally for $\mu_0 H$ =75 mT $c_{44} = 0.6 \cdot 10^4\,\mathrm{TAm}^{-1}$. The calculated temperature dependence of c_{44} is weak for all fields and reflects the temperature dependence of the equilibrium induction B.

A qualitative agreement between the theoretical value of $c_{44}(T,H)$ and the measured values of $c_{44}^{\tau_1}(T,H)$, $c_{44}^{\tau_1'}(T,H)$ and $c_{44}^{\tau_3}(T,H)$ is observed: At first, the magnetic field behaviour which was observed is consistent with an increased vortex lattice stiffness c_{44} for increasing field, according to eq. (3.25). The most accurate agreement is obtained for $c_{44}^{\tau_1}(T,H)$. The origin of the slight deviation is most likely due to uncertainties of the extrapolation of the normal conducting resistivity ϱ_n to low temperatures, associated with the extrapolation of the residual resistivity ratio. Moreover, the involvement of the shear modulus c_{66} in the relaxation process is still unclear. The shear modulus is responsible for the perfection of the *local structure* of the vortex lattice. However, no azimuthal smearing of the scattering pattern was observed *during* the relaxation process of the vortex lattice, indicating a loss of long range order akin to a melting transition of the vortex lattice. The values $c_{44}^{\tau_1'}(T,H)$ are undersized by a factor two from the expected values. In contrast, the values for $c_{44}^{\tau_3}(T,H)$ exceed the calculated values by a factor of 3.5. This deviation is presumably resulted by the definition, used for τ_1' and τ_3.

We have introduced in the previous paragraphs that the Fourier modes of the vortex lattice relaxation decay independently with a time constants $\propto 1/n^2$. Note, that the values of τ_1 exceed τ_3 by a factor of approximately two to three. Whereas the fundamental

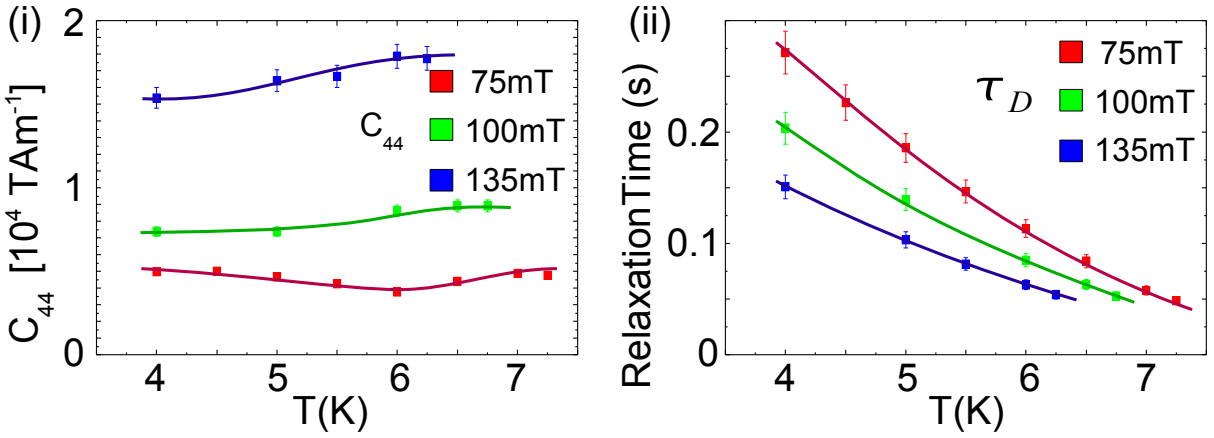

Figure 3.35: The vortex lattice tilt modulus c_{44} calculated of literature values is plotted in panel (i), whereas panel (ii) yields the calculated timescale for the diffusion of a vortex lattice distortion in a cylindric niobium sample, according to the model of Brandt [12]. The lines serve as guide to the eye.

relaxation mode τ_1 may be easily identified with the Fourier mode for $n = 1$ [11], the values obtained for τ_3 suggest that the corresponding relaxation process is a mixture of several different mechanisms. This leads to the following picture of the vortex lattice relaxation, schematically given for a half-infinite sample in Fig. 3.36, already accounting for most the observed features:

- In general, a faster propagation of perturbations in the vortex lattice is observed for increasing temperatures and increasing magnetic fields. This general behaviour is explained by the decreased damping η for increasing temperature, according to an increase of $\varrho_n(T)$ with T as given in eq. (3.33) and increasing vortex lattice stiffness c_{44} with increasing field according to $c_{44} = BH$.

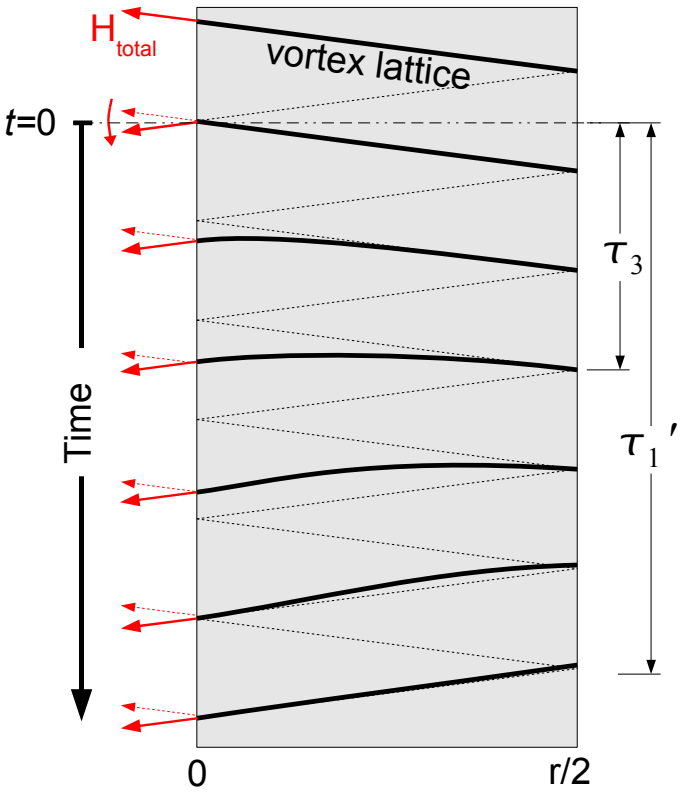

Figure 3.36: Schematic depiction of the vortex lattice diffusion and relaxation for a tilting of the magnetic field direction with respect to the vortex lattice. The vortex lattice relaxation is solely shown for the left half of the sample due to symmetry considerations. The magnetic field direction is switched at $t = 0$, the propagation of the initial perturbance through the sample is given as function of time: τ_3 is a measure for the time-scale, when a distortion of the vortex lattice has traveled through the sample. The complete relaxation of the vortex lattice into the new equilibrium position is given by τ_1'. The refraction of the magnetic field direction at the surface of the sample has been neglected.

- The *time resolved rocking scans* show that at high temperatures and high magnetic fields in the Shubnikov phase, the vortex lattice responds to the changed magnetic

[11] After a certain time, only the fundamental mode survives.

field direction as a whole, stiff lattice with its motion characterized by the diffusion constant D. A single, exponential relaxation is thus observed.

- In contrast, due to the low stiffness and strong damping for low temperatures and fields in the intermediate mixed state, the macroscopic relaxation is typical of a slow exponential relaxation with large mosaic spread which is characterized by an additional fast process on a short timescale. This is attributed to the decomposition of the vortex lattice into vortex lattice (Shubnikov) domains and Meissner phase domains in the intermediate mixed state, including a branching of the Shubnikov domains at the surface of the sample. The origin of the additional fast process will be discussed below.
- The macroscopic relaxation of the vortex lattice between the two equilibrium positions is associated with a large vortex displacement. It is strongly dependent on the vortex lattice topology, as the crossover from the intermediate mixed state to the Shubnikov phase is reflected in the mere temperature dependence of τ_1'.
- τ_3 is a measure for the time of a vortex lattice distortion propagating through the sample. No signature of the transition from intermediate mixed state to the Shubnikov phase is observed in the temperature and magnetic field dependence of τ_3 which is thus insensitive to the vortex lattice topology.

Vortex Lattice Relaxation in the Intermediate Mixed State

The intermediate mixed state is characterized by an increased mosaicity of the vortex lattice (cf. Fig. 3.26). In addition, for very short time-scales directly after the magnetic field direction is changed, certain characteristic features show up exclusively for data points, situated in the intermediate mixed state: Typical data of the relaxation process for $T = 4\,\mathrm{K}$ and $\mu_0 H = 100\,\mathrm{mT}$ in the intermediate mixed state is shown in Fig. 3.37. The time range displayed corresponds to a short time-scale after the magnetic field direction was changed. In the *time resolved rocking scan* (panel (i)), a sharp increase of mosaicity shows up which is associated with a sharp increase of intensity observed in the *fixed angle scans* for the equilibrium position at $\phi = 2.75°$ (panel (ii)). We note, that the characteristic time-scale of this feature is well below τ_3 for all temperatures and fields in the intermediate mixed state.

We have introduced in the previous sections, that τ_3 is a measure for the time, necessary for a perturbation of the vortex lattice to cross the sample from both sides. This locates the related relaxation process — responsible for the sharp increase of intensity and mosaicity — at the surface of the sample. This effect is therefore attributed to branching of the Shubnikov domains at the surface of the sample in the intermediate mixed state (cf. Fig. 3.8). The branching of Shubnikov domains leads to a fine vortex lattice structure at the surface, consisting of connected Shubnikov domains with open topology enclosing Meissner islands. In particular, no rigid vortex lattice is observed. Branching of the vortex lattice is responsible for the large intrinsic mosaicity as well.

As remaining feature, we now discuss the characteristic delay τ_2 when the vortex lattice

is *pulled out* of the Bragg condition for $\mu_0 H_{osc}$ increasing from $\mu_0 H_{osc}$ =0 mT to 5 mT. Fig. 3.37 shows typical data of the relaxation process for a short time-scale after the magnetic field direction was changed: The delay τ_2 =30 ms is visible in both the *time resolved rocking scan* (panel (i)) and the corresponding *fixed angle scan* for $\phi = 0.5°$. Note, that $\tau_2 \neq 0$ solely for data points in the intermediate mixed state. As described above, a sharp increase of intensity is observed simultaneously at the new equilibrium position ($\phi = 2.75°$) for these measurement points.

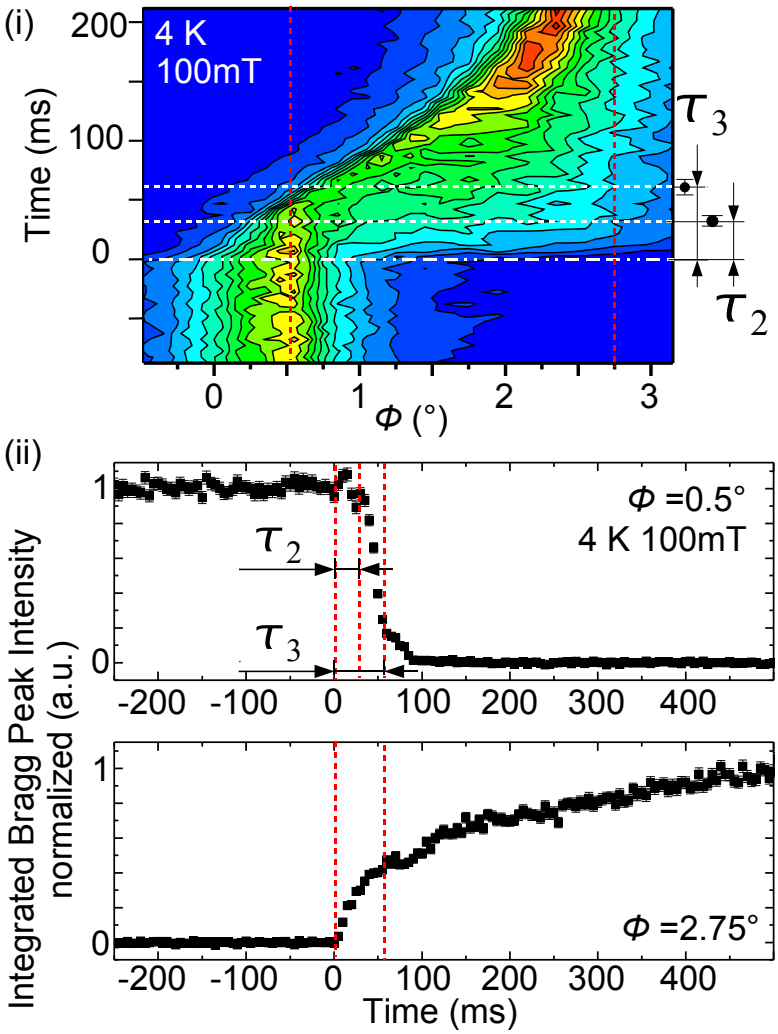

Figure 3.37: Panel (i): *Time resolved rocking scan* for T =4 K and $\mu_0 H$ =100 mT. The relaxation process of the vortex lattice is shown for a short time-scale after the magnetic field direction was switched. Panel (ii) shows the associated *fixed angle scans* for $\phi = 0.5°$ and $\phi = 0.2.75°$ as indicated with the vertical broken red lines in panel (i).

This sharp increase was attributed to a mechanism close to the surface of the sample. The intermediate mixed state is characterized by an intrinsically increased mosaicity of the vortex lattice which is caused by a bending of vortices at the surface. The scattered intensity *exactly* at the position $\mathbf{q} = \mathbf{G_{VL}} = \mathbf{k}_i - \mathbf{k}_f$ is caused by the vortex lattice which points to the initial equilibrium position, thus which is *not* bent due to branching. τ_2

thus describes the delayed reaction of the unbranched vortex lattice buried beneath the surface of the sample.

3.7.5 Conclusion and Outlook

In our study, we are able to show that it is possible to measure the intrinsic dynamic properties of bulk vortex lattices with time resolved stroboscopic small angle neutron scattering combined with a time varying magnetic field setup. We have shown that the qualitative magnetic field and temperature dependent behaviour of the vortex lattice for uniform distortions can be described in reasonable agreement with a diffusion model by Brandt [12, 117] and Kes [13]. The values obtained for the vortex lattice tilt modulus c_{44}, diffusivity D and damping η can be reproduced theoretically. We further argue that the topology of the vortex lattice is reflected sensitively in the associated diffusion process. This is readily seen for measurement points in the intermediate mixed state where a second, very fast relaxation process is attributed to branching of the vortex lattice domains at the surface of the sample. Branching was observed by previous high resolution decoration techniques on bulk niobium single crystal samples [152, 151]. To model the relaxation of the vortex lattice, computer simulations of the diffusion process are in progress.

This study represents a show-case how to access directly vortex lattice melting and the formation of vortex glass states in unconventional superconductors, notably the cuprates, heavy-fermion systems, boro-carbide or ironarsenide systems. The possibility to precisely determine the pinning properties of vortices in future experiments on samples of varying purity is of great relevance for the research on technical applications of superconducting devices, as the pinning properties are intimately related to the maximal critical current density of superconductors.

Furthermore, the technique developed for our study is of general relevance for materials exhibiting complex forms of magnetic order, i.e. long range helical order as observed in materials without inversion symmetry [78, 166], magnetic Skyrmion lattices, as observed recently in the helimagnet MnSi [30] or colloidal magnetic suspensions and liquid crystals. However, it is expected theoretically that the characteristic time-scales — in particular of ferromagnetic materials — are significantly faster compared to the characteristic time-scales of superconducting vortex lattices.

To further increase the time resolution, the TISANE technique can be used instead of stroboscopic small angle neutron scattering [167]. TISANE is benefiting from a neutron chopper which is placed upstream of the sample position at the distance L_1 to the sample. By carefully adjusting the distances L_2 and L_1, the chopper and control parameter duty cycle frequencies and phase, a coherent summation of the scattered neutrons at the detector position in *space and time* without time smearing can be achieved. The accessible time resolution of TISANE is mainly determined by the time resolution of the detector and the opening time of the chopper system. Timescales from μs to hours are possible, closing the gap to the inelastic technique NRSE. For a detailed description, we refer to [11, 167].

Chapter 4

Skyrmion Lattices in Chiral Magnets

4.1 Introduction

In chapter (3) we have presented neutron diffraction measurements on the structural and dynamic properties of the superconducting vortex lattice in the model system niobium. However, as we have introduced in section (1), it was suspected that vortex structures similar to those of superconductors can also exist in magnetic systems [14, 15, 16, 17, 18]. We have pointed out that, in particular, systems which exhibit helical ferromagnetic order have been identified [19] as promising candidates for the emergence of such *magnetic* vortices, as these materials naturally support a rotation of magnetic moments similar to Bloch domain walls. The rotation of magnetic moments with a long periodicity leads (i) to an efficient decoupling of the magnetic structure from the underlying crystal structure and is (ii) supposed to stabilize vortex structures, similar to superconducting vortices [19, 20, 21, 22] which are stabilized by the energy, associated with a normal to superconducting interface.

Helical magnetic order can be provided through the Dzyaloshinskii-Moriya (DM) interaction [24, 23]: For otherwise ferromagnetic systems, characterized by a crystalline structure lacking inversion symmetry, the DM interaction favours a perpendicular alignment of neighbouring magnetic moments. The competition between the DM interaction and ferromagnetic coupling, favouring a parallel alignment of the magnetic moments, leads to the formation of a helical instability of the ferromagnetic order with long periodicity on atomic scales.

In this chapter, we reinvestigate the magnetic phase diagram of the archetypal weak itinerant helical magnet MnSi by means of small angle neutron scattering, where we observe a magnetic spin crystal in the so-called A-phase of MnSi: The structure of the spin crystal is characteristic of topological knots of the magnetization, arranged in a macroscopic six-fold lattice, which we identify as skyrmion lattice. This work has been published in [30] as well.

This chapter is organised as follows: In section (4.2) we start with a short introduction

into the properties of the DM interaction. Adjacent in the second part of section (4.2) we briefly present the Bak-Jensen model for MnSi, where we introduce the properties of the helical magnetic order. We then give a detailed review of the properties of MnSi in section (4.3), where we concentrate on the magnetic phase diagram at ambient pressure and its evolution under hydrostatic pressure. We finally present our small angle neutron scattering experiments in section (4.4).

4.2 Helical Magnetic Order

In the following section, we introduce the Dzyaloshinskii-Moriya (DM) interaction [24, 23] and the Bak-Jensen model [31] in greater depth. We use the DM interaction and the Bak-Jensen model to explain the long wavelength helical order in the weak itinerant ferromagnet MnSi, where we use a simplified model of localized magnetic moments. The model we use for our description is considered as the standard model of helical magnetic order with long wavelength.

4.2.1 The Dzyaloshinskii-Moriya Interaction

For a long time, the weak ferromagnetic behaviour of otherwise antiferromagnetic compounds as observed e.g. in α-Fe_2O_3 (Hematite) and the carbonates of Mn and Co has been a controversial problem. In these materials, the magnitude of their spontaneous magnetic moments is extremely small and experimentally found to vary between 10^{-2} and 10^{-5} of the expected value for ferromagnetic coupling. The small value of the ordered moment indicates, that pure ferromagnetic coupling $H = J \cdot (\mathbf{S}_i \cdot \mathbf{S}_j)$ is excluded as origin of the behaviour observed. α-Fe_2O_3 (Hematite) belongs to the rhombohedral system and exhibits the space symmetry group D^6_{3d}. The unit cell is shown in Fig. 4.1: In the unit cell, four Fe^{3+} ions are distributed over the space diagonal of the rhombohedron (which is a trigonal axis).

Upon cooling, α-Fe_2O_3 changes at the so-called Morin [168] transition at $T_m = 260\,\mathrm{K}$ from state II, characterized by weak ferromagnetism, to the state I, assuming an antiferromag-

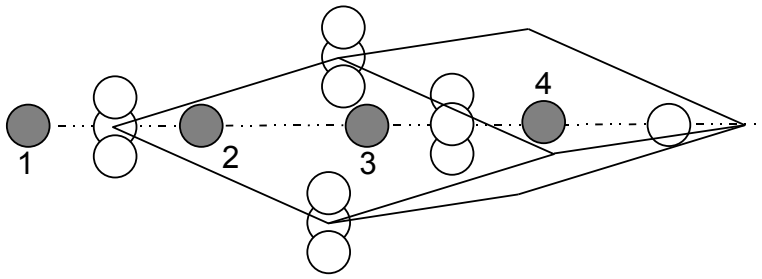

Figure 4.1: Crystal structure of α-Fe_2O_3 (Hematite). The open circles represent the O^{2-} ions and the dark circles represent the Fe^{3+} ions.

netic behaviour with vanishing spontaneous moment. Early neutron diffraction data by Shull *et al.* [169] and Brockhouse [170] showed, that the magnetic unit cell is identical to the crystalline unit cell in the antiferromagnetic state I of α-Fe_2O_3. The weak ferromagnetism of α-Fe_2O_3 in state II has been a controversial problem until Dyzaloshinskii 1958 [23] could show, that an α-Fe_2O_3 crystal in the antiferromagnetic state I, with spins along the crystalline $\langle 111 \rangle$ direction owns the same symmetry compared to a *canted* arrangement of spins. This canted arrangement exhibits a net magnetic moment perpendicular to the trigonal axis. By writing down the free energy in terms of spin variables, indicating four magnetic sublattices and by an expansion of the free energy Dzyaloshinskii showed, that a coupling term

$$\mathbf{D} \cdot (\mathbf{S}_i \times \mathbf{S}_j) \tag{4.1}$$

arises, which favours a perpendicular rather than an antiferromagnetic arrangement of magnetic moments. $\mathbf{D}$ is a constant vector, which is parallel to the trigonal axis in α-Fe_2O_3. The theory by Dzyaloshinskii however is based on purely phenomenological considerations and does neither explain the origin of the observed coupling nor how the vector $\mathbf{D}$ can be calculated.

In 1960 Moriya [24] was able to show that the coupling term eq. (4.1) naturally arises, extending the theory by Anderson [171] for anisotropic superexchange by taking the spin orbit coupling into account: Moriya could prove that when the symmetry of the crystal structure is sufficiently low, the largest term of the anisotropic superexchange which is linear in the spin-orbit coupling, has the antisymmetric form as reported earlier by Dyzaloshinskii [23]. It was further recognized by Moriya that the crystal symmetry is of particular importance for the magnetic coupling described by eq. (4.1): In actual crystals, some components of the symmetric or antisymmetric coupling tensors disappear due to the crystal symmetry. The following simple symmetry rules were derived for the orientation of the coupling vector $\mathbf{D}$. Imagine a crystal structure with two spins located at the points A and B. The point bisecting the line AB is denoted C:

1. When a centre of inversion is located at C,

$$\mathbf{D} = 0\,.$$

2. When a mirror plane perpendicular to AB passes through C,

$$\mathbf{D} \parallel \text{mirror plane or } \mathbf{D} \perp AB\,.$$

3. When there is a mirror plane including A and B,

$$\mathbf{D} \perp \text{mirror plane}\,.$$

4. When a two-fold rotation axis perpendicular to AB passes through C,

$$\mathbf{D} \perp \text{two fold axis}\,.$$

5. When an n-fold rotation axis ($n \leq 2$) is oriented along AB,

$$\mathbf{D} \parallel AB$$

For a Fe^{3+} - Fe^{3+} pair in α-Fe_2O_3 along the three-fold axis, this leads to the following orientation of **D**: **D** is parallel to the trigonal axis for the Fe^{3+} ions (1 or 4) and (2 or 3), whereas **D** is zero for the other pairs. This causes a non-zero coupling between the four sub-lattices of α-Fe_2O_3 with the coupling parameter **D** parallel to the trigonal axis, leading to a *canting* of the sublattices. A magnetic coupling as described by eq. (4.1) is hence called *Dzyaloshinskii-Moriya* interaction.

4.2.2 The Bak-Jensen Model

We have introduced in the previous sections, that the DM interaction may lead to a helical instability of ferro- and antiferromagnets, if allowed by a particular crystal symmetry, whereas evidence of such helical structures was still lacking for a long time. In 1980 Bak and Jensen [31] proved, that the long range helical ordering, observed by neutron diffraction experiments in the weak ferromagnet MnSi and in the cubic phase of FeGe by Hansen 1977 [172] and Ishikawa *et al.* 1979 [173] is due to a DM instability:

In MnSi, a left handed helical order with a pitch of λ_h=180 Å ($\sim 0.035\,\text{Å}^{-1}$) oriented along the crystalline $\langle 111 \rangle$ directions was identified. FeGe exhibits a pitch of λ_h=700 Å. MnSi as well as FeGe crystallize in the cubic B20 ($P2_13$) structure, lacking inversion symmetry. A depiction of the corresponding chemical unit cell of MnSi is given in Fig. 4.4.

The central point of the model, introduced by Bak and Jensen for MnSi and FeGe is an expansion of the free energy in terms of a slowly varying spin density $\mathbf{S}(\mathbf{r})$. Following the theory of phase transitions by Landau and Lifshitz, especially taking into account the crystal symmetry it follows for the free energy

$$\begin{aligned} F(\mathbf{r}) = & \frac{1}{2}A(S_x^2 + S_y^2 + S_z^2) + D\mathbf{S}(\nabla \times \mathbf{S}) \\ & + \frac{1}{2}B_1[(\nabla S_x)^2 + (\nabla S_y)^2 + (\nabla S_z)^2] \\ & + \frac{1}{2}B_2\left[\left(\frac{\partial S_x}{\partial x}\right)^2 + \left(\frac{\partial S_y}{\partial y}\right)^2 + \left(\frac{\partial S_z}{\partial z}\right)^2\right] \\ & + C(S_x^2 + S_y^2 + S_z^2)^2 + E(S_x^4 + S_y^4 + S_z^4)\,, \end{aligned} \tag{4.2}$$

which is the most general expression up to fourth order in spin and to second order in gradients. Note, that this expression is invariant with respect to the symmetry operations of the space group of MnSi and FeGe, B20 ($P2_13$). The term A represents the ferromagnetic exchange, the term D stands for the DM interaction destabilizing the ferromagnetic order and the terms B_1 and B_2 represent first and second order anisotropy terms. D is a small correction, compared to the other second order terms. In the absence of D and for positive B_1 and B_2, a minimization of $F(\mathbf{r})$ leads to an uniform $\mathbf{S}(\mathbf{r})$ (ferromagnetic coupling).

Near to the transition temperature T_c the free energy is minimized by periodic structures of the form

$$\mathbf{S}(\mathbf{r}) = \frac{1}{\sqrt{2}}[\mathbf{S}_\mathbf{k} e^{i\mathbf{kr}} + \mathbf{S}_\mathbf{k}^\star e^{-i\mathbf{kr}}]\,. \tag{4.3}$$

If eq. (4.3) is inserted into eq. (4.2), Bak and Jensen obtain (to second order in $\mathbf{S}_\mathbf{k}$)

$$\begin{aligned} F(\mathbf{k}) = &\frac{1}{2}A|\mathbf{S}_\mathbf{k}|^2 + iD\mathbf{k}(\mathbf{S}_\mathbf{k} \times \mathbf{S}_\mathbf{k}^\star) \\ &+ \frac{1}{2}B_1 k^2 |\mathbf{S}_\mathbf{k}|^2 \\ &+ \frac{1}{2}B_2(k_x^2|\mathbf{S_{kx}}|^2 + k_y^2|\mathbf{S_{ky}}|^2 + k_z^2|\mathbf{S_{kz}}|^2)\,. \end{aligned} \tag{4.4}$$

With $\mathbf{S}_\mathbf{k} = \alpha_\mathbf{k} + i\beta_\mathbf{k}$, they find that eq. (4.4) is minimized if $\alpha_\mathbf{k} \perp \beta_\mathbf{k}$, $|\alpha_\mathbf{k}| = |\beta_\mathbf{k}|$ and $\mathbf{k}$ antiparallel to $\alpha_\mathbf{k} \times \beta_\mathbf{k}$ for $D > 0$. For $D < 0$, $\mathbf{k}$ is parallel to $\alpha_\mathbf{k} \times \beta_\mathbf{k}$. Both possibilities represent a left-handed or right-handed spiral arrangement of magnetic moments, respectively. As the term D owns full rotational symmetry, no preferential orientation of the wavevector (or propagation vector) $\mathbf{k}$ is inferred. Nevertheless, the direction of the propagation vector $\mathbf{k}$ is defined by the anisotropic second-order gradient term with its coefficient B_2:

$$\begin{aligned} B_2 < 0 \;&: \mathbf{k} \parallel \langle 111 \rangle \\ B_2 > 0 \;&: \mathbf{k} \parallel \langle 100 \rangle \end{aligned} \tag{4.5}$$

Neutron diffraction results by Ishikawa *et al.* [173] on MnSi and Hansen [172] on FeGe show, that MnSi and FeGe exhibits $B_2 < 0$, as the propagation vector $\mathbf{k}$ of the helical order is aligned in the crystalline $\langle 111 \rangle$ directions. However, for FeGe a reorientation to the crystalline $\langle 100 \rangle$ axes was observed as function of decreasing temperature below $T_2 \sim 211 - 245\,\mathrm{K}$. In addition, the parameter B_2 is small as the propagation vector $\mathbf{k}$ can

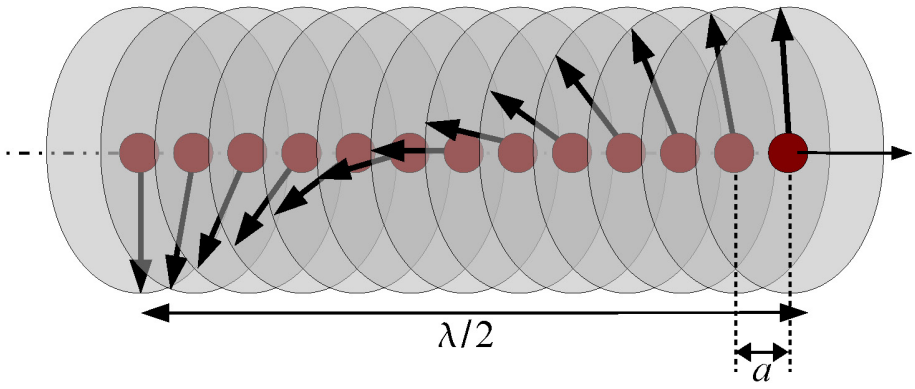

Figure 4.2: Schematic depiction of a helical magnetic structure with a wavelength of λ. The individual magnetic moments are aligned perpendicular to the propagation vector $\mathbf{k}$. Only the half pitch of the helix is shown. The given helical order is incommensurate, i.e. its pitch λ_h in no integer multiple of the lattice constant a.

be rotated into the magnetic field direction by a small applied magnetic field ($\sim 0.1\,\mathrm{T}$ for MnSi). Bak and Jensen finally obtain for the free energy

$$F(k) = (\frac{1}{2}A - |D|k)|\mathbf{S_k}|^2 + (\frac{1}{2}B_1 + \frac{1}{6}B_2)k^2|\mathbf{S_k}|^2 \tag{4.6}$$

which is minimized by

$$k = \frac{|D|}{B_1 + \frac{1}{3}B_2}\,. \tag{4.7}$$

The spin structure can then be expressed conveniently in terms of real vectors in the form

$$\mathbf{S}(\mathbf{r}) = \alpha_k \cos(\mathbf{kr}) - \beta_k \sin(\mathbf{kr}) \tag{4.8}$$

describing a long wavelength helical spiral as given in Fig. 4.2. The helix in MnSi and FeGe is incommensurate, i.e. the pitch of the helical order λ_h is no integer multiple of the crystal lattice constant a.

The small value of $\mathbf{k}$ and the associated long pitch of the helical order in MnSi and FeGe follows from the smallness of D compared to $B_1 + \frac{1}{3}B_2$. The free energy of a left-handed ($D < 0$) and a right-handed ($D > 0$) helical structure is given in Fig. 4.3. The ferromagnetic solution $\mathbf{k} = 0$ is unstable. For comparison, the free energy of a system with inversion symmetry $D = 0$ is plotted on a broken line. Note, that the left- and right-handed solutions are degenerate, thus a further source of anisotropy is necessary to lift this degeneracy. In MnSi, as upon today, solely left-handedness was observed for the crystal structure [174] as well as for the helical magnetic structure [175, 174].

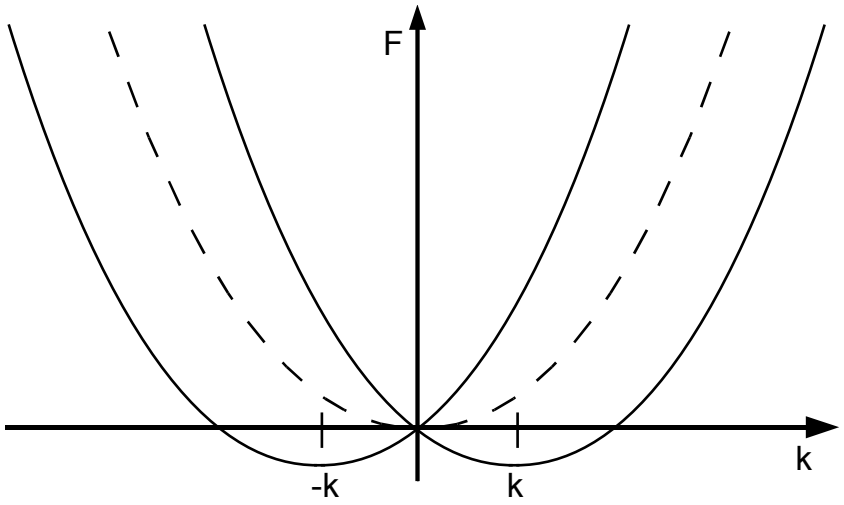

Figure 4.3: The free energy is depicted as function of wavevector $\mathbf{k}$ for left- and right-handed spirals. The broken line depicts the free energy for a system with inversion symmetry $b = 0$ (ferromagnetic order). The plot is adapted from [31].

4.3 Properties of MnSi

We have used the Bak-Jensen model [31] to explain the prerequisites for the long range helical order of the archetypal helical magnet MnSi in the previous section. In the following section, we review the properties of MnSi, where we discuss the magnetic phase diagram at ambient pressure and its evolution upon applied hydrostatic pressure [97].

4.3.1 Properties of MnSi at Ambient Pressure

The 3d intermetallic compound MnSi crystallizes in the cubic B20 structure. Its unit cell is depicted in Fig. 4.4: Four Mn and four Si atoms are located at the positions (x, x, x), $(\frac{1}{2} + x, \frac{1}{2} - x, -x)$, $(\frac{1}{2} - x, -x, \frac{1}{2} + x)$, $(-x, \frac{1}{2} + x, \frac{1}{2} - x)$ with $x_{Mn} = 0.137$ and $x_{Si} = 0.841$, respectively, giving rise to left-handed, chiral crystal structure. The transport properties of MnSi at ambient pressure are characteristic of a metal, exhibiting a quadratic temperature dependence of the electrical resistivity $\varrho(T) \propto T^{\alpha}$ $(\alpha = 2)$, as explained by the usual Fermi-liquid model [25, 176].

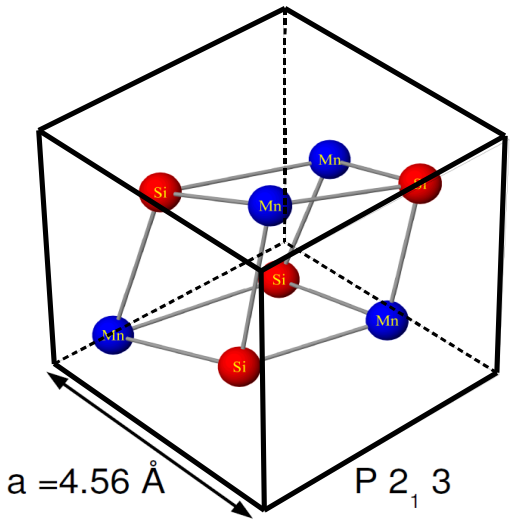

Figure 4.4: A schematic depiction of the chemical unit cell of MnSi is given. The manganese atoms are represented by the blue circles, red circles represent the silicon atoms, respectively. MnSi is characterized by a left-handed crystalline structure.

Magnetic Phase Diagram

MnSi exhibits weak itinerant helical magnetic order. The magnetic phase diagram at ambient pressure is shown in Fig 4.5. It may be comprehensively interpreted as result of the interplay of three hierarchical energy scales:

- The strongest scale is determined by weak *itinerant* ferromagnetism below a transition temperature of $T_c = 29.5\,\mathrm{K}$. MnSi is characterized by a spontaneous magnetic

moment of $0.4\,\mu_B$ per Mn atom and a fluctuating moment of $2.2\,\mu_B$ estimated from the Curie-Weiss behaviour in the paramagnetic regime [25]. The susceptibility of MnSi follows a Curie-Weiss law over a large temperature range above T_c, a behaviour normally viewed as more characteristic of the conventional Heisenberg model.

In contrast to large moment canted ferro- or antiferromagnets described by a classical Heisenberg exchange (including the DM interaction), weak itinerant ferromagnets exhibit a small T_c, and a small localized but large fluctuating moment so that p_{eff}/p_0 is larger than unity. The qualitative behaviour of weak itinerant ferromagnets was explained by Lonzarich and Taillefer 1985 [25] by means of an extended Stoner theory including enhanced fluctuations in the local magnetization: In particular, Lonzarich and Taillefer perform a self-consistent renormalization of the linear response, taking into account the effects of interactions, causing non-linear behaviour and magnetic order. The transition temperature of MnSi and the size of the ordered moment can be quantitatively explained by the model of Lonzarich and Taillefer.

- The formation of the helical order of MnSi was derived in section (4.2) using the symmetry considerations by Dzyaloshinskii [23] and Moriya [24] and the theoretical model by Bak and Jensen [31]: Due to the relative smallness of the DM interaction compared with the ferromagnetic exchange, an incommensurate helical order with a long periodicity of $\lambda \sim 180\,\text{Å}$ emerges.
- We have furthermore derived in section (4.2) that the propagation vector $\mathbf{k}$ of the helices in MnSi is locked to a crystalline $\langle 111 \rangle$ direction by the weakest energy scale, represented by cubic crystal field anisotropy.

The magnetic phase diagram of MnSi — as given in Fig 4.5 — comprises three distinct phases: In the helical phase below $T_c = 29.5\,\text{K}$ and below H_{c1} with $\mu_0 H_{c1}(T \to 0) = 0.1\,\text{T}$ (represented by the medium blue region), numerous small angle neutron scattering studies established a left-handed helical order [172, 173, 177, 29]. Four degenerate helical domains are observed corresponding to the four crystalline $\langle 111 \rangle$ directions, each giving rise to scattering in $\pm\mathbf{k}$.

For magnetic fields exceeding $\mu_0 H_{c1} = 0.1\,\text{T}$, the helices unpin and their propagation vector $\mathbf{k}$ starts to realign in the direction of the magnetic field. This phase is called conical phase (indicated by the light blue shading) as the helix is simultaneously deformed into a conical helix, as observed by Ishikawa *et al.* [173]. With increasing field, the helices align more and more into the direction of the magnetic field, leading to a single domain state. In addition, the cone angle decreases for increasing field until a fully field polarised state is reached at the upper critical field H_{c2} with $\mu_0 H_{c2}(T \to 0) = 0.6\,\text{T}$. The field polarised ferromagnetic state exhibits a spontaneous moment of $0.4\,\mu_B$ per Mn site. Note, that the modulus of the propagation vector $\mathbf{k}$ of the helical order shows only slight changes as function of temperature T or magnetic field H.

Close to the transition temperature T_c and at $\sim 1/2 H_{c2}$, an additional phase is observed, denoted as A-phase (shaded in dark blue), separated by weak first order phase boundaries inferred from measurements of the AC susceptibility, the specific heat [26], and torque magnetometry [178]. Small angle neutron scattering experiments established that the

propagation vector **k** of the helical order aligns perpendicular to the direction of the applied magnetic field in the A-phase [177, 27, 28, 29]. The data was interpreted for a long time that the A-phase is characterized by a single **k** helix.

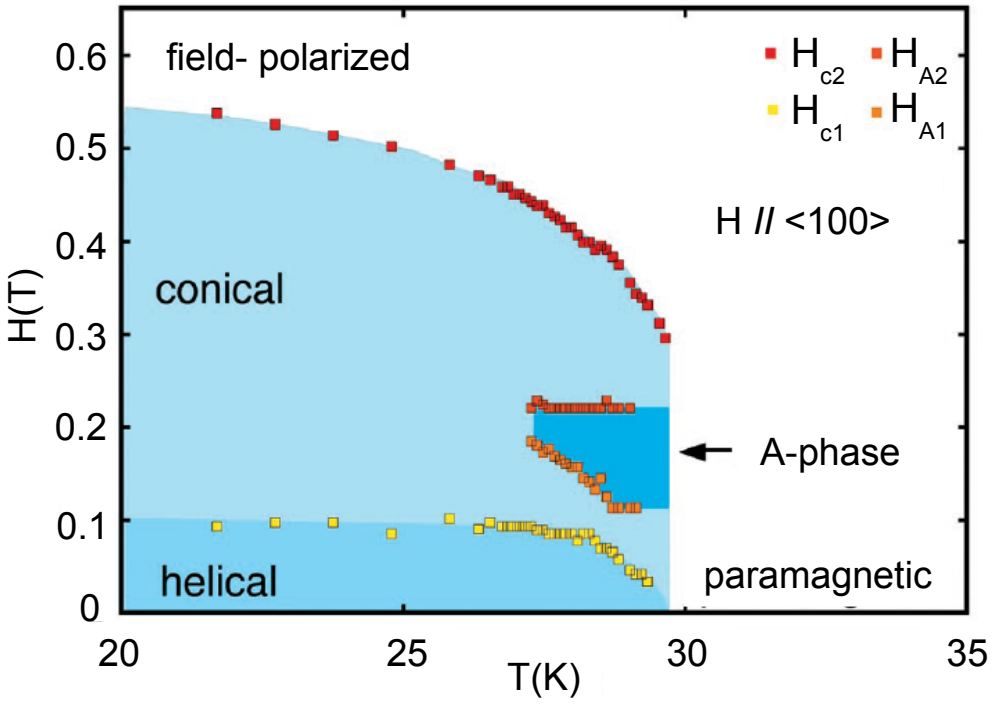

Figure 4.5: Magnetic phase diagram of MnSi at ambient pressure as function of temperature T and applied magnetic field H parallel to a crystalline $\langle 100 \rangle$ direction. The phase diagram for H along the crystalline $\langle 110 \rangle$ and $\langle 110 \rangle$ directions is qualitatively identical, whereas the temperature regime of the A-phase slightly differs. Plot adopted from [30]. For details see text.

Possible Intermediate Phase at T_c

Measurements of the specific heat C of MnSi at zero magnetic field [95, 179] show that the temperature dependence of C exhibits a characteristic lambda-shaped peak at T_{c1}, associated with the breakdown of the long-range helical order. Typical data is given in Fig. 4.6, panel (i). Moreover, a pronounced shoulder is observed at T_{c2}, approximately 1 K above the transition temperature T_{c1}. Measurements of different samples indicate a significant dependence of the shape of the shoulder at T_{c2} on the purity of the samples [180].

Small angle neutron scattering experiments in zero magnetic field [112, 181, 95, 96] show a ring of intensity emerging in vicinity of T_c where the $|\mathbf{q}|$-vector of the ring is identical to $|\mathbf{k}|$. Typical data is shown in Fig. 4.6, panel (ii) for a temperature of $T = 29.6$ K. The temperature range where the ring is observed approximately corresponds to the anomaly in specific heat. Further measurements [96] reveal that the ring of intensity represents a cut through a homogeneous sphere in reciprocal space with radius $|\mathbf{k}|$. Integrating the intensity of the sphere thereby approximately yields the extrapolated intensity of

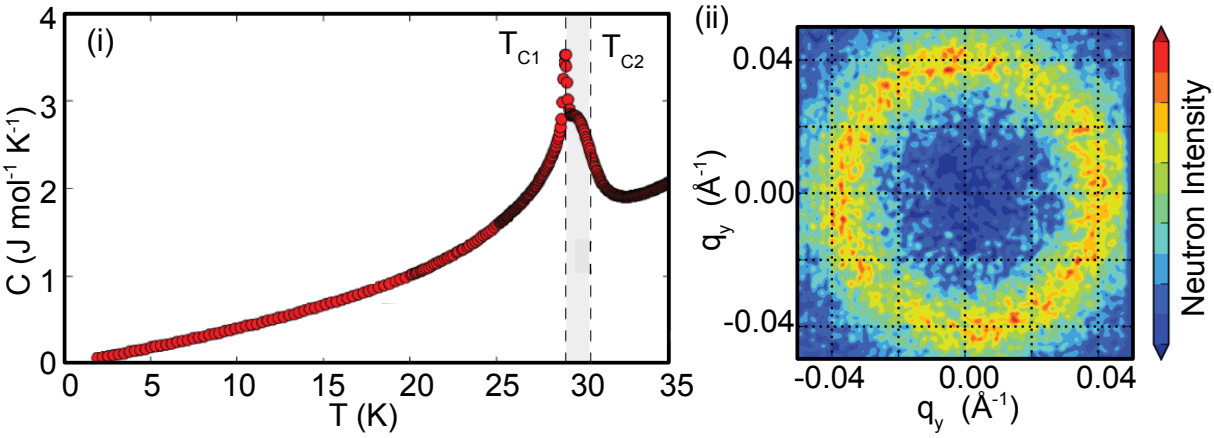

Figure 4.6: Panel (i): Specific heat C of MnSi as function of temperature in zero magnetic field as reported in [96]. Panel (ii): Small angle scattering pattern of MnSi at zero magnetic field for T =29.6 K, taken from [96]. For details see text.

the helical phase for $T \to 0$. Recent measurements [182] using a combination of spherical neutron polarimetry and the neutron spin echo technique show that chirality is still present in the disordered state above T_c.

The microscopic origin of the behaviour in vicinity to T_c is controversly discussed, especially considering the possible existence of an intermediate phase and the connection between the ring of intensity and the specific heat anomaly: Grigoriev *et al.* [112] attribute both to critical paramagnetic scattering around the phase transition. A softening of the pinning of the helices to the cubic crystal field anisotropy was reported by Janoschek [96], using the model of Maleyev [183]. This leads to randomly disordered helices, explaining the observed sphere in reciprocal space. Nevertheless, data obtained by spherical polarimetry [96] suggest that additional contributions arise besides critical scattering.

4.3.2 Properties of MnSi under Hydrostatic Pressure

In the following paragraphs, we summarize the properties of MnSi as function of pressure. The phase diagram as function of hydrostatic pressure and temperature at zero magnetic field is given in Fig. 4.7, panel (i). For increasing pressure, the heli-magnetic transition temperature T_c is suppressed and assumes $T_c = 0$ at the critical pressure of p_c =15 kbar. The character of the phase-transition thereby changes from second order to weak first order at $p^\star$ =12 kbar as inferred from AC-susceptibility [184, 185].

Extended Non-Fermi-Liquid Regime

An extended region of non-Fermi-liquid (NFL) behaviour emerges for pressures above p_c [186, 187, 188]. It is characterized by an exponent of the electrical resistivity $\varrho(T) \propto T^\alpha$ with $\alpha = 3/2$. The crossover from Fermi liquid to non-Fermi-liquid behaviour is

characteristic of first order transition. The regime of the NFL behaviour (green shading in Fig 4.7 panel (i)), extends over three orders of magnitude in temperature, from few mK to $\sim 12\,\mathrm{K}$ and up to pressures of $\sim 30\,\mathrm{kbar}$. Above $\sim 45\,\mathrm{kbar}$, the exponent α starts to increase [189].

Measurements of the magnetic field dependence of the electrical resistivity [188] suggest that the NFL regime survives to fields substantially exceeding H_{c2}. Its large temperature and pressure range and the magnetic field stability naturally rises the question if the NFL state is a signature of an unknown metallic state. However, no broadly accepted explanation of the low temperature dependence of the electrical resistivity exists for MnSi [78].

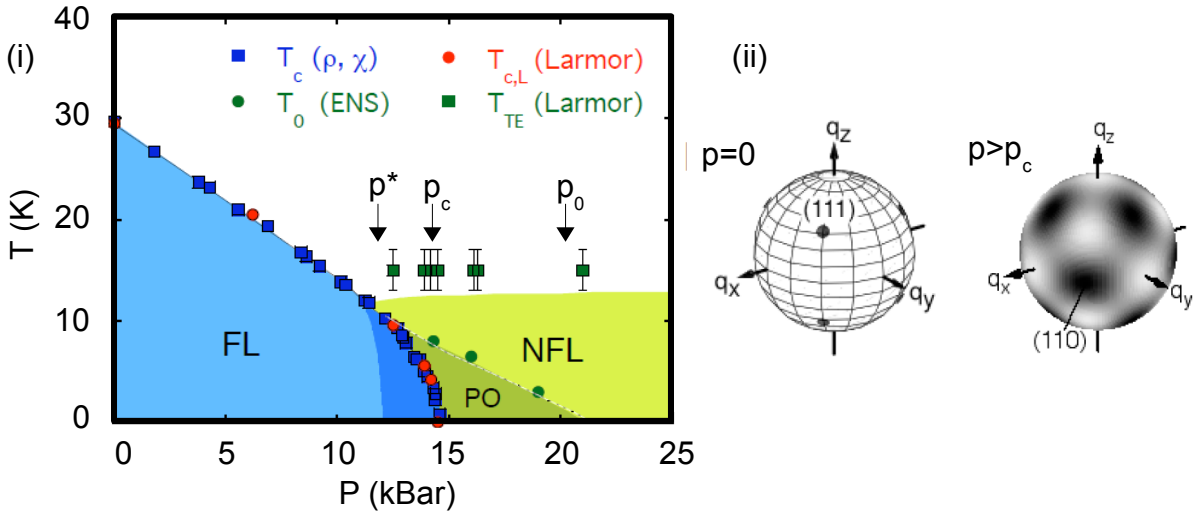

Figure 4.7: Panel (i): Phase diagram of MnSi as function of hydrostatic pressure and temperature, taken from [78]: The regime of the helical order is shaded in blue, exhibiting the typical fermi liquid behaviour of a metal. Under pressure, a partial order (PO) seen in neutron scattering experiments emerges (shaded in dark blue and dark green) above the pressure $p^\star$. Between $p^\star$ and p_c, a crossover from the helical order to the partial order is observed. The partial order is embedded in an extended NFL regime. The transition temperature T_c is deduced from the susceptibility and transport measurements [185, 186]. The upper boundary T_0 of the PO is deduced from elastic neutron scattering measurements [97]. $T_{c,L}$ and T_{TE} are deduced from Lamor diffraction measurements of the thermal expansion [190]. Panel (ii): Intensity distribution in reciprocal space of the helical order in MnSi at ambient pressure and zero field (left). The propagation vectors $|\mathbf{k}|$ of the helices are aligned along the crystalline $\langle 111\rangle$ directions. Partial order in MnSi under pressure (right). For details see text.

Partial Order Above $p^\star$

A weak partial magnetic order (PO) is observed by elastic neutron scattering above $p^\star$=12 kbar. The regime of the partial order (indicated by the dark blue and dark green shading in Fig. 4.7 [97]) is significantly smaller, compared to the non-Fermi-liquid region: Between $p^\star$ and p_c, a crossover from helical order to partial order is observed, whereas

the intensity of the helical order tracks T_c as function of pressure which is not the case for the partial order. μSR measurements [191] showed signs of phase segregation, indicated in the dark blue shading in Fig. 4.7, panel (i). The partial order gradually disappears for increasing pressure until it vanishes at p_0=20 kbar.

The partial order is characterized by a smooth distribution of intensity on the surface of a small sphere in reciprocal space with radius **k**. The intensity distribution shows weak, smeared-out maxima in the crystalline $\langle 110 \rangle$ directions, given in Fig. 4.7, panel (ii) [1]. However, the value for the intensity integrated over the complete sphere is large. Further small angle neutron scattering measurements reveal a highly hysteretic magnetic field behaviour of the partial order: The scattered intensity can be aligned into the direction of the magnetic field [193]. No significant pressure dependence of the critical fields H_{c1} and H_{c2} was reported by means of small angle neutron scattering [194] data and AC susceptibility measurements [185, 26].

In addition to elastic neutron scattering, which reflects an energy resolution of $\delta E = 0.05$ meV, μSR measurements [191] show no magnetic intensity above p_c, revealing that the partial order is not static on the slower timescales probed by μSR and hence is dynamic on a time scale between $\tau = 10^{-10}$ to $\tau = 10^{-11}$ s. The upper boundary of the partial order T_0 as inferred from elastic neutron scattering is featureless in the AC-susceptibility.

4.3.3 Motivation

We have pointed out that systems exhibiting helical magnetic order have been identified as promising candidates for the existence of ferromagnetic vortices with topological properties [19, 20, 21, 22]. Both the possible intermediate phase in the proximity of T_c and the partial order above $p^\star$ have recently been interpreted in terms of magnetic spin crystals with topological properties. An introduction into the properties of such topological states has been given in section (1).

Theoretical considerations by Rössler *et al.* [18] in 2006 discuss the possible spontaneous formation of a skyrmionic groundstate at zero field for a helical magnet: In their study, an additional, purely phenomenological term stabilizes a doubly twisted, *fan-like* helical structure with varying amplitude of the magnetic moments.

Calculation by Binz *et al.* [15, 14] and Fischer [16] by means of Landau theory compare favourably with existing data on the high pressure behaviour: Binz *et al.* construct a magnetic spin crystal by means of a linear superposition of single **k** helices and calculate its stability by means of Landau theory, where they find, that the *bcc* spin crystal is favoured. Tewari *et al.* [17] evoke close analogies to the blue phases in cholesteric liquid crystals and propose that similar condensation transitions involving a chiral order parameter can occur in itinerant helimagnets.

[1] Note, that for randomly oriented helices on a sphere, an intensity pattern with maxima in the crystalline $\langle 110 \rangle$ directions is expected for MnSi, when measured near a [110] nuclear Bragg reflection due to a selection rule [192]. However, the intensity is supposed to drop to its half value, whereas the experimentally observed decrease is much faster, ruling out experimental artifacts.

We have introduced that several small angle neutron scattering studies have shown that the A-phase of MnSi is characterized by a perpendicular alignment of the propagation vector **k** and the magnetic field. However, the detailed structure of the A-phase was unclear [177, 28, 29, 95, 27]. This lack of information originated in the measurement setup where the applied magnetic field was aligned perpendicular to the incident neutron beam. With this setup, only **k**-vectors aligned parallel to the intersection line of a plane perpendicular to the field direction and a plane, perpendicular to the incident neutron beam satisfy the Bragg condition and are observable. However, it has been speculated, that *the spin structure is unlikely to be helical, it is probably either a fan or a sinusoidal structure, in which case the spins would still be perpendicular to the magnetic field* [29].

In our work, we use small angle neutron scattering to revisit the magnetic phase diagram of MnSi at ambient pressure. In particular, we focus on the structure of the A-phase. In contrast to previous studies, we choose both a perpendicular alignment of the magnetic field with respect to the incoming neutron beam as well as a parallel alignment, where we succeed to resolve the complete magnetic structure of the A-phase, a skyrmion lattice, reminiscent of a superconducting vortex lattice.

4.4 Skyrmion Lattice in the A-Phase of MnSi

In this section, we present our small angle neutron scattering study on the magnetic structure of the A-phase of the helical magnet MnSi. We give a short outline: We first explain the preparation of the samples (section (4.4.1)) and the details of the experimental setup (section (4.4.2)) which were used for our studies, before we present our experimental results in section (4.4.3) and the salient features of their interpretation by means of a Ginzburg-Landau ansatz in section (4.4.4). A detailed description of the theoretical considerations is given [30].

4.4.1 Samples Used for Investigation

For our studies, three different MnSi samples have been examined. A picture of the samples is given in Fig. 4.8: Sample I corresponds to a flat disk with a diameter of 19 mm and a thickness of $d = 3$ mm. The normal vector of the disk is slightly misaligned with respect to a crystalline $\langle 110 \rangle$ axis. Sample II has the form of a small parallelepiped with a length of 14 mm and 1.5 mm $\times$ 1.5 mm in cross section. The long axis of the parallelepiped coincides with a crystalline $\langle 110 \rangle$ direction. Sample III consists of an irregular shaped thin plate with a length of $\sim$ 14 mm, a width of $\sim$ 9 mm and a thickness of $\sim$ 1.4 mm. The normal vector of sample III is aligned in the crystalline $\langle 110 \rangle$ direction.

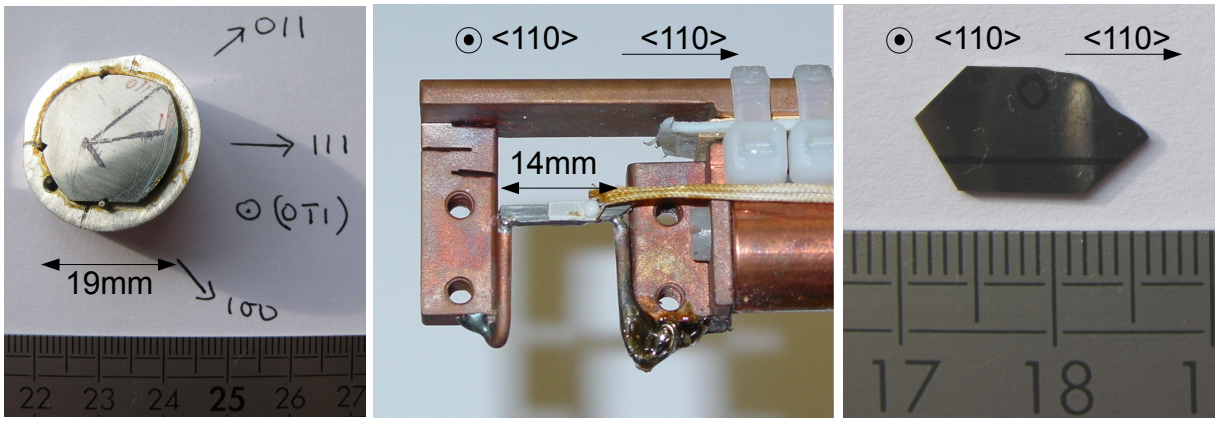

Figure 4.8: The figure shows the MnSi samples which were used for our studies: Sample I has the form of a disk with a diameter of 19 mm and a thickness of 3 mm. A crystallographic $\langle 110 \rangle$ direction is slightly misaligned with respect to the normal vector of the disk. Sample II has the form of a long parallelepiped with a length of $\sim$ 14 mm and 1.5 mm $\times$ 1.5 mm in cross section. A crystalline $\langle 110 \rangle$ direction is oriented along the long side of the parallelepiped. Sample III consists of a irregular shaped thin plate with a length of $\sim$ 14 mm, a width of $\sim$ 9 mm and a thickness of $\sim$ 1.4 mm. A crystalline $\langle 110 \rangle$ direction is oriented perpendicular to the thin plate.

The samples have been cut from a single crystalline MnSi rod using spark erosion and a diamond wire saw, respectively. The MnSi rod has been produced with the Bridgeman method using high purity starting materials. Sample I as well as other MnSi samples cut

from the rod described above have previously been studied in experiments using triple axis spectroscopy [96, 195, 196] and small angle neutron scattering, revealing excellent sample quality [96, 95]. The crystalline mosaic of sample I is $\sim 0.15°$. Measurements of specific heat and resistivity reproduce literature values [95]. The residual resistivity ratio (RRR) was determined to be RRR$\sim$100 [197], proving good sample quality.

4.4.2 Experimental Setup

To further study the magnetic phase diagram and in particular the magnetic structure of the A-phase of MnSi, we have carried out small angle neutron scattering measurements on the cold diffractometer MIRA at FRM II on sample I, sample II and sample III at ambient pressure. MIRA is a versatile instrument that can be used like a small angle neutron scattering instrument. A schematic drawing is given in Fig. 4.9. The samples were aligned by means of X-ray Laue backscattering. They were mounted inside the sample tube of a cryogenic free pulsetube cryostat [198], thermally coupled to the cryostat by means of He exchange gas of low pressure. The temperature was controlled with a thermometer and a heater, mounted next to the sample on the sample holder. A temperature stability of better than $T \pm 0.01\,\mathrm{K}$ was achieved for sample II and sample III, $T \pm 0.05\,\mathrm{K}$ for sample I, respectively.

A magnetic field up to $\mu_0 H$ =0.5 T, generated by bespoke water cooled Helmholtz-coils [164] could be applied either vertical or parallel to the incident neutron beam. A schematic depiction of both geometries is given in Fig. 4.9, panels (ii) and (iii). Both the magnetic field *and* the cryostat containing the sample could be rocked *together* with respect to a vertical axis by the angle ϕ, as indicated in Fig 4.9. The magnetic field was characterized by a Hall probe and found to be uniform within <1% over the sample volume. The wavelength of the neutron beam was adjusted to λ =9.7 Å with a wavelength spread $\Delta\lambda/\lambda$ = 5% FWHM by means of a multilayer monochromator. The neutron beam was collimated over a distance of L_1 =1.5 m. The diffracted neutrons were recorded by means of a position sensitive ^{3}He delay-line detector at a distance to the sample between L_2 =0.8 m and L_2 =1.3 m.

Note, that the instrumental resolution was relaxed for sample I in order to increase intensity and search for higher order diffraction peaks and double scattering: For sample I, a source aperture with an opening of $8\times8\,\mathrm{mm}^2$ and a sample aperture of equal size were chosen. The resolution of the detector was $2\times2\,\mathrm{mm}^2$. The instrumental resolution, which is a result of the convolution of beam divergence, wavelength spread and detector resolution is derived in section (A.1). The instrumental resolution for the low resolution setup yields $\Delta\beta_{az} = 10°$ in azimuthal direction, $\Delta\beta_{\mathbf{q}} = 0.006\,\mathrm{Å}^{-1}$ in radial direction and $\Delta\beta_{\mathbf{k_f}} = 0.63°$ parallel to $\mathbf{k}_f$.

Sample II and sample III were measured using a high resolution setup to increase the resolution in the rocking scans and to resolve the magnetic structure: For sample II and III, both source aperture and sample aperture were adjusted to an opening of $4 \times 4\,\mathrm{mm}^2$

[2]. We obtain an instrumental resolution of $\Delta\beta_{az} = 4°$, $\Delta\beta_{\mathbf{q}} = 0.004\,\text{Å}^{-1}$ and $\Delta\beta_{\mathbf{k_f}} = 0.35°$ for the high resolution setup.

The diffraction patterns presented in this study have been obtained by a summation over the individual diffraction patterns during rocking the sample about typically $\pm 8°$ with respect to a vertical axis (as indicated in Fig. 4.9). Rocking the sample further yields the magnetic mosaicity of the helical order convoluted with the instrumental resolution $\Delta\beta_{\mathbf{k_f}}$. The spot size at the detector represents the resolution limit for sample I, sample II and sample III, respectively. The position of the diffraction spots at the two-dimensional detector have been obtained by 2-D Gaussian fits. Note, that the error of the fitted position of the diffraction spots is significantly below the instrumental resolution due to a good signal to noise ratio.

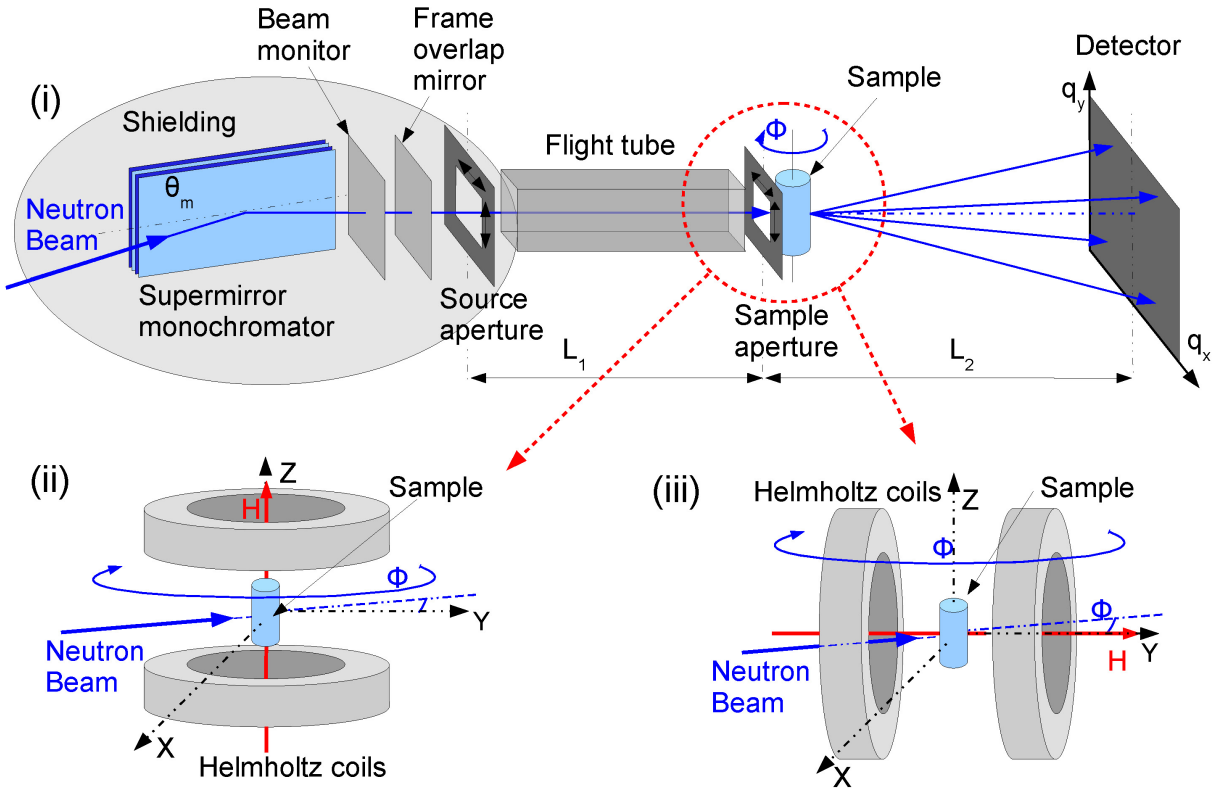

Figure 4.9: Panel (i) shows the setup used for the measurements on the cold diffractometer MIRA: Instead of a velocity selector, usually used for small angle neutron scattering, a multilayer monochromator is used on MIRA due to geometrical constrains. Panel (ii) and (iii) depict both magnetic field setups which were used for our experiments. Note, that the sample and the magnet can be rocked together with respect to a vertical axis by the angle ϕ.

Sample I, II and III (cf. Fig. 4.8) have been measured with the neutron beam aligned parallel to a crystalline $\langle 110 \rangle$ axis. In particular, the neutron beam was aligned almost parallel to the normal vector of the disk for sample I, perpendicular to the long axis of

[2]However, due to the size of sample II with a width of 1.5 mm and a length of 14 mm, an effectively smaller sample aperture was the result.

sample II and parallel to the normal vector of the flat plate for sample III. The vertical axis of sample I corresponds to a $\langle 112 \rangle$ axis, whereas the vertical axis of sample II corresponds to a $\langle 110 \rangle$ axis. Sample III was measured in two configurations, with a $\langle 110 \rangle$ crystalline direction aligned vertical as well as horizontal, respectively. To avoid hysteretic effects, all data at finite field was taken after zero-field cooling to the desired temperature, followed by a field ramp to the desired field value.

4.4.3 Experimental Results

In the following section, we first discuss the results, obtained in zero magnetic field in the helical phase, before we focus on the conical phase and finally on the A-phase of MnSi. Measurements of the helical and conical phase of all three samples reproduce the behaviour as reported in the literature [28, 95, 27].

Helical Phase

Fig. 4.10, panels (i) and (iv) show scattering patterns characteristic of the helical phase for sample I at $T = 27\,\mathrm{K}$ and sample II at $T = 16\,\mathrm{K}$ in zero magnetic field, respectively: The spots of panel (iv) are labeled for reference. Four diffraction spots are visible, each pair (spots 1 and 3) and (spots 2 and 4) corresponds to one $\langle 111 \rangle$ helical domain with $\pm\mathbf{k}$. The diffraction spots in the $\langle 100 \rangle$ directions arise due to double scattering [3]. The value obtained for $\mathbf{k} = 0.034\,\mathrm{\AA}^{-1}$ yields a periodicity of the helical order of λ_h=180 Å. A transition temperature $T_c = 29.5\,\mathrm{K}$ was obtained.

This behaviour is underscored by a plot of the helical phase of sample II at $T = 16\,\mathrm{K}$ and $\mu_0 H$ =0 T as function of the azimuthal angle ψ, which is given in Fig. 4.11, panel (i): The labels of the diffraction spots correspond to Fig. 4.10, panel (iv). Note, that ψ=0° corresponds to a vertical direction. The spots appear along the $\langle 111 \rangle$ directions under approximately 35° with respect to the crystalline $\langle 110 \rangle$ direction (ψ=0°), their full width half maximum yields $\sim 5°$. This is consistent with the azimuthal instrumental resolution $\Delta\beta_{AZ} = 4°$. The difference in intensity between the pairs of spots (1 and 3) and (2 and 4) is due to intrinsically different domain populations.

A typical rocking curve of the helical phase obtained in the high resolution setup for sample II at $T = 16\,\mathrm{K}$ is given in Fig 4.12, panel (i). Again, the labels of the diffraction spots correspond to Fig. 4.10, panel (iv). The rocking curve is well fitted by a Gaussian function yielding a full width at half maximum of $\eta_m \sim 3.5°$, consistent with previous work [29, 194]. The instrumental resolution of a rocking scan yields $\Delta\beta_{\mathbf{ki}} = 0.35°$ for the high resolution setup.

[3] Note, that for an ideal helical arrangement of magnetic moments, no higher order diffraction peaks are observed due to the single $\mathbf{k}$.

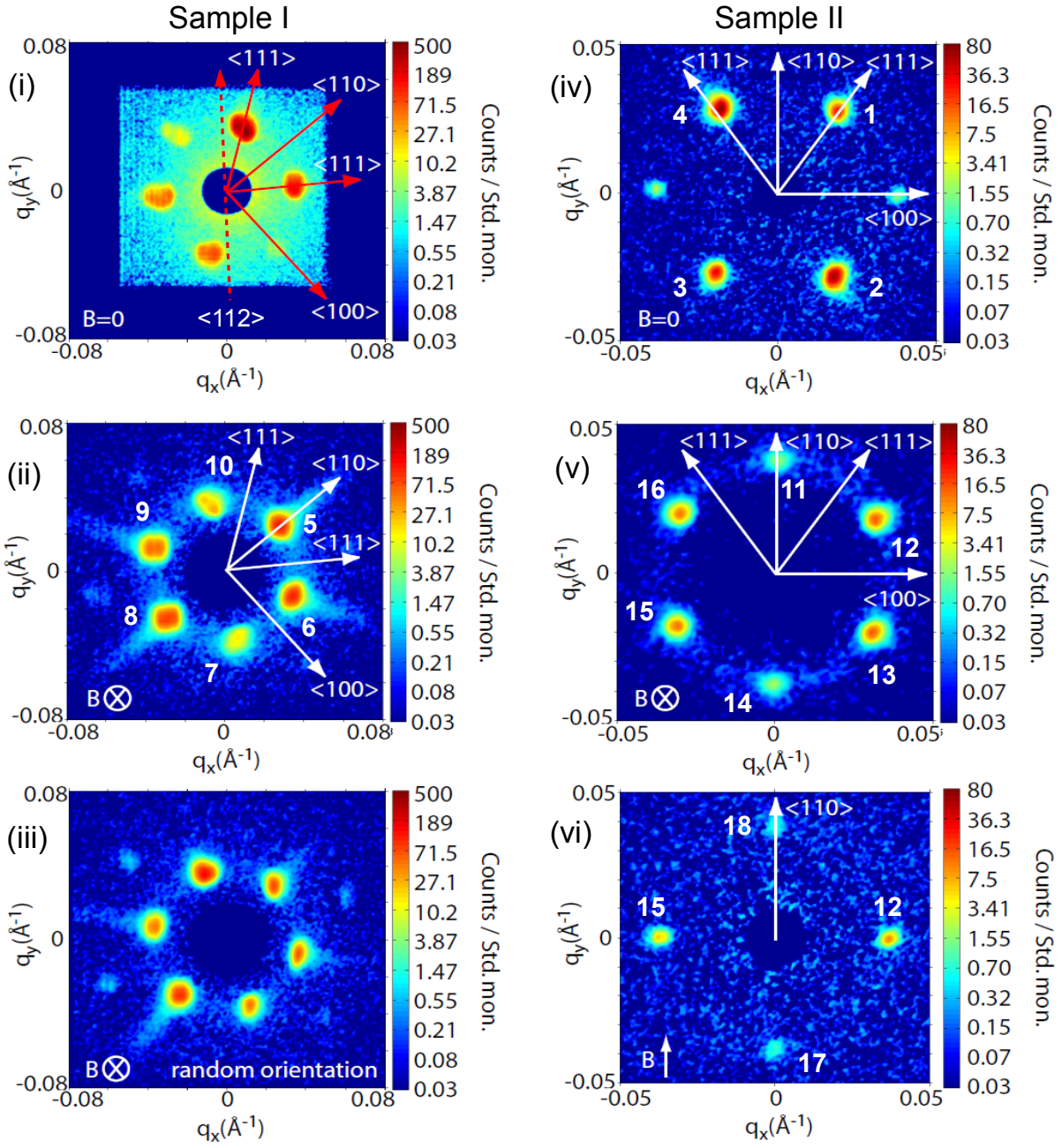

Figure 4.10: Typical small angle neutron scattering patterns. Note, that the color scale is logarithmic to make weak features visible. The data represents the sum over rocking scans with respect to a vertical axis. The background was measured above T_c and subtracted in all panels except (i). Spots are labeled for reference. Panels (i) to (iii) show data, obtained on sample I, where we allow for a large neutron beam divergence to increase the neutron intensity. Panels (iv) to (vi) correspond to sample II which was measured with high resolution. For both, sample I and II the spot size represents the resolution limit. Panel (i) shows the helical order in sample I at 27 K at zero field. Panel (ii) depicts the A-phase of sample I at 26.45 K and 0.16 T, same orientation as (i), whereas panel (iii) depicts the A-phase for a random crystalline orientation of sample I at 26.77 K and 0.16 T. Panel (iv) depicts the helically ordered state of sample II at 16 K in zero field whereas panel (v) depicts the A-phase of sample II at 27.7 K and 0.16 T. Panel (vi) shows the coexisting conical phase and A-phase in conventional setup with the magnetic field perpendicular to the incident neutron beam at 27.7 K and 0.19 T. Spots (12) and (15) correspond to spots (12) and (15) in panel (v). See text for details.

Conical Phase

In the conical phase, the propagation vector **k** of the helical order is aligned in the direction of the applied magnetic field while the cone angle decreases with increasing field. The conical phase is observed with the applied magnetic field aligned perpendicular to the incident neutron beam as given in Fig. 4.9, panel (ii).

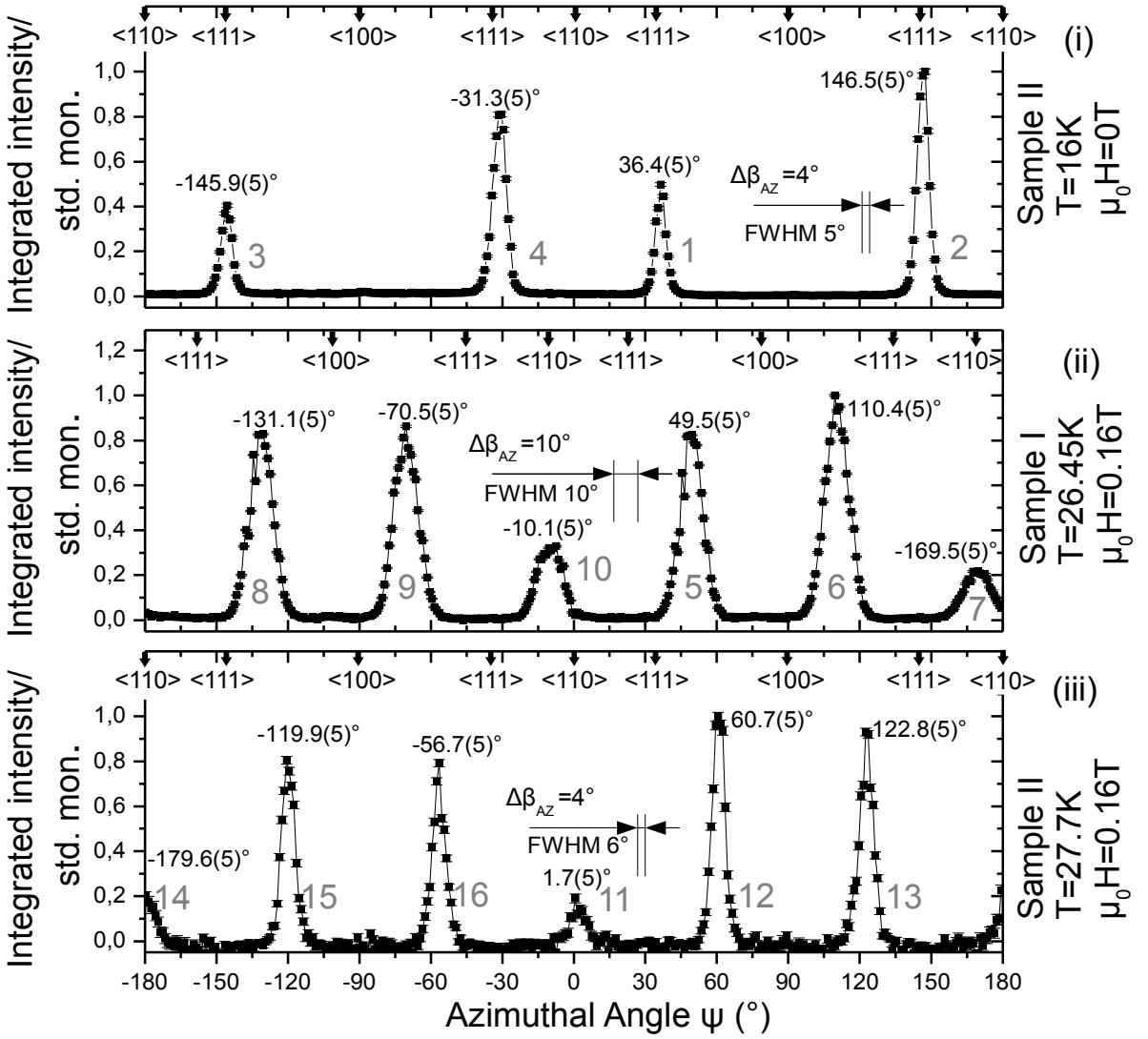

Figure 4.11: Panel (i): Azimuthal plot of the helical phase in sample II at 16 K and 0 T, corresponding to Fig. 4.10, panel (iv). Panels (ii) and (iii): Azimuthal plot of the A-phase of sample I at 26.45 and sample II at 27.7 K and 0.16 T, corresponding to Fig. 4.10, panels (ii) and (v), respectively. Spots are numbered for reference. The width of the spots is limited by the instrumental resolution. Note that for sample II, a small deviation of the ideal six-fold symmetry is observed. Further note, that ψ=0° corresponds to a vertical direction for all panels.

Typical data obtained for the conical phase is given in Fig. 4.10 panel (vi) for sample II at a temperature of $T = 27.7$ K and at $\mu_0 H$ =0.19 T. The magnetic field was aligned parallel to a crystalline $\langle 110 \rangle$ direction: Four diffraction spots are visible. The spots labeled with

(17) and (18) are aligned parallel to the direction of the magnetic field, they correspond to the conical phase. The pair of diffraction spots labeled with (12) and (15) are oriented perpendicular to the applied magnetic field and belong to the A-phase.

A-Phase

It was long believed that the A-Phase was explained by a single helix with its propagation vector **k** aligned perpendicular to the applied magnetic field [28, 29, 95, 27]. Using a scattering geometry where the magnetic field is applied perpendicular to the neutron beam, as given in Fig. 4.9, panel (ii), the intensity of the spots associated with the conical phase (spots 17 and 18 in Fig. 4.10, panel (iv)) gradually weaken when entering the A-phase, whereas strong scattering appears perpendicular to the applied field (spots 12 and 15) associated with the A-phase. The modulus of the reciprocal lattice vector **k** is conserved at the transition to the A-phase. This behaviour is consistent with previous work and may be attributed to phase coexistence characteristic of a weak first-order phase transition with possible extra effects of demagnetizing fields.

We, however, emphasize, that this scattering geometry where the magnetic field is aligned perpendicular to the neutron beam — as used for all previous work—cannot map all **k**-vectors which are oriented perpendicular to the applied magnetic field. Solely **k**-vectors are visible, which are oriented parallel to the intersection line of the Ewald sphere and the plane, perpendicular to the magnetic field. For detailed investigations of the complete structure of the A-phase, we have chosen the direction of the incident neutron beam parallel to the magnetic field. A schematic depiction of the setup is given in Fig. 4.9, panel (iii). In this scattering geometry, all **k**-vectors perpendicular to the applied magnetic field simultaneously satisfy the Bragg condition.

Fig. 4.10, panel (ii) and panel (v) show typical data, obtained in the A-phase for sample I and sample II at $T = 26.45\,\mathrm{K}$ and $T = 27.7\,\mathrm{K}$ at $\mu_0 H = 0.16\,\mathrm{T}$, respectively: The A-phase is characterized by six diffraction spots which emerge on a regular hexagon. The diffraction spots are labeled for reference. We have tested the variation of the scattering pattern on the orientation of the field relative to the crystal direction in all samples. Whereas the field was always aligned parallel to the incident neutron beam, the sample was rotated for a large number of orientations. Typical data is shown in Fig. 4.10, panel (iii) for a random orientation of sample I at $T = 26.77\,\mathrm{K}$ and $\mu_0 H = 0.16\,\mathrm{T}$: For all samples and all crystalline directions a regular six-fold scattering pattern always emerges. However, a weak pinning of the nearest neighbour direction of the six-fold structure in the crystalline $\langle 110 \rangle$ direction is observed, if a $\langle 110 \rangle$ direction is contained in the plane, perpendicular to the magnetic field.

Fig. 4.11, panels (ii) and (iii) show the integrated intensity of the A-phase plotted as function of the azimuthal angle ψ for sample I at $T = 26.45\,\mathrm{K}$ and in $\mu_0 H = 0.16\,\mathrm{T}$ and sample II at $T = 27.7\,\mathrm{K}$ and $\mu_0 H = 0.16\,\mathrm{T}$. Again, $\psi = 0^\circ$ indicates the vertical direction. The labels of the diffraction spots correspond to Fig. 4.10, panels (ii) and (v): For both samples, the symmetry direction of the regular hexagon is aligned along a $\langle 110 \rangle$ crystalline direction. For sample I, the spots appear strictly under an angle of $\Delta\psi = 60^\circ$ characteristic

of the six-fold symmetry. A small distortion of $\sim 1.5°$ of the ideal six-fold structure to an ellipsoidal shape is observed for sample II. The reason for the deviation from the regular hexagonal shape is unclear, it may be attributed to the weak pinning in the crystalline $\langle 110 \rangle$ direction. However, the distortion is below the instrumental resolution.

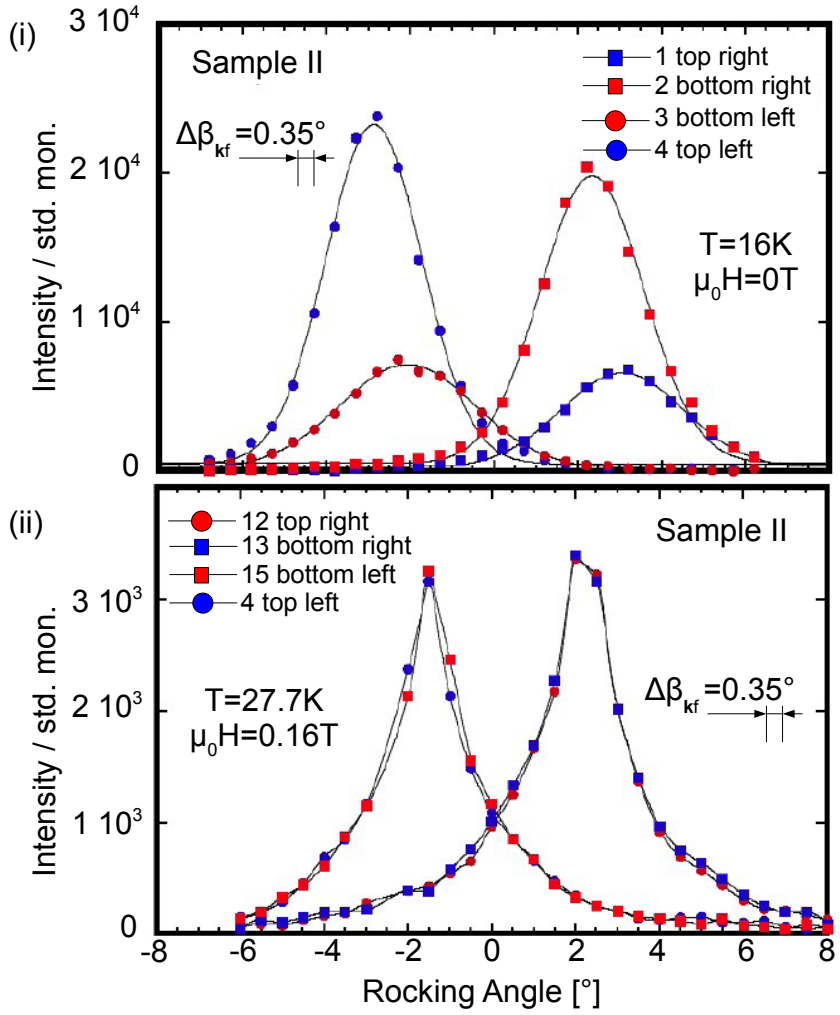

Figure 4.12: Panel (i) and (ii): Both plots depict typical rocking scans of sample II. The intensity represents counts integrated over the individual spots during the rocking scan with labels referring to Fig. 4.10, panels (iv) and (v). Lines serve as guide to the eye. The upper plot corresponds to the helical state at 16 K and zero field. A spontaneous difference of intensity between the domain populations (1,3) and (2,4) is observed. The lower panel corresponds to the A-phase at 27.7 K and 0.16 T.

The azimuthal width of the spots is limited by the instrumental resolution and yields $\sim 6°$ for sample II and $\sim 10°$ for sample I, which is approximately consistent with the calculated instrumental resolution $\Delta\beta_{AZ} = 10°$ for the low resolution setup and $\Delta\beta_{AZ} = 4°$ for the high resolution setup, as derived in section (A.1). Note, that the intensity of spots, lying

on the axis rotation[4] (namely spots 7, 10, 11, 14) is systematically lower. The reason for this behaviour will be discussed below.

We have performed rocking scans in the A-phase where the sample *and* the magnetic field have been rocked together with respect to a vertical axis. Foremost, the rocking scans performed show that the magnetic structure in the A-phase is *strictly* aligned perpendicular to the applied magnetic field, independent of the underlying crystalline orientation. In comparison to the helical order where the rocking curve is described by a Gaussian function with a half width at full maximum of $\eta_m \sim 3.5°$, the rocking curve obtained in the A-phase exhibits a characteristic change of shape and full width at half maximum: The shape of the rocking scans is characteristic of an exponential function with a full width at half maximum of η_A =1.75°, taking the Lorentz factor of 15% into acount. The instrumental resolution for rocking scans yields $\Delta\beta_{\mathbf{k_i}} = 0.35°$. However, the shape of the rocking curve is very sensitive to demagnetizing effects as well.

Finally, due to the misalignment of the crystalline ⟨110⟩ axis with respect to the normal vector of sample I, a deflection of the magnetic field direction inside the sample was observed which is caused by demagnetizing effects. A schematic depiction of the magnetic field direction inside and outside of sample I is given in Fig 4.13, panel (iii).

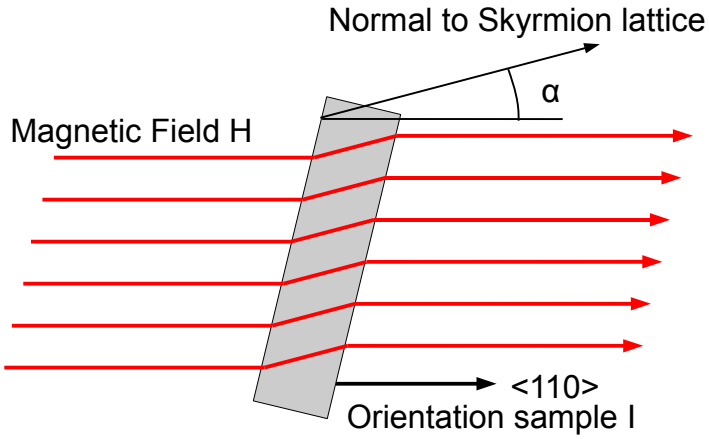

Figure 4.13: Caused by the misalignment of the normal vector of sample I with respect to the ⟨110⟩ crystalline direction, the orientation of the A-phase is deflected by the angle α due to demagnetizing effects inside sample I.

High Resolution Rocking Scans

To quantize the influence of demagnetizing fields on the structure and the rocking curve of the A-phase we have performed further scans using sample III in the high resolution setup. With a sample aperture of 4×4 mm^2, only the central part of sample III is exposed to the neutron beam. Edge effects can be neglected. Sample III can be regarded as flat,

[4]The diffraction patterns are obtained by the summation over a rocking scan with respect to a vertical axis.

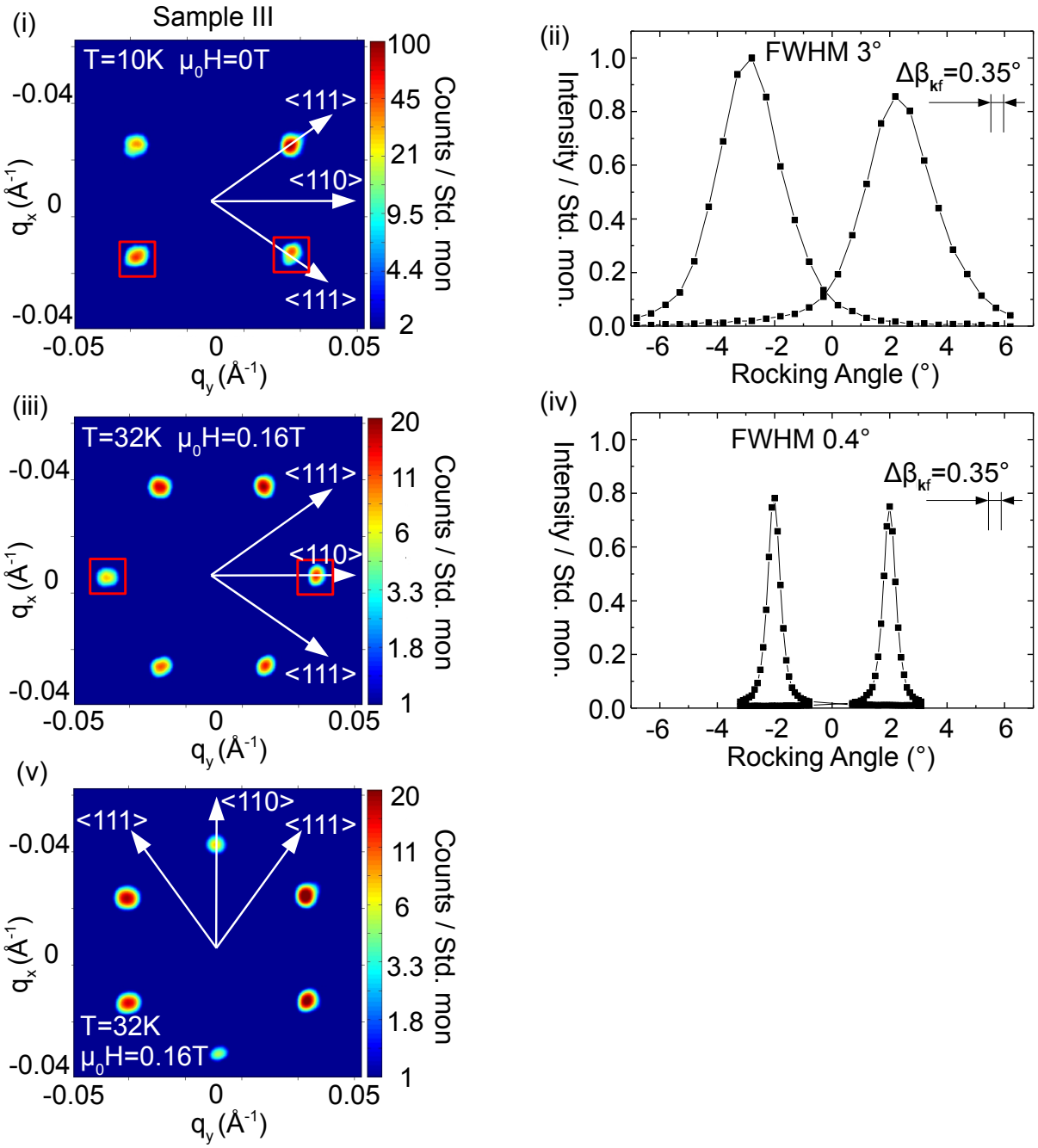

Figure 4.14: Panel (i): Scattering pattern characteristic of the helical phase of sample III at T =10 K and zero magnetic field. The crystalline $\langle 110 \rangle$ axis is aligned horizontal. Panel (ii) depicts a rocking scan of the helical phase of sample III at T = 10 K and zero magnetic field: The integrated intensity of the diffraction spots as indicated in panel (i) is plotted with respect to the rocking angle. Panel (iii): Scattering pattern characteristic of the A-phase of sample III at T = 32 K and at $\mu_0 H$ =0.16 T. Due to a non-optimal thermal coupling of the sample to the sample holder, a shift of the transition temperature T_c was observed. The crystalline $\langle 110 \rangle$ axis is aligned horizontal. Panel (iv) depicts the corresponding rocking scan of the A-phase of sample III, where the integrated intensity of the diffraction spots as indicated in panel (iii) is plotted with respect to the rocking angle. Panel (v): Scattering pattern characteristic of the A-phase of sample III at T = 32 K and at $\mu_0 H$ =0.16 T. The crystalline $\langle 110 \rangle$ axis is aligned vertical.

thin plate, oriented perpendicular to the applied magnetic field and the neutron beam. A demagnetizing factor $N = 1$ applies.

Rocking scans with respect to a vertical axis with a step-size of $\eta = 0.075°$ have been performed in the helical phase at a temperature $T = 10\,\mathrm{K}$ and at zero field as well as in the A-phase at a temperature $T = 32\,\mathrm{K}$ and a magnetic field $\mu_0 H = 0.16\,\mathrm{T}$. Due to a non-optimal thermal coupling of the sample to the sample holder, a shift of the transition temperature T_c was observed. Typical data is shown in Fig. 4.14, panel (i) for the helical phase and panel (iii) for the A-phase. The horizontal axis corresponds to a $\langle 110 \rangle$ crystalline direction.

Consistent with sample II and previous work [29, 194], a rocking width of $\eta_m = 3.0 \pm 0.3°$ has been obtained for the helical phase of sample III, well described by a Gaussian line shape, taking the Lorentz factor into account. The rocking curve is given in Fig. 4.14, panel (ii). However, the rocking width obtained for the A-phase in sample III yields a value of $\eta_A = 0.4°$ which represents the instrumental resolution limit $\Delta\beta_{\mathbf{k}f} = 0.35°$. The line shape is characteristic of a Gaussian function as depicted in Fig. 4.14, panel (iv). The small value of $\eta_A = 0.4°$ indicates a well ordered state exhibiting long range order over several 1000 Å and underscores the influence of demagnetizing effects on the shape of the rocking scans, seen in sample II.

To check, whether the distortion of the hexagonal scattering pattern of the A-phase to an ellipsoidal shape as observed for sample II is an intrinsic feature, rocking scans of sample III have been recorded in the high resolution setup with both a crystalline $\langle 110 \rangle$ direction aligned vertical as well as horizontal. The data is shown in Fig. 4.14: Panel (iii) depicts the typical hexagonal scattering pattern of the A-phase at a temperature $T = 32\,\mathrm{K}$ and a magnetic field $\mu_0 H = 0.16\,\mathrm{T}$ where the $\langle 110 \rangle$ crystalline direction is aligned horizontal. Panel (v) depicts the typical hexagonal scattering pattern of the A-phase at identical temperature and magnetic field where the $\langle 110 \rangle$ crystalline direction is aligned vertical. A regular hexagonal shape with diffraction spots aligned under $\Delta\psi = 60 \pm 0.4°$ was obtained for the crystalline $\langle 110 \rangle$ direction aligned horizontal whereas $\Delta\psi = 60 \pm 0.7°$ was obtained for the crystalline $\langle 110 \rangle$ direction aligned vertical. This strongly indicates that the elliptical distortion, observed for sample II is a result of demagnetizing effects due to the sample geometry or caused by instrumental artifacts.

Summary

We now briefly summarize the salient features of the A-phase as inferred from our small angle neutron scattering measurements as well as other studies:

- The A-phase is stabilized at finite fields, approximately $1/2H_{c2}$ and close to T_c, separated by weak first order phase boundaries as inferred from AC-susceptibility [26], specific heat [26], torque magnetometry [178] and several small angle neutron scattering measurements [28, 27].
- The complete structure of the A-phase is characteristic of a regular six-fold scattering pattern, whereby the **k**-vectors are strictly aligned perpendicular to the applied

magnetic field. The scattering pattern is independent of the underlying crystal structure. Moreover, we have shown that the orientation of the scattering pattern is extremely sensitive to demagnetizing effects as indicated by the shape of the rocking curves for different sample geometries. Note, that all data obtained at finite field have been measured after zero field cooling to the desired temperature followed by a field ramp to the desired field value. However, the results obtained for the A-phase upon field cooling were identical.

- A weak pinning of the nearest neighbour direction of the six-fold scattering pattern is observed in a crystalline $\langle 110 \rangle$ direction, for the case that a $\langle 110 \rangle$ direction is contained in the plane, perpendicular to the magnetic field.

- The modulus of the **k**-vector of the A-phase is identical to the propagation vector **k** of the helical phase.

We now address various additional features which account for less than 1% of the total integrated scattering intensity: Weak, continuous streaks of intensity emerge radially outward from the six main spots in the A-phase (cf. Fig. 4.10, panels (ii) and (iii)) and the coexistance of conical and A-phase (cf. Fig. 4.10, panel (vi)), which may be the result of weak heterogeneities resulting from the generic first-order boundaries of the A-phase, possibly in combination with demagnetizing effects.

Measurements with high incident neutron flux and relaxed instrumental resolution, performed in the A-phase on sample I (cf. Fig 4.10, panels (ii) and (iii)) show weak intensity at the positions of higher order peaks, although this may arise from double scattering rather than true higher order reflections. Note, that for a perfect sinusoidal arrangement of magnetic moments, no higher order reflections are expected.

Furthermore, we observe that the integrated intensity distribution of the six spots, associated with the A-phase is systematically inhomogeneous for all samples (cf. Fig. 4.10, panel (v), Fig. 4.11 panels (ii) and (iii) and Fig. 4.14, panel (v)): The diffraction spots along the vertical direction are weaker. For a neutron beam divergence comparable to the rocking width, only the tail of the Bragg peaks can satisfy the Bragg condition, especially for a vertical rocking axis. Therefore, when summing over a rocking scan with respect to a vertical axis, these spots remain weak.

4.4.4 Interpretation

We have summarized the key results of our neutron scattering data on the structure of the A-phase in MnSi in the last part of the previous section. A theoretical interpretation of the data in terms of a triple-**q** spin crystal, composed of the superposition of three helices with fixed modulus under an angle of 120° with respect to each other, has been given by Rosch and Binz [30] based on previous work [14, 15, 199, 16]. In the following section, we summarize the salient features of the theoretical model. For a detailed description we refer to [30].

Triple-Q Spin Crystal

For our theoretical account to explain the A-phase, we evoke strong analogies to the solidification of ordinary crystals out of the liquid state: The formation of crystals is driven by three main features: Foremost, the interplay of long range attractive and short range repulsive interactions leads to an instability of the liquid, whereas the correlations are completely isotropic and show no preferred direction. Second, the free energy is lowered by cubic interactions of density waves (three particle collisions) which may be written in momentum space by the expression

$$\sum_{\mathbf{q}_1,\mathbf{q}_2,\mathbf{q}_3} \varrho_{\mathbf{q}_1}\varrho_{\mathbf{q}_2}\varrho_{\mathbf{q}_3}\delta(\varrho_{\mathbf{q}_1}+\varrho_{\mathbf{q}_2}+\varrho_{\mathbf{q}_3})\,. \tag{4.9}$$

The free energy is lowered when the three ordering vectors of the crystal structure add up to zero. This naturally leads to a body centered cubic symmetry which is the crystal structure with the largest number of such triples of reciprocal lattice vectors [200]. However, exceptions arise due to strong first order transitions. Third, the atoms form countable entities.

It was long believed that the formation of similar structures in magnetic systems was not possible due to (i) the strong breaking of the translational and inversion symmetry by the underlying atomic lattice and Fermi surface. (ii) Three particle collisions are forbidden by time-reversal symmetry for paramagnetic fluctuations. (iii) The magnetic entities, playing the analog role of the quantized atoms are still unknown, possible candidates are topologically stable objects as vortex-like structures or topological solitons (cf. section 1).

We start with writing down the free energy functional near to T_c, using a standard Ginzburg-Landau ansatz [201, 31]. We thereby closely follow [30]. The free energy is given by

$$F(\mathbf{M}) = \int d^3r \left(r_0\mathbf{M}^2 + J(\nabla\mathbf{M})^2 + 2D\mathbf{M}\cdot(\nabla\times\mathbf{M}) + U\mathbf{M}^4 - \mathbf{B}\cdot\mathbf{M}\right) \tag{4.10}$$

where the first and the second term represent the usual quadratic contribution with the conventional gradient term, the third term represents the DM interaction and the last term represents the coupling to an external induction $\mathbf{B}$. The quartic term $U\mathbf{M}^4$ accounts in lowest order for the effects of mode-mode coupling and stabilizes the magnetic order. Higher order spin orbit coupling terms, representing anisotropy are neglected for this description. r_0, J, U and D are parameters, where we chose $D > 0$ (see the Bak-Jensen model introduced in section (4.2)).

In the presence of a finite uniform magnetisation $\mathbf{M}_f$ —which breaks time-reversal symmetry — allowing for three particle interactions of *magnetic* excitations, a similar mechanism, compared to the solidification of crystals can occur in MnSi. It is possible to single out the uniform ferromagnetic magnetization of the magnetic structure $\mathbf{M}_f = \int \mathbf{M}(\mathbf{r})d^3\mathbf{r}/V$ with the volume V. The uniform magnetization $\mathbf{M}_f||\mathbf{B}$ is induced by the external magnetic

field. The actual order parameter is thus given by $\mathbf{\Phi} = \mathbf{M} - \mathbf{M}_f$. The quadratic part of eq. (4.10) is minimized by a helix with wave length $2\pi/|\mathbf{k}|$ with $\mathbf{k} = D/J$, described by

$$\mathbf{M}^h_{\mathbf{Q}}(\mathbf{r}) = A(\mathbf{n}_1 \cos[\mathbf{kr}] + \mathbf{n}_2 \sin[\mathbf{kr}])]. \tag{4.11}$$

The propagation vector $\mathbf{k}$ of the helices and the two unit vectors, $\mathbf{n}_1, \mathbf{n}_2$ are orthogonal to each other. The sign of D in eq. (4.10) determines the chirality of the helices where $\mathbf{k} \cdot (\mathbf{n}_1 \times \mathbf{n}_2) > 0$ leads to left-handed helices for $D > 0$.

To quadratic order, the free energy is also minimized by arbitrary *linear combinations* of such helices and the magnetic structure is selected by the interaction $\mathbf{M}^4$. Expanding the quartic term $\mathbf{M}^4$, we obtain

$$\mathbf{M}^4 = \mathbf{M}_f^4 + 4\mathbf{M}_f^2\, \mathbf{\Phi} \cdot \mathbf{M}_f + 2\mathbf{M}_f^2 \mathbf{\Phi}^2 + 4(\mathbf{M}_f \cdot \vec{\Phi})^2 + 4\vec{\Phi}^2\, \vec{\Phi} \cdot \mathbf{M}_f + \mathbf{\Phi}^4 \tag{4.12}$$

The crystalline state can gain energy from the second last term $\propto \mathbf{\Phi}^2\, \mathbf{\Phi} \cdot \mathbf{M}_f$, which is cubic in the order parameter. Fourier transformation leads to

$$\int \mathbf{M}_f \cdot \mathbf{\Phi}\, \mathbf{\Phi}^2\, d^3\mathbf{r} = \sum_{\mathbf{k}_1, \mathbf{k}_2, \mathbf{k}_3 \neq 0} (\mathbf{M}_f \cdot \mathbf{m}_{\mathbf{k}_1})(\mathbf{m}_{\mathbf{k}_2} \cdot \mathbf{m}_{\mathbf{k}_3}) \delta(\mathbf{k}_1 + \mathbf{k}_2 + \mathbf{k}_3), \tag{4.13}$$

where $\mathbf{m}_{\mathbf{k}}$ is the Fourier transform of $\mathbf{M}(\mathbf{r})$. Therefore, the cubic term vanishes unless the magnetic structure contains Fourier modes of at least three wavevectors $\mathbf{k}_j$ with $\mathbf{k}_1 + \mathbf{k}_2 + \mathbf{k}_3 = 0$. Similar to the formation of ordinary crystals, the free energy for this expression is lowered when the three $\mathbf{k}$-vectors add up to zero.

The modulus of the $\mathbf{k}$ vectors thereby is given by the interplay of the gradient terms of eq. (4.13) $|\mathbf{q}| = |\mathbf{k}| = D/J$. This naturally leads to a relative angle of 120° of the $\mathbf{k}$-vectors. The $\mathbf{k}$-vectors thus define a plane, characterized by the normal vector $\mathbf{n}$. The energy change thereby is proportional to $\mathbf{M}_f \cdot \mathbf{n}$. Therefore, all three $\mathbf{k}$-vectors have to be oriented perpendicular to the applied field. A schematic depiction of the structure is given in Fig. 4.15.

With this intuitive model, we already can account for three main features of our experimental findings: (i) A triple-$\mathbf{q}$ structure with $\mathbf{k}$-vectors aligned under 120° explains the hexagonal scattering pattern, as each $\mathbf{k}$-vector gives rise to scattering in $\pm\mathbf{k}$. (ii) The alignment of the $\mathbf{k}$-vectors is strictly perpendicular to the applied field. (iii) For an ideal sinusoidal modulation of the helices, no higher order diffraction peaks are expected.

We therefore conclude that the A-phase is described by a chiral *spin crystal*, composed by the superposition of helices under 120° with respect to each other with fixed propagation vector $\mathbf{q} = \mathbf{k}$ and phase $\Delta\mathbf{r}_i$. It is approximately characterized by the magnetization

$$\mathbf{M}(\mathbf{r}) \sim \mathbf{M}_f + \sum_{i=1}^{3} \mathbf{M}^h_{\mathbf{k}_i}(\mathbf{r} + \Delta\mathbf{r}_i) \tag{4.14}$$

where $\mathbf{M}^h_{\mathbf{k}_i} = A(\mathbf{n}_{i1} \cos \mathbf{k}_i\mathbf{r} + \mathbf{n}_{i2} \sin \mathbf{k}_i\mathbf{r})$ represents the magnetization of a single helix with the propagation vector $\mathbf{k}_i$, the amplitude A and two unit vectors $\mathbf{n}_{i1}$ and $\mathbf{n}_{i2}$ perpendicular to $\mathbf{k}_i$.

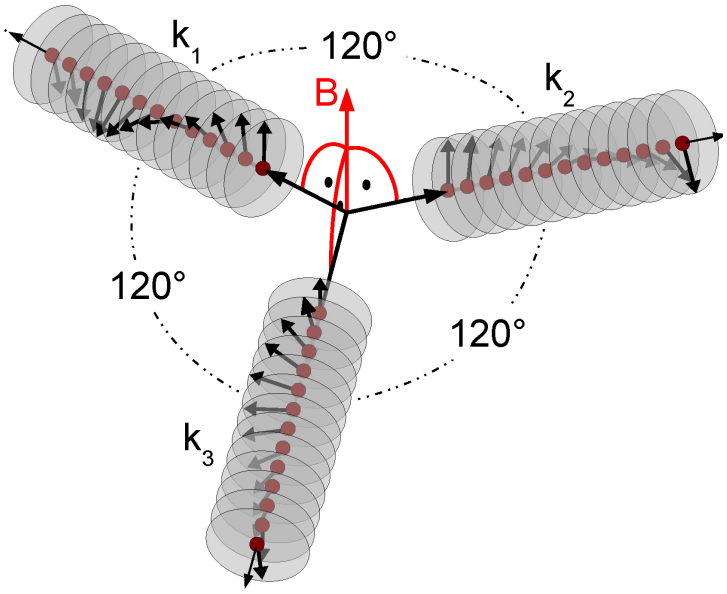

Figure 4.15: Schematic depiction of the triple-**q** crystal, formed by a superposition of three single-**k** helices under 120° with respect to each other and perpendicular to the applied magnetic field.

By computing the free energy of the spin crystal in the mean-field model, the minimum of $F(\mathbf{M})$ can be found rigorously. Within the parameter range where the A-phase is observed experimentally (close to T_c and at $\sim 0.4H_{c2}$), Rosch and Binz find that the energy difference between the conical phase and the spin crystal becomes very small. However, the conical phase still represents the ground state, as the spins can be tilted in the magnetic field direction easily. The conical phase evolves continuously into the helical state at zero field. The energy difference of the ferromagnetic (i), the spin crystal (iii) and a single helix (ii) oriented perpendicular to the applied magnetic field, with respect to the conical phase is given in Fig. 4.16.

The minimization process shows that the three helices have equal weight. The energy minimum for the spin crystal can be traced back to the size of the modulation of $|\mathbf{M}(\mathbf{r})|$, which is minimal at $\sim 0.4H_{c2}$. Note, that the spin crystal therefore is most stable, when the variation of the magnetization is smallest, rather than largest. In particular, the local suppression of the magnetization to zero would cost a large energy. In conclusion, within our Ginzburg-Landau model, the spin crystal thus appears as a metastable state. However, the free energy of the spin crystal becomes close compared to the conical phase.

Fluctuation Stabilized Groundstate

To account for thermal fluctuations, Binz and Rosch consider the leading correction arising from Gaussian fluctuations to the mean field theory from above

$$G \sim F(\mathbf{M}_0) + \frac{1}{2} \log \det \left(\frac{\delta^2 F}{\delta \mathbf{M} \delta \mathbf{M}} \right) \Bigg|_{\mathbf{M}_0} \tag{4.15}$$

with the mean field spin configuration for the A-phase as well as for the conical phase. A cutoff for short length scales at $|\mathbf{k}| < 2\pi/a$ has been introduced to make eq. (4.15) well defined. The nuclear lattice constant of MnSi is denoted a. Due to the long pitch of the helical order in MnSi of λ =180 Å, most contributions arise from fluctuations on a short length scale except for temperatures close to T_c. For intermediate magnetic fields, short *and* long range fluctuation favour the spin crystal. A detailed discussion is given in [30].

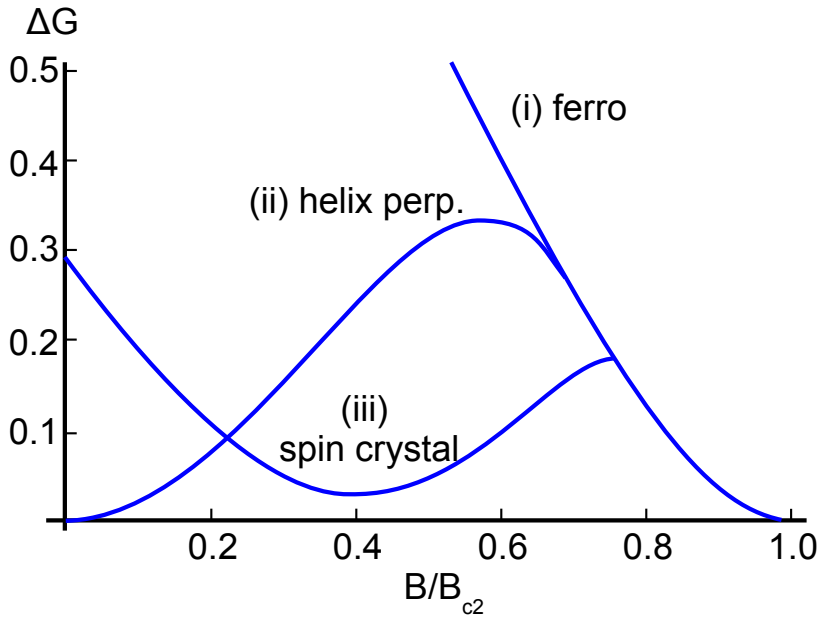

Figure 4.16: Difference of mean-field free energy between the conical state and (i) the ferromagnetic state, (ii) a single helix perpendicular to the applied magnetic field, and (iii) the spin crystal, as a function of magnetic field. The energy difference is plotted in reduced units in the limit of small temperatures [30].

The phase diagram, as obtained by means of numerical calculations by Rosch and Binz is depicted in Fig. 4.17 as function of the applied magnetic field B/B_0 and the renormalized temperature t which is approximately proportional to $T - T_c$. The regions of stability are indicated in the phase diagram for the paramagnetic, conical and spin crystal phase: The spin crystal is stable in the regions, shaded in grey, however at very low fields below the red dotted line, the spin crystal is unstable.

Eq. (4.15) is only valid for small fluctuations and cannot be applied to close to T_c. The strength of the fluctuations has been examined by a calculation of the leading correction to the order parameter for both conical and spin crystal phase. Above and to the right of the red dashed line in Fig. 4.17, the fluctuation correction to the order parameter becomes uncontrollable. The region on the left of the red dashed line corresponds to small corrections below 20%, so that eq. (4.15) is well defined. The inset shows the energy difference between the conical and the spin crystal as function of field for identical parameters where the energy of the spin crystal is lowered by fluctuations. The area shaded in dark grey therefore reliably establishes the regime where the spin crystal is stabilized within our mean field model including fluctuations.

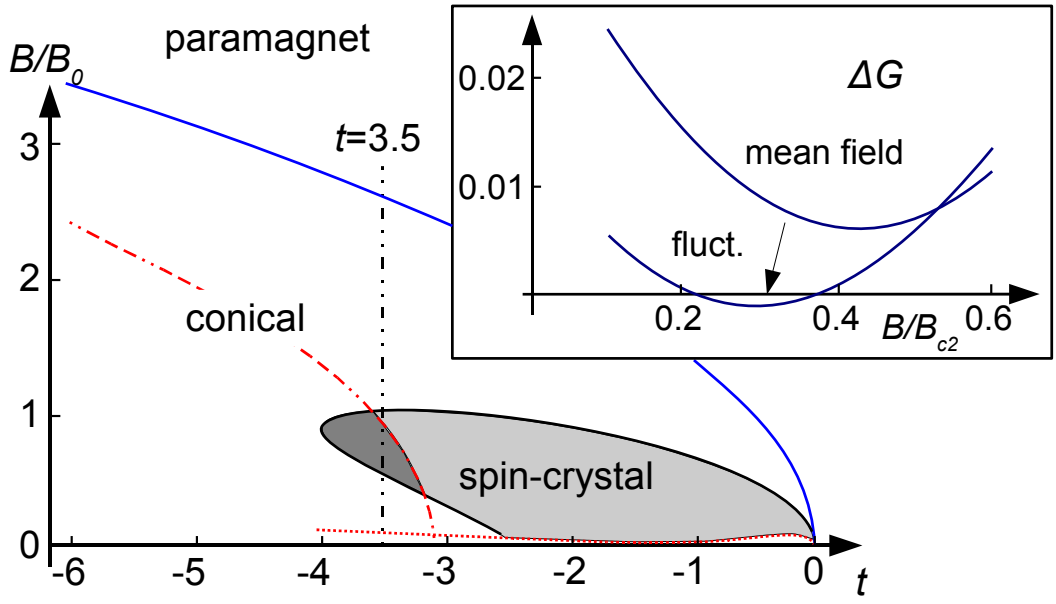

Figure 4.17: Theoretical phase diagram of MnSi as function of magnetic field B/B_0 and temperature t in reduced units. The light grey area indicated with *spin-crystal* marks the region where the spin crystal solution exhibits a minimum of the free energy. The layer shaded in dark grey marks the region where the spin crystal is stable and the fluctuations are controlled. The inset shows the energy difference between the conical and the spin crystal as function of field for identical parameters and $t = -3.5$, both in mean field approximation with fluctuation corrections.

Pinning of the Spin Crystal to the Atomic Lattice

Our experiments indicate that a nearest neighbour direction of the spin crystal is aligned in a crystalline $\langle 110 \rangle$ direction, if such a direction is contained in the plane, perpendicular to the magnetic field. Eq. (4.10) owns full rotational symmetry. A rotation of the spin crystal is described by $\mathbf{M}(\mathbf{r}) \rightarrow R\mathbf{M}(R^{-1}\mathbf{r})$, with the $SO(3)$ operator R. The coupling to the external magnetic field breaks the rotation symmetry to $SO(2)$, describing rotations around the direction of the magnetic field. Higher-order terms in spin-orbit coupling which have been neglected so far in eq. (4.10) break this symmetry. Then, a coupling of the spin crystal to the atomic lattices can arise.

In the model by Binz and Rosch, these terms are organized in powers of spin-orbit coupling, taking into account the temperature regime of the spin crystal which is close to T_c. The leading anisotropy terms are fourth order in spin-orbit coupling and are treated perturbatively. Due to the six-fold symmetry of the spin-crystal, it turns out that the pinning of the spin-crystal is provided by sixth order terms of spin orbit coupling. Finally, the pinning of the spin crystal in the crystalline $\langle 110 \rangle$ directions can be reproduced. For a detailed description, we refer to [30].

Topology of the Spin Crystal

We finally consider the topology of the spin crystal, obtained in the previous paragraphs. A schematic real space depiction of the spatial arrangement of magnetic moments in a plane perpendicular to the applied magnetic field H is given in Fig. 4.18, panel (i): Note, that the structure of the spin crystal is translation invariant in magnetic field direction. The depicted arrangement can be comprehensively interpreted in two different ways: On a short length-scale, the spin crystal is characteristic of a doubly twisted, helical structure. However, on a large scale, a hexagonal lattice of knots of the magnetization is observed, similar to a superconducting vortex lattice. The magnetization in the cores of the knots is aligned anti-parallel to the uniform magnetization $\mathbf{M}_f$.

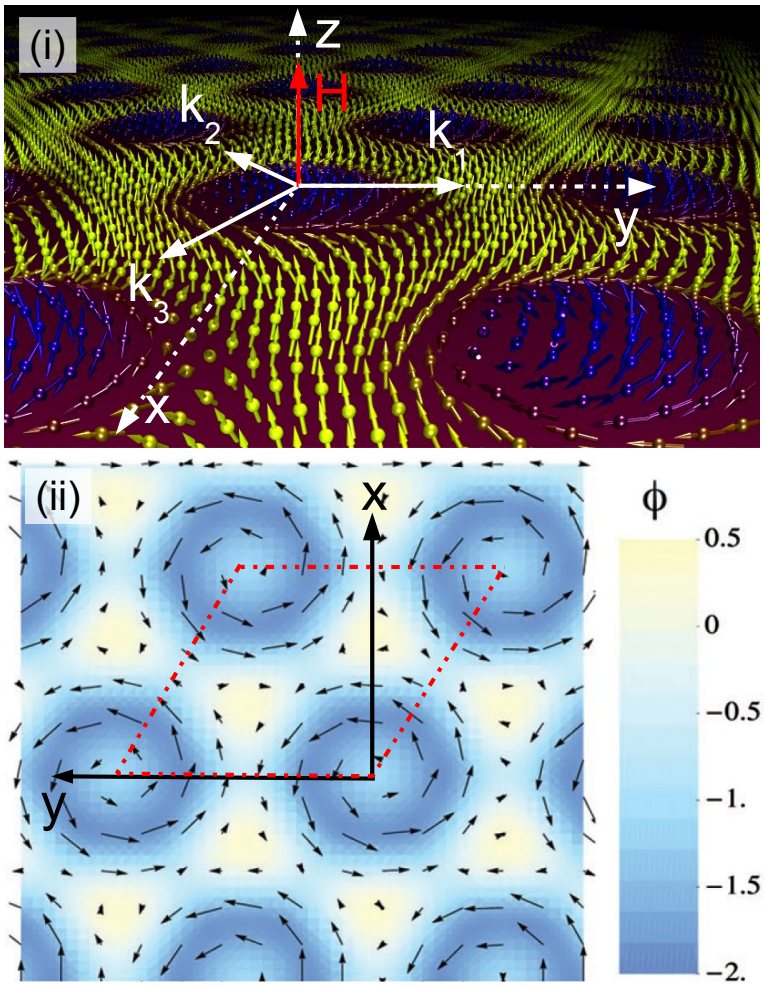

Figure 4.18: Panel (i): Real space depiction of the spin crystal in a plane, perpendicular to the magnetic field H. Note, that the spin crystal is translation invariant in magnetic field direction. The spin crystal is composed of the superposition of three helices under 120° perpendicular the applied magnetic field. The spin crystal may be seen as regular hexagonal macroscopic lattice of topological knots of the magnetization. Panel (ii) depicts the winding density ϕ of the spin crystal plotted as function of x and y, where x and y are perpendicular to the applied magnetic field. For details see text.

We have introduced in section (1) that topological solitons are characterized by their integer topological charge $C_{top} \neq 0$. The topological charge can be obtained by integration of the winding density or skyrmion density. The winding density is comprehensively given by

$$\phi = \frac{1}{4\pi}\mathbf{n} \cdot \frac{\partial \mathbf{n}}{\partial x} \times \frac{\partial \mathbf{n}}{\partial y} \tag{4.16}$$

where x and y are perpendicular to the magnetic field $\mathbf{H}$ and $\mathbf{n} = \mathbf{M}(\mathbf{r})/|\mathbf{M}(\mathbf{r})|$ is the normalized direction of the magnetization. The vector ϕ is a measure for the variation of the direction or *winding* of the normalized magnetization. The flux of ϕ through any two-dimensional rectangle with periodic boundary conditions is then a measure for the winding of a structure, i.e. an integer for a stable configuration. ϕ is even under inversion, thus a broken inversion symmetry is not necessarily connected to $\phi \neq 0$ [199].

In Fig. 4.18, panel (ii), the winding density ϕ of the spin crystal is plotted as function of x and y for a plane perpendicular to the magnetic field H. Integration of ϕ over one primitive unit cell of the spin crystal (marked in broken red lines in Fig. 4.18, panel (ii)) then yields a topological charge

$$C_{top} = \int \phi(\mathbf{r}) \mathrm{d}^2\mathbf{r} = -1\,. \tag{4.17}$$

The sign of the topological charge thereby implies that the magnetization is oriented antiparallel to the applied magnetic field in the core of the vortex-like knots.

In contrast, the winding density vanishes for a single domain helical phase, as there, the normalized direction of the magnetization $\mathbf{n} = \mathbf{M}(\mathbf{r})/|\mathbf{M}(\mathbf{r})|$ only depends on one single space coordinate. This is also the case in the presence of a uniform magnetization in the conical phase. Thus, no smooth deformation without suppressing the magnetization to zero of the helical or conical phase can lead to the spin crystal as given in Fig. 4.18, panel (i). The helical/conical phase and the spin crystal thus belong to different topological groups.

This implies that the spin crystal can be interpreted as crystal, formed by the condensation of topological solitons of the magnetization. The spin crystal in the A-phase of MnSi can thus be described as skyrmion lattice, similar to a vortex lattice, found in superconductors. Due to the anti-parallel alignment of magnetic moments with respect to the magnetic field in the core of the skyrmion lines, the skyrmion lattice is in fact an anti-skyrmion lattice.

The non-trivial topology of the skyrmion lattice naturally leads to first order phase boundaries, consistent with experimental observations, explaining the stability of our solution. Note, that a fundamental difference to the vortex lattice characteristic of type II superconductors arises due to the coupling of the superconducting order parameter ψ to a gauge field, leading to the quantization of the magnetic flux. In contrast, the coupling to a gauge field is missing for the skyrmion lattice. The magnetic vortices, identified in the A-phase of MnSi thus can be described as *global* vortices (cf. section (1).

Further Remarks

We finally address issues, which are not covered by our theoretical account:

A weak deviation of the six-fold structure of the spin crystal to an ellipsoidal shape was observed for sample II for certain crystalline directions. It is assumed that a weak distortion can be caused by the weak pinning of the skyrmion lattice to the crystal lattice, akin to effects, observed for vortex lattices (cf. section (3)). However, the effect is weak and may be related to demagnetizing effects and instrumental artifacts as well. A systematic mapping of the structure of the skyrmion lattice as function of the underlying crystalline direction is proposed.

The mean-field model shows that the spin crystal is most stable when the modulation of the magnetic moments is minimal. Measurements of the uniform magnetization $\mathbf{M}_f$ show, that $\mathbf{M}_{f,A-phase}(T = 28\,\mathrm{K}) \sim 0.1\,\mu_\mathrm{B}$, which approximately corresponds one third of the spontaneous moment at $T = 28\,\mathrm{K}$. This yields that a considerable modulation of the magnetic moments is present. However, the delicate influence of phase coexistence with the conical phase, induced by demagnetizing fields and surface effects is unclear. Further measurements of the uniform magnetization for different sample geometries will help to quantify the detailed structure of the spin crystal and the precise distribution of magnetic moments.

Neutron scattering experiments do not couple directly to topology: A multi-$\mathbf{q}$ single domain state, as proposed for the skyrmion lattice thus cannot be ultimatively distinguished from a single-$\mathbf{q}$ multi-domain state. However, the fact that a six-fold scattering pattern is observed independent of the underlying crystalline orientation indicates that a single-$\mathbf{q}$ multi-domain state is very unlikely. This is underscored by the equally populated domains of the spin crystal leading to six diffraction spots [5]. In contrast, the domain population of the helical phase is inhomogeneous for most cases and additionally exhibits strong hysteretic behaviour.

In contrast to neutron diffraction, measurements of the Hall effect are sensitive to the magnetic topology. In recent measurements, an additional contribution to the anomalous Hall-effect was identified in the A-phase of MnSi [197]. When the conduction electrons are forced to follow the local magnetization $\mathbf{M}(\mathbf{r})$, they acquire a Berry's phase [199]. This effect may be regarded as extra effective field, proportional to the winding density ϕ. The integrated winding density is non-zero for the skyrmion lattice in the A-phase, but $\phi = 0$ for the trivial topology of the helical and conical phase. This additional contribution proves the existence of a skyrmion lattice in MnSi.

In our theoretical account, the structure and the topological properties of the skyrmion lattice emerge from the superposition of three single-$\mathbf{k}$ helices. This naturally leads to a fixed spacing of the skyrmion-lines which is identical to the pitch λ_h and the fixed hexagonal structure of the skyrmion lattice. In contrast, Bodanov and coworkers [21] use

[5] Diffraction spots lying on the vertical axis exhibit lower intensity due to the summation over a rocking scans with respect to a vertical axis.

a circular cell method to calculate the free energy of a single knot of the magnetization [6] surrounded by the conical phase and arrange these knots to a hexagonal lattice similar to the one introduced in our work. However, they find that the conical phase still represents the groundstate of the system [18]. In our study we show, that the difference of the free energy of the skyrmion lattice with respect to the conical phase is small and that introducing Gaussian fluctuation lowers the free energy of the skyrmion lattice. Using [21] and additionally introducing thermal fluctuation can provide a theoretical ansatz to evaluate the stability of different skyrmion phases. In analogy to the different phases of superconducting vortex matter, a dilute skyrmion gas, molten skyrmion liquids or skyrmion glasses may be introduced.

[6] Similar to the technique used for superconducting vortex lattices.

4.4.5 Conclusion and Outlook

Conclusion

By means of small angle neutron scattering, we established the existence of a skyrmion lattice in the A-phase of the weak itinerant helical magnet MnSi: The skyrmion lattice is characteristic of the condensation of topological knots of the magnetization into a macroscopic lattice in the presence of a magnetic field. Similar to vortex lattices in superconductors, the orientation of the skyrmion lattice is driven by the direction of the magnetic field, hence is independent of the orientation of the underlying crystal lattice. Within a mean field model including Gaussian fluctuations, we confirm that a magnetic spin crystal — composed of a superposition of three single-$\mathbf{k}$ helices under 120° with respect to each other and perpendicular to the applied magnetic field — forms a stable ground state. The integration of the winding density over one unit cell of the spin crystal proves a stable, non-trivial topology with a topological charge $C_{top} = -1$.

Measurements of the Hall effect, where an additional contribution to the anomalous Hall effect is attributed to the Berry's phase, the conduction electrons collect due to the non-trivial spin structure in real space proves the existence of stable, topological solitons of the magnetization. In contrast to earlier theoretical work [18], where a skyrmion lattice was stabilized by an additional artificial parameter in zero field, we show that it is sufficient to include the effects of thermal fluctuations to stabilize skyrmion lattices in a magnetic field.

Outlook

Our study paves the way to further detailed small angle neutron scattering studies of the magnetic properties of MnSi. In particular, the structural and dynamic properties of the possible intermediate phase in vicinity of T_c and the pressure induced partially ordered state will be investigated. Moreover, transport measurements of the anomalous Hall effect are foreseen in the pressure induced partially ordered phase to confirm a possible topological state. In contrast to the A-phase, both phases emerge in zero field. This raises the question if topological states in ferromagnets can form stable ground states at zero field as well. In addition, a systematic mapping of the pinning potentials and lock-in transitions of the skyrmion lattice with respect to the underlying crystalline direction is foreseen, using a MnSi sphere with constant demagnetizing factor. We point out, that a continuous pinning of the nearest neighbour direction of the skyrmion lattice in a crystalline $\langle 110 \rangle$ direction is impossible for all directions in space. The pinning has to vanish at least at two points on the unit sphere due to the *hairy ball* [7] theorem.

In the mean-field approximation, the skyrmion lattice appears as meta-stable state. Binz and Rosch [30] show that the difference of energy between the skyrmion lattice and the conical phase is lowered by thermal fluctuations and the skyrmion lattice assumes a stable ground state. The MIEZE technique, which is a variation of the neutron resonance

[7] It is not possible to comb a hairy ball without at least two discontinuities.

spin echo technique (NRSE), allows the determination of the *quasi-elastic* linewidth Γ with a very small energy resolution of a few μeV as function of magnetic field and temperature [202]. Preliminary measurements indicate an increased quasi-elastic linewidth in the A-phase compared to the helical phase at identical temperature. Parallel to the measurements of the *quasi-elastic* linewidth, first *inelastic* measurements of the spin-wave spectrum of the A-phase are performed currently on a cold triple axis spectrometer [203]. On a cold triple axis spectrometer, an energy resolution of 70 μeV can be achieved. Both the quasi-elastic as well as the inelastic measurements will provide helpful insight in the fluctuation spectrum of the spin crystal in the A-phase of MnSi.

The influence of doping and disorder on the evolution of the skyrmion lattice was addressed recently in the B20 siblings of MnSi, $Fe_{1-x}Co_xSi$, $Mn_{1-x}Co_xSi$ and $Mn_{1-x}Fe_xSi$: Measurements of the specific heat, the AC-susceptibility and the Hall effect [204] in combination with small angle neutron scattering experiments [166, 205], proved the existence and stability of skyrmion lattices in the A-phase of doped compounds as well. Fig., 4.19 depicts the typical six-fold scattering patterns of the skyrmion lattice in $Fe_{1-x}Co_xSi$ for $x = 0.2$ in panel (i), $Mn_{1-x}Fe_xSi$ for $x = 0.08$ in panel (ii) and $Mn_{1-x}Co_xSi$ for $x = 0.02$ panel (iii).

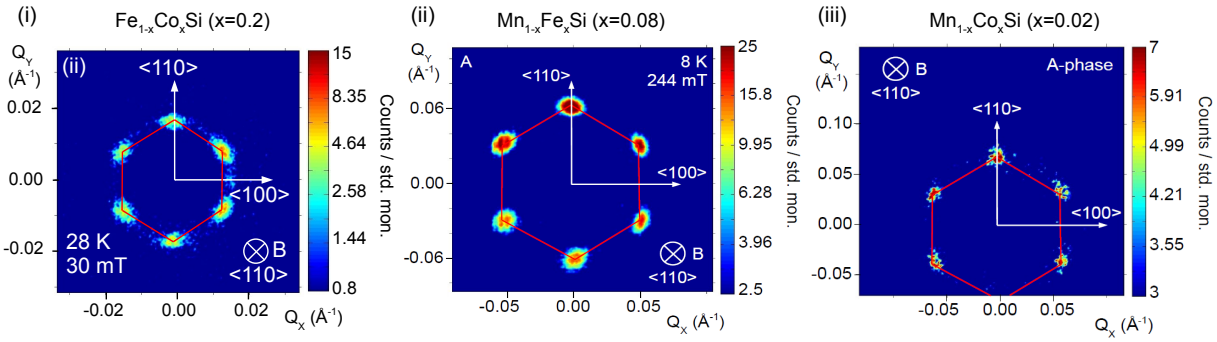

Figure 4.19: Typical six-fold scattering patterns of the skyrmion lattice in the doped B20 compounds $Fe_{1-x}Co_xSi$ for $x = 0.2$ panel (i), $Mn_{1-x}Fe_xSi$ for $x = 0.08$ in panel (ii) and $Mn_{1-x}Co_xSi$ for $x = 0.02$ panel (iii).

For both $Fe_{1-x}Co_xSi$ as well as MnSi doped with Fe or Co, the Skyrmion lattice exhibits increasing hysteretic behaviour and increasing disorder with increasing doping x. Moreover, the temperature regime of the A-phase simultaneously increases with respect to the helical phase upon increasing doping. However, especially for high doping, a clear determination of the phase transitions is intricate due to the large amount of disorder.

Interestingly, measurements of specific heat and AC-susceptibility furthermore indicate [205] that with increasing doping x an intermediate phase opens in vicinity of T_c in $Mn_{1-x}Co_xSi$ and $Mn_{1-x}Fe_xSi$: The transition temperature T_c of the *helical* phase systematically assumes lower values compared to the intermediate phase. Small angle neutron scattering measurements [205] reveal a distribution of intensity on a ring in the intermediate phase. Strong analogies are drawn to the possible existence of an intermediate phase in vicinity to T_c and the pressure induced partial order of undoped MnSi.

An important prerequisite enabling the existence of the Skyrmion lattice in pure MnSi

as well as in the doped systems $Mn_{1-x}Co_xSi$ and $Mn_{1-x}Fe_xSi$ and $Fe_{1-x}Co_xS$ is their helical magnetic structure, driven by a DM instability. The DM interaction is allowed by particular crystal symmetries, lacking inversion symmetry. However, a lack of space inversion is very common: Not only 65 of 230 space groups but also surfaces or interfaces break the inversion symmetry. This suggests that skyrmionic textures in fact represent a quite common structure in magnetism.

Chapter 5

Concluding Remarks

We have used both static as well as time resolved stroboscopic small angle neutron scattering as a versatile tool for the investigation of two different kinds of complex magnetic order characterized by topological properties: We have examined the static and dynamic properties of the vortex lattice of the superconducting model system niobium (chapter (3)) and we have proved that a skyrmion lattice exists in the A-phase of the archetypal helical magnet MnSi (chapter (4)). An overview of the properties of vortex lattices in superconductors and vortices with topological properties in ferromagnets was given in chapter (1). The fundamental principles of neutron scattering from superconducting vortex lattices and helical magnets have been introduced in chapter (2).

Our measurements show that the vortex lattices in superconductors and the skyrmion lattice, observed in the A-phase of MnSi, show intimate similarity however emerging from different physical backgrounds: Both the vortex lattice in a superconductor and the skyrmion lattice can be seen as a macroscopic lattice, formed by topological entities with particle-like properties, emerging from continuous fields.

A *superconducting* vortex is stabilized by the negative surface energy, associated with a normal- to superconducting interface, leading to a solution where the superconducting order parameter ψ exhibits periodic nodes. At these nodes the magnetic field penetrates the superconductor, shielded by a *circulating supercurrent*. Due to the continuity conditions of the superconducting phase $\oint \phi(\mathbf{r})\mathrm{d}\mathbf{s} = 2\pi n$ and the electromagnetic coupling to a gauge field, the magnetic flux of a single vortex is quantized and represents the flux quantum $\phi_0 = \hbar/2e$.

The *magnetic* vortices are stabilized by a rotation of the magnetic moments in a helical structure (similar to Bloch domain walls), provided by the DM interaction. A mean field ansatz including Gaussian fluctuations leads to the emergence of a stable ground state, a magnetic *spin crystal* with two-dimensional symmetry: The spin crystal can be regarded as crystal, composed of *topological knots of the magnetization*. The integration of the winding density proves that the spin-crystal belongs to a different topological class compared to the helical or conical phase, thus cannot be smoothly transformed into a helical or conical state without local suppression of the magnetization to zero. In contrast

to superconducting vortices, the order parameter is continuous and does not exhibit nodes. The magnetic flux of a single vortex is not quantized due to the missing coupling to a gauge field [51].

The similarity of superconducting vortices and magnetic vortices raises the question, how the properties of superconducting vortex lattices can be translated to magnetic skyrmion lattices: In particular the variety of different superconducting vortex matter, where pinned vortex lattices, vortex liquids, vortex glassy states and vortex Bragg glasses have been identified, suggests that similar phases may also exist for magnetic vortices. It is also unknown at the moment whether magnetic vortices can exist as stable ground states in zero magnetic field. Further open questions concern the behaviour of magnetic vortices in the presence of transport currents and their emergence in thin film materials, leading to possible applications in new magnetic and logical devices.

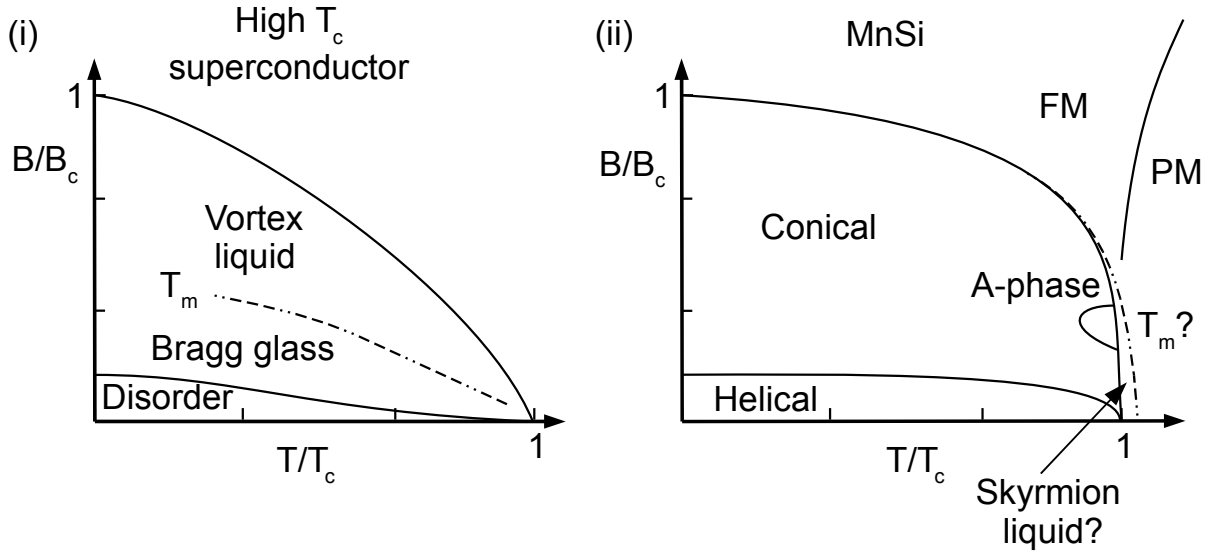

Figure 5.1: Panel (i) depicts a typical phase diagram of a high temperature superconductor. For low magnetic fields, the vortex lattice is disordered due to the large inter-vortex spacing. For increasing magnetic field, a Bragg glass vortex lattice emerges that undergoes a melting transition at the melting temperature T_m . Panel (ii) shows the magnetic phase diagram of MnSi at ambient pressure (a detailed description is given in section (4.3)). The dashed line indicates the possible intermediate phase observed in proximity of the transition temperature T_c.

Fig. 5.1, panel (i) depicts a schematic phase diagram of a high temperature superconductor as function of magnetic field and temperature. For low magnetic fields, the vortex lattice assumes a disordered state due to the large inter-vortex spacing and strong pinning. For increasing magnetic field, a vortex lattice Bragg glass emerges that undergoes a melting transition at the melting temperature T_m (a detailed description is given in section (3.3)). Panel (ii) of Fig. 5.1 shows the magnetic phase diagram of MnSi at ambient pressure (a detailed description is given in section (4.3)). The dashed line close above the transition temperature T_c indicates the possible intermediate phase observed by small angle neutron scattering [96, 95] and measurements of the specific heat [96]. It

was speculated [18] that the intermediate phase is characterized by a molten or disordered state of weakly stratified skyrmion lines, similar to molten superconducting vortex lattices.

Similar to superconducting vortex lattices, the dynamic and structural behaviour of skyrmion lattices is supposed to change at a melting transition. In our work, we have introduced a novel time resolved small angle neutron scattering technique for measurements of the intrinsic dynamic properties of superconducting vortex lattices. In addition, the newly realized MIEZE technique allows the application of neutron spin echo methods on samples in magnetic fields and ferromagnetic samples for precise measurements of the quasi-elastic line-width and dynamic. It is planned to apply both techniques to determine the structural and especially the dynamic properties of skyrmion lattices of undoped and doped materials to establish a complete phase diagram of the state of aggregation of skyrmion matter.

Chapter 6

Acknowledgments

This work would certainly not have been possible without the guidance, companionship and friendship of many different persons during the time of my thesis. I want to thank:

- **Prof. Peter Böni** for giving me the opportunity to work at his chair E21 of the Technische Universität München. Thank you very much for the open and creative spirit at your group and the interesting and fruitful discussions we had. Thank you for all your support and ideas but also for the freedom that I had to realize my own ideas. I really enjoyed the years at E21 very much. Isch guet gsi!
- **Prof. Christian Pfleiderer** for extraordinary support and advice - not only in physics - during the last four years. Thanks for all the inspiring and fruitful discussions we had. It was really a great pleasure working together with you on the MnSi and the vortex lattice projects. Thanks also for your interest and help concerning the progress of my scientific career.
- **Prof. Ted Forgan, Mark Laver, Jon White, Rich Heslop and Rich Lycett** from the University of Birmingham for introducing me into the world of vortex lattices. Thank you for your ideas, advice and support during the experiments we did together at the ILL, at PSI and in München. Without your help preparing and annealing the niobium sample, this work would not have been possible.
- **Dr. Robert Georgii** not only for the support concerning the experiments on MIRA. Thank you also very much for the great freedom I had working on MIRA and thanks a lot for many helpful discussions and shared activities.
- **Dr. Marc Janoschek** for many inspiring and open discussions about physics, MnSi, TeX and many other things. Thank you for providing the TeX template for this thesis and for proofreading the manuscript. Thanks very much for all the shared activities from biking to nightlife!
- **Prof. Achim Rosch, Dr. Benedikt Binz, Dr. Markus Garst and Dr. Mathias Vojta** from the Universität zu Köln for their very strong theoretical support and input during the MnSi skyrmion lattice project and the spin-torque measurements.

- **Dr. Ernst Helmut Brandt** from MPI Stuttgart for the fruitful discussions we had on vortex lattice elasticity and symmetries. Thank you very much for your theoretical support and for proofreading the vortex lattice chapters of this thesis.
- **Dr. Albrecht Wiedenmann and Dr. Uwe Keiderling** from Helmholtz Zentrum Berlin (former HMI) for their support during the experiments on V4. Thank you for the "extra days" and thank you very much for giving me the freedom to install our special magnetic field setup on the instrument.
- **Florian Jonietz and Tim Adams** for their support during the measurements on MnSi and $Fe_{1-x}Co_xSi$ we performed together on MIRA. Thanks for your tolerance and accurate work, thanks for the great time we had! And last but not least thanks for your enormous support during our MIRATHLON in March and April 2008.
- **Andreas Neubauer, Wolfgang Münzer and Andreas Bauer** not only for providing many very nice MnSi, FeCoSi, MnFeSi and MnCoSi crystals but also thank you very much for the great time we spent together.
- **Günter Behr** from the IFW Dresden for providing the ultra pure niobium sample.
- **Christian Franz -** Thank you specially for the bulk measurements on the $Fe_{1-x}Co_xSi$ and $Mn_{1-x}Fe_xSi$ samples during the final days of your diploma thesis. Thank you for many discussions about physics and running.
- **Reinhard Schwikowski, Andreas Mantwill and Peter Granz.** Thank you very much for your technical support during the measurements on MIRA and on V4. Without your great work, many of the experiments would not have been possible.
- I also want to specially mention the team of the **workshop** and the team from the **crystal lab** of the Physik Department of the Technische Universität München for their help and cooperation.
- **All the people of E21** for the creative and open spirit you created at the institute and on many conferences we visited together. Thanks to Andi, Stefan, Marc, Chris, Robert, Tim, Flo, Andreas, Wolfgang, Felicitas, Sarah, Christoph, Matze, Michi, Sylvia and of course Barbara for lots of discussions, jokes, laughter, shared activities and parties! Thanks for the friendship and for an awesome time!
- **My roommates and friends** Christoph, Michael, Kerstin, Oli, Alex, Kai, Betty, Roman, Thomas and Oscar for their companionship and friendship. You supported me in many occasions, each of you in a unique way. Thanks for the wonderful time we shared.
- **My family** not only for supporting me during my whole life but also providing me with the freedom and teaching me the curiosity to realize my own ideas and dreams. Thank you for your love, support and understanding.
- **Elena** — One should keep the best for the end. Thanks for your love and understanding. You are my source of inspiration and you have always been there, when I needed you. I enjoy every second we spend together.

Chapter 7

List of Publications

1. Magnetic field dependence of the domain populations in the skyrmion lattice of $Fe_{1-x}Co_xSi$
   T. Adams, S. Mühlbauer, A. Neubauer, W. Münzer, F. Jonietz, R. Georgii, B. Pedersen, P. Böni, A. Rosch, C. Pfleiderer,
   submitted to *Journal of Physics: Conference Series* (2009)

2. Skyrmion lattice in a doped semiconductor
   W. Münzer, A. Neubauer, S. Mühlbauer, C. Franz, T. Adams, F. Jonietz, R. Georgii, P. Böni, B. Pedersen, M. Schmidt, A. Rosch and C. Pfleiderer,
   arXiv:0903.2587, submitted to *Phys. Rev. Lett.* (2009)

3. Quantum order in the chiral magnet MnSi
   C. Pfleiderer, A. Neubauer, S. Mühlbauer, F. Jonietz, M. Janoschek, S. Legl, R. Ritz, W. Münzer, C. Franz, P. Niklowitz, T. Keller, R. Georgii, P. Böni, B. Binz, A. Rosch, U. K. Rössler and A. N. Bogdanov,
   Journal of Physics: Condensed Matter, **21** 164215 (2009).

4. Morphology of the superconducting vortex lattice in ultra-pure niobium
   S. Mühlbauer, C. Pfleiderer, P. Böni, M. Laver, E. M. Forgan, D. Fort, U. Keiderling and G. Behr,
   Phys. Rev. Lett., **102** 136408 (2009).

5. New angles on the border of antiferromagnetism in NiS_2 and URu_2Si_2
   P. G. Niklowitz, C. Pfleiderer, S. Mühlbauer, P. Böni, T. Keller, P. Link, J. A. Wilson, M. Vojta and J A. Mydosh,
   Physica B (2009), doi:10.1016/j.physb.2009.07.026

6. Intrinsic bulk vortex dynamics revealed by time resolved small angle neutron scattering
   S. Mühlbauer, C. Pfleiderer, P. Böni, E. M. Forgan, E. H. Brandt, A. Wiedenmann and U. Keiderling,
   Physica B (2009), doi:10.1016/j.physb.2009.07.080

7. Structure and degeneracy of vortex lattice domains in pure superconducting nio-

bium: A small-angle neutron scattering study
M. Laver, C. J. Bowell, E. M. Forgan, A. B. Abrahamsen, D. Fort, C. D. Dewhurst, S. Mühlbauer, D. K. Christen, J. Kohlbrecher, R. Cubitt and S. Ramos,
Phys. Rev. B, **79** 014518 (2009).

8. Skyrmion lattice in a chiral magnet
S. Mühlbauer, B. Binz, F. Jonietz, C. Pfleiderer, A Rosch, A. Neubauer, R. Georgii and P. Böni,
Science, **323** 915919 (2009).

9. Field and temperature dependence of the magnetization in ferromagnetic EuO thin films
S. Mühlbauer, P. Böni, R. Georgii, A. Schmehl, D. G. Schlom and J. Mannhart,
Journal of Physics: Condensed Matter, **20** 104230 (2008).

10. Elliptic neutron guides - focusing on tiny samples
S. Mühlbauer, P. G. Niklowitz, M. Stadlbauer, R. Georgii, P. Link, J. Stahn and P. Böni,
Nuclear Instruments and Methods in Physics Research A, **568** 77-80 (2008).

11. Epitaxial integration of the high spin polarization ferromagnetic semiconductor EuO with silicon and GaN
A. Schmehl, V. Vaithyanathan, A. Herrnberger, S. Thiel, C. Richter, M. Liberati, T. Heeg, M. Rückerath, L. F. Kourkoutis, S. Mühlbauer, P. Böni, D. A. Muller, Y. Barash, J. Schubert, Y. Idzerda, J. Mannhart and D.G. Schlom,
Nature Materials, **6** 882 887 (2007).

12. Multiple small angle neutron scattering (MSANS): A new two-dimensional ultra small angle neutron scattering technique
C. Grünzweig, T. Hils, S. Mühlbauer, M. Ay, K. Lorenz, R. Gerorgii, R. Gähler and P. Böni,
Appl. Phys. Lett., **91** 203504 (2007).

13. MIRA: Very cold neutrons for new methods
R. Georgii, N. Arend, P. Böni, D. Lamago, S. Mühlbauer and C. Pfleiderer,
Neutron News, **18** 2 (2007).

14. Performance of an elliptically tapered neutron guide
S. Mühlbauer, P. Böni, U. Filges, C. Schanzer, M. Stadlbauer and J. Stahn,
Physica B, **1247** 385-386 (2006).

Appendix A

Appendix

A.1 Resolution of Small Angle Neutron Scattering Instruments

We already have introduced in section (2) that small angle neutron scattering is a versatile tool for the measurement of large nuclear and magnetic structures on scales between 100 and 10^4 Å. The measured quantity is the scattering function $S(\mathbf{q})$ in reciprocal space, given by the Fourier transform of the scattering length distribution $G(\mathbf{r})$ in real space. For the scattering vector $\mathbf{q}$ follows

$$|\mathbf{q}| = 2\frac{2\pi}{\lambda}\sin\theta \tag{A.1}$$

with the scattering angle 2θ. Large structures in real space thus lead to small $\mathbf{q}$ vectors and small scattering angles.

For a small angle neutron scattering instrument, a large neutron wavelength λ and a tight collimation of the neutron beam is necessary to resolve small scattering angles. A schematic setup of a small angle neutron scattering instrument is given in Fig. A.1, panel (i), whereby the mostly used pinhole setup is depicted: The instrument consists of a variable collimation system with a source aperture and a sample aperture with radii R_1 and R_2, separated by the distance L_1, situated after the a monochromator or velocity selector. The position sensitive two-dimensional detector is situated at the distance L_2 to the sample.

The instrumental resolution of such a small angle neutron scattering instrument is mainly defined by three parameters: (i) The collimation of the beam, as defined by the aperture system. (ii) The monochromacity of the neutron beam and (iii) the spatial resolution of the neutron detector. In the following, we derive the resolution function of a small angle scattering setup according to [206], where the different contributions are approximated by Gaussian functions.

For our experiments on the vortex lattice structures performed at the instrument V4 at BENSC [114] (cf. chapter (3)) and the measurements of the magnetic structure of MnSi

(cf. chapter (4)) performed at the instrument MIRA at FRM II [115], the effects of finite neutron beam collimation dominate the instrumental resolution. We thus mainly focus on the effects of finite collimation for our calculation.

According to Fig. A.1, panel (ii), we define $\Delta\beta_1$ as FWHM value of the neutron beam divergence in the scattering plane and $\Delta\beta_2$ as FWHM of the neutron beam divergence perpendicular to the scattering plane, respectively. For a collimation system as given in Fig. A.1 panel (i) and (iii), consisting of a source aperture with radius R_1, a sample aperture with radius R_2 at the distance L_1 to the source aperture and for a sample detector distance L_2 then follows for $\Delta\beta_1$ and $\Delta\beta_2$ [206]

$$\begin{aligned}
\Delta\beta_1 &= \frac{2R_1}{L_1} - \frac{1}{2}\frac{R_2^2}{R_1}\frac{\cos^4(2\theta)}{L_2^2 L_1}\left(L_1 + \frac{L_2}{\cos^2(2\theta)}\right)^2 \quad \text{for } a_1 \geq a_2 \\
\Delta\beta_1 &= 2R_2\left(\frac{1}{L_1} + \frac{\cos^2(2\theta)}{L_2}\right) - \frac{1}{2}\frac{R_1^2}{R_2^2}\frac{L_2}{L_1} \\
&\quad \times \frac{1}{\cos^2(2\theta)(L_1 + L_2/\cos^2(2\theta))} \quad \text{for } a_1 < a_2
\end{aligned} \tag{A.2}$$

and

$$\begin{aligned}
\Delta\beta_2 &= \frac{2R_1}{L_1} - \frac{1}{2}\frac{R_2^2}{R_1}\frac{\cos^2(2\theta)}{L_2^2 L_1}\left(L_1 + \frac{L_2}{\cos(2\theta)}\right)^2 \quad \text{for } a_1 \geq a_2 \\
\Delta\beta_2 &= 2R_2\left(\frac{1}{L_1} + \frac{\cos(2\theta)}{L_2}\right) - \frac{1}{2}\frac{R_1^2}{R_2^2}\frac{L_2}{L_1} \\
&\quad \times \frac{1}{\cos(2\theta)(L_1 + L_2/\cos(2\theta))} \quad \text{for } a_1 < a_2
\end{aligned} \tag{A.3}$$

with the angles a_1 and a_2 as defined in Fig. A.1, panel (iii).

From $\Delta\beta_1$ and $\Delta\beta_2$, we define the azimuthal resolution $\Delta\beta_{az}$ in (°) and the radial resolution $\Delta\beta_{\mathbf{q}}$ in (Å^{-1}), as depicted in Fig. A.1 panel (iii), where we include the contributions from the finite detector resolution and the wavelength spread. In addition, the resolution in direction of $\mathbf{k_f}$ is denoted $\Delta\beta_{\mathbf{k_i}}$ in (°), which is mostly determined by the divergence of the neutron beam.

The modulus of the propagation vector $\mathbf{k}$ of the helical order in MnSi yields a Bragg angle of $\theta = 1.7°$ for a neutron wavelength of λ =9.7 Å as used for the experiments on MIRA. The width of the wavelength band yields 5 %. MIRA has been used either in a high resolution setup, characterized by $R_1 \sim 2\,\text{mm}$, $R_2 \sim 2\,\text{mm}$, $L_1 = 1.5\,\text{m}$ and $L_2 = 1.3\,\text{m}$. This yields $\Delta\beta_1 = 0.35°$ and $\Delta\beta_2 = 0.35°$ for the high resolution setup. For the low resolution setup with $R_1 \sim 4\,\text{mm}$, $R_2 \sim 4\,\text{mm}$, $L_1 = 1.5\,\text{m}$, and $L_2 = 0.8\,\text{m}$ then follows $\Delta\beta_1 = 0.62°$ and $\Delta\beta_2 = 0.60°$. Including a detector resolution of 2 mm and a wavelength spread of 5% we finally obtain $\Delta\beta_{az} = 4°$, $\Delta\beta_{\mathbf{q}} = 0.004\,\text{Å}^{-1}$ and $\Delta\beta_{\mathbf{k_f}} = 0.35°$ for the high resolution setup and $\Delta\beta_{az} = 10°$, $\Delta\beta_{\mathbf{q}} = 0.006\,\text{Å}^{-1}$ and $\Delta\beta_{\mathbf{k_f}} = 0.63°$ for the low resolution setup.

The modulus of the **q**-vector of a vortex lattice is defined by the vortex lattice symmetry and the applied magnetic field, as given by eq. (2.24). For a six-fold vortex lattice symmetry $\mathbf{G}_{VL} = 0.0047\,\text{Å}^{-1}$ for $\mu_0 H$ =100 mT, $\mathbf{G}_{VL} = 0.0063\,\text{Å}^{-1}$ for $\mu_0 H$ =200 mT and $\mathbf{G}_{VL} = 0.0081\,\text{Å}^{-1}$ for $\mu_0 H$ =300 mT. For a neutron wavelength of λ =12 Å± 5.5%, a detector resolution of 10 mm, a source aperture of $R_1 \sim 10$ mm, a sample aperture of $R_2 \sim 2$ mm, a detector and sample distance of $L_1 = 12$ m and $L_2 = 12$ m, we finally obtain $\Delta\beta_{\mathbf{q}} = 0.0013\,\text{Å}^{-1}$, $\Delta\beta_{\mathbf{k_f}} = 0.15°$ and $\Delta\beta_{az} = 15°$ for $\mu_0 H$ =100 mT, $\Delta\beta_{az} = 10°$ for $\mu_0 H$ =200 mT and $\Delta\beta_{az} = 8°$ for a field of $\mu_0 H$ =300 mT.

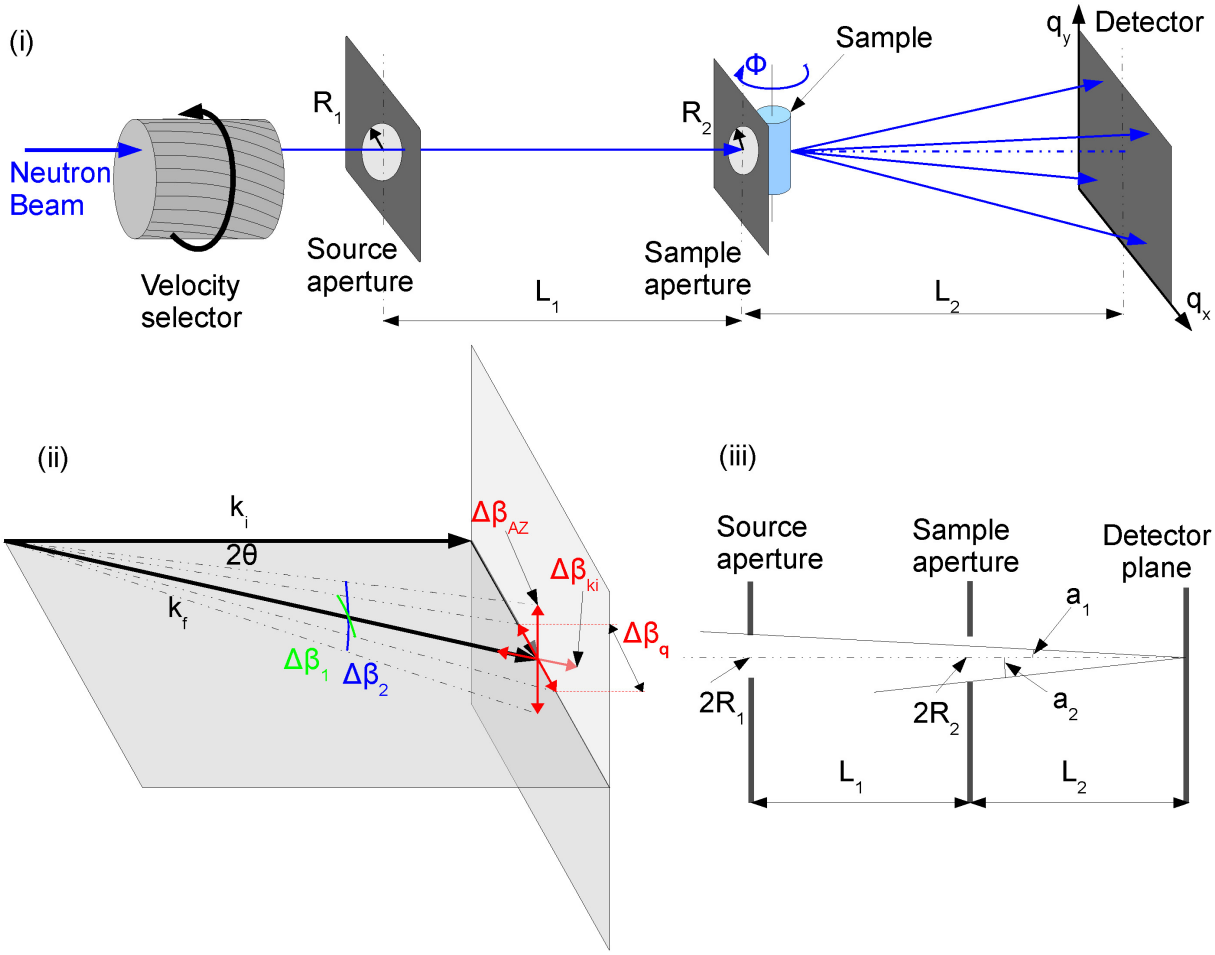

Figure A.1: Panel (i) shows a schematic drawing of a small angle scattering instrument. Panel (ii) depicts the connection of the beam divergences $\Delta\beta_1$ and $\Delta\beta_2$ with the instrumental resolution $\Delta\beta_{az}$, $\Delta\beta_{\mathbf{q}}$ and $\Delta\beta_{\mathbf{k_f}}$. Panel (iii) defines the angles a_1 and a_2, respectively.

Bibliography

[1] A. Huxley. *Neutron scattering from vortex lattices in superconductors, Chap. 18, pp. 301-320.* Solid State Sciences, Springer, 2002.

[2] Xu Du, Guhong Li, Eva Y. Andrej, M. Greenblatt, and P. Shuk. Ageing memory and glassiness of a driven vortex system. *Nature Physics*, 3:111, 2007.

[3] G. Li, E. Y. Andrej, Z. L. Xiao, P. Shuk, and M. Greenblatt. Onset of Motion and Dynamic Reordering of a Vortex Lattice. *Phys. Rev. Lett.*, 96:017009, 2006.

[4] E.Y. Andrej, Z.L. Xiao, O. Dogru, P. Shuk, and M. Greenblatt. Order Disorder Coexistence and Metastability in Vortex Lattices. *Condensed Matter Theories, Nova Science*, 18:159, 2003.

[5] Z.L. Xiao, E.Y. Andrej, and M. Higgins. Flow Induced Organization and Memory of a Vortex Lattice. *PRL*, 83:1664, 1999.

[6] D. P. Almond, M. J. Lea, and E. R. Dobbs. Ultrasonic evidence against multiple energy gaps in superconducting niobium. *Phys. Rev. Lett.*, 29(12):764–767, Sep 1972.

[7] V. Novotny and P. P. M. Meincke. Single superconducting energy gap in pure niobium. *Journal of Low Temperature Physics*, 18:147–157, 1975.

[8] M. Laver, E. M. Forgan, S. P. Brown, D. Charalambous, D. Fort, C. Bowell, S. Ramos, R. J. Lycett, D. K. Christen, J. Kohlbrecher, C. D. Dewhurst, and R. Cubitt. Spontaneous Symmetry-Breaking Vortex Lattice Transitions in Pure Niobium. *Phys. Rev. Lett.*, 96:167002, 2006.

[9] M. Laver, C. J. Bowell, E. M. Forgan, A. B. Abrahamsen, D. Fort, C. D. Dewhurst, S. Mühlbauer, D. K. Christen, J. Kohlbrecher, R. Cubitt, and S. Ramos. Structure and degeneracy of vortex lattice domains in pure superconducting niobium: A small-angle neutron scattering study. *Phys. Rev. B*, 79:014518, 2009.

[10] S. Mühlbauer, C. Pfleiderer, P. Böni, E.M. Forgan, M. Laver, U. Keiderling, G. Behr, and D. Fort. Morphology of the Superconducting Vortex Lattice in Ultra-Pure Niobium. *Phys. Rev. Lett.*, 99:99, 2009.

[11] A. Wiedenmann, U. Keiderling, K. Habicht, M. Russina, and R. Gähler. Dynamics of field-induced ordering in magnetic colloids studied by new time-resolved small-angle neutron-scattering techniques. *Phys. Rev. Lett.*, 97(5):057202, 2006.

[12] E. H. Brandt. Flux diffusion in high-T_c superconductors. *Z. Phys.B - Condensed Matter*, 80:167–175, 1990.

[13] P. H. Kes, J. Aarts, J. van den Berg, C. J. van der Beek, and J. A. Mydosh. Thermally assisted flux flow at small driving forces. *Supercond. Sci. Technol.*, 1:242–248, 1989.

[14] B. Binz and A. Vishwanath. Theory of helical spin crystals: phases, textures and properties. *Phys. Rev. B*, 74:214408, 2006.

[15] B. Binz, A. Vishwanath, and V. Aji. Theory of the Helical Spin Crystal: A Candidate for the Partially Ordered State of MnSi. *Phys. Rev. Lett.*, 96(20):207202, 2006.

[16] I. Fischer, N. Shah, and A. Rosch. Crystalline phases in chiral ferromagnets: Destabilization of helical order. *Phys. Rev. B*, 77(2):024415, 2008.

[17] S. Tewari, D. Belitz, and T. R. Kirkpatrick. Blue Quantum Fog: Chiral Condensation in Quantum Helimagnets. *Phys. Rev. Lett.*, 96(4):047207, 2006.

[18] U. K. Rößler, A. N. Bogdanov, and C. Pfleiderer. Spontaneous skyrmion ground states in magnetic metals. *Nature*, 442:797–801, 2006.

[19] A. Bogdanov and A. Hubert. Thermodynamically stable magnetic vortex states in magnetic crystals. *Jour. Mag. Mag. Mater.*, 138:255–259, 1994.

[20] A. N. Bogdanov. New localized solutions of the nonlinear field equations. *Sov. Phys. JETP*, 62:247, 1995.

[21] A. N. Bogdanov and D. A. Yablonskii. Thermodynamically stable "vortices" in magnetically ordered crystals. The mixed state of magnets. *Sov. Phys. JETP*, 68:101, 1989.

[22] A. N. Bogdanov and U. K. Rößler. Chiral Symmetry Breaking in Magnetic Thin Films and Multilayers. *Phys. Rev. Lett.*, 87(3):037203, Jun 2001.

[23] I. E. Dzyaloshinskii. A thermodynamic theory of weak ferromagnetism of antiferromagnets. *J. Phys. Chem Solids*, 4:241, 1958.

[24] T. Moriya. Anisotropic superexchange interaction and weak ferromagnetism. *Phys. Rev.*, 120:91, 1960.

[25] G. G. Lonzarich and L. Taillefer. Effect of spin fluctuations on the magnetic equation of state of ferromagnetic or nearly ferromagnetic metals. *J. Phys. C: Solid State Phys.*, 18:4339, 1985.

[26] C. Thessieu, C. Pfleiderer, A. N. Stepanov, and J. Flouquet. Field Dependence of the Magnetic Quantum Phase Transition in MnSi. *Phys. Rev. Lett.*, 9:6677, 1997.

[27] S. V. Grigoriev, S. V. Maleyev, A. I. Okorokov, Yu. O. Chetverikov, and H. Eckerlebe. Field-induced reorientation of the spin helix in MnSi near T_c. *Phys. Rev. B*, 73(22):224440, 2006.

[28] B. Lebech. *Recent Advances in Magnetism of Transition Metal Compounds, p. 167.* World Scientific, Singapore, 1993, 1993.

[29] B. Lebech, P. Harris, J. S. Pedersen, K. Mortensen, C. I. Gregory, N. R. Bernhoeft, M. Jermy, and S. A. Brown. Magnetic phase diagram of MnSi. *J. Magn. Magn. Mater.*, 140-144:119–120, 1995.

[30] S. Mühlbauer, B. Binz, F. Jonietz, C. Pfleiderer, P. Böni, A. Rosch, A. Neubauer, and R. Georgii. Skyrmion lattice in a chiral Magnet. *Science*, 323:5916, 2009.

[31] P. Bak and M. Høgh Jensen. Theory of helical magnetic structures and phase transitions in $MnSi$ and $FeGe$. *J.Phys C: Solid St. Phys.*, 12:L881–5, 1980.

[32] A. A. Abrikosov. On the magnetic properties of superconductors of the second group. *Zh. Eksp, Thor. Fiz (Engl Transl. 1957 Sov. Phys. JETP* **5** *1174)*, 32:1442, 1957.

[33] K.B. Davis, M.O. Mewes, M.R. Andrews, N.J. van Druten, D.S. Durfee, D.M. Kurn, and W. Ketterle. Bose-Einstein Condensation in a Gas of Sodium Atoms. *Phys. Rev. Lett.*, 75:3696–2973, 1995.

[34] E. H. Brandt, J. Vanacken, and V. V. Moshchalkov. Vortices in Physics. *Physica C*, 369:1–0, 2002.

[35] E. H. Brandt. Vortices in Superconductors. *Physica C*, 369:10–20, 2002.

[36] R. Descartes. *Principia philosophiae.* Amsterdam, 1644.

[37] `http://en.wikipedia.org/wiki/Spiral_galaxy`.

[38] `http://en.wikipedia.org/wiki/Von_Karman_vortex_street`.

[39] `http://en.wikipedia.org/wiki/Tornado`.

[40] E. J. Yarmchuk, M. J. V. Gordon, and R. E. Packard. Observation of stationary vortex arrays in rotating superfluid helium. *Phys. Rev. Lett.*, 43:214–217, 1979.

[41] `http://cua.mit.edu/ketterle_group/Projects_2001/Vortex_lattice/Vortex.htm`, 2001.

[42] W. T. Kelvin. *Mathematical and Physical Papers.* Cambridge University Press, Cambridge, 1878.

[43] J. J. Thomson. *Treatise on Vortex Rings.* Macmillan, London, 1883.

[44] W. Thomson. On Vortex Atoms. *Trans. R. Soc. Edin.*, 6:94, 1867.

[45] T. von Kàrmàn. *The Wind and Beyond, Pioneer in Avation and Pathfinder in Space.* Little, Brown, 1967.

[46] L. Onsager. . *Nuovo Cimento*, 6:249, 1949.

[47] R. P. Feynman. . *Progress in Low Temperature Physics (ed. C. G. Gorter)*, pages 17–51, 1955.

[48] D. R. Tilley and J. Tilley. *Superfluidity and Superconductivity*. Wiley, New York, 1974.

[49] M. Greiner, C. A. Regal, and D. S. Jin. Emergence of a Molecular Bose-Einstein Condensate from a Fermi Gas. *Nature*, 426:537, 2003.

[50] Portret von Ren Descartes, 1649, `http://en.wikipedia.org/`.

[51] N. Manton and P. Sutcliffe. *Topological Solitions*. Cambridge University Press, Cambridge, 2004.

[52] Soliton, `http://en.wikipedia.org/wiki/Soliton`.

[53] N. D. Mermin. The topological theory of defects in ordered media. *Rev. Mod. Phys.*, 51(3):591–648, Jul 1979.

[54] G. E. Brown (ed.). *Selected Papers, with Commentary, of Tony Hilton Royle Skyrme*. World Scientific, Singapore, 1994.

[55] M. C. Cross and P. C. Hohenberg. Pattern formation outside of equilibrium. *Rev. Mod. Phys.*, 65(3):851, Jul 1993.

[56] D. C. Wright and N. D. Mermin. Crystalline liquids: the blue phases. *Rev. Mod. Phys.*, 61(2):385–432, Apr 1989.

[57] S. L. Sondhi, A. Karlhede, S. A. Kivelson, and E. H. Rezayi. Skyrmions and the crossover from the integer to fractional quantum hall effect at small zeeman energies. *Phys. Rev. B*, 47(24):16419–16426, Jun 1993.

[58] D. Hsieh, D. Quian, L. Wray, Y. Xia, Y. Hor, R. Cava, and M. Hasan. A topological Dirac insulator in a quantum spin Hall phase. *Nature*, 452:970, 2008.

[59] M. Konig, S.Wiedmann, C. Brune, A. Roth, H. Buhmann, L. Molenkamp, X.-L. Qi, and S.-C. Zhang. Quantum Spin Hall Insulator State in HgTe Quantum Wells. *Science*, 318:766, 2007.

[60] M. J. Lawler, H.-Y. Kee, Y. B. Kim, and A. Vishwanath. Topological Spin Liquid on the Hyperkagome Lattice of $Na_4Ir_3O_8$. *Phys. Rev. Lett.*, 100(22):227201, 2008.

[61] E. M. Forgan, E. P. Gibbons, K. A. McEwen, and D. Fort. Observation of a quadruple-q magnetic structure in neodymium. *Phys. Rev. Lett.*, 62(4):470–473, Jan 1989.

[62] `http://hopf.chem.brandeis.edu/yanglingfa/pattern/t2/index.html`.

[63] `http://en.wikipedia.org/wiki/Blue_Phase_Mode_LCD`.

[64] `http://www.tcm.phy.cam.ac.uk/~nrc25/QHS.html`.

[65] W. Meissner and R. Ochsenfeld. Ein neuer Effekt bei Eintritt der Supraleitfähigkeit. *Die Naturwissenschaften*, 21:787, 1933.

[66] F. London and H. London. The Electromagnetic Equations of the Supraconductor. *Proc. Roy. Soc. (London)*, page 71, 1935.

[67] V. L. Ginzburg and L. D. Landau. . *Zh. Eksp. Teor. Fiz.*, 20:1064, 1950.

[68] D. Cribier, B. Jacrot, L. Madhav Rao, and B. Farnoux. Mise en evidence par diffraction de neutrons d'une structure periodique du champ magnetique dans le niobium supraconducteur. *Phys. Lett.*, 9:106–107, 1964.

[69] J. Bardeen, L. N. Cooper, and J. R. Schrieffer. Microscopic theory of superconductivity. *Phys. Rev.*, 106(1):162–164, Apr 1957.

[70] N. N. Bogoliubov. On a New Method in the Theory of Superconductivity. *Journal of Experimental and Theoretical Physics*, 34:1, 1958.

[71] D. D. Osheroff, R. C. Richardson, and D. M. Lee. Evidence for a New Phase of Solid 3He. *Phys. Rev. Lett.*, 28(14):885–888, Apr 1972.

[72] J. G. Bednorz and K. A. Mueller. Possible high Tc superconductivity in the Ba-La-Cu-O system. *Z. Physik*, pages 189–193, 1986.

[73] F. Steglich, J. Aarts, C. D. Bredl, W. Lieke, D. Meschede, W. Franz, and H. Schäfer. Superconductivity in the Presence of Strong Pauli Paramagnetism: $CeCu_2Si_2$. *Phys. Rev. Lett.*, 43(25):1892–1896, Dec 1979.

[74] Y. C. Kim, J. R. Thompson, J. G. Ossandon, D. K. Christen, and M. Paranthaman. Equilibrium superconducting properties of grain-aligned $HgBa_2Ca_2Cu_3O_{8+\delta}$. *Phys. Rev. B*, 51(17):11767–11772, May 1995.

[75] L. Gao, Y. Y. Xue, F. Chen, Q. Xiong, R. L. Meng, D. Ramirez, C. W. Chu, J. H. Eggert, and H. K. Mao. Superconductivity up to 164 K in $HgBa2Ca_{m-1}Cu_mO_{2m+2+\delta}$ (m=1, 2, and 3) under quasihydrostatic pressures. *Phys. Rev. B*, 50(6):4260–4263, Aug 1994.

[76] Y. Kamihara, H. Hiramatsu, M. Hirano, R. Kawamura, H. Yanagi, T. Kamiya, and H. Hosono. Iron-Based Layered Superconductor: LaOFeP. *J. Am. Chem. Soc.*, 128(31):10012–10013, 2006.

[77] N. Reyren, S. Thiel, A. D. Caviglia, L. Fitting Kourkoutis, G. Hammerl, C. Richter, C. W. Schneider, T. Kopp, A.-S. Ruetschi, D. Jaccard, M. Gabay, D. A. Muller, J.-M. Triscone, and J. Mannhart. Superconducting Interfaces Between Insulating Oxides. *Science*, 317(5842):1196–1199, 2007.

[78] C. Pfleiderer. Superconducting phases of f-electron compounds. *In preparation*, page n.a., 2009.

[79] M. R. Eskildsen, A. B. Abrahamsen, V. G. Kogan, P. L. Gammel, K. Mortensen, N. H. Andersen, and P. C. Canfield. Temperature Dependence of the Flux Line Lattice Transition into Square Symmetry in Superconducting $LuNi_2B_2C$. *Phys. Rev. Lett.*, 86(22):5148–5151, May 2001.

[80] N. Nakai, P. Miranović, M. Ichioka, and K. Machida. Reentrant vortex lattice transformation in fourfold symmetric superconductors. *Phys. Rev. Lett.*, 89(23):237004, Nov 2002.

[81] B. Keimer, W. Y. Shih, R. W. Erwin, J. W. Lynn, F. Dogan, and I. A. Aksay. Vortex Lattice Symmetry and Electronic Structure in $YBa_2Cu_3O_7$. *Phys. Rev. Lett.*, 73(25):3459–3462, Dec 1994.

[82] A. D. Huxley, M.-A. Measson, K. Izawa, C. D. Dewhurst, R. Cubitt, B. Grenier, H. Sugawara, J. Flouquet, Y. Matsuda, and H. Sato. Flux-Line Lattice Distortion in $PrOs_4Sb_12$. *Phys. Rev. Lett.*, 93(18):187005, Oct 2004.

[83] A. D. Bianchi, M. Kenzelmann, L. DeBeer-Schmitt, J. S. White, E. M. Forgan, J. Mesot, M. Zolliker, J. Kohlbrecher, R. Movshovich, E. D. Bauer, J. L. Sarrao, Z. Fisk, C. Petrovic, and M. R. Eskildsen. Superconducting Vortices in $CeCoIn_5$: Toward the Pauli-Limiting Field. *Science*, 319:177–180, 2008.

[84] V. P. Mineev and K. V. Samokhin. *Introduction to Unconventional Superconductivity*. Gordon and Breach Science publishers, Amsterdam, 1999.

[85] R. Cubitt, E. M. Forgan, G. Yang, S. L. Lee, D. McK. Paul, H. A. Mook, M. Yethiraj, P. H. Kesparallel, T. W. Liparallel, A. A. Menovsky, Z. Tarnawski, and K. Mortensen. Direct observation of magnetic flux lattice melting and decomposition in the high-Tc superconductor $Bi_{2.15}Sr_{1.95}CaCu_2O_{8+x}$. *Nature*, 365:407–411, 1993.

[86] V. M. Vinokur, M. V. Feigelman, V. B. Geshkenbein, and A. I. Larkin. Resistivity of high-T_c superconductors in a vortex-liquid state. *Phys. Rev. Lett.*, 65:259–262, 1990.

[87] T. Klein, I. Joumard, S. Blanchard, J. Marcus, R. Cubitt, T. Giamarchi, and P. Le Doussal. A Bragg glass phase in the vortex lattice of a type II superconductor. *Nature*, 413:404, 2001.

[88] M. B. Maple, B. J. Taylor, Shi Li, N. A. Frederick, V. F. Nesterenko, and S. S. Indrakanti. Vortex- and Bragg-glass phases in bulk MgB_2. *Physica C: Superconductivity*, 387:131–136, 2003.

[89] G. Li, O. Dogru, E. Y. Andrej, P. Shuk, and M. Greenblatt. Dynamic phase boundary of a moving Bragg glass. *Physica C: Superconductivity*, 408:510–511, 2004.

[90] D. Charalambous, P. G. Kealey, E. M. Forgan, T. M. Riseman, M. W. Long, C. Goupil, R. Khasanov, D. Fort, P. J. C. King, S. L. Lee, , and F. Ogrin. Vortex motion in type-II superconductors probed by muon spin rotation and small-angle neutron scattering. *Pys. Rev. B*, 66:054506, 2002.

[91] F. Laube, G. Goll, J. Hagel, H. v. Loehneysen, D. Ernst, and T. Wolf. Superconducting energy gap distribution of MgB_2 investigated by point-contact spectroscopy. *Europhys. Lett.*, 56:296–301, 2001.

[92] E. Boaknin, M. A. Tanatar, J. Paglione, D. Hawthorn, F. Ronning, R. W. Hill, M. Sutherland, L. Taillefer, J. Sonier, S. M. Hayden, and J. W. Brill. Heat Conduction in the Vortex State of $NbSe2$: Evidence for Multiband Superconductivity. *Phys. Rev. Lett.*, 90(11):117003, Mar 2003.

[93] F. Mohamed, M. Troyer, G. Blatter, and I. Luk'yanchuk. Interaction of vortices in superconductors with κ close to 1/2. *Phys. Rev. B*, 65(22):224504, May 2002.

[94] A. B. Butenko, A. A. Leonov, A. N. Bogdanov, and U. K. Roessler. Stabilization of skyrmion textures by uniaxial distortions in noncentrosymmetric cubic helimagnets. *arXiv:0904.4842*, 2009.

[95] D. Lamago. *Critical Magnetic Fluctuations in Localized and Itinerant Magnets studied by Neutron Scattering.* PhD in Physics, Technische Universität München, 2006.

[96] M. Janoschek. *Investigation of the chiral magnets* $NdFe_3(^{11}BO_3)_4$ *and MnSi by means of neutron scattering.* PhD in Physics, Technische Unitversität München, 2008.

[97] C. Pfleiderer, D. Reznik, L. Pintschovius, H. v. Lohneysen, M. Garst, and A. Rosch. Partial order in the non-Fermi-liquid phase of MnSi. *Nature*, 427:227, 2004.

[98] G. E. Bacon. *Neutron Diffraction.* Claredon Press, Oxford, 1975.

[99] S. W. Lovesey. *Theory of Neutron Scattering from Condensed Matter Vol I/II.* Oxford Science Publications, 1984.

[100] G. L. Squires. *Introduction to the theory of thermal neutron scattering.* Dover Publications, 1978.

[101] G. Shirane, M. Shapiro, and J.M. Tranquada. *Neutron Scattering with a Triple-Axis Spectrometer - Basic Techniques.* Cambridge University Press, 2002.

[102] O. Halpern and M. R. Johnson. On the Magnetic Scattering of Neutrons. *Phys. Rev.*, 55(898), 1939.

[103] P. G. De Gennes. *Magnetism, Ed. G. T. Rado and H. Suhl, Vol. III, p.115.* Academic Press, New York, 1963.

[104] R. M. Moon, T. Riste, and W.C. Koehler. Polarization analysis of thermal neutron scattering. *Phys. Rev.*, 181(920), 1969.

[105] E. H. Brandt. Theory of small-angle neutron scattering from the imperfect vortex lattice in type-II superconductors. *Phys. Rev. B*, 18(11):6022–6034, Dec 1978.

[106] M. R. Eskildsen. *Small Angle Neutron Scattering Studies of the Flux Line Lattices in the Borocarbide Superconductors, PhD Thesis.* Riso National Laboratory, Denmark, 1998.

[107] B. W. Maxfield and W. L. McLean. Superconducting penetration depth of niobium. *Phys. Rev.*, 139(5A):A1515–A1522, Aug 1965.

[108] E. Bauer, G. Hilscher, H. Michor, Ch. Paul, E.W. Scheidt, A. Gribanov, Yu. Seropegin, H. Noel, M. Sigrist, and P. Rogl. Heavy Fermion Superconductivity and Magnetic Order in Noncentrosymmetric $CePt_3Si$. *Phys. Rev. Lett.*, 92(2):027003, Jan 2004.

[109] W. Pesch and L. Kramer. Local structure and thermodynamic properties of clean type II superconductors near H_{c1} at arbitrary temperature. *J. of Low Temp. Phys.*, 15:367, 1973.

[110] Z. Hao and J. R. Clem. Limitations of the London model for the reversible magnetization of type-II superconductors. *Phys. Rev. Lett.*, 67(17):2371–2374, Oct 1991.

[111] Y. A. Izyumov, V. E. Naish, and R. P. Ozerov. *Neutron Diffraction of Magnetic Materials*. Plenum Publishing Corporation, New York, 1991.

[112] S. V. Grigoriev, S. V. Maleyev, A. I. Okorokov, Yu. O. Chetverikov, R. Georgii, P. Boeni, D. Lamago, H. Eckerlebe, and K. Pranzas. Critical fluctuations in MnSi near T_c: A polarized neutron scattering study. *Phys. Rev. B*, 72:134420, 2005.

[113] S. V. Grigoriev, S. V. Maleyev, A. I. Okorokov, Yu. O. Chetverikov, P. Böni, R. Georgii, D. Lamago, H. Eckerlebe, and K. Pranzas. Magnetic structure of MnSi under an applied field probed by polarized small-angle neutron scattering. *Phys. Rev. B*, 74(21):214414, 2006.

[114] U. Keiderling and A. Wiedenmann. New SANS instrument at the BER II reactor in Belin, Germany. *Physica B: Condensed Matter*, 213-214:895–897, 1995.

[115] R. Georgii, P. Böni, M. Janoschek, C. Schanzer, and S. Valloppilly. MIRA–A flexible instrument for VCN. *Physica B*, 397:150–152, 2007.

[116] J. R. Clem. Simple model for the vortex core in a type II superconductor. *J. Low Temp. Phys.*, 18:427, 1974.

[117] E. H. Brandt. The flux-line lattice in type-II superconductors. *Rep. Prog. Phys.*, 58:1465–1594, 1995.

[118] E. Brandt. Precision Ginzburg-Landau Solution of Ideal Vortex Lattices for Any Induction and Symmetry. *Phys. Rev. Lett.*, 78(11):2208–2211, Mar 1997.

[119] E. H. Brandt. The Magnetic Field of Pure Superconductors with Non-Isolated Flux-Lines at Arbitrary Temperature. *Phys. Stat. Sol.*, 64:467, 1974.

[120] E. H. Brandt. Ginzburg-Landau Theory of the Vortex Lattice in Type-II Superconductors for All Values of κ and B. *Phys. Stat. Sol.*, 51:345, 1972.

[121] W. H. Kleiner, L. M. Roth, and S. H. Autler. Bulk Solution of Ginzburg-Landau Equations for Type II Superconductors: Upper Critical Field Region. *Phys. Rev.*, 133(5A):A1226–A1227, Mar 1964.

[122] G. Eilenberger. Ableitung verallgemeinerter Ginzburg-Landau-Gleichungen für reine Supraleiter aus einem Variationsprinzip. *Z. Phys.*, 182:427, 1965.

[123] G. Eilenberger. Transformation of Gorkov's equation for type II superconductors into transport-like equations . *Z. Phys.*, 214:195, 1968.

[124] S. T. Johnson, E. M. Forgan, S. H. Lloyd, C. M. Aegerter, S. L. Lee, R. Cubitt, P. G. Kealey, C. Ager, S. Tajima, A. Rykov, and D. McK. Paul. Flux-Line Lattice

Structures in Untwinned $YBa2Cu3O7-\delta$. *Phys. Rev. Lett.*, 82(13):2792–2795, Mar 1999.

[125] H. R. Kerchner, D. K. Christen, and S. T. Sekula. Equilibrium propertied of the fluxiod lattice in single crystal niobium. I. Magnetization measurements. *Phys. Rev. B*, 21:86, 1980.

[126] K. H.Berthel. *Beiträge zur Supraleitung, Elektronenstruktur und zum elektrischen Widerstand von hochreinem Niob*. Dissertation, Dresden, 1976.

[127] J. A. Sauls. The order parameter for the superconducting phases of UPt_3. *Advances in Physics*, 43:113–141, 1994.

[128] G. Goll. *Unconventional Superconductors, Experimental Investigation of the Order-Parameter Symmetry of Unconventional Superconductors*. Springer Berlin / Heidelberg, 2006.

[129] E. H. Brandt and A. Sudbo. On the tilt modulus of the flux-line lattice in type-II superconductors. *Physica C*, 180:426–440, 1991.

[130] R. Labusch. Calculation of the critical field gradients in type-II superconductors. *Crystal Lattice Defects*, 1:1–16, 1969.

[131] A.I. Larkin and Y. Ovchinnikov. Pinning in type II superconductors. *J. Low. Temp. Phys.*, 73:109, 1979.

[132] E. Zeldov, D. Majer, M. Konczykowski, V. B. Geshkenbein, V. M. Vinokur, , and H. Shtrikman. Thermodynamic Observation of First-Order Vortex-Lattice Melting Transition in Bi2Sr2CaCu2O8. *Nature*, 375:373–376, 1995.

[133] R. Okazaki, Y. Kasahara, H. Shishido, M. Konczykowski, K. Behnia, Y. Haga, T.D. Matsuda, Y. Onuki, T. Shibauchi, and Y. Matsuda. Vortex lattice melting in the heavy-fermion superconductor URu_2Si_2. *Physica C: Superconductivity*, 468:1258–1261, 2008.

[134] X. S. Ling, S. R. Park, B. A. McClain, S. M. Choi, D. C. Dender, and J. W. Lynn. Superheating and Supercooling of Vortex Matter in a Nb Single Crystal: Direct Evidence for a Phase Transition at the Peak Effect from Neutron Diffraction. *Phys. Rev. Lett.*, 86(4):712–715, Jan 2001.

[135] E. M. Forgan, S. J. Levett, P. G. Kealey, R. Cubitt, C. D. Dewhurst, and D. Fort. Intrinsic behavior of flux lines in pure niobium near the upper critical field. *Phys. Rev. Lett.*, 88(16):167003, Apr 2002.

[136] M. V. Feigel'man, V. B. Geshkenbein, A. I. Larkin, and V. M. Vinokur. Theory of collective flux creep. *Phys. Rev. Lett.*, 63(20):2303–2306, Nov 1989.

[137] Y. B. Kim, C. F. Hempstead, and A. R. Strnad. Flux-Flow Resistance in Type-II Superconductors. *Physical Review*, 139:1163–1172, 1965.

[138] E. H. Brandt. Properties of the ideal Ginzburg-Landau vortex lattice. *Phys. Rev. B*, 68:054506, 2003.

[139] A. Hubert. Attractive Interactions between Flux Lined as Derived from a Generalized Neumann-Tewordt Functional. *Phys. Stat. Sol. (b)*, 53:147, 1972.

[140] I. Luk'yanchuk. Theory of superconductors with κ close to $1/\sqrt{2}$. *Phys. Rev. B*, 63:174504, 2001.

[141] D. K. Christen, F. Tasset, S. Spooner, and H. A. Mook. Study of the intermediate mixed state of niobum by small angle neutron scattering. *Phys. Rev. B*, 15:4506, 1977.

[142] D. K. Christen, H. R. Kerchner, S. T. Sekula, and P. Thorel. Equilibrium propertied of the fluxiod lattice in single crystal niobium. II. Small-angle neutron diffraction measurements. *Phys. Rev. B*, 21:102, 1980.

[143] L. D. Landau. . *Zh. Eksp. Teor. Fiz.*, 7:371, 1937.

[144] L. D. Landau. . *Zh. Eksp. Teor. Fiz.*, 13:377, 1943.

[145] R. P. Huebener and J. R. Clem. Magnetic flux structures in superconductors - a conference summary. *Reviews of Modern Physics*, 46:409, 1974.

[146] R. Prozorov. Equilibrium Topology of the Intermediate State in Type-I Superconductors of Different Shapes. *Phys. Rev. Lett.*, 98:25700, 2007.

[147] M. Seul and D. Andelmann. Domain Shapes and Patterns: The Phenomenology of Modulated Phases. *Science*, 267:476, 1995.

[148] M. Menghini and R. J. Wijngaarden. Patterns close to the critical field in type-I superconductors. *Phys. Rev. B*, 75:014529, 2007.

[149] A. T. Dorsey and R. E. Goldstein. Shapes of flux domains in the intermediate state of type-I superconductors. *Phys. Rev. B*, 57:3058, 1998.

[150] R. P. Huebener. *Magnetic Flux Structures in Superconductors*. Springer-Verlag, 1979.

[151] U. Essmann and W. Traeuble. Ein hochauflösendes Verfahren zur Untersuchung magnetischer Strukturen von Supraleitern. *Phys. Stat. Sol.*, 18:813, 1966.

[152] A. O. Golubok and L. Y. Vinnikov. Observation of branching of domains of the Shubnikov phase in a niobium single crystal. *JETP Lett.*, 35:642, 1982.

[153] L. F. Mattheiss. Electronic structure of niobium and tantalum. *Phys. Rev. B*, 1(2):373–380, Jan 1970.

[154] "Zentralinstitut für Festkörperphysik und Werkstoffprüfung" of the "Akademie der Wissenschaften" of the German Democratic Republic.

[155] A. Koethe and J. I. Mönch. . *Mat. Trans, JIM*, 41:7, 2000.

[156] G. W. Webb. Low-temperature electrical resistivity of pure niobium. *Phys. Rev.*, 181:1127–1135, 1969.

[157] J. Schelten. *Anisotropy Effects in Type-II Superconductors, edited by H. W. Weber, p. 113.* Plenum, New York, 1977, 1977.

[158] K. Fischer and H. Teichler. . *Phys. Lett. A*, 458:402, 1977.

[159] L. Kramer. Thermodynamic behavior of type-ii superconductors with small κ near the lower critical field. *Phys. Rev. B*, 3(11):3821–3825, Jun 1971.

[160] E. Fawcett, W. A. Reed, and R. R. Soden. High-field galvanomagnetic properties of niobium and tantalum. *Phys. Rev.*, 159(3):533–539, Jul 1967.

[161] W. A. Reed and R. R. Soden. High-field galvanomagnetic properties of niobium. *Phys. Rev.*, 173(3):677–679, Sep 1968.

[162] Z. G. Xu, H. Drulis, J. W. Brill, L. E. De Long, and J-C. Hou. Vibrating reed study of a magnetically reversible region in Nb and $NbSe_2$. *Supercond. Sci. Technol.*, 5:491–494, 1992.

[163] P. Thorel, R. Kahn, Y. Simon, and D. Cribier. Creation and study of a vortex single crystal in superconducting niobium. *J. Physique*, 34:447, 1973.

[164] S. Mühlbauer. *Das Flussgitter in Niob. Untersuchungen mit polarisierten und unpolarisierten Neutronen.* Masters Thesis, München, 2005.

[165] E. H. Brandt. private communication, 2009.

[166] W. Münzer, A. Neubauer, S. Mühlbauer, C. Franz, T. Adams, F. Jonietz, C. Pfleiderer, A. Rosch, R. Georgii, P. Böni, B. Pedersen, M. Schmidt, and Y. Grin. Skyrmion Lattice in a Doped Semiconductor. *arXiv:0903.2587*, 2009.

[167] D. Kipping, R. Gähler, and K. Habicht. Small angle neutron scattering at very high time resolution: Principle and simulations of TISANE. *Physics Letters A*, 372:1541–1546, 2008.

[168] F. J. Morin. Magnetic Susceptibility of αFe_2O_3 and αFe_2O_3 with Added Titanium. *Phys. Rev.*, 78(6):819–820, Jun 1950.

[169] C. G. Shull, W. A. Strauser, and E. O. Wollan. Neutron diffraction by paramagnetic and antiferromagnetic substances. *Phys. Rev.*, 83(2):333–345, Jul 1951.

[170] B. N. Brockhouse. Antiferromagnetic Structure in Cr_2O_3. *J. Chem. Phys.*, 21:961—2, 1953.

[171] P. W. Anderson. New Approach to the Theory of Superexchange Interactions. *Phys. Rev.*, 115:2, 1959.

[172] P. A. Hansen. . *Risoe Report (thesis), Risoe National Laboratory, Gjellerup, Copenhagen*, No. 360:69, 1977.

[173] Y. Ishikawa, K. Tajima, D. Bloch, and M. Roth. Helical spin structure in manganese silicide MnSi. *Solid State Commun.*, 19:525, 1976.

[174] M. Ishida, Y. Endoh, S. Mitsuda, Y. Ishikawa, and M. Tanaka. Crystal Chirality and Helicity of the Helical Spin Density Wave in MnSi. II. Polarized Neutron Diffraction. *J. Phys. Soc. Jpn.*, 54:2975–2982, 1985.

[175] G. Shirane, R. Cowley, C. Majkrzak, J.B. Sokoloff, B. Pagonis, C. H. Perry, and Y. Ishikawa. Spiral magnetic correlation in cubic MnSi. *Phys. Rev. B*, 28(11), 1983.

[176] T. Moriya. *Spin Fluctuations in itinerant electron magnetism.* Springer, 1985.

[177] Y. Ishikawa and M. Arai. Magnetic Phase Diagram of MnSi near Critical Temperature Studied by Neutron Small Angle Scattering. *J. Phys. Soc. Jpn.*, 53:2726–2733, 1984.

[178] F. Birkelbach. *Aufbau eines Drehmomentmagnetometers.* Zulassungsarbeit, München, 2009.

[179] S. M. Stishov, A. E. Petrova, S. Khasanov, G. Kh. Panova, A. A. Shikov, J. C. Lashley, D. Wu., and T. A. Lograsso. Heat capacity and thermal expansion of the itinerant helimagnet mnsi. *Journal of Physics: Condensed Matter*, 20(23):235222 (6pp), 2008.

[180] C. Pfleiderer. private communication, 2006.

[181] R. Georgii, P. Böni, D. Lamago, S. Stüber, S. V. Grigoriev, S. V. Maleyev, A. I. Okorokov, H. Eckerlebe, P. K. Pranzas, B. Roessli, and W. E. Fischer. Critical small-angle scattering of polarised neutrons in MnSi. *Physica B*, 350:45–47, 2004.

[182] C. Pappas, E. Lelièvre-Berna, P. Falus, P. M. Bentley, E. Moskvin, S. Grigoriev, P. Fouquet, and B. Farago. Chiral Paramagnetic Skyrmion-like Phase in MnSi. *Phys Rev. Lett.*, 102(19):197202, 2009.

[183] S. V. Maleyev. Cubic magnets with Dzyaloshinskii-Moriya interaction at low temperature. *Phys. Rev. B*, 73(17):174402, 2006.

[184] C. Pfleiderer, G. J. McMullan, and G. G. Lonzarich. Pressure induced crossover of the magnetic transition from second to first order near the quantum critical point in MnSi. *Physica B: Condensed Matter*, 206-207:847–849, 1995.

[185] C. Pfleiderer, G. J. McMullan, S. R. Julian, and G. G. Lonzarich. Magnetic quantum phase transition in MnSi under hydrostatic pressure. *Phys. Rev. B*, 55:8330–8338, 1997.

[186] A. J. Schofield. Non-Fermi liquids. *Cont. Phys.*, 40:95–112, 1999.

[187] C. Pfleiderer, S. R. Julian, and G. G. Lonzarich. Non-fermi liquid nature of the normal state of itinerant-electron ferromagnets. *Nature*, 414:427, 2001.

[188] N. Doiron-Leyraud, I. R. Walker, L. Taillefer, M. J. Steiner, S. R. Julian, and G. G. Lonzarich. Fermi-liquid breakdown in the paramagnetic phase of a pure metal. *Nature*, 425:595–599, 2003.

[189] P. Pedrazzini, D. Jaccard, G. Lapertot, J. Flouquet, Y. Inada, H. Kohara, and Y. Onuki. Probing the extended non-Fermi liquid regimes of MnSi and Fe. *Physica B: Condensed Matter*, 378-380:165 – 166, 2006. Proceedings of the International Conference on Strongly Correlated Electron Systems - SCES 2005.

[190] C. Pfleiderer, P. Böni, T. Keller, U. K. Rößler, and A. Rosch. Non Fermi Liquid Metal Without Quantum Criticality. *Science*, 2871:8330–8338, 2007.

[191] Y. J. Uemura, T. Goko, I. M. Gat-Malureanu, J. P. Carlo, P. L. Russo, A. T. Savici, A. Aczel, G. J. Macdougall, J. A. Rodriguez, G. M. Luke, S. R. Dunsiger, A. Mccollam, J. Arai, C. Pfleiderer, P. Böni, K. Yoshimura, E. Baggio-Saitovitch, M. B. Fontes, J. Larrea, Y. V. Sushko, and J. Sereni. Phase separation and suppression of critical dynamics at quantum phase transitions of MnSi and $(Sr_{1x}Ca_x)RuO_3$. *Nature*, 3:29, 2007.

[192] J. M. Hopkinson and H-Y. Kee. Origin and consequence of an unpinned helical magnet: application to partial order in MnSi under pressure. *arXiv*, pages 8330–8338, 2007.

[193] C. Pfleiderer, D. Reznik, L. Pintschovius, and J. Haug. Magnetic Field and Pressure Dependence of Small Angle Neutron Scattering in MnSi. *Phys. Rev. Lett.*, 99(15):156406, 2007.

[194] C. Pfleiderer, D. Reznik, L. Pintschovius, and J. Haug. Magnetic Field and Pressure Dependence of Small Angle Neutron Scattering in MnSi. *Phys. Rev. Lett.*, 99(15):156406, 2007.

[195] B. Roessli, P. Böni, W.E. Fischer, and Y. Endoh. Chiral Fluctuations in MnSi above the Curie Temperature. *Phys. Rev. Lett.*, 88(23), 2002.

[196] F. Semadeni, P. Böni, Y. Endoh, B. Roessli, and G. Shirane. Direct observation of spin-flip excitations in MnSi. *Physica B*, 267-268:248, 1999.

[197] A. Neubauer, C. Pfleiderer, B. Binz, A. Rosch, R. Ritz, P. G. Niklowitz, and P. Böni. Topological Hall Effect in the A Phase of MnSi. *Phys. Rev. Lett.*, 102(18):186602, 2009.

[198] `http://www.frm2.tum.de/dienste/probenumgebung/ausstattung/ccr/index.html`.

[199] B. Binz and A. Vishwanath. Chirality induced anomalous-Hall effect in helical spin crystals. *Physica B*, 403:1336, 2008.

[200] P. M. Chaikin and T. C. Lubensky. *Principles of Condensed Matter Physics*. Cambridge University Press, 1995.

[201] O. Nakanishi, A. Yanase, A. Hasegawa, and M. Kataoka. The origin of the helical spin density wave in MnSi. *Solid State Communications*, 35(12):995 – 998, 1980.

[202] T. Keller, R. Golub, and R. Gähler. Neutron spin echo - a technique for high resolution neutron scattering. *R. Pike, P. Sabatier (Eds.), Scattering and Inverse*

Scattering in Pure and Applied Science, Academic Press, San Diego, CA, 1264:2002, 2002.

[203] M. Janoschek. private communication, 2009.

[204] A. Bauer. *Quantenphasenübergänge und Skyrmion-Gitter in $Mn_{1-x}Fe_xSi$ und $Mn_{1-x}Co_xSi$.* Masters Thesis, München, 2009.

[205] T. Adams. *Skyrmion Gitter und partielle Ordnung in B20 Übergangsmetall Verbindungen.* Masters Thesis, München, 2009.

[206] J. S. Pedersen, D. Posselt, and K. Mortensen. Analytical Treatment of the Resolution Function for Small-Angle Scattering. *J. Appl. Cryst.*, 23:321, 1990.